VNIVERSITAT DE VALÈNCIA

Facultad de Química
Departamento de Química Inorgánica
Instituto de Ciencia Molecular (ICMol)

Biocompatible Porous Coordination Polymers and their Application in Catalysis and Environmental Remediation

Polímeros de Coordinación Porosos Biocompatibles y su Aplicación en Catálisis y Remediación Ambiental

Tesis Doctoral
Programa de Doctorado en Química

Paula Sara Escamilla Berenguer

Mayo 2023

Dirigida por los Dres. Emilio Pardo Marín y Jesús Ferrando Soria

D. **Emilio Pardo Marín**, Doctor en Ciencias Químicas, profesor titular del departamento de Química Inorgánica de la Facultad de Química de la Universitat de València y miembro del Instituto de Ciencia Molecular (ICMol) y D. **Jesús Ferrando Soria**, Doctor en Ciencias Químicas, miembro del Instituto de Ciencia Molecular (ICMol) y del Dpto. de Química Inorgánica de la Facultad de Química de la Universitat de València

CERTIFICA/N:

Que la memoria que presenta Dña. **Paula Sara Escamilla Berenguer**, titulada "***Polímeros de coordinación porosos biocompatibles y su aplicación en catálisis y remediación ambiental***", corresponde al trabajo realizado bajo nuestra dirección en el Instituto de Ciencia Molecular y el Departamento de Química Inorgánica de la Universitat de València, para su presentación como Tesis Doctoral en el Programa de Doctorado en Química de la Universitat de València.

Y para que así conste, firmamos el presente certificado en Paterna, a 25 de mayo de 2023.

Fdo.: Dr. Emilio Pardo Marín

Fdo.: Dr. Jesús Ferrando Soria

A mi familia, en especial
a mi madre y hermana;
sin ellas, no sería quien soy.

Agradecimientos / Acknowledgments

Hace 4 años, a una recién graduada en química le propusieron hacer un viaje, y no un viaje cualquiera, sino uno lleno de montañas rusas, donde a veces te encuentras en lo más alto y otras en lo más bajo, donde a veces nada tiene sentido y donde otras aparece un rayo de luz para iluminar el camino. Ahora ese viaje está acabando y aunque a veces las fuerzas flaquean, la constancia y perseverancia siempre prevalecen, haciendo que este viaje llegue a su fin de la mejor manera, que, por supuesto, no hubiera sido posible sin la ayuda y apoyo de un gran número de personas.

En primer lugar, quiero agradecer inmensamente a mis directores la oportunidad que me dieron de trabajar junto a ellos. Gracias, Emilio, por confiar en aquella estudiante de 22 años y darme la oportunidad de investigar junto a ti. Gracias por todas las horas dedicadas a mi formación profesional, por esas clases de CrystalMaker, por ayudarme a ver la luz cuando solo veía oscuridad y confiar siempre en mí. Jesús, gracias por ser un apoyo incondicional en este viaje, por las infinitas charlas sobre ciencia y vida, por entenderme y aconsejarme, por transmitirme tu pasión por la investigación y por creer en mí.

Además de mis directores de tesis, tengo que hacer una mención especial a la Prof. Donatella Armentano. Gracias por el inmenso esfuerzo y dedicación que has puesto en la resolución de cada una de las estructuras presentes en esta tesis. Sé que no ha sido tarea fácil, considerando que el tamaño de los cristales no era en absoluto el más adecuado. Espero que aún te queden muchas neuronas para seguir resolviendo un sinfín de nuevas estructuras. También agradecer al Dr. Antonio Leyva su dedicación puesta en “explotar” todos los sitios activos catalíticamente de estos nuevos MOFs.

Por otra parte, me gustaría agradecer a todos mis compañeros que me han acompañado durante este recorrido, con los que he compartido logros pero también lloros. En especial, a Marta V. por acogerme, guiarme y por todos esos consejos que me diste y que he ido aplicando. A José Miguel, aunque el camino profesional juntos fue corto, los dos sabemos que tenemos un amigo para siempre, gracias por contagiarme con tus curiosidades, tanto científicas como personales. A Cristina, juntas emprendimos este viaje y juntas acabamos. A pesar de nuestras discrepancias, que bonito es poder decir que somos un claro ejemplo de compañerismo, porque siempre hemos estado apoyándonos y guiándonos la una a la otra. A Fani, gracias por ser tan buena y por poner paz en medio de la tormenta. A Nuria, aunque tu paso fue breve, gracias por amenizar esas mañanas de labo con nuestros “radiopatios”. A Xavi, por esta última etapa en el que has tenido que aguantar mis días malos, mis desahogos y siempre has sabido encontrar palabras de ánimo y apoyo y transmitirme tu serenidad. A Nico, por tus

gestiones de compra y por esas medidas de magnetismo, las que espero algún día salgan a la luz. Y Thais, la más veterana y nueva al mismo tiempo, aunque has llegado en el último momento, gracias por escucharme, entenderme y por tus innumerables consejos.

No podía olvidarme sin duda alguna de Loli, amiga y compañera. Gracias por esas comidas que nos han servido de desahogo tanto a nivel profesional como personal, por esos ratitos al mediodía de desconexión, por estar siempre dispuesta a encenderme el "teamViewer" para que pueda conectarme al equipo de adsorción, por mantenerme informada de cada movimiento del "dewar" y de cuántos "puntitos" tengo en las gráficas, por esas medidas de XPS, aunque a veces me saques picos que no quiero, por esos partidos de pádel, que sin duda alguna, tenemos que mejorar, pero sobre todo, gracias por estar siempre ahí durante estos años.

Walter, qué bonito que el destino nos haya hecho coincidir. Es difícil encontrar a alguien con quien conectar, y sin duda alguna, tú y yo hacemos "matching" en casi todos los sentidos. Has llegado en una de las etapas más difíciles para mí. Gracias por abrazarme cuando lloro, por animarme a seguir, por darme consejos, aunque después haga lo que quiera, gracias por las infinitas carcajadas que compartimos juntos, por tus masajes reconfortantes, por sacudirme de vez en cuando y decirme lo que no quiero escuchar, por esas terapias de choque, por nuestros momentos de locura, por esos cantos en el "FordFi" y por esas sesiones intensas en el gym. Sin duda alguna, eres una de las cosas más bonitas que me ha dado este viaje.

Por supuesto que no puedo olvidarme de mi segundo grupo. Gracias por invitarme a cada una de vuestras fiestas, por compartir momentos únicos en Granada, en la cena del ICMol o haciendo slime. Rita, Irene, Miguel, Alessandro, Juan, Delia, Nacho y Carlos, gracias por adoptarme y hacerme sentir como una más. Alejandro, mira que me gusta la fiesta, pero tú no te quedas atrás. Gracias por enseñarme un poco vuestro mundo de espectros, por ser un gran profesor del fluorímetro, espero que algún día se nos vean recompensadas todas las horas que nos hemos tirado en esa sala. Raquel, gracias por creer en mis MOFs, por tratar de dar una explicación a todas esas bandas, por intentar darles una bonita aplicación y por hacerme sentir parte de vosotros.

Tampoco puedo olvidarme del resto de compañeros del ICMol, a los chicos de al lado (como yo les llamo): Rubén, Carlos y Alejandro; y a los de Coordi, en especial a Marta O., Renato, Perucho y Nadia. Espero no haberos molestado mucho con mis sesiones de música en el labo. A Alejandro, gracias por preparar y enviar cada uno de los paquetes que he necesitado. A Alejandra, por tu paciencia infinita, por las tantísimas muestras que me has medido y por estar

siempre predispuesta a encontrar una solución cuando el equipo se estropeaba. A Pascual y Cristian, por solucionar cualquier problema electrónico o mecánico con los que he tropezado. También a Enrique, Javier y Pilar, por las tantísimas horas que he pasado en vuestra sección, muchas de ellas a vuestro lado, absorbiendo todo el conocimiento que tenéis sobre SEM.

¿Qué decir de mi estancia en Italia? Gracias Donatella, Teresa, Rita, Pegah y Waseem por hacerme sentir como una más de vosotros. Sin duda alguna, fue una experiencia única que me permitió crecer tanto profesional como personalmente. Además, el destino hizo que coincidiera allí con gente española increíble. Gracias Nuria, Miguel, Irene y María, por hacerme sentir como en casa, a pesar de estar a miles de kilómetros de distancia.

También me gustaría agradecerles a mis amigas (las + bonitas): Adriana, Loli, Mjo, Almu, Andrea M., Andrea G. y Yoli, por todo el apoyo incondicional que recibo. Aunque no comprendáis mi mundo al 100%, siempre estáis ahí, creyendo y confiando en mí. Gracias por esos momentos de desconexión, ya sea con una cervecita o un heladito en la mano, o haciendo lo que más nos gusta, comer. No importa el lugar, ya sea en la playa, en un cumpleaños, en una discoteca, en Nochevieja o en Fallas, cualquier momento es bueno si estamos juntas. Chicas, la vida es más vida si estáis a mi lado. ¡Os quiero!

Por último, quiero expresar lo afortunada que me siento de tener la gran familia que tengo. Sin duda alguna, ellos son el motor de mi vida. Gracias a todos y cada uno de los miembros de la familia Escamilla Berenguer, pero en especial a mis padres (Alfredo y Yolanda), a mi hermana (Yoli), a Juanjo, a Manu, a mis abuelos (Pepa, Justina y Alfredo) y a mi hija perruna (Gucci) por vuestra ayuda incondicional, por apoyarme en todas mis decisiones, por dejarme caer, recogerme y curarme las heridas de la vida. Pero, sobre todo, gracias por creer y confiar en mí SIEMPRE. Gracias a vosotros, hoy soy la mujer que soy ahora. Os quiero incondicionalmente.

No te rindas, aun estas a tiempo
de alcanzar y comenzar de nuevo,
aceptar tus sombras, enterrar tus miedos,
liberar el lastre, retomar el vuelo.

No te rindas que la vida es eso,
continuar el viaje,
perseguir tus sueños,
destrabar el tiempo,
correr los escombros y destapar el cielo.

No te rindas, por favor no cedas,
aunque el frio queme,
aunque el miedo muerda,
aunque el sol se esconda y se calle el viento,
aun hay fuego en tu alma,
aun hay vida en tus sueños,
porque la vida es tuya y tuyo también el deseo,
porque lo has querido y porque te quiero.

Porque existe el vino y el amor, es cierto,
porque no hay heridas que no cure el tiempo,
abrir las puertas quitar los cerrojos,
abandonar las murallas que te protegieron.

Vivir la vida y aceptar el reto,
recuperar la risa, ensayar el canto,
bajar la guardia y extender las manos,
desplegar las alas e intentar de nuevo,
celebrar la vida y retomar los cielos,

No te rindas por favor no cedas,
aunque el frio queme,
aunque el miedo muerda,
aunque el sol se ponga y se calle el viento,
aun hay fuego en tu alma,
aun hay vida en tus sueños,
porque cada dia es un comienzo,
porque esta es la hora y el mejor momento,
porque no estas sola,
porque yo te quiero.

Mario Benedetti

INDEX

Abbreviations

MOFs: Metal-Organic Frameworks

PCPs: Porous Coordination Polymers

IUPAC: International Union of Pure and Applied Chemistry

COFs: Covalent Organic Frameworks

1D: One-Dimensional

2D: Two-Dimensional

3D: Three-Dimensional

SBUs: Secondary building units

HKUST: Hong Kong University of Science and Technology

ZIF: Zeolitic imidazolate frameworks

SCXRD: Single-crystal X-ray diffraction

MIL: Materials of Institut Lavoisier

PSMs: Post-synthetic methods

SC to SC: Single-crystal to single-crystal

PSMO: Post-synthetic metathesis and oxidation

DMF: *N,N*-Dimethylformamide

BET: Brunauer-Emmett-Teller

IRMOFs: Isoreticular metal-organic frameworks

DUT: Dresden University of Technology

T_c: Curie temperature

SCO: Spin-crossover

HS: High spin

LS: Low spin

SMM: Single-molecule magnets

SIMs: Single-ion magnets

LMOFs: Luminescent metal-organic frameworks

LMTC: Ligand-to-metal charge transfer

MLCT: Metal-to-ligand charge transfer

VOCs: Volatile organic compounds

SACs: Single-atom catalyst

SCCs: Supramolecular coordination complexes

SNMCs: Sub-nanometer metal nanoclusters

PBS: Phosphate-buffered solution

CAs: Contrast agents

MRI: Magnetic resonance imaging

PPCP: Pharmaceuticals and personal care products

MTV-MOFs: Multivariate metal-organic frameworks

TMAOH: Tetramethyl ammonium hydroxide

DFT: Density functional theory

BG: Brilliant green

EO: ethylene oxide

EC: ethylene carbonate

PO: propylene carbonate

PC: propylene carbonate

Resumen

De acuerdo con el reglamento sobre depósito, evaluación y defensa de la tesis doctoral, establecido en el real decreto 99/2011, de 28 de enero, por el cual se regulan las enseñanzas oficiales de doctorado, y según lo dispuesto en el artículo 7 (tesis doctoral presentada en una lengua diferente de las oficiales de la Universitat de València), en esta sección se presenta un resumen amplio, en castellano, de la temática que aborda la presente tesis resaltando los objetivos, la metodología empleada y las conclusiones.

Introducción

Uno de los principales objetivos de la investigación científica es buscar soluciones a problemas reales de la sociedad. Debido a la constante evolución de las distintas sociedades humanas, y al continuo cambio en el estilo de vida de éstas, cada día nos enfrentamos a nuevos retos y problemas que deben ser abordados por la ciencia. En particular, la ciencia de los materiales, encargada de sintetizar y caracterizar nuevos materiales, y de mejorar los ya conocidos, permite, en muchas ocasiones, encontrar una solución a problemas existentes. Por ejemplo, el desarrollo de los materiales porosos ha sido fundamental tanto en el desarrollo de nuevas tecnologías, usadas en nuestra vida diaria, como en la mejora de muchos procesos industriales. Estos materiales porosos han llamado la atención de muchos científicos debido al interés que suscita obtener materiales con un espacio confinado, de tamaño nanométrico, y la posibilidad de utilizar estos poros, a modo de nanoreactores químicos, llevando a cabo reacciones químicas en su interior.

Los materiales porosos se pueden definir como aquellos que presentan una red interconectada de poros (vacíos) accesibles, que son además permeables a cualquier fluido (líquido o gaseoso). Estos tipos de materiales han sido

ampliamente utilizados desde el antiguo Egipto hasta la actualidad, siendo los más conocidos el carbón activo y las zeolitas, que han sido muy utilizados en campos tan importantes como la descontaminación ambiental o la catálisis. En 1995, el investigador Omar M. Yaghi, al revisar diversas publicaciones de otros investigadores y adentrarse en la exploración de materiales porosos innovadores, acuñó el término "metal-organic framework (MOF)" para referirse a una nueva clase de materiales porosos, formados por la combinación de metales y ligandos orgánicos. Desde entonces, las publicaciones donde aparece el término “MOF” han experimentado un crecimiento exponencial, año tras año, dedicadas tanto al descubrimiento de estructuras desconocidas hasta el momento como al estudio de nuevas propiedades y aplicaciones.

Los MOFs, también conocidos como polímeros de coordinación porosos (PCPs), se definen como estructuras híbridas orgánicas-inorgánicas de naturaleza cristalina, formadas por iones metálicos o grupos de metales polinucleares (también llamados unidades de construcción secundarias o SBUs, siglas del término inglés “secondary-building units”) coordinados a una gran variedad de ligandos orgánicos para formar estructuras, bi- o tridimensionales, porosas. Debido a la gran cantidad de metales y de ligandos orgánicos disponibles para construir estas redes, el número de posibles estructuras con diferentes composiciones, topologías y, por tanto, distintas propiedades físicas y químicas, es prácticamente infinito. En este contexto, seleccionando de manera racional las unidades de construcción (química reticular), se pueden obtener materiales diseñados “a la carta”.

Entre las características más destacadas de los MOFs podemos encontrar una gran porosidad, lo que se traduce en una gran área superficial, una elevada cristalinidad, permitiendo su caracterización mediante técnicas de difracción de rayos X y una riquísima química huésped-anfitrión, lo que permite encapsular, por medio de estas interacciones estabilizantes, una gran variedad de moléculas

tanto de naturaleza orgánica como inorgánica, en el interior de estos canales. Por todo lo expuesto, los MOFs tienen aplicaciones en muchos y bien diferenciados campos, como en adsorción y separación de gases, remediación ambiental, transporte y liberación de fármacos, magnetismo, sensores luminiscentes, catálisis, etc.

Objetivos

En general, los objetivos principales de la presente tesis son, por una parte, obtener y caracterizar nuevos polímeros de coordinación porosos (MOFs) ensamblados con ligandos oxamidatos, derivados de biomoléculas como son los aminoácidos, y métales biocompatibles como el zinc y, por otra, el estudio de las propiedades y aplicaciones que éstos presentan. En este sentido, pretendo mostrar en esta tesis ejemplos reales donde estos nuevos MOFs podrían ser aplicados, resaltando así la importancia que estos compuestos tienen en diferentes áreas tecnológicas. De este modo, los resultados obtenidos pretenden expandir el conocimiento que mi grupo de investigación tiene en la obtención de nuevos MOFs.

Los materiales sintetizados en esta tesis doctoral tienen una doble funcionalidad. Por un lado, gracias a las propiedades intrínsecas que tienen las estructuras formadas, permiten ser utilizados como fotocatalizadores para la degradación de contaminantes orgánicos en ecosistemas acuáticos (capítulo 2) o como catalizadores heterogéneos, bien catalizando una reacción enzimática conocida, lo que permitirá entender de manera más precisa, el funcionamiento y mecanismo de algunas enzimas (capítulo 3) o bien catalizando, de manera eficiente, una reacción industrial de importancia (capítulo 4). Por otra parte, estos materiales combinan una química huésped-anfitrión increíble y, presumiblemente, biocompatibilidad, por el uso de biomoléculas y biometales. Este hecho permite augurar que estos MOFs puedan servir como “vasijas” para

encapsular fármacos en sus canales, permitiendo su uso en medicina, en procesos de liberación lenta de medicamentos, y también para encapsular metales catalíticamente activos con la finalidad de crear nuevos catalizadores.

Para la consecución de estos objetivos, se han seguido los siguientes pasos:

(i) Diseño de procedimientos sintéticos adecuados tanto para obtener MOFs a gran escala (polvo microcristalino) como para la obtención de monocristales, pudiendo así caracterizarlos a través de difracción de rayos X en monocristal. Para ello, se han llevado a cabo métodos de precipitación directas y de difusión lenta, respectivamente.

(ii) Estudiar las características, físicas y químicas, que los nuevos materiales obtenidos presentan, con el objetivo de poder aplicarlos en los campos donde pueden mostrar un mejor desempeño. Con este fin, se han recurrido a técnicas de caracterización comúnmente utilizadas en estos tipos de compuestos, como son: difracción de rayos X (DRX), tanto en monocristal, lo que permite conocer con exactitud la estructura de la red formada, como en polvo, para confirmar que el nuevo material sintetizado sea isoestructural o isoreticular a otro de estructura conocida; análisis elemental (AE), para determinar, de forma cuantitativa, la composición elemental de estos materiales (C, H, N y S); espectroscopia de infrarrojo (IR), que permite relacionar las señales con los grupos presentes y ayuda a interpretar la coordinación de los metales; análisis termogravimétrico (ATG), que permite determinar las moléculas de disolvente, tanto de cristalización como de coordinación, presentes en la estructura y aporta información sobre la

estabilidad térmica del MOF, y adsorción de gases, generalmente N_2, para estudiar la porosidad permanente así como el área superficial de cada material.

(iii) Explorar las posibles propiedades físico-químicas de los nuevos materiales sintetizados, y las aplicaciones que puedan surgir de éstas. Cabe destacar que algunos de estos estudios se han hecho en colaboración con otros grupos de investigación. En particular, las medidas catalíticas han sido llevadas a cabo en colaboración con el profesor Antonio Leyva (UPV-CSIC) y la resolución estructural con la profesora Donatella Armentano de la Universidad de Calabria (Italia).

Metodología

Para llevar a cabo las síntesis de los diferentes materiales que se presentan en esta tesis, hemos utilizado tanto las herramientas que nos proporcionan la química orgánica –para la síntesis de ligandos– como la química de coordinación, con el fin de ensamblar las redes tridimensionales. Además, se ha aprovechado la experiencia que mi grupo de investigación ha adquirido, en las dos últimas décadas, con ligandos de tipo oxamato y oxamidato en la síntesis de compuestos de coordinación y, más recientemente en la construcción de nuevos polímeros de coordinación porosos multifuncionales.

En la presente tesis, todos los ligandos oxamidatos que han sido utilizados, ya habían sido preparados y utilizados previamente por mi grupo de investigación. Se sabe que la utilización de ligandos oxamidato, derivados de amino ácidos, son quirales y, como consecuencia, esta quiralidad es transmitida al MOF final formado. Además, los MOFs formados con estos ligandos presentan gran estabilidad en medio acuoso y, como característica sintética fundamental, el empleo de estos ligandos en la síntesis de MOFs permite controlar la naturaleza

de los grupos funcionales presentes en los poros del MOF, ya que estos provienen del residuo del aminoácido utilizado. De este modo se pueden introducir nuevas propiedades a la estructura final. En concreto, se han empleado dos ligandos derivados de los aminoácidos *L*- serina y *S*-metil-*L*-cisteina, cuyos residuos poseen un grupo hidroxilo y un grupo tioeter, respectivamente.

En la química de los MOFs, cada vez hay más rutas sintéticas que permiten ganar cierto control sobre la dimensionalidad, topología y estabilidad de las redes que se pretenden formar. Entre las diferentes metodologías sintéticas existentes, en la presente tesis se ha utilizado la conocida como precipitación directa, eligiendo de manera racional tanto el ligando utilizado como los metales empleados. La precipitación directa en la síntesis de MOFs presenta varias ventajas en comparación con otros métodos sintéticos:

1. Sencillez y facilidad. Este método no requiere condiciones de reacción extremas ni el empleo de equipos sofisticados, por lo que hace que la síntesis sea más accesible y reproducible. Además, no requiere de otras etapas sintéticas complejas, reduciendo así el tiempo y aumentando la facilidad de producción.
2. Bajo coste. Como consecuencia de lo descrito en el punto anterior, la precipitación directa suele ser un método económico para la síntesis de MOFs.
3. Control de tamaño y morfología de partícula. Ajustando los diferentes parámetros, como la velocidad de adición, la temperatura o el volumen de las disoluciones se pueden controlar el tamaño y la morfología de los MOFs formados.
4. Rendimientos elevados. Seleccionar los precursores y disolventes adecuados, así como un control adecuado de las condiciones de reacción permite una precipitación cuantitativa de los materiales

sintetizados, permitiendo, por tanto, la obtención de rendimientos altos.

5. Escalabilidad. Este método es fácilmente escalable, lo que significa que se pueden obtener grandes cantidades del material en un solo paso. Este punto tiene especial relevancia para aquellos MOFs con futuras o potenciales aplicaciones industriales, donde la síntesis a gran escala es fundamental.

Tal y como se ha descrito con anterioridad, la metodología sintética para obtener los compuestos se basa en técnicas de precipitación directa. Estas técnicas consisten en la desprotonación e hidrólisis de los ligandos oxamidato obtenidos previamente con ayuda de una base, en este caso el hidróxido de tetrametilamonio (TMAOH) y la posterior coordinación de Zinc(II) y, en algunos MOFs, también de otros metales alcalinotérreos como Ca(II) o Sr(II). De esta manera se obtienen las redes tridimensionales, en disolución acuosa y a temperatura ambiente. Estas redes se pueden obtener en dos formas cristalinas diferentes:

(ii) Monocristales, mediante técnicas de difusión lenta. En concreto, se han empleado los llamados “tubos en H”, los cuales permiten introducir en una parte una disolución que contenga los metales y, en la otra parte, otra disolución con el ligando desprotonado por la adición de la base. Estos tubos se rellenan con un disolvente adecuado que permita una lenta difusión de ambos componentes y, por tanto, una buena cristalización. La correcta elección del disolvente, así como la temperatura, la concentración de ambas disoluciones y la sal del metal empleado, permitirá la obtención de monocristales adecuados para su resolución mediante difracción de rayos X en monocristal.

(ii) Polvo microcristalino, a través de técnicas de precipitación directa en una sola etapa. Para ello, se preparan dos disoluciones acuosas, una que contiene

el/los metal/es necesarios para formar la red y por otra parte, una disolución también acuosa que contenga el ligando desprotonado e hidrolizado con ayuda de la base. A temperatura ambiente y con ayuda de un agitador magnético, se adiciona la disolución que contiene el ligando (gota a gota) sobre la disolución de metal/es, apareciendo rápidamente un polvo cristalino blanco, fácil de aislar mediante filtración.

En el caso del MOF derivado de la *L*-serina, se ha obtenido un MOF homometálico que solo contiene zinc como metal, coordinando los grupos oxamidato del ligando en posición *trans*, formando unidades diméricas que se unen entre ellas mediante los grupos carboxilatos. Para los dos MOFs obtenidos a partir del derivado de la *S*-metil-*L*-cisteina, se han obtenido dos estructuras heterometálicas isoestructurales que contienen Zn(II) y M(II) (siendo M = Ca(II) o Sr(II)). En ambos casos, el zinc coordina los grupos oxamidatos en posición *trans*, formando complejos dinucleares que se unen entre ellos mediante la coordinación de cationes Ca(II) o Sr(II) a través de los grupos carboxilato para formar la red tridimensional final.

Estructura de la tesis

La presente tesis se ha estructurado en cinco capítulos. El primero de ellos es una introducción general. En éste se ha realizado una revisión de los MOFs más relevantes que han sido sintetizados y utilizados desde su descubrimiento. Con este fin, se han resaltado las aportaciones más relevantes de una serie de investigadores que han ayudado a desarrollar este campo, como son Hoskins, Robson, Yaghi, Kitagawa y Férey, entre otros. De forma paralela al desarrollo de este tipo de materiales porosos (MOFs) se han desarrollado también diferentes técnicas de caracterización como la microscopia electrónica (SEM y TEM) y , sobre todo, la difracción de rayos X en monocristal, la cual ha permitido situar a los MOFs como el material poroso mejor caracterizado, debido

al desarrollo de nuevos y más eficientes difractómetros. En la introducción también se ha hecho especial mención a los principales métodos sintéticos utilizados hasta la fecha para la obtención de nuevas estructuras y se explican las principales propiedades y características que estos compuestos presentan. Los MOFs presentan una serie de características únicas que explican este auge y creciente interés. En concreto, podemos resaltar su gran porosidad, su elevada cristalinidad y una increíblemente rica química "huésped-anfitrión", propiedades que hacen que estos compuestos sean ampliamente utilizados en diferentes campos tecnológicos, los cuales se detallan en el penúltimo apartado de la introducción, dándose también ejemplos representativos de cada una de las aplicaciones expuestas. Por último, se ofrece una visión general de los resultados previos obtenidos por mi grupo de investigación, relacionados con la preparación de MOFs basados en oxamidatos de Cu(II), derivados de aminoácidos, y las propiedades que éstos exhiben, de manera que sirven como antecedentes y punto de partida del trabajo realizado en esta tesis doctoral.

Los capítulos dos, tres y cuatro recogen todos los resultados obtenidos durante la realización de esta tesis. En ellos se presentan tres nuevos MOFs, que han sido caracterizados de manera laboriosa, y se muestran sus propiedades más destacadas y sus posibles aplicaciones.

El quinto y último capítulo, llamado conclusiones y perspectivas, se puede dividir en dos partes: la primera, donde se recopilan todos los materiales sintetizados en esta tesis, y que han sido totalmente caracterizados y cuyas propiedades y aplicaciones han sido exploradas en profundidad, y la segunda, en la cual se presentan otros materiales, que han sido también obtenidos durante esta tesis junto a medidas preliminares que permiten evaluar su potencial en una gran variedad de aplicaciones. Todo lo expuesto en la presente tesis refleja el potencial de esta familia de MOFs y constata la cantidad de trabajo que aún queda por hacer.

Resultados experimentales

En este apartado se resumen los resultados, más relevantes, obtenidos en esta tesis, los cuales han sido enumerados en los capítulos comprendidos del 2 al 4. Se pueden clasificar en tres partes bien diferenciadas: MOFs utilizados como fotocatalizadores para la remediación ambiental, MOFs usados como catalizadores en reacciones enzimáticas y MOFs empleados como catalizadores heterogéneos en aplicaciones industriales.

Uso de MOFs como fotocatalizadores para la remediación ambiental:

En el capítulo 2, llamado "Photodegradation of brilliant green dye by a Zinc bioMOF" se obtuvo y caracterizó un nuevo MOF, sintetizado a partir del ligando oxamidato derivado del aminoácido *L*-Serina y cationes Zinc(II), con fórmula $\{Zn^{II}_2[(S,S)\text{-serimox}](H_2O)_2\} \cdot H_2O$ (**Zn^{II}_2-serimox**) (dónde (*S,S*)-serimox es [bis[(*S*)-serine]oxalil diamida]).

Gracias a la obtención de monocristales, este MOF se pudo caracterizar mediante difracción de rayos X en monocristal. **Zn^{II}_2-serimox** cristaliza en el grupo espacial quiral $P4_12_12$ del sistema tetragonal y consiste en una red tridimensional con canales cuadrados, en la cual los fragmentos $[Zn^{II}_2(S,S)\text{-serimox}]$ se encuentran situados en los vértices de estos canales. Estas redes robustas se construyen a partir de unidades diméricas de Zn(II) con puentes *trans*-oxamidato~~s~~, $[Zn^{II}_2(S,S)\text{-serimox}]$, que se ensamblan entre sí a través de los grupos carboxilato. Esta nueva estructura presenta poros cuadrados de aproximadamente 0.3 nm, que crecen a lo largo del eje *b*. Estos canales están decorados por el grupo alcohol primario (grupo hidroximetilo) procedentes del residuo de la serina, que apuntan hacia el interior de los poros y son los responsables de la química resultante huésped–anfitrión.

Tras una completa caracterización del compuesto, el MOF se testó como fotocatalizador para degradar el colorante verde brillante. El material demostró ser capaz de degradar completamente dicho colorante (a CO_2 y H_2O) en disolución acuosa bajo irradiación UVC (250 nm) en solo 120 min con una eficacia del 100 %, en ausencia de cualquier otro oxidante o co-catalizador. Además, se pudo visualizar, por medio de la cristalografía, la molécula de CO_2 resultante, alojada en los poros del MOF.

Uso de MOFs como catalizadores enzimáticos:

En el capítulo 3, llamado "Degradation of penicillinic antibiotics by biomimetic Zn-based metal–organic frameworks" se obtuvo un nuevo MOF, sintetizado a partir del ligando oxamidato derivado del aminoácido *S*-metil-*L*-cisteina con cationes Zinc(II) y Calcio(II), con fórmula $\{Ca^{II}Zn^{II}_6[(S,S)\text{-Mecysmox}]_3(OH)_2(H_2O)\} \cdot 12H_2O$ (**$Ca^{II}Zn^{II}_6$-Mecysmox**) (dónde (*S,S*)-Mecysmox es bis[*S*-metil-*L*-cisteina]oxalil diamida]).

Mediante técnicas de difusión lenta, se obtuvieron cristales de este nuevo MOF siendo así capaces de resolver la estructura mediante difracción de rayos X en monocristal. **$Ca^{II}Zn^{II}_6$-Mecysmox** cristaliza en el grupo quiral espacial $P6_3$ y consiste en redes tridimensionales (3D) de calcio(II)-zinc(II) con canales hexagonales, de aproximadamente 0.7 nm de diámetro, donde se ubican las cadenas de tioeter ($–CH_2SCH_3$) del aminoácido. La red está construida a partir de unidades diméricas de zinc(II) con puentes *trans*-oxamidato, $\{Zn^{II}_2[(S,S)\text{-Mecysmox}]\}$, que actúan como uniones entre los cationes Ca(II) a través de los grupos carboxilatos y, además, están interconectados, mediante grupos de agua/hidróxido, con unidades diméricas de zinc(II) vecinas. Ambas características, el espacio vacío funcional del MOF y el entorno de coordinación de los cationes zinc(II), sugirieron que **$Ca^{II}Zn^{II}_6$-Mecysmox** podría actuar como un

catalizador eficiente, imitando a las enzimas β-lactamasas, que son responsables de la degradación de los antibióticos betalactámicos.

En este contexto, se evaluó la actividad que tenía este MOF como catalizador enzimático, observando una degradación eficiente del anillo β-lactámico de cuatro miembros presente en la amoxicilina. Este notable resultado constituye uno de los pocos ejemplos de MOFs capaces de imitar procesos enzimáticos catalíticos, que ha sido muy limitado hasta el momento. Además, este MOF también fue capaz de degradar otro antibiótico, como la ceftriaxona, dando como resultado tiotriazinona y 3-desacetildefotaxima, una reacción que anteriormente solo se podía llevar a cabo, en ausencia de catalizador, a pH = 5 y tras 12 h. de reacción. Gracias a la cristalinidad y robustez que caracteriza a esta familia de MOFs, se pudo resolver la estructura del MOF con la amoxicilina en sus canales, lo que permitió obtener dos resultados: por una parte, poder visualizar las interacciones huésped-anfitrión (interacciones llamadas "σ-hole"), responsables en última instancia de la actividad de la β-lactamasa y, por otra, permitió llevar a cabo cálculos teóricos (DFT), los cuales, de alguna manera confirman que la hidrólisis de la amoxicilina tiene lugar a través de la activación de una molécula de agua, que es promovida por el grupo hidroxilo puente de los cationes Zn(II), y, de manera concertada, se produce un ataque nucleofílico al carbonilo y la ruptura del enlace C-N del anillo β-lactámico. Todo esto representa un paso adelante en la comprensión de las enzimas β-lactamasas.

<u>Uso de MOFs como catalizadores heterogéneos en aplicaciones industriales:</u>

En el capítulo 4, llamado "Zinc based metal-organic frameworks for selective cycloaddition reactions" se obtuvó un nuevo MOF sintetizado a partir del ligando oxamidato, derivado del aminoácido *S*-metil-*L*-cisteina, con cationes zinc(II) y estroncio(II), con fórmula $\{Sr^{II}Zn^{II}_6[(S,S)\text{-Mecysmox}]_3(OH)_2(H_2O)\} \cdot 9H_2O$

(**$Sr^{II}Zn^{II}_6$-Mecysmox**) (dónde (*S,S*)-Mecysmox es bis[*S*-metil-*L*-cisteina]oxalil diamida]).

Este nuevo MOF es isoreticular al obtenido en el capítulo 3, presentando una única diferencia en la composición –la sustitución de los cationes Ca(II) por Sr(II)– lo que ha permitido una mayor robustez en el material. Dada la experiencia previa que tiene mi grupo de investigación en MOFs oxamidatos derivados de la *L*-metionina y S-metil-*L*-cisteina, que han mostrado capacidad de encapsular moléculas huésped de diferente naturaleza dentro de sus canales funcionales y la existencia de cationes Zn(II), que son accesibles dentro de la estructura y pueden actuar como centros catalíticos activos, se ha evaluado este MOF (**$Sr^{II}Zn^{II}_6$-Mecysmox**) como catalizador heterogéneo para la reacción de cicloadición de óxido de etileno y óxido de propileno con CO_2 para producir carbonatos de etileno y propileno. Ello permite ofrecer una alternativa atractiva a otros catalizadores heterogéneos. Se demostró el gran poder catalítico de este material, obteniéndose un rendimiento de hasta el 95 % en la obtención de carbonato de etileno y una selectividad del 100 %, sin reacciones competitivas de hidrólisis ni de polimerización. En cuanto a la obtención de carbonato de propileno, cuyo estudio se realizó con una mezcla equimolar de óxidos de etileno y propileno, se obtuvo una mezcla del 50 % de cada producto deseado. Teniendo en cuenta que el óxido de propileno es menos reactivo que el de etileno debido a factores estéricos, este resultado sugirió que el entorno catalítico del MOF permite una buena activación del oxido de propileno frente a la cicloadición de CO_2. Estos resultados muestran, una vez más, el poder catalítico que tienen los MOFs en síntesis selectivas de productos relevantes a nivel industrial.

Conclusiones

En la presente tesis doctoral, se ha sintetizado con éxito una nueva familia de estructuras metal-orgánicas (MOFs) basadas en ligandos de tipo

oxamidato, derivados de biomoléculas como son los aminoácidos, y metales biocompatibles como el Zn(II), y, en algunos casos, también el Ca(II) o Sr(II). Estos MOFs han sido ampliamente caracterizados mediante un gran abanico de técnicas de caracterización, destacando, gracias a su gran cristalinidad, la difracción de rayos X en monocristal. Así mismo, se han estudiado sus propiedades como (foto)-catalizadores para la degradación de contaminantes orgánicos y en reacciones de relevancia industrial y de interés para la salud pública. Los estudios presentados en esta tesis doctoral han permitido ampliar el conocimiento de los MOFs basados en ligando oxamidato, tanto a nivel de su distinta naturaleza como de sus aplicaciones.

En particular, se han sintetizado y caracterizado tres nuevos MOFs: un MOF homometálico, formado por cationes Zn(II) y ligandos oxamidato derivados del aminoácido natural *L*-serina, con fórmula $\{Zn^{II}_2[(S,S)\text{-serimox}](H_2O)_2\} \cdot H_2O$ (**Zn^{II}_2-serimox**) , el cual ha sido estudiado como fotocatalizador para degradar colorantes orgánicos presentes en aguas residuales (Capítulo 2: MOFs para la descontaminación ambiental); y dos MOFs heterobimetálicos, con fórmulas $\{Ca^{II}Zn^{II}_6[(S,S)\text{-Mecysmox}]_3(OH)_2(H_2O)\} \cdot 12H_2O$ (**$Ca^{II}Zn^{II}_6$-Mecysmox**) y $\{Sr^{II}Zn^{II}_6[(S,S)\text{-Mecysmox}]_3(OH)_2(H_2O)\} \cdot 9H_2O$ (**$Sr^{II}Zn^{II}_6$-Mecysmox**), utilizando en ambos casos un ligando oxamidato derivado del aminoácido *S*-metil-*L*-cisteína. Para **$Ca^{II}Zn^{II}_6$-Mecysmox,** se ha explorado su actividad en catálisis enzimática. En particular, como mímicos de las enzimas β-lactamasa, (Capítulo 3: MOFs en catálisis enzimática). Mientras que **$Sr^{II}Zn^{II}_6$-Mecysmox** ha sido investigado como catalizador en la reacción de cicloadición de óxido de etileno o óxido de propileno con CO_2 para la producción de carbonato de etileno y propileno (Capítulo 4: MOFs como catalizadores heterogéneos en aplicaciones industriales).

Además de los resultados expuestos, también ha sido posible obtener otros miembros de esta nueva familia de MOFs con ligandos oxamidato derivados de aminoácidos y cationes metálicos biocompatibles como zinc(II) y calcio(II), así

como se han podido realizar estudios preliminares para evaluar su potencial en diferentes aplicaciones.

En particular, se han preparado los siguientes dos MOFs y tres MTV-MOFs isoreticulares a los presentados en esta tesis doctoral: $\{Ca^{II}Zn^{II}_6[(S,S)\text{-alamox}]_3(OH)_2(H_2O)\} \cdot 10H_2O$ (**$Ca^{II}Zn^{II}_6$-alamox**) [donde alamox es bis[*L*-alanina]oxalil diamida], $\{Ca^{II}Zn^{II}_6[(S,S)\text{-methiomox}]_3(OH)_2(H_2O)\} \cdot 8H_2O$ (**$Ca^{II}Zn^{II}_6$-methox**) [donde methox es bis[*L*-metionina]oxalil diamida], $\{Ca^{II}Zn^{II}_6[(S,S)\text{-Mecysmox}]_{1.5}[(S,S)\text{-methox}]_{1.5}(OH)_2(H_2O)\} \cdot 9H_2O$ (**$Ca^{II}Zn^{II}_6$-Mecysmox/methox**), $\{Ca^{II}Zn^{II}_6[(S,S)\text{-Mecysmox}]_{1.5}[(S,S)\text{-alamox}]_{1.5}(OH)_2(H_2O)\} \cdot 11H_2O$ (**$Ca^{II}Zn^{II}_6$-Mecysmox/alamox**) y $\{Ca^{II}Zn^{II}_6[(S,S)\text{-methox}]_{1.5}[(S,S)\text{-alamox}]_{1.5}(OH)_2(H_2O)\} \cdot 8H_2O$ (**$Ca^{II}Zn^{II}_6$-methox/alamox**).

Estos materiales presentan una gran diversidad de composición tanto en número de ligandos constituyendo las redes, como en la naturaleza de los grupos funcionales decorando sus poros. De ahí surge el potencial de los mismos, y los dota de diferentes características para poder presentar aplicación en campos tan diversos como sensores luminiscentes, fotocatálisis, liberación de fármacos, remediación ambiental, separación de gases y catálisis heterogénea.

Los cationes Zn(II) pueden exhibir luminiscencia bajo ciertas condiciones y sus propiedades luminiscentes se ven afectadas en función de su entorno de coordinación. En este contexto, se han llevado a cabo estudios preliminares de luminiscencia, los cuales muestran el potencial de este material para actuar como sensor luminiscente, al presentar una banda de emisión entorno a 480nm –atribuida al Zn(II)–, y la habilidad de albergar moléculas huésped en su interior. Esta doble funcionalidad, nos permitiría estudiar el efecto en la luminiscencia de la interacción de las moléculas huésped con el Zn(II), y por ende, usar esa diferente respuesta como señal característica de cada uno de los analitos que se quieran detectar.

Un buen número de complejos de coordinación de Zn(II), incluidos los polímeros de coordinación o MOFs, se han estudiado como fotocatalizadores. En concreto, en esta tesis hemos presentado los resultados del **Zn^{II}_2-serimox**, el cual se ha mostrado como un fotocatalizador eficiente en la degradación total del colorante orgánico verde brillante. En este contexto, nos hemos planteado dar un paso hacia delante en el uso de MOFs como fotocalizadores, haciendo uso de su rica química huésped-anfitrión. Así, hemos encapsulado un complejo con propiedades fotocatalíticas, dicloruro de bis(ciclopentadienil)titanio, dentro del MTV-MOF **$Ca^{II}Zn^{II}_6$-Mecysmox/alamox**. Cabe destacar que gracias a la gran cristalinidad de estos materiales, hemos podido resolver la estructura del adsorbato, lo cual nos ha proporcionado información muy relevante sobre la especie fotocatalítica encapsulada y nos sitúa en una posición excelente para estudiar su potencial como fotocatalizador.

La lenta liberación de fármacos en el cuerpo humano representa una línea de investigación muy importante dentro del campo de la nanomedicina. La naturaleza porosa de los MOFs, y la posibilidad de preparar MOFs biocompatibles, los convierte en excelentes candidatos como portadores de fármacos, que puedan posteriormente ser liberados lentamente. Así, por ejemplo, los materiales MIL-100 y 101(Fe) han mostrado resultados muy relevantes. La familia de MOFs presentados en esta tesis reúnen todos los requisitos para ser utilizados como liberadores de fármacos: (i) una rica química huésped-anfitrión, que garantiza una adecuada carga e inmovilización de los fármacos y, (ii) una elevada biocompatibilidad, al estar constituidos por bioligandos derivados de aminoácidos y metales biocompatibles como Zn y Ca – ver ensayos de biocompatibilidad en el capítulo 5. Por ello, con los materiales presentados en esta tesis tenemos previsto estudiar las propiedades de adsorción y desorción de fármacos de interés.

Los MOFs de cobre isoreticulares a los presentados en esta tesis han mostrado excelentes propiedades en la captura de contaminantes del agua (remediación del agua) y en la captura y separación de gases. Así pues, en base a las mejoras que muestran los MOFs presentados en esta tesis –*i.e*. facilidad de sintetizar a gran escala y naturaleza benigna con el medioambiente de sus componentes–, como perspectiva de trabajo hemos planteado estudiar sus propiedades para ambas aplicaciones. En particular, resultarán de especial interés los nuevos MTV-MOFs, al ofrecer la posibilidad de una mayor eficiencia en la captura de contaminantes/separación de gases por efectos sinérgicos entre los diferentes grupos funcionales decorando los poros.

En los últimos años, muchas son las investigaciones que se han centrado en utilizar los MOFs como nanorreactores químicos, aprovechando el espacio limitado dentro de los poros para hacer crecer pequeñas especies metálicas *in situ*. En particular, mi grupo de investigación ha demostrado el enorme potencial de los MOFs de cobre, isoreticulares a los presentados en esta tesis, para preparar especies metálicas sub-nanométricas con propiedades catalíticas muy interesantes. Por ello, y siguiendo este enfoque, se prevé utilizar los MOFs obtenidos en esta tesis con el mismo fin. Además, la ventaja añadida de los materiales presentados en esta tesis es que también podrían explotarse las propiedades ópticas de las especies metálicas sub-nanométricas albergadas en los poros, al haberse eliminado los iones cobre y sus efectos de “quenching” de las mismas. En particular, en base a la experiencia de mi grupo de investigación, los candidatos más adecuados serían todas aquellas estructuras con grupos funcionales tioéter decorando los canales, dada la gran afinidad que el azufre posee por los iones metálicos blandos, como por ejemplo plata, paladio y platino. Así, hemos obtenido dos resultados preliminares muy prometedores, resultado de encapsular cationes Ag(I) o Pd(II) dentro del MOF **$Ca^{II}Zn^{II}_6$-Mecysmox**,

demostrando una vez más el gran potencial que presentan los MOFs preparados durante la realización de esta tesis doctoral.

Abstract

This thesis falls within the field of Materials Science and Coordination Chemistry, as it focuses on the design of new porous materials. Specifically, it explores the synthesis, characterization, and applications of new Zn-based Metal-Organic Frameworks (MOFs).

In general, the main objectives of this thesis are twofold. Firstly, to obtain and characterize new porous coordination polymers (MOFs) assembled with oxamidate ligands derived from biomolecules such as amino acids, as well as biocompatible metals like zinc. Secondly, to study the properties and potential applications of these materials. In this sense, I aim to provide real-life examples showcasing the potential applications of these new MOFs, thereby emphasizing the significance of these compounds in different technological areas. The obtained results are intended to contribute to the expansion of knowledge within my research group regarding the synthesis of novel MOFs.

To achieve these objectives, the following tasks have been carried out:

(i) Designing suitable synthetic procedures to obtain MOFs on a large scale (microcrystalline powder) and single crystals, thereby enabling their characterization through single-crystal X-ray diffraction. For this purpose, direct precipitation methods and slow diffusion methods have been employed, respectively.

(ii) To study the physical and chemical characteristics of the newly obtained materials in order to apply them in fields where they can demonstrate better performance, several commonly used characterization techniques for these types of compounds have been employed. These techniques include single-crystal X-ray diffraction (SCXRD), powder X-ray diffraction (PXRD), elemental

analysis (EA), infrared spectroscopy (FT-IR), thermogravimetric analysis (TGA) and N_2 adsorption.

(iii) Explore the potential physical and chemical properties of the newly synthesized materials and the applications that may arise from them. It is worth noting that some of these studies have been conducted in collaboration with other research groups. In particular, catalytic measurements have been carried out in collaboration with Professor Antonio Leyva (UPV-CSIC), and structural resolution has been conducted in collaboration with Professor Donatella Armentano from the University of Calabria (Italy).

The results obtained in this work are classified intro three different chapters. In chapter 2, it is present a novel bio-friendly water-stable Zn-based MOF (**Zn^{II}_2-serimox**), derived from the natural amino acid *L*-serine, which was able to efficiently photodegrade water solutions of brilliant green dye in only 120 min. The total degradation was followed by UV-Vis spectroscopy and further confirmed by single-crystal X-ray crystallography, revealing the presence of CO_2 within its channels. Reusability studies further demonstrate the structural and performance robustness of **Zn^{II}_2-serimox**.

In chapter 3, a novel Zn-based metal–organic framework derived from the amino acid *S*-methyl-*L*-cysteine is presented (**$Ca^{II}Zn^{II}_6$-Mecysmox**), possessing functional channels capable to accommodate and interact with antibiotics, which catalyze the selective hydrolysis of the penicillinic antibiotics amoxicillin and ceftriaxone. In particular, MOF **$Ca^{II}Zn^{II}_6$-Mecysmox** degrades, very efficiently, the four-membered β-lactam ring of amoxicillin, acting as a β-lactamase mimic, expanding the very limited number of MOFs capable of mimicking catalytic enzymatic processes. Combined single crystal X-ray diffraction (SCXRD) studies and density functional (DFT) calculations offer unique snapshots on the host guest-interactions established between amoxicillin and the functional channels

of **$Ca^{II}Zn^{II}_6$-Mecysmox**. This allows to propose a degradation mechanism based on the activation of a water molecule, promoted by a Zn-bridging hydroxyl group, concertedly to the nucleophilic attack to the carbonyl moiety and the cleaving of C-N bond of the lactam ring.

In chapter 4, another Zn-based metal-organic framework isoreticular to the previous one shown in chapter 3 is presented (**$Sr^{II}Zn^{II}_6$-Mecysmox**) with a slight different in composition- the substitution of Ca(II) cations with Sr(II) ones- which has resulted in enhanced robustness of the material. Taking advantage of the catalytic properties of Zn(II) atoms and the confined spaces that this structure offer, porous size and available open metal sites, this MOF was able to catalyze the cycloaddition of ethylene oxide and propylene oxide with CO_2 to obtain ethylene and propylene carbonates, obtaining yields up to 95% and complete selectivity. These results further confirm the catalytic power that MOFs have in selective syntheses of industrially relevant products, providing an appealing alternative to the current heterogeneous catalysts.

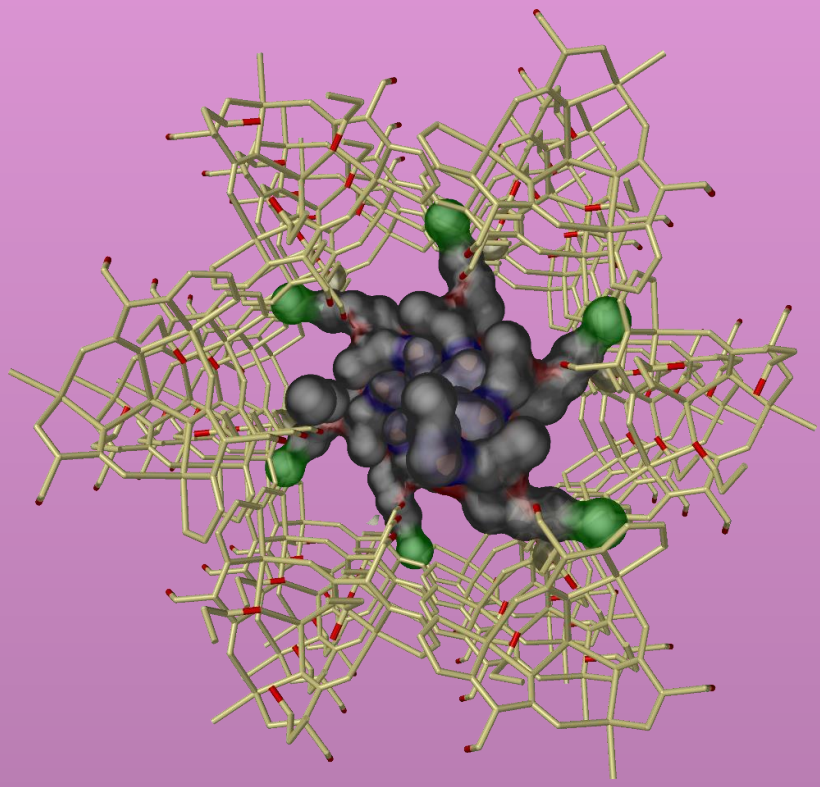

CHAPTER 1

Introduction

1.1. Porous materials: an overview

Historically, the development and evolution of societies have been closely related to their ability to meet new needs. From a scientific perspective, materials science plays a crucial role in synthesizing new compounds to address these needs and facilitate societal progress. This field of science is responsible for developing synthesis processes for the preparation of functional and structural materials, as well as establishing relationships between structure and properties. Another objective of this field is to evaluate the diverse applications of new materials. In particular, developing porous materials has been essential for numerous technologies in our daily lives and in various industrial applications. Furthermore, these types of materials have attracted the attention of many scientists around the world because of the interest in obtaining nanometer-sized confined spaces and the possibility of creating new chemistry inside them.[1]

By definition, a porous material is a solid matrix composed of an interconnected network of pores (voids) filled with a fluid (liquid or gas). It is known that these materials have been used since ancient Egypt. In particular, around 1500 BC, the Egyptians used charcoal as a medical absorbent.[2] In 400 BC, Hippocrates recommended water filtration to remove contaminants and prevent illness.[3] Kaolinite, a type of clay mineral, has been used worldwide for its antidiarrheal properties. Even in the commercial medication “Kaopectate”, this porous material was used as an active ingredient until the 1980s.[4] Through the 18th and 19th centuries, these compounds were increasingly used in different fields. For example, activated carbon was used to produce the well-known Tennessee whiskey[5] and served as the main adsorbent in gas masks during World War I due to its improved adsorption capacity over traditional cotton or fiber adsorbents.[6]

During the 18th century, a new type of porous material was discovered by Cronstedt, a Swedish chemist. During his analysis, he observed that heating the mineral "stilbite" produced large amounts of steam from water that had been previously adsorbed by the material. Based on this, he named the material "zeolite", from the Greek words "zeo" (to boil) and "lithos" (stone).[7] Since then, many scientists have focused on studying the properties of these materials and developing new synthetic zeolites. The research and synthesis of new classes of zeolites led to their increasing use in industry during the mid-20th century. They are still widely used today, particularly in the fields of catalysis and sorbents.[8]

So far, only classical porous materials have been discussed. However, in the 20th century, due to new industrial needs and the development of new characterization techniques, a new large group of porous materials known as porous coordination polymers (PCPs) emerged. According to the International Union of Pure and Applied Chemistry (IUPAC), a coordination polymer is "a coordination compound with repeating coordination entities extending in 1, 2, or 3 dimensions"[9] and a coordination compound is "any compound that contains a coordination entity. A coordination entity is an ion or neutral molecule composed of a central atom, usually that of a metal, to which is attached a surrounding array of atoms or groups of atoms, each of which is called a ligand".[10] The first publication where the term "coordination polymer" was used was in 1916 by Y. Shibata[11] to describe dimers and trimers of various cobalt(II) ammine nitrates. However, it was not used again until 1963 when J. Bailar reintroduced it to describe bis-(β-diketone)-beryllium complexes.[12]

Thanks to advances in X-ray crystallography, these materials became well-known during the second half of the 20th century. In 1965, E. A. Tomic[13] published a series of high molecular weight porous coordination polymers using

di- or trivalent aromatic carboxylic acids as ligands and different metals such as nickel, iron and zinc, highlighting their thermal stability.

Between the 1980s and 1990s, it became evident that coordination polymers could exhibit high levels of crystallinity. In 1990, Robson, Hoskins et al.[14] introduced a novel cationic porous coordination polymer with the formula $[Cu(TCTPM)]^+$ (TCTPM = 4,4',4'',4'''-tetracyanotetraphenylmethane) (Figure 1.1). This polymer was capable of exchanging anions, with an estimated pore volume of 700 $Å^3$ occupied by BF_4^- ions that could be exchanged by PF_6^- while the crystallinity of the material is maintained.[15] The researchers also applied the simplified description of crystal structures developed by Prof. Wells, which represented the structures as networks consisting of polyhedral with various geometries (e.g., tetrahedral, octahedral, etc.) linked together by sticks.[16]

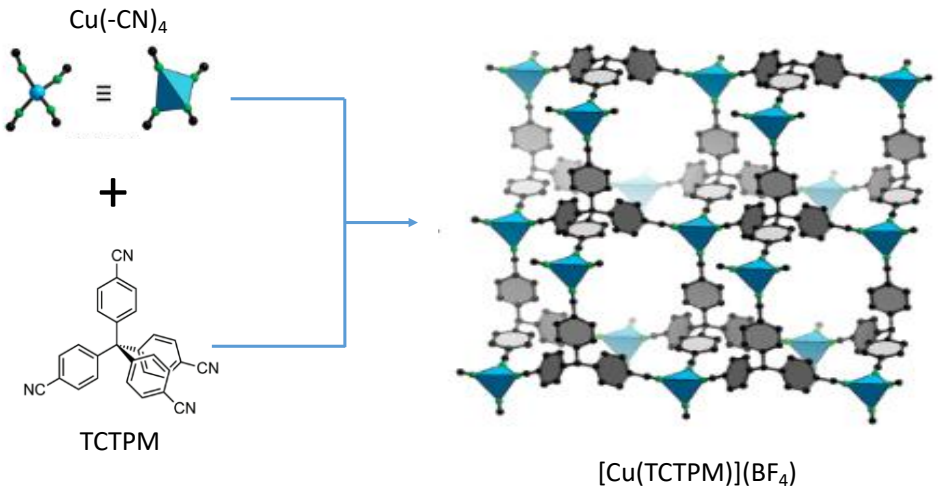

Figure 1.1. Crystal structure of cationic PCP $[Cu(TCTPM)(BF_4)$. Colour code: Cu, blue; C, gray; N, green. Adapted from ref. 15.

In 1994, Fujita and co-workers reported the catalytic properties of a two-dimensional coordination polymer (CP) $[Cd(4,4'\text{-bipy})_2(NO_3)_2]$ (4,4'-bipy = 4, 4'-bipyridine).[17] Also in the same year, Susumu Kitagawa made significant

advancements in the field by designing porous hybrid inorganic-organic materials. He reported three different copper(I) compounds using the same linker (phenazine) but varying the salt used.[18]

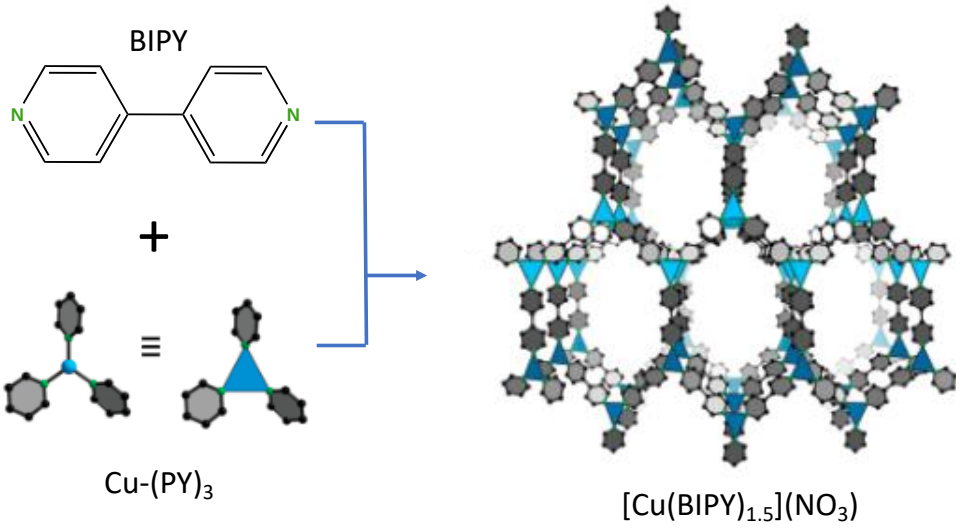

Figure 1.2. Crystal structure of $[Cu(BIPY)_{1.5}](NO_3)$. Colour code: black, C; green, N; blue polyhedral, Cu. Adapted from ref. 15.

At this stage, scientists worldwide were aware that the science of porous materials was undergoing significant progress due to the unique properties and potential applications of these compounds, as well as the possibility of achieving an infinite number of controlled structures by changing the metallic center and organic ligand.

Just one year later, in 1995s, Omar M. Yaghi[19] introduced the term metal-organic frameworks (MOFs), for the first time, after the hydrothermal synthesis of a 3D-polymeric coordination compound of copper with the formula $Cu^{I}(4,4'\text{-bpy})_{1.5}NO_3(H_2O)_{1.25}$ (4,4'-bpy = 4,4'-bipyridine) (Figure 1.2), characterized by X-ray diffraction and showed large rectangular channels filled by nitrate ions. In this work, he also demonstrated the accessibility of the channels, as nitrate ions could

be exchanged in aqueous media with other simple ions such as SO_4^{2-} and BF_4^-. This property was later recognized with the term "host-guest" chemistry.

Reticular chemistry emerged at the moment that new structures of these porous materials started to be discovered and the need to explain them arose. Today, it is understood as the chemistry of linking well-defined molecular building blocks by strong bonds to form extended crystalline structures.[20] This definition implies that: a) the control in the construction of frameworks is achieved due to molecular building blocks providing a well-defined structure and geometry, b) the resulting frameworks exhibit thermal and chemical stability due to the strong bonds, and c) these materials can be definitively characterized by X-ray or electron diffraction techniques, thanks to their crystallinity.

In 2005, a new class of porous materials known as COFs (Covalent-Organic Frameworks) emerged. They are also classified as reticular frameworks. The first COFs to be reported were 2D structures (COF-1 and COF-5),[21] while two years later, in 2007, the first 3D COFs, COF-105 and COF-108, were reported also by Prof. O. Yaghi.[22] Unlike MOFs, which are composed of secondary building blocks consisting of metal ions/clusters and organic ligands, COFs are made up of molecular organic building units connected by covalent bonds, comprising light elements such as H, B, C, N, and O.

1.2. Metal-Organic Frameworks

When Omar M. Yaghi introduced the term Metal-Organic Framework, he did not know how important this term would become in the fields of chemistry, materials science, and nanotechnology. But what exactly is a MOF? The IUPAC defines a MOF as "*a Coordination Compound continuously extending in 1, 2 or 3 dimensions through coordination bonds (Coordination Polymer or alternatively Coordination Network) with an open framework containing potential voids*".[9] In

other words, a Metal-Organic Frameworks, also knowns as Porous Coordination Polymers (PCPs), are a new class of hybrid organic-inorganic crystalline compounds made up of metal ions or polynuclear metal clusters (also called secondary building units or SBUs) coordinated to organic ligands to form one-, two-, or three-dimensional structures that present porosity (Figure 1.3). Therefore, in this doctoral thesis, the terms Metal-Organic Frameworks (MOFs) and Porous Coordination Polymers (PCPs) will be used interchangeably.

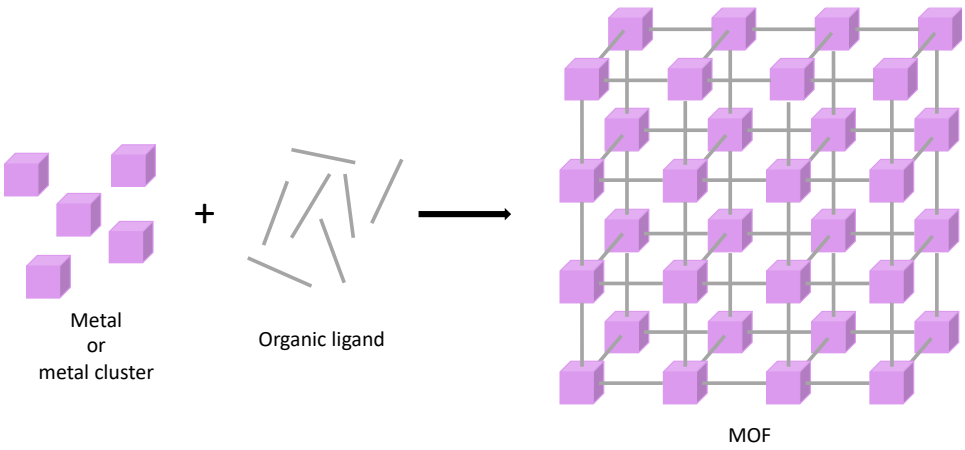

Figure 1.3. Schematic representation of the components to assemble a Metal-Organic Framework.

Over the last almost three decades, interest in MOFs has grown exponentially due to the infinite number of possible structures that can be obtained, each with different compositions, topologies, and chemical and physical properties. This is made possible by the wide variety of organic ligands and metal ions that can be used to build them, allowing for the design of polymers with different shapes, pore sizes, and surface functionality. Additionally, the possibility of post-synthetic modifications (PSMs) adds another dimension to the variability of these compounds.[23] Consequently, having good synthetic control allows for obtaining multifunctional materials,[24–26] where more than one physical/chemical property can be integrated in the compounds. This has led to

the use of MOFs in many different fields, such as gas sorption,[27] catalysis,[28] drug delivery,[29] magnetism,[25] among others.

1.2.1. Synthesis of Metal-Organic Frameworks

MOFs are basically composed of two main components: metal ions or metal clusters (SBUs) and organic ligands. Due to the possibility offered by reticular chemistry to rationally design MOFs and considering also the wide variety of available ligands and metals, a great structural variety with specific topologies can be obtained depending on the components used and the synthetic conditions.

Although there are examples of MOFs with species belonging to all metal groups, those most commonly used in synthesis are those of the first or second transition series. Depending on the metal used and its oxidation state, the coordination number can vary between 2 and 7, resulting in different geometries: linear, angular, Y- or T-shaped, tetrahedral, square planar, square pyramidal, trigonal bipyramidal, octahedral, and their corresponding distorted forms. The metal used will determine the degree and dimensionality of coordination of the ligands and the chemical and thermal stability of the resulting materials. It is becoming increasingly common to find MOFs constructed from lanthanides, which have a higher coordination number, between 7 and 10, resulting in new topologies in the structures and unsaturated coordination centers, which are very useful in catalytic applications, adsorption processes and the use of MOFs as sensors.[1] Additionally, in recent years, it is also very common to synthesize new heterobimetallic structures, taking advantage of the synergistic effects that both metals can present, such as the stability of a metal with a high formal charge and the catalytic properties of another metal with a lower charge.[30]

Organic ligands can be classified according to the number of binding sites they have with the metal or metal cluster as ditopic, tritopic, tetratopic, hexatopic, or octatopic. Polyamines, carboxylates, pyridyl and cyano groups, crown ethers, phosphonates, and imidazolates/pyrazolates are among the most widely used ligands.[31] Initially, carboxylic acids were the most commonly used ligands as each O-donor atom can coordinate with up to three metal ions, resulting in a wide variety of structures. However, due to the lability of the M-O bond, many structures are sensitive to hydrolysis, such as in the case of MOF-5, [Zn_4O(benzene-1,4-dicarboxylate)$_3$]. Therefore, there was a trend to replace carboxylate ligands with imidazole/pyrazole-type ligands, which are also capable of coordinating to metals, obtaining more robust M-N coordination bonds than M-O bonds. The choice of the ligand is crucial when establishing the rational synthesis of the MOF, as many of the properties of the final structure are determined by the ligand, such as flexibility, chemical stability, and porosity.

In the synthesis of MOFs, in addition nature of the metals and organic ligands used, there are many other factors that also play a major role in the formation of the final structure, such as concentration, pH, solvent nature, reaction time, temperature, and pressure. All of these can be controlled depending on the synthetic method employed.

1.2.1.1. Conventional synthesis

The term "conventional synthesis" refers to reactions that are carried out by conventional heating. Temperature is the main synthesis parameter in MOFs, and two methods can be distinguished: direct precipitation (or non-solvothermal) and solvothermal. The former is the simplest method that can be found in the literature. The reaction takes place after mixing all the reagents in the appropriate solvent below its boiling point and at atmospheric pressure. Some of the well-known MOFs have been synthesized using this route, such as MOF-5,

MOF-74, MOF-177, HKUST-1, or ZIF-8.[32,33] The advantages of this method are its speed and low cost. Since the conditions used are mild, the integrity of the basic components is guaranteed, allowing for good control of the final structure. The building entities have been rationally selected according to a specific coordination mode. In order to obtain single crystals for resolution, via single crystal X-ray diffraction, the reagents are introduced slowly to reduce the nucleation rate through different methods, such as slow evaporation, stratification, or slow diffusion through a membrane, gel, or H-tube. In this thesis, all the new materials obtained have been synthesized via direct precipitation, mixing the metals with the deprotonated ligand to obtain microcrystalline powder, and the respective crystals have been obtained through the slow diffusion technique using H-tubes.

The second method is known as solvothermal synthesis. Temperature is one of the main parameters to control in this type of synthesis, which takes place in closed containers under autogenous pressure above the solvent boiling point. If water is used as the solvent, they are known as hydrothermal synthesis. The temperature is increased to favor the formation of bonds, especially if kinetically inert ions are used, and is also used to ensure adequate crystallization and morphology. However, a balance must be struck in this parameter, as prolonged reaction times and high temperatures can lead to the decomposition of the organic ligand or final product. Another important parameter to consider is the cooling rate as, if it is too fast, it can affect the formation and growth of the crystals. It is one of the most commonly used classical methods in the synthesis of these compounds.[19]

1.2.1.2. Alternative synthesis

Every chemical reaction requires a transfer of energy. As previously mentioned, MOF syntheses are generally carried out through an energy transfer

in the form of conventional electrical heating. However, in recent years, the use of different energy sources such as microwave, ultrasound, or electric potential have been studied to synthesize new structures or improve the synthesis yield of already known structures. The importance of resorting to new synthetic methods is due to the possibility of obtaining new structures that could not be obtained otherwise. In addition, these new synthetic routes allow us to obtain different particle sizes and size distributions, as well as different morphologies that directly influence the properties of the material.

Microwave radiation synthesis has begun to be used to construct MOFs due to its improvements compared to conventional syntheses, such as shorter reaction times. This is because the radiation penetrates the reactants, heating them from the inside out, generating more uniform heating, higher yields, lower costs, and higher quality products without impurities. An example of an improvement compared to conventional synthesis is reported by Chang and co-workers. In the article, they indicate that the synthesis of HKUST-1 with the formula $Cu_3(BTC)_2(H_2O)_3]$ (BTC^{3-} = benzene-1,3,5-tricarboxylate) using microwave methods results in shorter reaction times, improved yield, and physical properties.[34]

Sonochemical methods are responsible for carrying out a chemical reaction through high-energy ultrasonic radiation. This method is based on acoustic cavitation, which involves the sequential formation, growth, and collapse of bubbles at a point where a high amount of energy is available, permitting reactions that were previously difficult to achieve.[35] Therefore, this method improves the reaction kinetics in the synthesis of many MOFs. In 2008, Jian and co-workers reported the first synthesis of MOFs through ultrasound, synthesizing the MOF $Zn_3(BTC)_2{\cdot}12H_2O$. When playing with different reaction times, they observed significant changes in yield and particle size.[36]

Finally, the electrochemical method is the most commonly used for the synthesis of MOFs in powder form on an industrial scale. The metal ion is continuously introduced by anodic dissolution into the reaction medium, which contains the organic ligands and a conductive salt, thus removing the anions of metal salts like nitrates, chlorides, perchlorates, etc. The main advantages of this method are the speed at which products are obtained and the use of milder reaction conditions such as not very high temperatures. Many well-known MOFs, such as HKUST-1, ZIF-8, MIL-100 (Al), and MIL-53 (Al), have been synthesized by this method, and various parameters including yield and properties have been compared depending on the synthesized method.[37]

1.2.1.3. Post-synthetic methods

Despite the number of ligands and metals that can be used to synthesize MOFs and the diversity of synthetic routes that have been studied so far to achieve new structures, it is often impossible to functionalize the material from the beginning due to problems in solubility, thermal or chemical stability of the precursors, incompatibility of functional groups, undesired reactions through functional groups of ligands and metal ions, among other causes. Post-synthetic modifications (PSMs) are presented as a solution to all these problems, they are an indispensable tool to obtain MOFs with improved properties that cannot be synthesized directly. Post-synthetic treatments do not modify the topology and the original structure of the compound through a transformation from a single crystal to a single crystal (SC-SC).[38] Several PSM approaches have been studied to date and can be grouped into modifications in the nature of the metal or ligand and adsorption/exchange of guest species, all through various mechanisms. [39] Figure 1.4 shows a schematic classification of the different PSMs applied to MOFs.

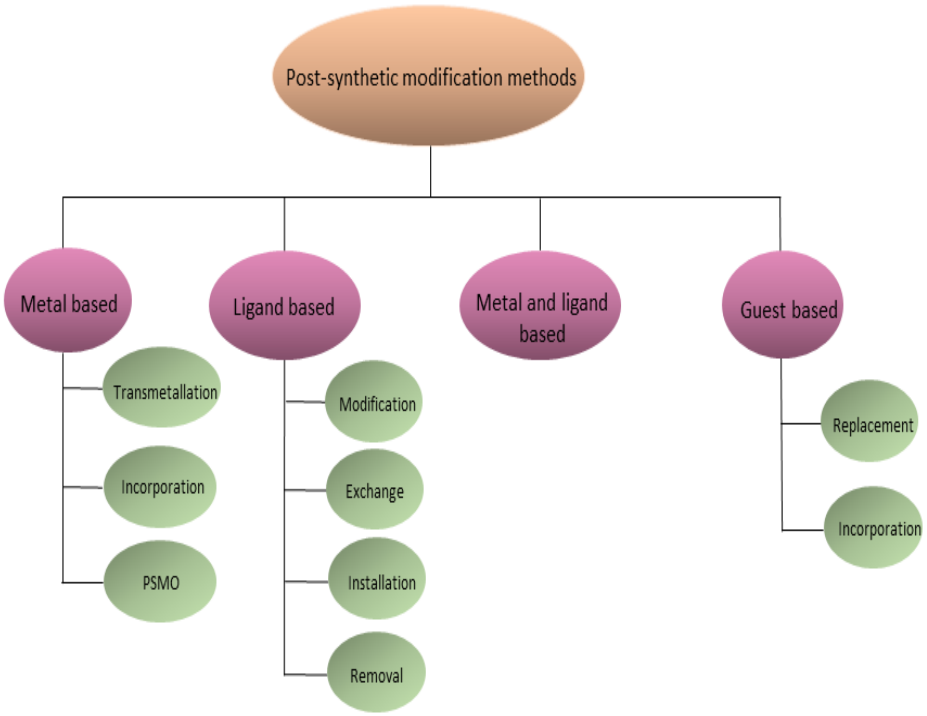

Figure 1.4. Classification of post-synthetic methods used in MOFs.

Among the PSMs that affect the metal of the framework, three procedures can be differentiated: (i) transmetallation of the metal nodes, partial or complete depending on the lability of the metal ions to be exchanged, the valence and coordination preferences of the incoming metal ion, the solvent used, and the chemical stability of the resulting MOF, (ii) inclusion of a metal ion or cluster, which can be carried out by coordination to an unsaturated site in the structure or by inclusion in the porous cavities. It is one of the most commonly used PSMs for the formation of MOFs as chemical nanoreactors for catalytic applications,[40] and (iii) post-synthetic metathesis and oxidation (PSMO), which is the least explored PSM of the three and is used to obtain MOFs with high-valent metals, such as creating titanium MOFs with valence (IV).[41]

As previously mentioned, the ligand also plays a very important role in the functionality of the MOF, therefore, PSMs that affect the ligand allow for materials with improved properties to be achieved. Among the PSMs for modifying the ligand are: (i) ligand modification, whose objective is to insert a ligand with a new functional group that can act as a site for the adsorption of new molecules without changing the initial structure of the parent MOF. For example, Wang and co-workers reported the synthesis of a MOF functionalized with a thiol group by modifying the exposed amine of the initial MOF (MOF NH_2-MIL-68) for use as an adsorbent for Hg(II) ions,[42] (ii) ligand exchange, which can result in structures similar to the initial MOF or completely different. Secondary or tertiary functional groups are usually used to construct structures that contain free functionalities,[39] (iii) ligand installation, which involves introducing a new ligand into predetermined sites without altering the original structure, and (iv) removal or labilization of ligands, which involves the use of a MOF containing saturated metals, a prolabil ligand, and a non-labile ligand. The prolabil ligand is removed after various procedures to achieve the defective MOF.

Finally, taking advantage of the most characteristic property of these materials, which is their porosity, PSMs can be applied by manipulating the molecules hosted in the cavities of the MOFs to achieve new functionalities. The removal of solvent molecules, that are usually retained in the pores, can be considered a PSM since the resulting structure has different properties, such as greater surface area than the initial MOF. In addition to the removal of molecules, new ones can also be incorporated, with the ultimate goal of obtaining multifunctional materials with different properties. The fact that MOFs can be used in various application areas based on their properties situates PSMs as an extremely powerful tool in MOF research.

1.2.2. Main characteristics of MOFs

As previously stated, MOFs are a type of materials that are primarily characterized by their porosity. Therefore, studying this property is crucial for a complete characterization of the compound and its correct application. The porosity of a material is defined as the ratio between the volume of the pores and the total volume occupied by the solid. In the case of MOFs, the term “porous” should be understood in such a way that even after removing the solvent molecules that occupy these cavities, the structure does not collapse (irreversible loss of crystallinity) and, therefore, the porosity is maintained (permanent porosity).

According to IUPAC, porous materials are classified into three main groups based on their pore size: (i) "microporous materials" with a pore size less than 2 nm, (ii) "mesoporous materials" with a pore size between 2 and 50 nm, and (iii) “macroporous materials” with pore sizes greater than 50 nm (Figure 1.5).[43] MOFs are typically classified as micro- to mesoporous materials. Gas adsorption isotherm measurements, usually using N_2 and Ar at standard boiling points, are the most commonly used technique for characterizing porous materials, generally, and MOFs in particular. These measurements allow us to study:

(i) Permanent porosity, which is determined by studying the structure's robustness after a process of thermal activation aimed at removing the solvent molecules present in the pores.

(ii) Accessible porosity and pore size distribution.

(iii) The different adsorption capacity of the gases, which depend on the MOF’s properties.

In general, gas adsorption results are usually represented on a graph that shows "the amount of gas adsorbed" as a function of "relative pressure". The IUPAC classifies these isotherms into six main groups,[43,44] with type I characteristic of microporous crystalline materials, and type II, III, and VI characteristic of mesoporous. In addition, macroporous materials can exhibit type II, III, IV, V, or VI isotherms.

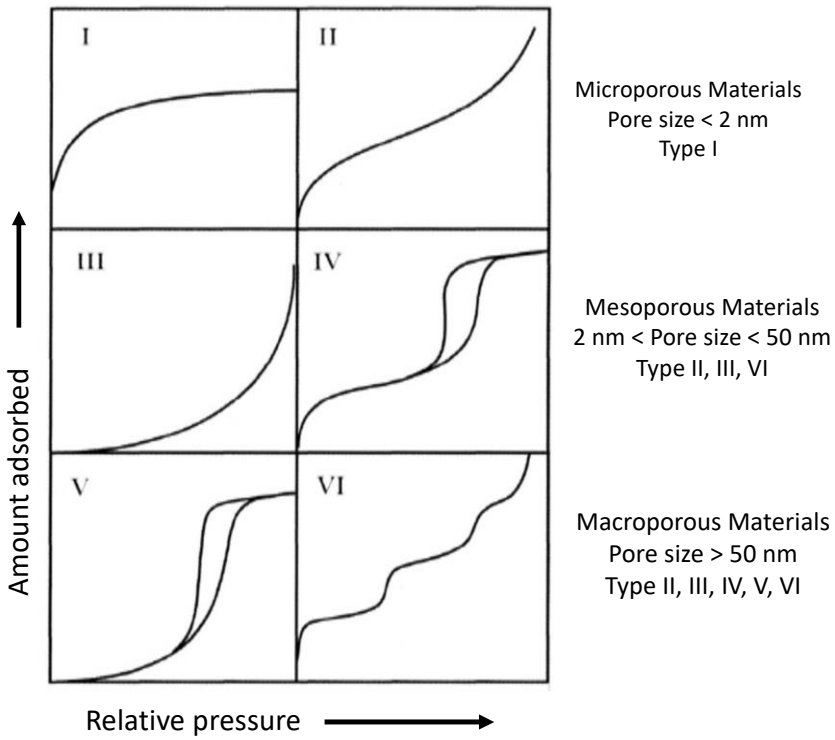

Figure 1.5. Adsorption isotherms types according to the IUPAC classification.

Although gas adsorption had been used to characterize traditional porous materials like zeolites, it was not until 1997 when Kitagawa, Kondo, and collaborators reported the adsorption isotherms of CH_4, N_2, and O_2 at high pressures and room temperature on the 3D structures $\{[M_2(4,4'\text{-bpy})_3(NO_3)_4](H_2O)_x\}_n$ (M=Co, Ni or Zn),[45] demonstrating that PCPs could adsorb guest molecules in the gas phase. However, under these measurement

conditions, accurate determination of the surface area and pore volume was not possible. One year later, in 1998, O. Yaghi demonstrated the permanent porosity of the MOF Zn(BDC)(DMF)(H_2O) (BDC^{2-}=1,4-benzenedicarboxylate), known today as MOF- 2, through nitrogen and carbon dioxide adsorption isotherms at low pressures (Figure 1.6).[46] These measurements allowed Yaghi to fully characterize the compound, including its surface area and pore volume.

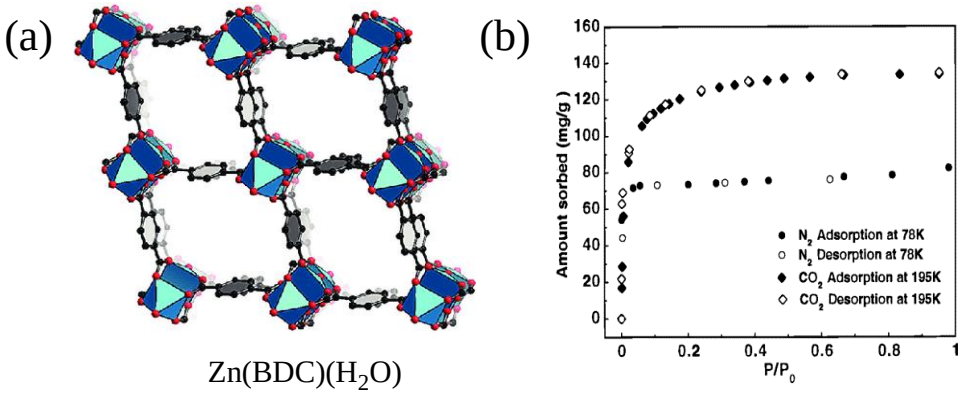

Figure 1.6. (a) Structure of Zn(BDC)(H_2O), (b) adsorption isotherm of previously activated Zn(BDC)(H_2O). Adapted from ref. 15 and 46.

Due to the wide variety of microporous coordination compounds that had been reported, Kitagawa and Kondo suggested a classification in 1998 into three groups based on their porous properties: first, second, and third generations (Figure 1.7).[47,48]

- First generation: porous compounds that only sustain guest molecules, and the framework collapses when these molecules are removed.[49]

-Second generation: porous compounds that exhibit permanent porosity. These materials are stable and robust even without guests in the pores.[19,50]

-Third generation: porous compounds that respond to external stimuli (light, electric field, guest molecules, pressure, among others)[51] by reversibly

changing their channels or pores. These compounds exhibit a flexible and dynamic framework. This generation introduces flexibility and adaptability of the frameworks as properties,[52] which were not studied until the early 2000s.[53]

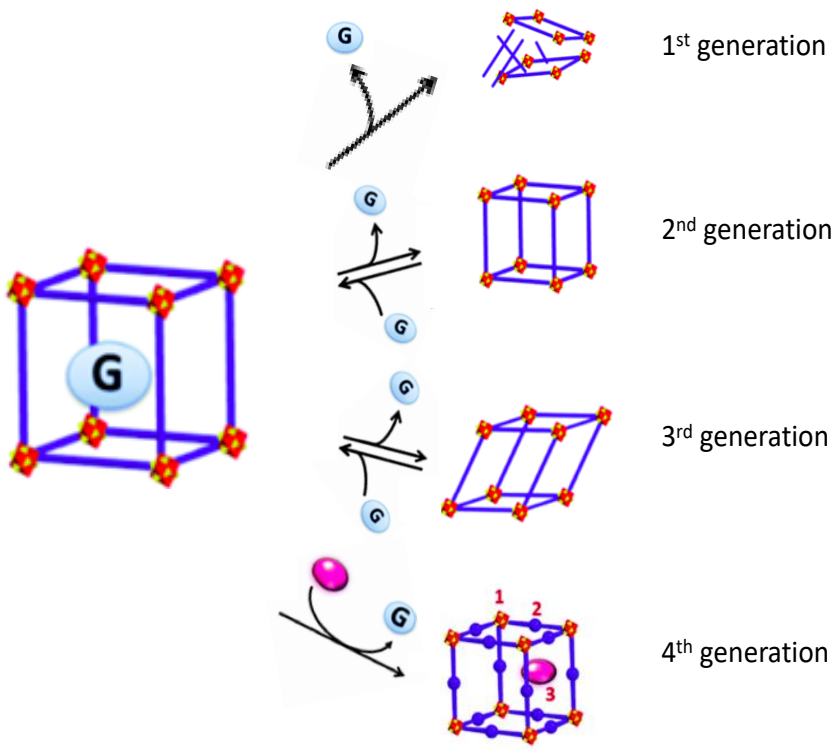

Figure 1.7. Classification of MOFs based on the response to the removal of guests encapsulated within the pores. Adapted from ref. 28.

In recent years, with the development of PSMs of MOFs,[23] Liu et al.[28] defined a fourth generation of porous materials as those whose pore size and chemistry can be modified through PSMs while maintaining the topology and structural integrity. More recently, in 2021, Kitagawa[54] proposed that the fourth generation should include MOFs with the following attributes abbreviated as HAD: (1) hybrid and hierarchy, (2) anisotropy and asymmetry, and (3) defect and disorder.[55,56]

In 1999, O. Yaghi and coworkers synthesized MOF-5 with formula $Zn_4O(BDC)_3(DMF)_8(C_6H_5Cl)$, which represented a breakthrough in the study of the porosity of these materials.[57] MOF-5 was synthesized using Zn_4O cluster and 1,4-benzo dicarboxylic acid as an organic linker by solvothermal technique. The structure exhibits a cubic and flexible 3D framework with higher surface area and pore volume than most porous crystalline zeolites (BET surface area of 2320 m^2g^{-1}, 0.92-1.04 $cm^3\ g^{-1}$ micropore and thermal stability up to 400°C).

Three years later, in 2002, this scientific incorporated the concept of the isoreticular series and reported that MOF-5 had a modular structure, with 16 isoreticular frameworks (IRMOF-1 to IRMOF-16) (Figure 1.8).[58] Yaghi, was able to obtain 16 different frameworks simply by changing the functionalized groups (– Br, $–NH_2$, $–OC_3H_7$, $–OC_5H_{11}$, $–C_2H_4$, and $–C_4H_4$) and the length of the linkers (biphenyl, tetrahydropyrene, pyrene, and terphenyl). One of these frameworks, IRMOF-16 represents up to 91.1% of the crystal volume, and their homogenous pores could vary from 3.8 to 28.8 Å, without changing the cubic 3D structure. Another member of this series, IRMOF- 6, can store a high amount of methane (240 cm^3g^{-1} at 36 atmospheres and ambient temperature) and others exhibit the lowest densities for a crystalline material at room temperature (0.41 to 0.21 g/cm^3 per gram, IRMOF-8, -10, -12, -14, -15 and -16).

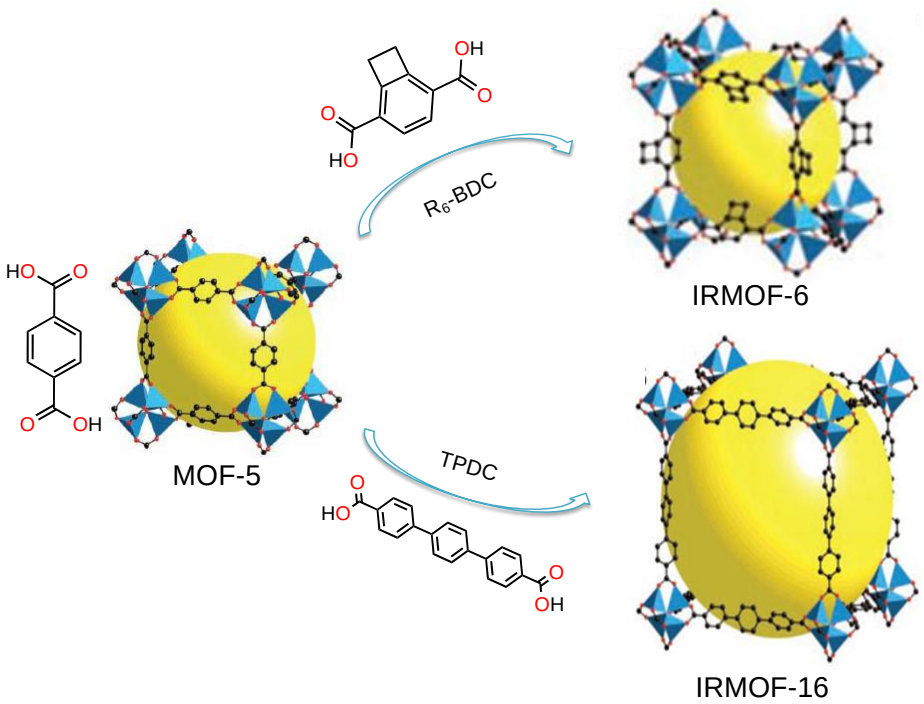

Figure 1.8. Structures of MOF-5, IRMOF-6, and IRMOF-16 illustrated for a single cube fragment of their respective cubic three-dimensional extended frameworks. Colour code: Zn (blue polyhedral), O (red spheres), C (black spheres). The yellow spheres indicate the maximum size of van der Waals spheres that can fit within the cavities without touching the framework. Adapted from ref. 58.

Metal-Organic Frameworks are micro- and mesoporous coordination compounds that can be classified not only as second-generation materials (known for their robustness and excellent gas storage and separation applications), but also as third-generation materials.[48,59] The third-generation MOFs exhibit flexible and dynamic structures due to weak bonds such as hydrogen bonds, pi-pi stacking, or van der Waals interactions, making them suitable for guest adsorption. The framework of the third-generation MOFs can be modified reversibly in response to guest molecules, undergoing transformation such as shrinkage or expansion of the framework,[53,60,61] rotation of bridging ligands[62] or interdigitation, and interpenetration of the framework.[63,64]

One of the first reported MOF of this generation is MIL-53, which Férey and co-workers synthesized in the 1990s.[53] This MOF is built up from octahedral chromium(III) chains linked through terephthalate dianions with one-dimensional diamond-shaped pores. MIL-53 exhibits a flexible behavior, where the pore cross-section changes by more than 5 Å. In presence of water molecules, the pores shrink, and without the water molecules, the channels reopen. This effect is recognized as breathing effect (Figure 1.9).

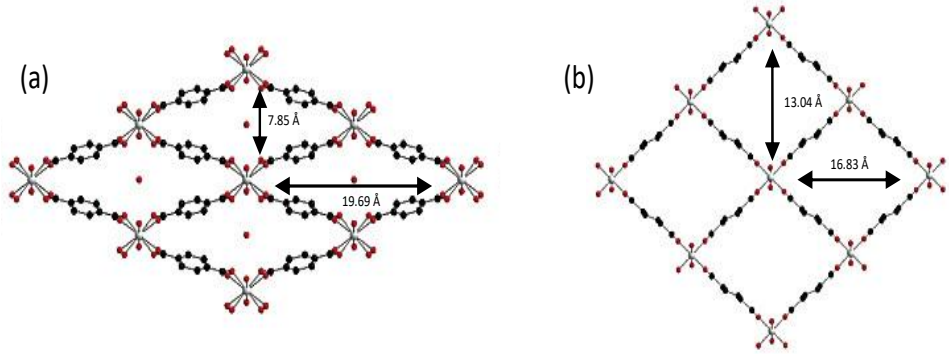

Figure 1.9. (a) Structure of MIL-53 with a water molecule adsorbed in its channels (closed phase). (b) Structure of MIL-53 at high temperature without water molecules (open phase). Colour code: C, black; O, red; Cr, white. Hydrogen atoms have been omitted for clarity. Adapted from ref. 53.

Everything described before demonstrates the ability to obtain PCP in a rational way, according to the reticular synthesis, which is based on the assembly of secondary building units to obtain ordered and highly porous structures linked by strong metal-ligand bonds. This chemistry can obtain materials designed to have determined structures, compositions and properties by utilizing different metals and organic ligands, as well as PSMs. For instance, using ligands with varying lengths can modify the size of the pores of the resulting PCP, as demonstrated in the Yaghi isoreticular serie.[58] Additionally, the rigidity/flexibility of the ligand used can affect the materials flexibility. Furthermore, functionalizing these ligands with different chemical substituents can yield various properties

such as polarity, hydrophobicity, and hydrophilicity. For example, incorporating amino groups can confer a polar character to the pores.[65] Enantiomeric ligands can also be used to obtain chiral MOFs.[66] Finally, different physicochemical properties such as magnetic, electrical, optical, and catalytic can be achieved depending on the metal(s) used, although it should be noted that these properties may also depend on the ligand used or even the interaction between the metal and ligand.

1.2.3. Main advantages and disadvantages of MOFs

Since the discovery of MOFs, the chemistry of porous materials has continued to evolve. These materials have certain advantages, some of which have been explained before, compared to classic porous materials such as zeolites and activated carbon:

- Many MOFs possess flexible and ordered porous structures, allowing them to adapt and exhibit dynamic behaviors in response to host molecules.

- Thanks to the wide range of different metals and organic ligands that can be used for their assembly, and the recent PSMs that can be applied once the framework is formed, infinite structures with different compositions, topologies, and physicochemical properties can be obtained.

- The high porosity, enormous surface area, and low density of these compounds make them very attractive for gas storage and many other applications.

- Due to their high crystallinity, they can be characterized by using single-crystal X-ray diffraction (SCXRD) as a definitive characterization technique.

On the contrary, the thermal stability of MOFs has been considered as the main disadvantage in this field. Two main factors contribute to the structural integrity of these compounds: the characteristics of the organic ligands and the metal-linker bonds. Despite the fact that nowadays it is known a wide large of different MOFs structures, the majority of them starting not to be stable between 300-450 °C, rarely more than 500 °C.[61]

1.2.4. Applications of MOFs

Due to the properties mentioned above -particularly their rational capacity for synthesis, high surface areas, flexibility shown by many reported structures and the ability to function through PSMs- MOFs have a wide range of applications. These characteristics make them suitable for various applications, such as gas storage and separation,[27,67] ion exchange,[19,68] catalysis,[69,70] drug delivery,[29] luminescence and sensor technology,[71,72] water remediation[73] and magnetism,[25] among many others.

Nowadays, a good number of companies are focusing on transferring laboratory-scale research to industry, allowing society to benefit from the discovery of these compounds. This involves adapting synthesis procedures to reduce costs and improve yields to facilitate the transfer of research from academia to real industrial applications. Indeed, some MOFs, such as HKUST-1, MIL-53 (Al), ZIF-8, Fe-BTC, etc., are marketed under the name of Basolite by Merck and synthesized by the chemical company BASF.

1.2.4.1. Gas storage and separation

Charcoal and zeolites, among other classical porous compounds, have been considered as gas adsorbents for many years. In order to achieve effective gas treatment, it is essential to develop porous materials with high storage

capacity and separation efficiency.[74] MOFs are exceptional candidates for gas storage and separation due to the their high porosity, large surface areas (up to 7800 m^2g^{-1} in DUT-60)[75] and tunable pores.

Gas storage:

In order to optimize and maximize the gas loading capacity in MOFs through physisorption, their surface areas play a crucial role. Adsorption is mainly due to the interactions between guest molecules and the atoms of the walls of the MOF's cavities; thus, a larger surface area implies a greater load capacity. However, factors such as free volume and the strengths of adsorbent/adsorbate interactions also affect this application.[76]

Improving gas sorption properties requires a deep understanding of the MOF design, particularly the pore architecture. The surface area generated by the structure is utilized efficiently for gas storage, as mentioned above, while the size of the pores and the functional groups they possess, are used for the selective recognition and uptake of molecules based on their size.[77] Moreover, the activation of MOF cavities through guest removal is crucial for the material's ability to store and separate molecules.

The first to introduce the application of gas storage in PCPs was Kitagawa in 1997,[45] where small gaseous molecules of CH_4, N_2 and O_2 were introduced at high pressures. Since then, this has been one of the most extensively studied applications. MOFs have also been explored for storing different gases, such as H_2 and light hydorcarbons[78] as well as to capture toxic volatile organic compounds such as benzene and xylenes[79], toxic industrial gases like NH_3, SO_2, NO_2 and H_2S, chemical warfare agents[80] or greenhouse gases like NO_x, SO_x, CO and CO_2 (Figure 1.10).[27]

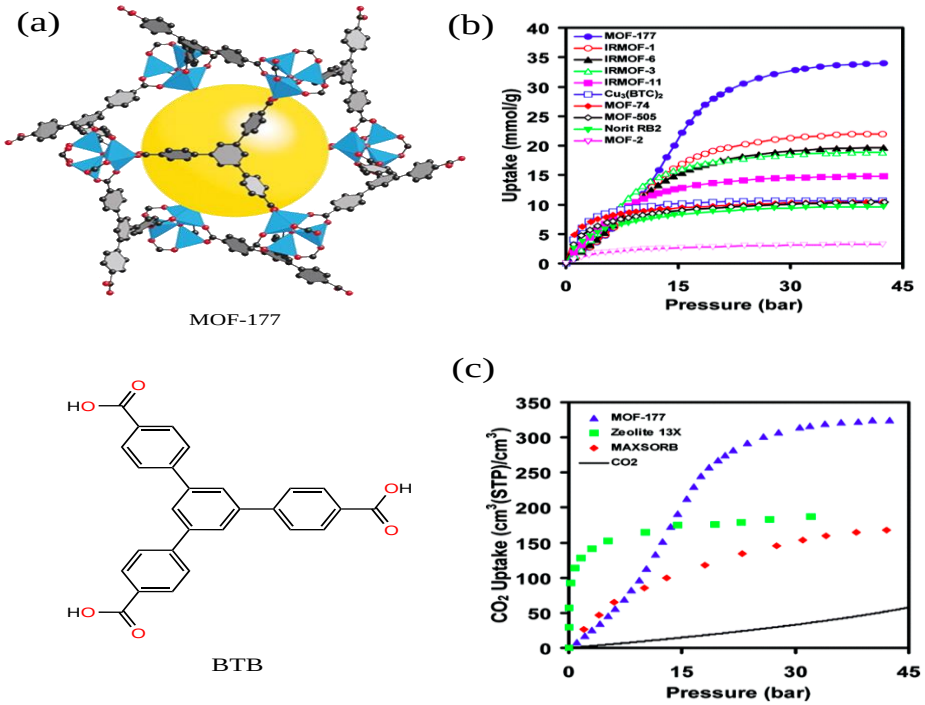

Figure 1.10. (a) Crystal structure of MOF-177. Organic linker formula, pore size and surface area are given. (b) Comparison of gravimetric CO_2 capacities for several MOFs (using activated carbon as reference) at ambient temperature and pressures up to 42 bar. (c) Volumetric CO_2 capacity of MOF-177 comparison with other adsorbents and pressurized CO_2. Adapted from ref. 27.

Gas separation:

On the other hand, the versatility of MOFs allows their possible application in gas separation and purification, which is crucial in the industry. Different MOFs capable of separating mixtures, such as CO_2/CH_4,[81] light hydrocarbons[82] and olefin/paraffin mixtures,[83] among others, have been reported. Gas separation by porous materials is achieved through the following mechanisms:[84]

- Molecular sieving effect: this occurs when the separation of different gases is based on their size and shape. Only molecules of a certain size and shape can be hosted at MOF cavities.

- Thermodynamic equilibrium effect: this occurs when the adsorbate/adsorbent interactions are different between the components of the mixture. These interactions play a crucial role in the separation process.

- Kinetic effect: this occurs when the components of the mixture have different diffusion rates, causing some components to be adsorbed faster than others.

A relevant example of a MOF, capable of capturing, selectively, toxic gases, is the MFM-300(Al), also known as NOTT-300.[85] This MOF can store up to 14.1 mmol g^{-1} of NO_2, a gas known to cause environmental damage and health problems. Even in mixtures at low concentrations (NO_2 concentrations below 1 ppm).

1.2.4.2. Magnetism

In the field of magnetism, MOFs (initially named coordination polymers) are widely used materials. The main objective of this field is to design magnets with high T_c, which means obtaining a molecular material with magnetic properties above room temperature or, at least, above the temperature of liquid nitrogen. Currently, the focus is on creating multifunctional magnetic materials, where magnetism coexists with other properties of interest, such as conductivity, superconductivity, luminescence, porosity, etc.[86] In so doing, a plethora of examples of magnetic sensors could be obtained. In this regard, MOFs are excellent candidates for obtaining multifunctional materials, i.e., porous materials that exhibit magnetic properties. These materials can be used as magnetic sensors,[87] molecular magnets or for magnetic separations.[25]

MOFs can exhibit magnetic properties by selecting appropriate metallic nodes to form the SBUs, organic ligands, and how they are connected to the

structural network, or by including functional magnetic molecules in the porous cavities.[25,88]

Magnetic MOFs can exhibit two types of properties based on the magnetic dimensionality:[25] i) Cooperative properties, where interaction or coupling takes place between the spins of the paramagnetic metal centers through organic ligands, such as cooperative spin crossover or magnetic ordering, and ii) molecular properties, in which the magnetic behavior is due to a single ion that is isolated from the rest by organic ligands, such as single-ion or single-molecule magnets.

The difficulty of synthesizing magnetic MOFs with both cooperative properties and high porosity arises from the fact that porosity is typically achieved with long organic ligands. In contrast, short ligands are necessary to transmit magnetic information between metal centers. To address this issue and combine this problem, three different synthetic routes can be distinguished: (i) the use of short linkers,[89] such as formiates, cyanides, azolates, diazines and lactates, (ii) the "complex as ligand" strategy,[87] in which a preformed metal complex with vacant coordination sites acts as a building block toward other metal ions and (iii) the use of radical ligands, which act as additional spin carriers in organic ligands.[90]

The first example of a MOF built from a radical ligand with magnetic properties was reported by Veciana *et al.* (Figure 1.11).[91] They reported a MOF built by polychlorinated triphenylmethyl tricarboxylic acid radical ligand (ptmtc) and Cu(II) as the metal, known as MOROF-1 (MOROF = metal-organic radical open framework), forming a 2D framework with hexagonal channels of dimension 2.8 x 3.1 nm^2. Furthermore, this MOF exhibits a reversible and selective solvent-induced "shrinking-breathing" process, which involves large volume changes (25-35%) and has a significant impact on its magnetic properties.

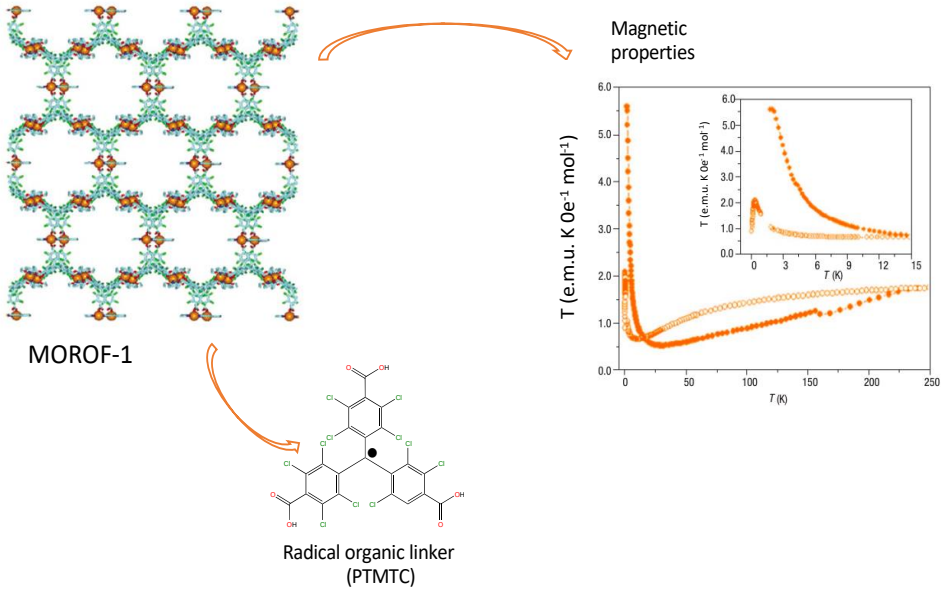

Figure 1.11. Structure of MOROF-1 with a schematic representation of the PTMC radical ligand and magnetic properties in the form of $\chi_M T$ as a function of the temperature for MOROF-1 (orange filled circle, MOROF-1; open circle, evacuated MOROF-1). Adapted from ref. 91.

Another common phenomenon exhibited by magnetic MOFs is spin-crossover (SCO), where the electronic configuration of a transition metal ion switches between high-spin (HS) and low-spin (LS) states in response to external stimuli, such as pressure, temperature, light irradiation, and magnetic field, among others.[92] This leads to changes in magnetism, colour and structure. In this case, the design of a MOF with first-row transition metals having a suitable coordination environment is needed to allow the transition between the HS and LS states, while the length of the ligands used is not a determining factor. However, the cooperative effect is still important and is favoured by the polymeric nature of the framework, which allows the connection of the spin-crossover centres. For this reason, these compounds exhibit high sensitivity to structural changes that may be caused by guests molecules in the pores.[93]

To conclude this topic, another example of MOFs with magnetic behaviour arising from molecular properties are the single-molecule magnets-based MOFs (SMM-based MOFs), where the MOF either present single-molecule magnets (magnetic polynuclear clusters with high spin values and high magnetic anisotropy) at the inorganic nodes or as a guest in the pores. These materials have the peculiarity of exhibiting slow relaxation of the magnetization (superparamagnetic behaviour) at low temperatures. When they are made up of mononuclear metal complexes are known as Singe-Ion Magnets (SIMs-based MOFs). SIMs, have an additional interest in quantum technologies as they are ideal examples of quantum bits.[94]

1.2.4.3. Luminescent sensors

Nowadays, detecting of certain analytes is necessary for a wide range of applications, including emission and environment monitoring, quality controlling, medical diagnostics, chemical threat detection and industrial process management, among others. Chemical sensors are responsible for selectively detecting a certain substance by adsorption or even reacting with it. This produces an electrical, photophysical, optical or mechanical response.[95] The characteristics that a good chemical sensor must have are sensibility and selectivity, response time, stability and reusability.

MOFs have emerged as good candidates for sensing diverse compounds, such as pesticides, explosives, biological markers, small molecules, solvents and so on,[96] due to their high porosity, large surface area, rich host-guest chemistry and the possibility of tuning the pore through PSMs to increase sensibility and selectivity towards specific analytes. Two different types of sensors based on MOFs can be distinguished: (i) those MOFs whose response is based on their own structure, and (ii) those whose response depends on the guest molecule encapsulated in their frameworks.

Although MOFs have many properties that make them useful as sensors, their application in the field has been limited due to their low signal transduction. Currently, MOF-based sensors can be broadly classified into three categories: luminescent,[71] electrochemical[97] and, as mentioned in 1.2.4.2, magnetic sensors.[87] Among them, luminescent MOFs (LMOFs) have received the most attention. In LMOFs, the MOF acts as receptors and transducers, recognizing certain molecules and producing an optical signal as a result. Luminescence is a well-established technique with low detection limits, and in some cases, the signal can even be visible to the naked eye (Figure 1.12).[71]

The origins of luminescence in MOFs can come from either the organic ligand or the metal used (and even guest luminescent species hosted in the channels, see below). The most common type is linker-centered luminescence, which includes three subtypes: linker emission, ligand-to-metal charge transfer (LMTC) and metal-to-ligand charge transfer (MLCT). Ligands with emission properties usually contain aromatic or π-conjugated backbones.[98] LMTC and MLTC are usually observed in MOFs made up of transition metal ions, d^{10} configuration,[99] such as Zn(II) and Cd(II), for LMTC because these ions contain core-like orbitals, and Cu(I) and Ag(I) for MLTC because d electrons are localized in the valence orbitals. MOFs with fluorescent properties due to the metal centre are usually built using lanthanoid ions. Moreover, some MOFs are non-emissive, but by taking advantage of the host-guest chemistry and PSMs, it is possible to encapsulate metals or chromophore groups into the pores to obtain LMOFs.[98]

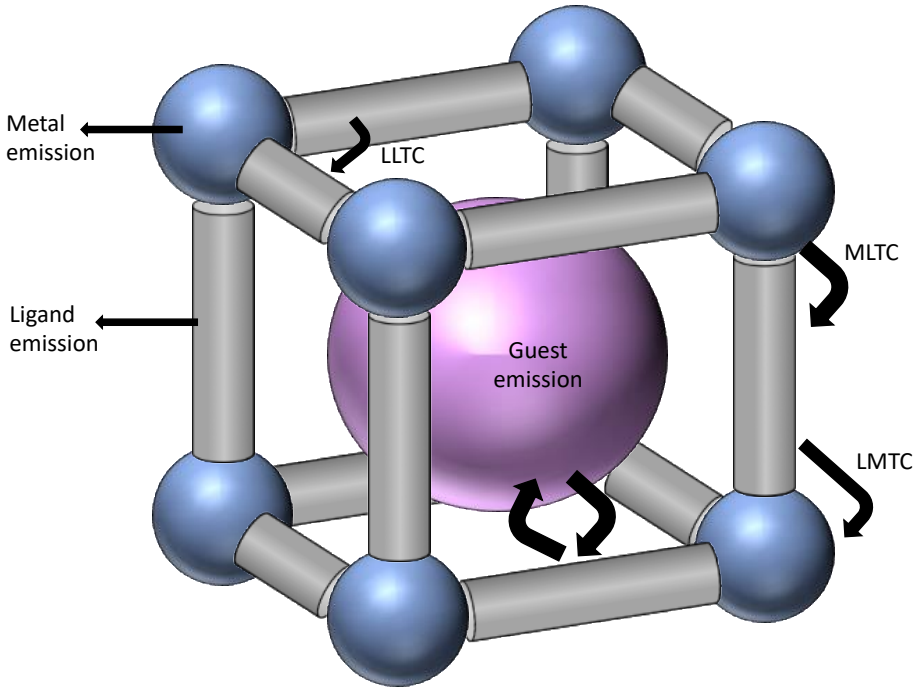

Figure 1.12. Representation of possible emission modes in a porous MOF. Inorganic SBUs, blue spheres; Organic ligands, grey cylinders; Guest chromophores, pink sphere inside. Adapted from ref. 71.

The advantages that LMOFs present as sensors compared to other traditional luminescent sensors are: (i) high sensitivity due to their ability to adsorb and preconcentrate analytes, increasing the possibility of host-guest interactions, (ii) increased selectivity achieved by playing with the pore size, (iii) reusability, thanks to the permanent porosity of the MOFs, which allows them to be reactivated for several cycles without loss of crystallinity and (iv) thanks to the crystallinity of these compounds, the detection mechanisms can be investigated at the molecular level, which allows optimization of the sensors based on these materials. Therefore, LMOFs have been reported detecting analytes of different natures, such as explosives, volatile organic compounds (VOCs),[100] ions,[101] gases,[102] biomolecules,[103] antibiotics, toxic species,[104] temperature and humidity,[105] or pH,[106] demonstrating the efficacy and versatility of these compounds.

1.2.4.4. Catalysis

A catalyst is a substance capable of accelerating a chemical reaction, while itself remains unaltered. They can be classified into two types: homogeneous, in which the catalyst is in the same phase as the reactants, and heterogeneous, in which the catalyst is in a different phase. The latter type of catalyst is the most widely used in the chemical industry today, mainly due to the ease of separating the catalyst from the products obtained and the possibility of recycling and reusing it. The catalytic application of MOFs was first studied by Fujita in 1994[17]. Since then, the interest in these compounds as catalysts has grown exponentially, mainly due to the possibility of obtaining one or more well-defined catalytic centres in the pores,[107] as well as to possessing other interesting features that make them excellent catalysts, such as high porosity and surface areas, rich host-guest chemistry and possibility to fine tune the pore size and shape, and apply PSMs that allow the introduction of active species into the porous channels.

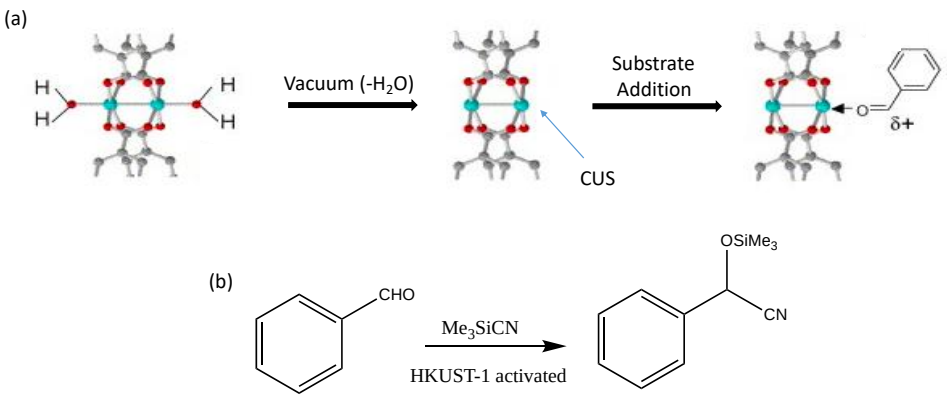

Figure 1.13. (a) Structure of Cu_2-paddle-wheel in HKUST-1 with coordination water (left), removing water molecules to form CUS (middle) and substrate addition in CUS (right). (b) Cyanosylation reaction of benzaldehyde catalyzed by activated HKUST-1. Adapted from ref. 109.

So far, various synthetic strategies have been developed to design MOFs with catalytic activity, including open metal sites, functionalization of organic ligands and the use of MOFs as supports to create other catalytic species.[108] The creation of open metal sites to obtain catalytically active centres can be achieved by removing guest solvent molecules that are not involved in the construction of the framework and are coordinated to the metal, heating the MOF at moderate temperatures generating coordinated unsaturated sites (CUS) around the metal. An illustrative example can be found in HKUST-1, a MOF formed by Cu(II) metal ions and benzene 1,3,4-tricarboxylate (BTC) as ligand, with the resulting formula $Cu_3(BTC)_2(H_2O)_3 \cdot XH_2O$. In the structure, Cu(II) ions are coordinated by a water molecule pointing toward the pores. Kaskel and co-workers[109] studied the elimination of this molecule by heat treatment at 383K, thus allowing Cu to be directly accessible to catalyze, for example, benzaldehyde cyanosilylation (Figure 1.13).

The second synthetic strategy is the use of organic ligands with active catalytic centers. The functional groups commonly used for the synthesis of these catalysts are alcohols, amides, amines, carboxylates and pyridines. Sometimes, the ligand used does not contain these groups, but thanks to PSMs, they can be introduced by functionalizing the MOF once it has been synthesized. Gascon and co-workers studied the catalytic activities derived from the functional groups present in the ligand using IRMOF-3, which has free $-NH_2$ groups in the pore channels, for Knoevenagel condensations.[110]

Finally, the third synthetic strategy to create MOFs as catalysts is the encapsulation of active species in the pores, such as metal nanoparticles,[111] metal complexes[112] and organic (macro)molecules[113] through PSMs. In recent years, MOFs have been also investigated as chemical nanoreactors[40] for the controlled preparation of ligand-free single-atom catalysts (SACs), sub-nanometer metal

nanoclusters (SNMCs) and supramolecular coordination complexes (SCCs), as they exhibit unique catalytic properties. For example, Jiang and co-workers used the MOF Al-TCPP with the formula $(AlOH)_2H_2TCPP$, where H_2TCPP is 4,4',4'',4'''(porphyrin-5,10,15,20-tetrayl)tetrabenzoate), to encapsulate Pt(II), which was subsequently reduced at 180 °C in an H_2 atmosphere to obtain isolated Pt(0) atoms stabilized within the MOF thanks to strong interactions with the pyrrolic N atoms. This new catalyst is capable of producing hydrogen by water splitting under visible light irradiation (Figure 1.14).[114]

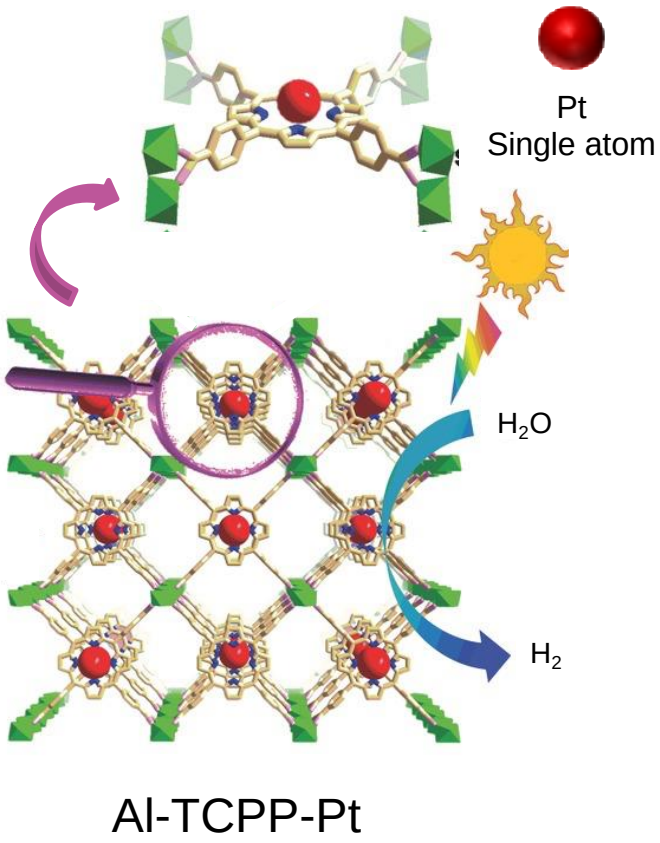

Figure 1.14. Schematic representation of Al-TCPP forming a Pt-SAC for photocatalytic hydrogen production. Adapted from ref. 114.

In addition to their catalytic activity, whether intrinsic or introduced by external agents, the high crystallinity of MOFs enables us to have the possibility to directly visualize, using single-crystal X-ray diffraction (SCXRD), what is occurring during the catalytic cycle. This allows obtaining important information on metastable reaction intermediates, products and unprecedented adopted catalytic conformations within MOFs cavities. This is illustrated in the manuscript of Sumby *et al*., where they have reported one of the most comprehensive studies on the use of SCXRD for the study and characterization of a catalytic cycle. Using a Mn(II)-based MOF to catalyze azide-alkyne cycloaddition reactions, studied both the atomic structure of the reactants and the products obtained through SCXRD.[115]

1.2.4.5. Drug delivery

In recent years, the use of MOFs in biomedicine and drug delivery has attracted interest of many researchers. Horcajada and Férey[29] introduced this application using mesoporous MOFs from the MIL family, specifically MIL-100 and MIL-101, to encapsulate analgesics and anti-inflammatories and subsequently release them in physiological media. The most remarkable characteristics that make MOFs promising in this application area are:[116]

(i) High porosity, which allows the encapsulation of large active molecules.

(ii) Biologically friendly composition, with MOFs composed of non-toxic metals, such as Ca, Mg, Zn, Fe, Ti and Zr, and ligands belonging to two categories: endogenous, which are molecules present in the body composition, and exogenous, which are synthetic or naturally compounds but do not intervene in body cycles. Among the most commonly used ligands are

polycarboxylic or imidazolate, which are easily eliminated under physiological conditions.

(iii) Metal-ligand bonds that are robust enough to prevent rapid degradation of the MOF in physiological media, but sufficiently labile to allow for degradation once the drug is released, thus avoiding bioaccumulation of the material.

(iv) The presence of unsaturated metal centers, where bioactive molecules can be coordinated, and the ability to functionalize the ligand, allowing the pore to adapt for reversible host-guest interaction. These interactions enable control on the kinetics of drug release.

In 2010, Serre introduced a synthetic alternative to synthesize MOFs with active molecules for drug delivery, where the therapeutic molecule is introduced as the organic linker that constitutes the MOF structure. This alternative takes advantage of the fact that most drugs have complexing groups, such as carboxylates, phosphates, amines or heterocycles. Thus, highly porous structures with high surface areas are not necessary to achieve high drug loads, and the release of the biomolecule is achieved through the biodegradation of the material, without side effects due to the release of the organic ligand. The first example of an active MOF for therapeutic use is BioMIL-1,[117] which was reported by Serre *et al*. (Figure 1.15). It is synthesized using iron and nicotinic acid as the organic ligand. Nicotinic acid is an endogenous acid that reduces total cholesterol, LDL cholesterol and triglyceride levels, while increasing HDL cholesterol levels. The biodegradation of the material was studied under simulated physiological conditions, using a phosphate-buffered solution (PBS) at pH = 7.4 and a temperature of 37 °C. The results showed that the nicotinic acid from BioMIL-1 was released in approximately one hour.

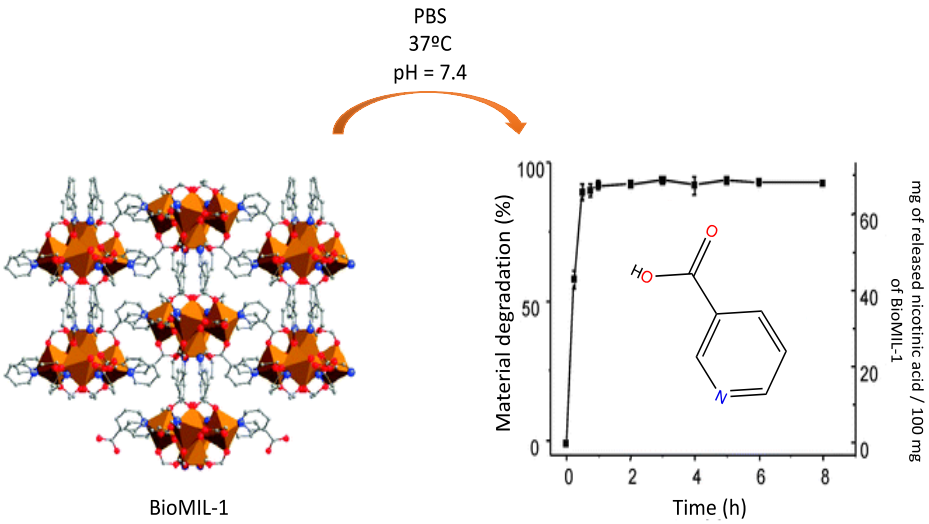

Figure 1.15. Crystal structure of BioMIL-1. Colour code: iron, orange octahedra; oxygen, carbon, and nitrogen, as red, grey and blue balls, respectively. Hydrogen atoms have been omitted for clarity (left). Release of nicotinic acid under simulated physiological conditions (right). Adapted from ref. 117.

Another biomedical application of MOFs is their use as contrast agents (CAs) in magnetic resonance imaging (MRI), particularly in the form of nano-MOFs. Gadolinium(III) is typically used as CA because it reduces proton relaxation times. The first MOF reported for this application was based on Gd(III) by Lin *et al.*,[118] showing relaxations several orders of magnitude higher than other MRI contrast agents based on the same metal. However, due to the toxicity of this metal, the possibility of replacing it with other less toxic metals such as Mn(II) has been studied.[119]

1.2.4.6. Water remediation

Today, almost half of the world's population lives with water scarcity, mainly due to the contamination of the aquatic ecosystem by rapid industrialization and drought caused by global warming. Therefore, reducing the amount of contaminants present in wastewater is a 21st century challenge so that

everyone has access to clean water. The most common contaminants found in water can be divided into two large groups based on their chemical composition:

(i) Inorganic contaminants: this category includes oxyanions/cations and metal ions, with a special emphasis on heavy and radioactive ones. Due to their charged nature, they are highly soluble in aqueous media, making them more persistent in the aquatic ecosystem than organic pollutants. Some of these metals have a narrow range between deficiency and toxicity and toxic/lethal character, making them a focus of study for water decontamination.

(ii) Organic contaminants: pesticides, insecticides, herbicides, pharmaceuticals and personal care products (PPCP), polyaromatic hydrocarbons, oils, detergents and dyes are examples of organic contaminants that can be found in water. While not as persistent as inorganic pollutants, their widespread use in modern society means they are frequently found in ecosystems.

MOFs are exceptional materials for removing contaminants present in aqueous media due to:[73,120] (i) their high sorption capacity closely related to the large surface area and pore volume, (ii) stability of these compounds in water, (iii) presence of active sites, where contaminants can be degraded and/or chemisorbed, (iv) the fascinating host-guest chemistry, where the cavities are easily functionalized to enhance these interactions, therefore improving MOFs capture properties, (v) the high crystallinity of these compounds allows the use of X-ray crystallography as a characterization tool, allowing to study of the final structure as well as host-guest interactions, which allows for the establishment of correlations between structure and functionality and thus opens new frontiers

of knowledge, and (vi) the possibility of processing MOFs as monoliths, granules, membranes, or columns, to adapt them to different decontamination devices.

In addition to the use of MOFs as selective adsorbents in water decontamination, they have also been studied as platforms for the degradation of contaminants thanks to the catalytic activity that many of them exhibit, either intrinsically or after PSMs.[120] These compounds can degrade organic pollutants to less toxic substances or completely degrade them to CO_2 and H_2O. The first work on the use of MOFs for the degradation of contaminants in water was reported by Prof. Hermenegildo García in 2007, in which he used MOF-5, taking advantage of the catalytic environment presented by Zn, for the degradation of an industrial product (phenol-PH).[121]

1.3. Oxamidato-based MOFs: previous results

As we have described above, the field of porous materials science has made great progress over the last 30 years, mainly thanks to the emergence of MOFs. A large part of the scientific community has focused on investigating these compounds due to the variety of applications they have in diverse fields ranging from planet decontamination to medicine, as seen in the previous section. In this thesis, we have focused on the development of new oxamidato-based MOFs (Figure 1.16), synthesized by conventional direct precipitation methods, using biocompatible metals such as zinc. Thus, I will focus in this section on describing both, the chemical nature and most relevant applications of oxamidato-based MOFs reported in recent years.

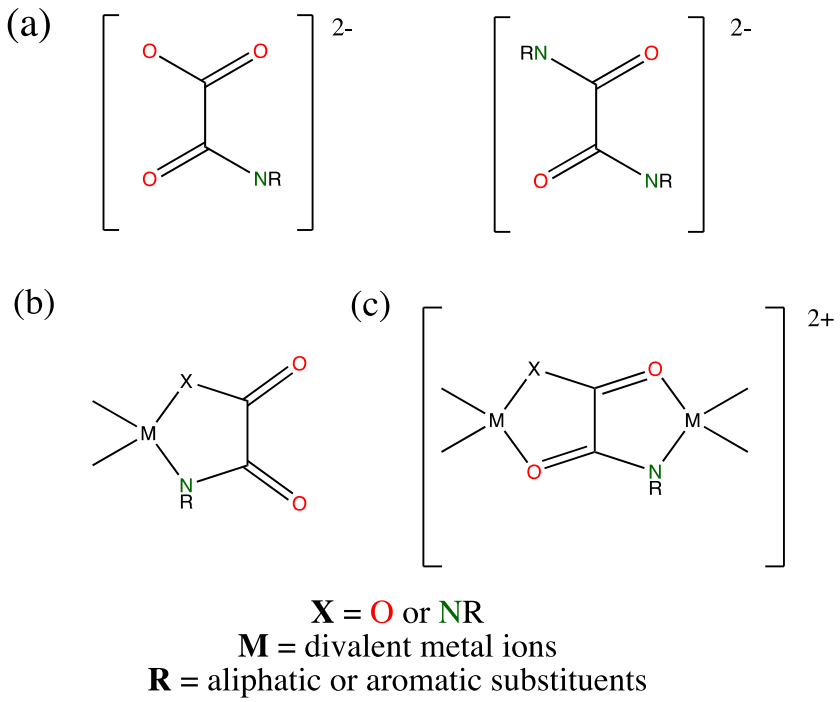

Figure 1.16. (a) Oxamato (left) and Oxamidato (right) dianions; (b) mono- and (c) dinuclear complexes.

It is not accidental that my research group (multifunctional porous materials, mupomat) has extensive experience in coordination chemistry, especially with the use of oxamato and oxamidato-type ligands, which were initially used to synthesize magnetic coordination polymers[26] and later to build new highly-dimensional multifunctional MOFs with functionalizable pores.[122,123] In recent years, in addition to obtaining new structures, our group has also focused on the use of MOFs as chemical nanoreactors –taking advantage of PSMs– to construct unique active species within the functional channels of these MOFs.[40]

In general, the first fundamental step to achieve a suitable MOF is the choice of the appropriate organic ligand, as it will play a very important role in both the properties of the material and its final structure. In particular, oxamate

and oxamidate ligands (Figure 1.16a), dianionic once deprotonated, usually adopt two different coordination modes: bidentate or bis(bidentate), which leads to mono- or dinuclear coordination compounds in *cis* or *trans* conformation (Figure 1.16b), and they ultimately constitute the secondary building units (SBUs) in the final MOFs. These ligands traditionally showed a high affinity for divalent first-row transition metals such as Co(II) and, especially, Cu(II) cations, forming highly stable complexes in solution due to the strong electron-donating capacity of the *N,N*-oxamidate groups.[124] Additionally, they present free carbonyl-oxygen atoms that can act as metalloligands towards other divalent transition metal ions (Mn(II), Co(II), Ni(II)) or alkaline earth metals (Ca(II), Sr(II), and Ba(II)) to form heterobimetallic CPs or MOFs.[125,126] This synthetic strategy is known as "complex as ligand" and has been widely used in our research group, being the synthetic method employed for all the MOFs obtained before this doctoral thesis. As explained, this synthetic strategy is based on using a complex whose coordination sphere is unsaturated and can therefore act as a ligand (metalloligand) towards other metal ions.

Among the different families of oxamato- and oxamidato-based MOFs reported by my group, I will focus, in this section, on describing a quite recently obtained family of isostructural $Cu^{II}_6M^{II}$ MOFs (where M^{II} = Ca(II), Sr(II) or Ba(II)) using oxamidate ligands derived from enantiopure amino acids (Figure 1.17).[122,127] There are a number of reasons that justify this choice: (*i*) the resulting isostructural MOFs possess medium-size functional channels, whose porosity possesses different functional groups depending on the amino acid chosen. Thus, allowing to control the functional groups decorating the channels depending on the amino acid residue. (*ii*) This family of MOFs exhibits great crystallinity and robustness, which is important when using MOFs as chemical nanoreactors. This allows the use of PSMs without degrading the materials, and also, facilitates the use of single crystal X-ray diffraction (SCXRD) to unveil the nature of host-guest

species. (*iii*) The construction of MOFs with oxamidate ligands derived from amino acids gives to the final structure a series of general properties such as biocompatibility, rich structural diversity, chirality (due to the presence of α-asymmetric carbon atoms), water stability, and depending on the amino acid used, specific properties. In particular, the possibility to obtain biocompatible MOFs seems very appealing considering the potential biomedical applications of resulting MOFs. (*iv*) Last but not least, a good number of the novel $Zn^{II}_6M^{II}$ MOFs reported in this thesis (see next chapters) are isostructural to this family of amino acid based $Cu^{II}_6M^{II}$ MOFs. Thus, all these features make it convenient to describe the most remarkable and recent results with analogous $Cu^{II}_6M^{II}$ MOFs.

Overall, the general syntheses of amino acid $Cu^{II}_6M^{II}$ MOFs are carried out through three common steps: (i) formation of the oxamidate ligand derived from the selected amino acid (proligand) by reacting oxalyl chloride with the corresponding enantiopure amino acid methyl ester derivative (Figure 1.17a), (ii) formation of the Cu(II) dinuclear complex (metalloligand) using different bases such as tetramethyl or tetrabutyl ammonium hydroxide to assist in the deprotonation of the amidate and carboxylate groups, resulting in different sites where Cu can coordinate (Figure 1.17b) and (iii) the formation of the MOF by reacting the synthesized metalloligand, which acts as a bis(tridentate) bridging ligand toward alkaline earth divalent metals, such as Ca(II), Sr(II) or Ba(II). Thus, yielding the final chiral heterobimetallic 3D MOFs that display hexagonal pores decorated with the residues of the employed amino acids (Figure 1.17c).[123] Another alternative synthesis that has also been studied in our group is based on modifying the pH in the solution containing the precursor copper complex

(metalloligand). In this case, homometallic 3D MOFs are obtained.[128] The relevant selected examples are described in detail in sections 1.3.1-1.3.4.

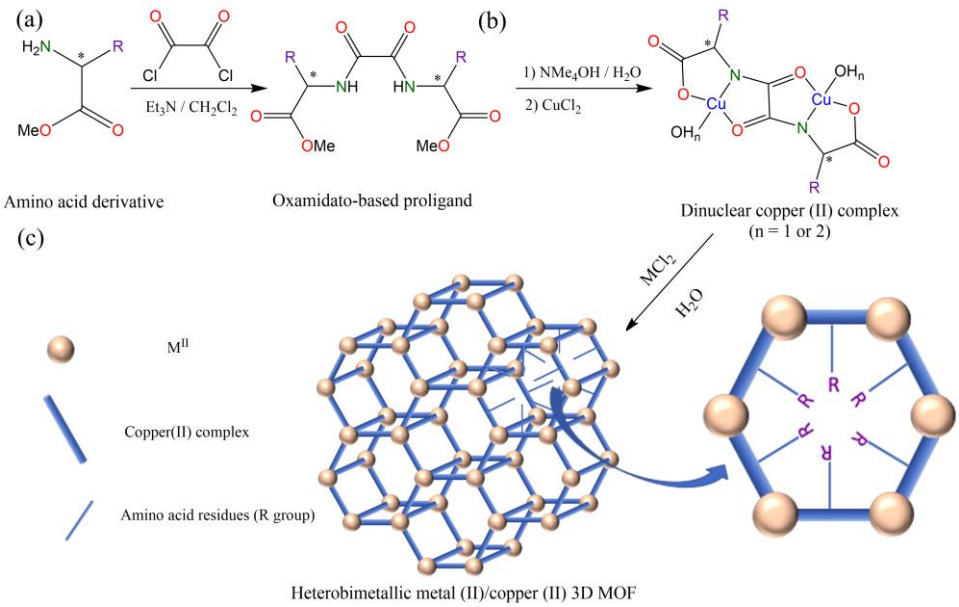

Figure 1.17. Scheme of synthetic procedure to obtain oxamidate-Cu-based MOF. (a) Synthesis of oxamidate ligands functionalized with amino acids as precursor amine, (b) synthesis of dicopper(II) complexes (metalloligands) and (c) synthesis of 3D heterobimetallic MOFs.

1.3.1. Oxamidato-based MOFs for gas separation

Using the synthetic strategy "complex as a ligand," the first isoreticular series of copper-calcium-based MOFs was obtained, employing the natural amino acids *L*-alanine, *L*-valine and *L*-leucine as amines to functionalize the oxamidate ligands. This series of isostructural MOFs presents hexagonal pores decorated with alkyl groups of different sizes, and therefore, an increase in the length of the aliphatic residue decreased the pore size. Taking advantage of the different surface areas and different charge densities in the channels of these MOFs, their ability to separate methane from other light hydrocarbons present in natural gas was studied (Figure 1.18).[129]

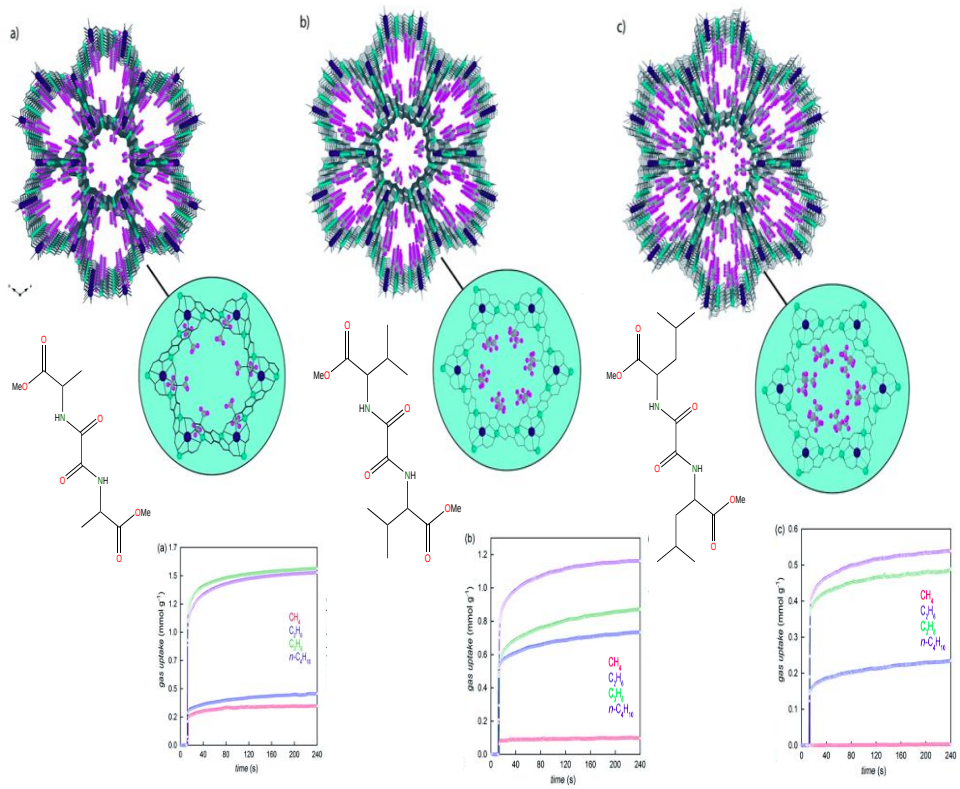

Figure 1.18. SCXRD of oxamidate-based MOF synthesized by *L*-alanine (a), *L*-valine (b) and *L*-leucine (c), emphasizing the different alkyl groups in the boxed structures (above) and their adsorption kinetic profiles of different gases (below). Adapted from ref. 129.

This study unveiled that while the pore size of a metal-organic framework (MOF) structure is important for explaining bulk N_2 adsorption capabilities, interactions between alkyl groups of gases and residues that decorate the cavities of MOFs play a very important role in selectivity. These results showed that increasing the length of aliphatic side chains within the pores, not only affected the sorption capacity of the material but also the adsorption kinetics. Therefore, by adjusting the pore size and functional groups present in the cavities, methane selectivity and separation from other hydrocarbons in natural gas can be controlled.

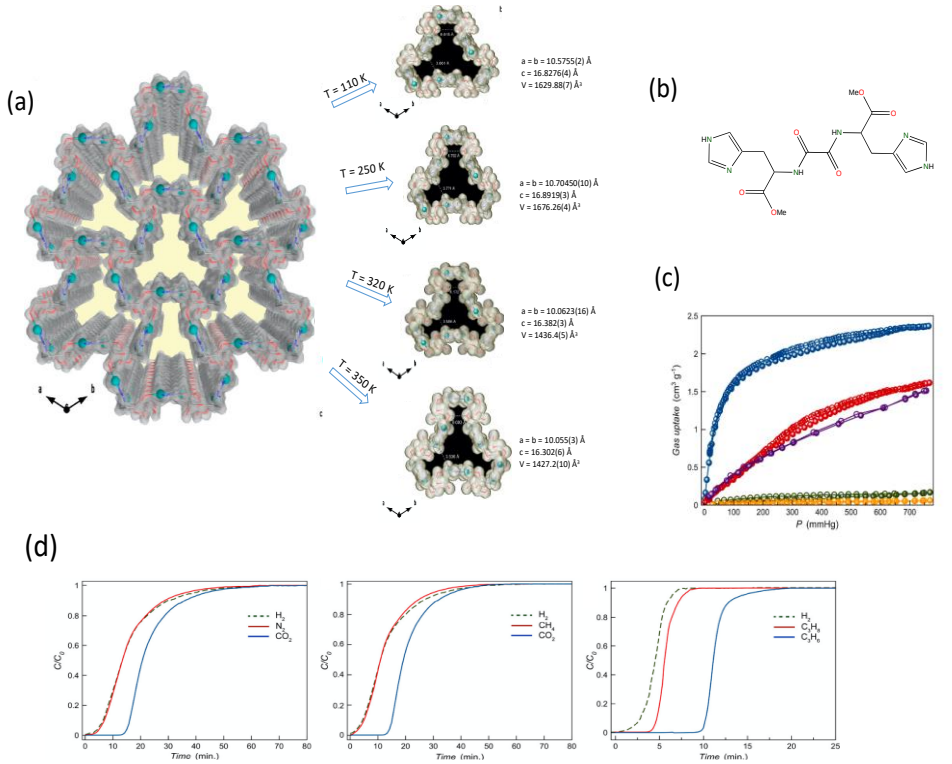

Figure 1.19. (a) Perspective view of the 3D open-framework of Cu^{II}_2(S,S)-hismox · $5H_2O$ along the c axes and view of one single channel in the ab plane for different temperatures (the crystallization water molecules have been omitted for clarity). (b) Ligand H_2Me_2-(S, S)-Hismox used to build the MOF. (c) Adsorption isotherms of C_3H_6 (blue), C_3H_8 (red), CO_2 (purple), CH_4 (green) and N_2 (orange) at 298 K for the activated compound. Filled and empty symbols indicate the adsorption and desorption isotherms, respectively. (d) Experimental column breakthrough curves of the gas mixture measured at 298K and 1 bar in a column using the 3D MOF as stationary phase. Adapted from ref. 130.

Another oxamidato-based MOF synthesized by my research group is Cu^{II}_2(*S,S*)-hismox · $5H_2O$ (hismox = bis[(*S*)-histidine]oxalyl diamide), where, in this case, *L*-histidine was used as the amino acid to functionalize the porous cavities (Figure 1.19). This material showed excellent robustness and flexible behavior thanks to its structural characteristics sensitive to temperature and the corresponding adsorbate. These properties allow the MOF to experience a reversible and continuous breathing behavior observed through SCXRD (Figure 1.19a).[130]

The adsorption isotherms of this material for hydrocarbons such as CH_4, C_3H_8, and C_3H_6, as well as for N_2 and CO_2, indicated that only CO_2, C_3H_6, and C_3H_8 could be adsorbed. These results suggested the possibility of separating gas mixtures such as CO_2/N_2, CO_2/CH_4, and C_3H_8/C_3H_6. Columns were prepared by packing the *L*-histidine-derived MOF as the stationary phase, and the gas mixture was passed through it, observing that the material was able to efficiently separate these mixtures.

1.3.2. Oxamidato-based MOFs for water remediation

Another main research line of my group is the use of MOFs for water treatment and decontamination. Over the years, different PCPs have been synthesized, among which we will highlight some obtained with oxamidate ligands functionalized with the amino acids *L*-methionine and *L*-serine.

Two different MOFs have been synthesized using the amino acid *L*-methionine: $\{Ca^{II}Cu^{II}_6[(S,S)\text{-methox}]_3(OH)_2(H_2O)\} \cdot 16H_2O$[131] and $\{Cu_4^{II}[(S,S)\text{-methox}]_2\} \cdot 5H_2O$,[128] where methox is bis[(*S*)-methionine]oxalyl diamide (Figure 1.20). Both MOFs have pores decorated with highly flexible ethylenethiomethyl chains from the amino acid residue (R-$CH_2CH_2SCH_3$), but they differ in size, shape, and structural composition.

Both MOFs have demonstrated the ability to capture dangerous species such as $HgCl_2$ and CH_3HgCl in water, thanks to the strong affinity that sulfur atoms have for mercury. The confined space offered by these two structures, along with the flexibility of the "arms" decorating the pores, allowed for strong and specific S-Hg interactions, which explained the highly selective and efficient capture process. The heterobimetallic MOF has also been used to selectively capture gold(III) and gold(I) in the presence of other metal salts typically found in electronic waste (Figure 1.20).[132] This is also due to S-Au affinity, similar to the

previous case. In addition, the resulting new species, *i.e.* Au^{III}@MOF and Au^{I}@MOF, were used as heterogeneous catalysts for the hydroalkoxylation of alkynes, thus expanding the applications of these multifunctional materials.

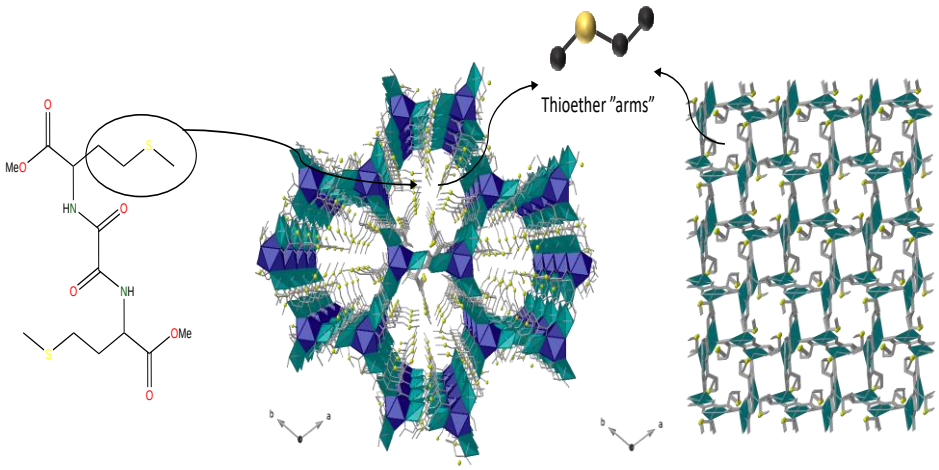

Figure 1.20. Oxamidato-based proligand derived from amino acid *L*-methionine (left) and perspective views along c axis of the 3D porous structures synthesized from the methox organic ligand (right). Colour code: Cu, cyan polyhedra; Ca, blue polyhedra; organic ligand, grey sticks and sulfur atoms, yellow. Adapted from ref. 128 and 131.

On the other hand, another three-dimensional MOF derived from the amino acid *L*-serine was also synthesized, with the formula $\{Ca^{II}Cu^{II}_6[(S,S)\text{-serimox}]_3(OH)_2(H_2O)\} \cdot 39H_2O$, where serimox is bis[(*S*)-serine]oxalyl diamide, presenting hexagonal pores functionalized with highly flexible hydroxyl groups, derived from the amino acid residue used (Figure 1.21). The presence of this group in the confined environment of the MOF allowed for the capture of organic molecules of different nature. On one hand, this material was able to efficiently remove organic dyes, such as pyronine Y, auramine O, methylene blue and brilliant green from water, being able to capture over 90% of the initial content of each dye.[133] On the other hand, the capacity to encapsulate some drugs such as ascorbic acid, pyridoxine, bupropion, and 17-β-estradiol and their subsequent release in a sodium chloride buffer solution at pH = 2 were also studied.[134] These results demonstrated not only the ability of this material to capture organic

molecules that pollute the aquatic ecosystem, but also that it can be used in the field of medicine, the reason why we have decided to enhance the biocompatibility of this family of MOFs by replacing Cu with Zn. In addition, thanks to its high crystallinity, unprecedented snapshots of the interactions that this MOF establishes with the encapsulated organic molecules were obtained.

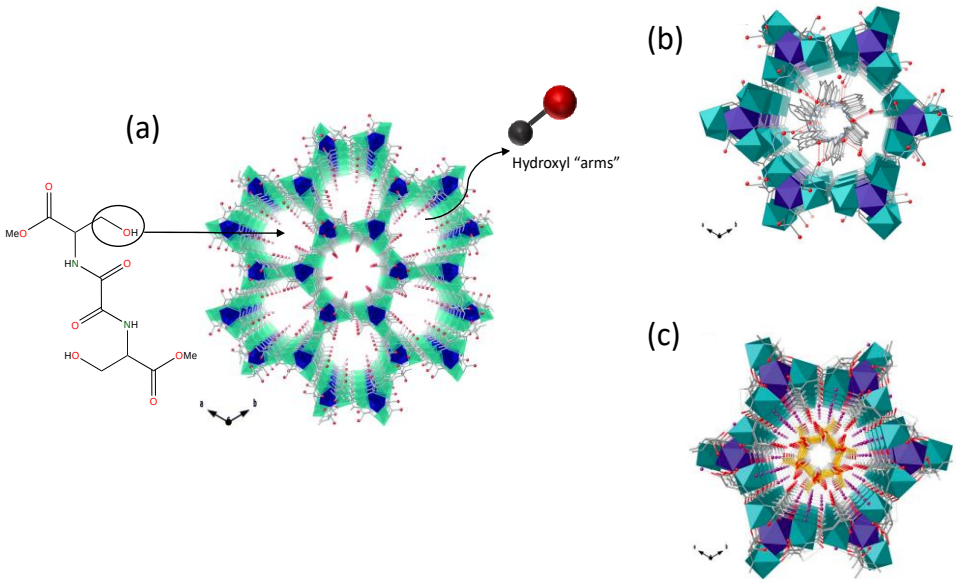

Figure 1.21. Oxamidato-based proligand derived from the amino acid *L*-serine and perspective view along *c* axis of the 3D porous structure of {$Ca^{II}Cu^{II}_6$[(*S,S*)-serimox]$_3(OH)_2(H_2O)$} · $39H_2O$ (a), and a single channel of X-ray crystal structure along *c* axis emphasizing pore filled by pyronin Y (b) and vitamin C (c). Colour code: Cu, cyan polyhedral; Ca, blue polyhedral; O, red spheres; pyronin Y, grey sticks; vitamin C, gold sticks. Adapted from ref. 133 and 134.

1.3.3. Oxamidato based MOFs for catalysis

The use of MOFs as catalysts is an area of application for the materials synthesized by my research group. Generally, PSMs such as metal encapsulation have been used to create MOFs with sites that exhibit catalytic activity. In my group, we wanted to go one step further by using PSMs to synthesize, within MOF channels subnanometer metal clusters (SNMCs) or single-atom catalysts (SACs)

in a two-step dual strategy consisting first on the insertion of the metal atoms and the concomitant reduction within the functional porous space. For example, a new oxamidate MOF derived from the amino acid *S*-methyl-*L*-cysteine was reported with the formula $\{Cu_6Sr[(S,S)\text{-Mecysmox}]_3(OH)_2(H_2O)\} \cdot 15H_2O$ (Mecysmox = bis[*S*-methylcysteine]oxalyl diamide),[135] presenting pores densely decorated with dimethyl thioether groups that are responsible for stabilizing Pd atoms within the functional channels for the formation of SACs (Figure 1.22).

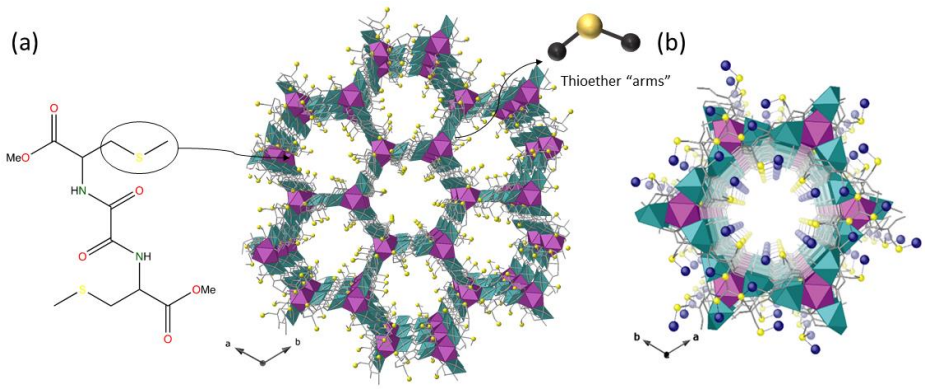

Figure 1.22. Oxamidato-based proligand derived from the amino acid *S*-methyl-*L*-cysteine (left) and perspective view along *c* axis of the 3D porous structure of $\{Cu_6Sr[(S,S)\text{-Mecysmox}]_3(OH)_2(H_2O)\} \cdot 15H_2O$ (a) and view of a single channel of X-ray crystal structure of Pd(II)/Pd(0)@MOF along *c* axes (b). Colour code: Cu, cyan polyhedra; Sr, purple polyhdra; organic ligands, grey sticks; S atoms, yellow spheres; Pd atoms, blue spheres. Adapted from ref.135.

The synthesis of this catalyst consisted of several steps: (i) formation of the new three-dimensional MOF through the "complex as ligand" synthetic strategy, (ii) insertion of $[Pd(NH_3)_4]Cl_2$ to form a phase named Pd(II)@MOF. The retention of Pd(II) cations homogeneously in the MOF cavities was achieved thanks to the S-Pd affinity, and (iii) partial reduction of the Pd(II) cations with $NaBH_4$ to obtain the mixed-valence Pd(II)/Pd(0) hybrid compound. The crystal structure of each step was obtained through SC-XRD given the high crystallinity and robustness of the initial MOF, and the catalytic activity of this compound was

demonstrated to be capable of catalyzing the oxidation of benzyl alcohols to carboxylic acids.

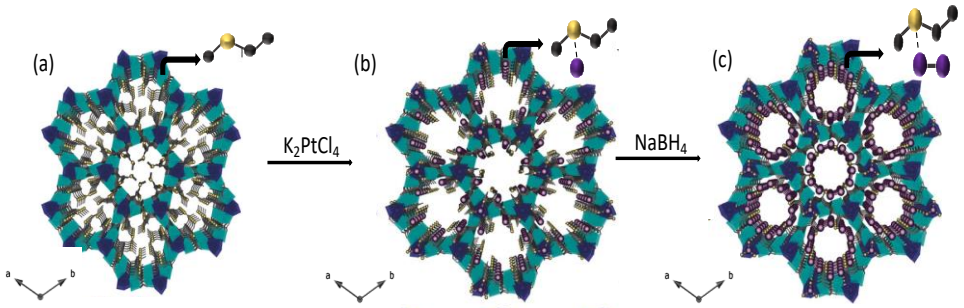

Figure 1.23. Perspective views along c axis of ({$Ca^{II}Cu^{II}_6$[(S,S)-methox]$_3$$(OH)_2$$(H_2O)$} · $16H_2O$) (MOF)(a), Pt(II)@MOF (b) and Pt^0_2@MOF (c). Colour code: Cu and Ca are shown in cyan and blue polyhedral, organic ligand in grey sticks, sulfur and platinum atoms in yellow and purple spheres, respectively. Adapted from ref. 136.

Another nice example was achieved with the amino acid based MOF ({$Ca^{II}Cu^{II}_6$[(*S,S*)-methox]$_3$$(OH)_2$$(H_2O)$} · $16H_2O$) (Figure 1.23). First, Platinum atoms were encapsulated, anchored to the sulfur atoms decorating the pores and immediately reduced with $NaBH_4$, forming sub-nanometer dinuclear clusters Pt^0_2 within the MOF (Figure 1.23a). This material was capable of catalyzing the synthesis of NH_4CN at room temperature, hydrogenation of CO_2 at low-temperature (< 140 °C), and the hydrogenation of alkenes at 60 °C.[136]

Finally, we have selected another example where these MOFs do not act as chemical reactors to synthesize, *in situ*, metal species but as vessel encapsulating catalytically-active species. Thus, $VO(acac)_2$ was encapsulated to give rise to a hybrid material with the formula [V^{IV}O(acac)(H_2O)]@{$Ca^{II}Cu^{II}_6$[(*S,S*)-methox]$_3$$(OH)_3$} · $8H_2O$ (Figure 1.24), which was highly efficient in the dehydrogenation of allylic alcohols.[137]

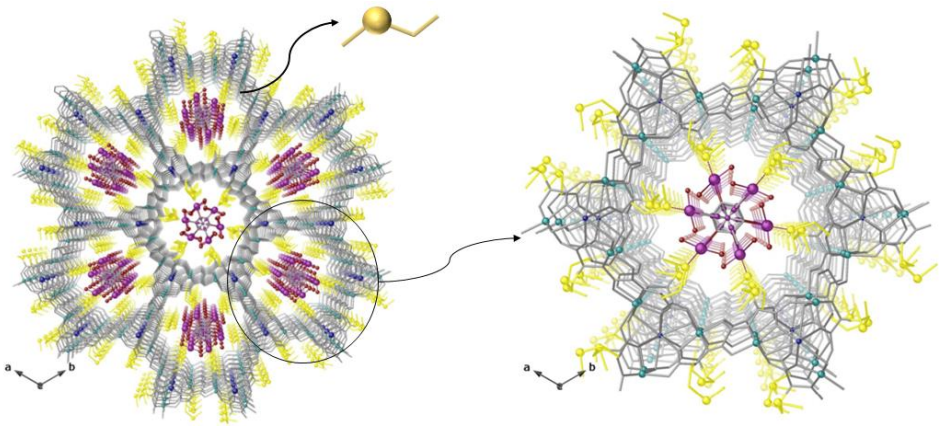

Figure 1.24. Perspective view of the structure $[V^{IV}O(acac)(H_2O)]@\{Ca^{II}Cu^{II}_6[(S,S)\text{-methox}]_3(OH)_3\} \cdot 8H_2O$ (left) and perspective details of a single pore showing $VO(acac)(H_2O)^+$ complexes well-packed within pore (right) of the same structure along *c* crystallographic axes. Colour code: copper and calcium are represented in cyan and blue spheres, 3D network as grey sticks and ethyl chain and sulfur atoms from methionine residue as yellow sticks (carbon) and yellow spheres (sulfur). For the complex $VO(acac)(H_2O)^+$ hosted in the channels, vanadium, carbon and oxygen are shown as purple, grey and red spheres, respectively. Crystallization water molecules have been omitted for clarity. Adapted from ref. 137.

1.3.4. Multivariate oxamidato-based MOFs

As the last illustrative example, I have selected certain preliminary results, obtained by my group, consisting on the preparation of a family of $Cu^{II}_6M^{II}$ MOFs containing equimolar amounts of two (or more) different amino acid-based ligands. This emerging class of MOFs, characterized by possessing distinct linker functionalities, are named multivariate MOFs (MTV-MOFs),[138] and they are characterized by introducing heterogeneity while maintaining the same structure. The ultimate goal of synthesizing MTV-MOFs is two-fold: to improve the complexity of the pore and to achieve synergistic effects in their applications –thanks to the presence of several functional groups within the same pore, introduced by the residues of the amino acids used in the formation of the ligand. In this context my group have been capable to obtain a family of MTV-MOF

containing 50% of the different amino acid-based ligands than can be visualized in Figure 1.25 (see caption for details).

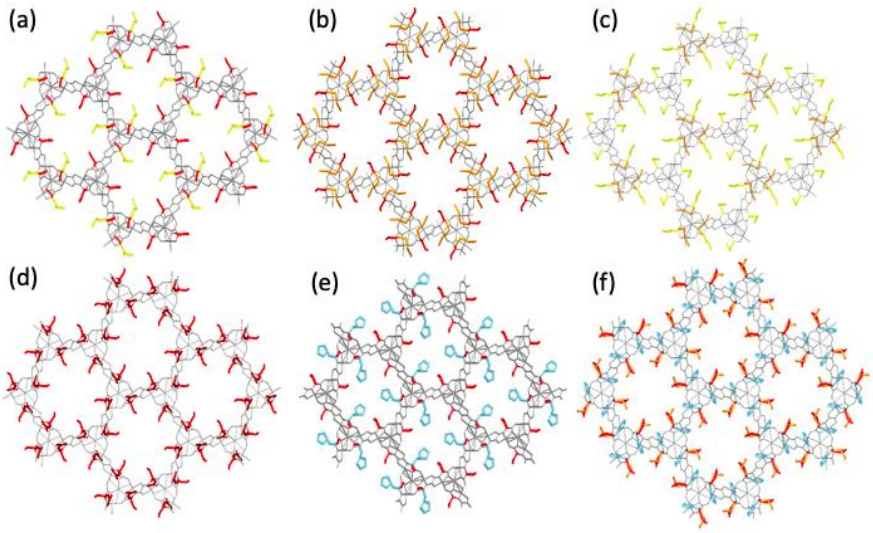

Figure 1.25. Selected examples of recently synthesized oxamidate-based MTV-MOFs containing the following amino acids: *S*-methyl-*L*-cysteine (yellow) / *L*-serine (red) (a), *L*-methionine (orange) / *L*-serine (red) (b), *S*-Methyl-*L*-cysteine (yellow) / *L*-methionine (orange) (c), aspartic acid (dark red) / *L*-serine (red) (d), *L*-histidine (blue) / *L*-serine (red) (e), *L*-histidine (blue) / *L*-serine (red) / *L*-methionine (orange) (f).

These types of MOFs offer potential rewards in fields like water remediation and catalysis. Moreover, in this thesis, I pretend to synthesize also $Zn^{II}_6M^{II}$ MTV-MOFs, which is another reason that prompted me to describe these materials in this section. As a nice illustrative example of the potential of MTV-MOFs in water remediation, we present a reported MTV-MOF prepared by the "complex as ligand" synthetic strategy using a combination of two metal-ligands based on different oxamidate derivates of the natural amino acids *L*-serine and *L*-methionine.

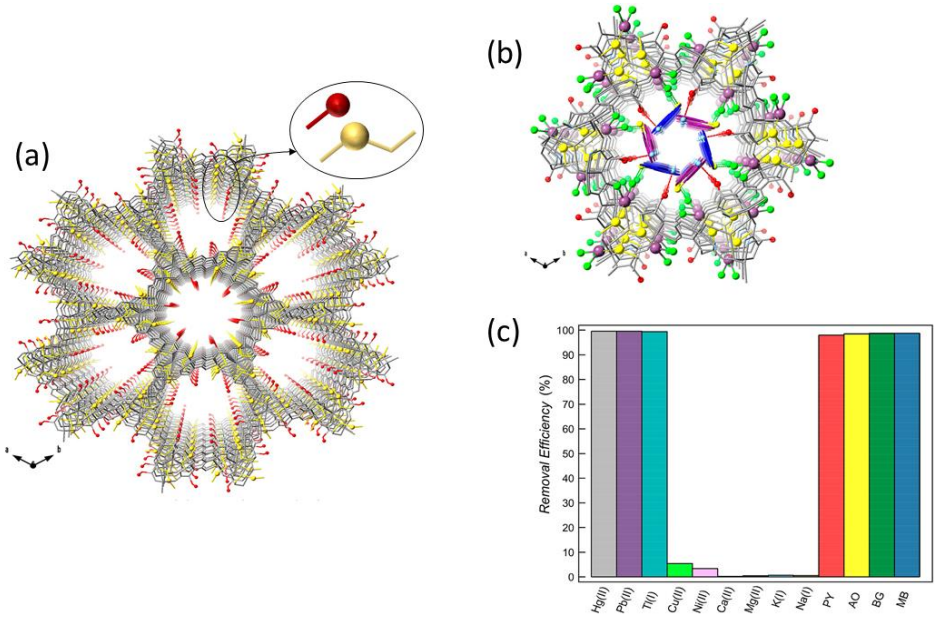

Figure 1.26. (a) Perspective view of MTV-MOF along *c* axis containing the amino acids *L*-methionine and *L*-serine. Ligands and metal atoms from the network are representing as grey sticks with the exception of the amino acid residues, which are represented as red (hydroxyl groups) and yellow (thioether arms) sticks. Oxygen and sulphur atoms from the residues are shown as red and yellow spheres, respectively. (b) Perspective view of a single pore of MTV-MOF along the *c* axis, containing an organic dye (methylene blue) and $HgCl_2$ as guest molecules held in the hexagonal nanopores. Colour code of the net as previously said. Mercury(II) and chlorine atoms are represented as magenta and green spheres. Carbon atoms of organic dye are represented as blue or magenta sticks (two different configurations). (c) Maximum uptake (after 6h) of both inorganic and organic contaminants adsorbed by MTV-MOF. Adapted from ref. 138.

The ultimate goal of synthesizing this new material is to decorate the cavities of the MOF with residues of different natures. So that, they can interact with both inorganic pollutants (thiol group from *L*-methionine) and organic pollutants (hydroxyl group from *L*-serine). Thus, demonstrating the synergy and importance of creating multivariate multifunctional materials. This MOF with the formula $\{Ca^{II}Cu^{II}_6[(S,S)\text{-methox}]_{1.43\text{-}1.46}(S,S)\text{-serimox}]_{1.57\text{-}1.54}(OH)_2(H_2O)\} \cdot 30H_2O$ is capable of simultaneously and efficiently removing heavy metals such as Hg(II), Pb(II), and Tl(I) as well as organic dyes (Figure 1.26).[138]

1.4. References

(1) Kitagawa, S.; Kitaura, R.; Noro, S. *Angew. Chem. Int. Ed.* **2004**, *43* (18), 2334–2375.

(2) Bryan, C. P. Ancient Egyptian Medicine : The Papyrus Ebers; 1974.

(3) Wu, J.; Cao, M.; Tong, D.; Finkelstein, Z.; Hoek, E. M. V. *npj Clean Water* **2021**, *4* (1), 40.

(4) Carretero, M. I. *Appl. Clay Sci.* **2002**, *21* (3–4), 155–163.

(5) Kerley, T.; Munafo, J. P. *J. Agric. Food Chem.* **2020**, *68* (36), 9759–9767.

(6) Spiers, E. M. The Gas War, 1915–1918: If Not a War Winner, Hardly a Failure. In *One Hundred Years of Chemical Warfare: Research, Deployment, Consequences*; Springer International Publishing: Cham, 2017; pp 153–168.

(7) Millini, R.; Bellussi, G. Chapter 1. Zeolite Science and Perspectives; 2017; pp 1–36.

(8) Li, Y.; Yu, J. *Nat. Rev. Mater.* **2021**, *6* (12), 1156–1174.

(9) Batten, S. R.; Champness, N. R.; Chen, X.-M.; Garcia-Martinez, J.; Kitagawa, S.; Öhrström, L.; O'Keeffe, M.; Paik Suh, M.; Reedijk, J. *Pure Appl. Chem.* **2013**, *85* (8), 1715–1724.

(10) Conelly, N. G.; Hartshron, R. M.; Damhus, T.; Hutton, A. T. *NOMENCLATURE OF INORGANIC CHEMISTRY - IUPAC Recommendations 2005*, Royal Soci.; 2005.

(11) Shibata, Y. *J. Coll. Sci. Imp. Univ. Tokyo* **1916**, *37*, 1–17.

(12) Klein, R. M.; Bailar Jr, J. C. R. *Inorg. Chem.* **1963**, *2* (6), 1190–1194.

(13) Tomic, E. A. T *J. Appl. Polym. Sci.* **1965**, *9* (11), 3745–3752.

(14) Hoskins, B. F.; Robson, R. *J. Am. Chem. Soc.* **1990**, *112* (4), 1546–1554.

(15) Schoedel, A.; Yaghi, O. M. Porosity in Metal-Organic Compounds. In *Macrocyclic and Supramolecular Chemistry*; John Wiley & Sons, Ltd: Chichester, UK, 2016; pp 200–219.

(16) Frank Wells, A. *Three-Dimensional Nets and Polyhedra*; John Wiley and Sons, New York, 1977.

(17) Fujita, M.; Kwon, Y. J.; Washizu, S.; Ogura, K. *J. Am. Chem. Soc.* **1994**, *116* (3), 1151–1152.

(18) Munakata, M.; Kuroda-Sowa, T.; Maekawa, M.; Honda, A.; Kitagawa, S. *J. Chem. Soc. Dalt. Trans.* **1994**, No. 19, 2771.

(19) Yaghi, O. M.; Li, H. *J. Am. Chem. Soc.* **1995**, *117* (41), 10401–10402.

(20) Yaghi, O. M. *ACS Cent. Sci.* **2019**, *5* (8), 1295–1300.

(21) Côté, A. P.; Benin, A. I.; Ockwig, N. W.; O'Keeffe, M.; Matzger, A. J.; Yaghi, O. M. *Science.* **2005**, *310* (5751), 1166–1170.
(22) El-Kaderi, H. M.; Hunt, J. R.; Mendoza-Cortés, J. L.; Côté, A. P.; Taylor, R. E.; O'Keeffe, M.; Yaghi, O. M. *Science.* **2007**, *316* (5822), 268–272.
(23) Wang, Z.; Cohen, S. M. *Chem. Soc. Rev.* **2009**, *38* (5), 1315.
(24) Dechambenoit, P.; Long, J. R. *Chem. Soc. Rev.* **2011**, *40* (6), 3249.
(25) Mínguez Espallargas, G.; Coronado, E. *Chem. Soc. Rev.* **2018**, *47* (2), 533–557.
(26) Grancha, T.; Ferrando-Soria, J.; Castellano, M.; Julve, M.; Pasán, J.; Armentano, D.; Pardo, E. *Chem. Commun.* **2014**, *50* (57), 7569–7585.
(27) Millward, A. R.; Yaghi, O. M. *J. Am. Chem. Soc.* **2005**, *127* (51), 17998–17999.
(28) Liu, J.; Chen, L.; Cui, H.; Zhang, J.; Zhang, L.; Su, C.-Y. *Chem. Soc. Rev.* **2014**, *43* (16), 6011–6061.
(29) Horcajada, P.; Serre, C.; Vallet-Regí, M.; Sebban, M.; Taulelle, F.; Férey, G. *Angew. Chem. Int. Ed.* **2006**, *45* (36), 5974–5978.
(30) Castells-Gil, J.; Padial, N. M.; Almora-Barrios, N.; Albero, J.; Ruiz-Salvador, A. R.; González-Platas, J.; García, H.; Martí-Gastaldo, C. *Angew. Chem. Int. Ed.* **2018**, *130* (28), 8589–8593.
(31) Safaei, M.; Foroughi, M. M.; Ebrahimpoor, N.; Jahani, S.; Omidi, A.; Khatami, M. A. *TrAC, Trends Anal. Chem.* **2019**, *118*, 401–425.
(32) Huang, L.; Wang, H.; Chen, J.; Wang, Z.; Sun, J.; Zhao, D.; Yan, Y.. *Microporous Mesoporous Mater.* **2003**, *58* (2), 105–114.
(33) Tranchemontagne, D. J.; Hunt, J. R.; Yaghi, O. M. *Tetrahedron* **2008**, *64* (36), 8553–8557.
(34) Seo, Y.-K.; Hundal, G.; Jang, I. T.; Hwang, Y. K.; Jun, C.-H.; Chang, J.-S. *Microporous Mesoporous Mater.* **2009**, *119* (1–3), 331–337.
(35) Vaitsis, C.; Sourkouni, G.; Argirusis, C. *Ultrason. Sonochem.* **2019**, *52*, 106–119.
(36) Qiu, L.-G.; Li, Z.-Q.; Wu, Y.; Wang, W.; Xu, T.; Jiang, X. *Chem. Commun.* **2008**, *31*, 3642.
(37) Martinez Joaristi, A.; Juan-Alcañiz, J.; Serra-Crespo, P.; Kapteijn, F.; Gascon, J. *Cryst. Growth Des.* **2012**, *12* (7), 3489–3498.
(38) Mukherjee, G.; Biradha, K. *Chem. Commun.* **2012**, *48* (36), 4293.
(39) Mandal, S.; Natarajan, S.; Mani, P.; Pankajakshan, A. *Adv. Funct. Mater.* **2021**, *31* (4), 2006291.
(40) Escamilla, P.; Guerra, W. D.; Leyva-Pérez, A.; Armentano, D.; Ferrando-

Soria, J.; Pardo, E. *Chem. Commun.* **2023**, *59* (7), 836–851.

(41) Zou, L.; Feng, D.; Liu, T.-F.; Chen, Y.-P.; Yuan, S.; Wang, K.; Wang, X.; Fordham, S.; Zhou, H.-C. *Chem. Sci.* **2016**, *7* (2), 1063–1069.

(42) Li, G.-P.; Zhang, K.; Zhang, P.-F.; Liu, W.-N.; Tong, W.-Q.; Hou, L.; Wang, Y.-Y. Thiol- *Inorg. Chem.* **2019**, *58* (5), 3409–3415.

(43) Sing, K. S. W. *Pure Appl. Chem.* **1985**, *57* (4), 603–619.

(44) Thommes, M.; Kaneko, K.; Neimark, A. V.; Olivier, J. P.; Rodriguez-Reinoso, F.; Rouquerol, J.; Sing, K. S. W. P *Pure Appl. Chem.* **2015**, *87* (9–10), 1051–1069.

(45) Kondo, M.; Yoshitomi, T.; Matsuzaka, H.; Kitagawa, S.; Seki, K. T. *Angew. Chem. Int. Ed.* **1997**, *36* (16), 1725–1727.

(46) Li, H.; Eddaoudi, M.; Groy, T. L.; Yaghi, O. M. *J. Am. Chem. Soc.* **1998**, *120* (33), 8571–8572.

(47) Kitagawa, S.; Kondo, M. *Bulletin of the Chemical Society of Japan*. 1998, pp 1739–1753.

(48) Kitagawa, S.; Uemura, K. *Chem. Soc. Rev.* **2005**, *34* (2), 109..

(49) Hoskins, B. F.; Robson, R. *J. Am. Chem. Soc.* **1989**, *111* (15), 5962–5964.

(50) Yaghi, O. M.; Li, G.; Li, H. *Nature* **1995**, *378* (6558), 703–706.

(51) Kawano, M.; Fujita, M. *Coord. Chem. Rev.* **2007**, *251* (21–24), 2592–2605.

(52) Horike, S.; Shimomura, S.; Kitagawa, S. *Nat. Chem.* **2009**, *1* (9), 695–704.

(53) Serre, C.; Millange, F.; Thouvenot, C.; Noguès, M.; Marsolier, G.; Louër, D.; Férey, G. *J. Am. Chem. Soc.* **2002**, *124* (45), 13519–13526.

(54) Yao, M.-S.; Otake, K.; Xue, Z.-Q.; Kitagawa, S. *Faraday Discuss.* **2021**, *231*, 397–417.

(55) Kitagawa, S. *Acc. Chem. Res.* **2017**, *50* (3), 514–516.

(56) Kitagawa, S. *Angew. Chem. Int. Ed.* **2015**, *54* (37), 10686–10687.

(57) Li, H.; Eddaoudi, M.; O'Keeffe, M.; Yaghi, O. M. *Nature* **1999**, *402* (6759), 276–279.

(58) Eddaoudi, M.; Kim, J.; Rosi, N.; Vodak, D.; Wachter, J.; O'Keeffe, M.; Yaghi, O. M. *Science.* **2002**, *295* (5554), 469–472.

(59) Bureekaew, S.; Shimomura, S.; Kitagawa, S. *Sci. Technol. Adv. Mater.* **2008**, *9* (1), 014108.

(60) Férey, G.; Latroche, M.; Serre, C.; Millange, F.; Loiseau, T.; Percheron-Guégan, A. *Chem. Commun.* **2003**, *24*, 2976–2977.

(61) Loiseau, T.; Serre, C.; Huguenard, C.; Fink, G.; Taulelle, F.; Henry, M.; Bataille, T.; Férey, G. *Chem. Eur. J.* **2004**, *10* (6), 1373–1382.

(62) Suh, M. P.; Cheon, Y. E.; Lee, E. Y. *Chem. Eur. J.* **2007**, *13* (15), 4208–4215.

(63) Horike, S.; Tanaka, D.; Nakagawa, K.; Kitagawa, S. *Chem. Commun.* **2007**, *32*, 3395.

(64) Jiang, H.-L.; Makal, T. A.; Zhou, H.-C. *Coord. Chem. Rev.* **2013**, *257* (15–16), 2232–2249.

(65) Cmarik, G. E.; Kim, M.; Cohen, S. M.; Walton, K. S. *Langmuir* **2012**, *28* (44), 15606–15613.

(66) Nickerl, G.; Henschel, A.; Grünker, R.; Gedrich, K.; Kaskel, S. *Chemie Ing. Tech.* **2011**, *83* (1–2), 90–103.

(67) Li, J.-R.; Kuppler, R. J.; Zhou, H.-C. *Chem. Soc. Rev.* **2009**, *38* (5), 1477.

(68) Kumar, P.; Pournara, A.; Kim, K.-H.; Bansal, V.; Rapti, S.; Manos, M. J. *Prog. Mater. Sci.* **2017**, *86*, 25–74.

(69) Gascon, J.; Corma, A.; Kapteijn, F.; Llabrés i Xamena, F. X. *ACS Catal.* **2014**, *4* (2), 361–378.

(70) Lee, J.; Farha, O. K.; Roberts, J.; Scheidt, K. A.; Nguyen, S. T.; Hupp, J. T. *Chem. Soc. Rev.* **2009**, *38* (5), 1450.

(71) Zhang, Y.; Yuan, S.; Day, G.; Wang, X.; Yang, X.; Zhou, H.-C. *Coord. Chem. Rev.* **2018**, *354*, 28–45.

(72) Stassen, I.; Burtch, N.; Talin, A.; Falcaro, P.; Allendorf, M.; Ameloot, R. *Chem. Soc. Rev.* **2017**, *46* (11), 3185–3241.

(73) Mon, M.; Bruno, R.; Ferrando-Soria, J.; Armentano, D.; Pardo, E. *J. Mater. Chem. A* **2018**, *6* (12), 4912–4947.

(74) Li, H.; Li, L.; Lin, R.-B.; Zhou, W.; Zhang, Z.; Xiang, S.; Chen, B. *EnergyChem* **2019**, *1* (1), 100006.

(75) Hönicke, I. M.; Senkovska, I.; Bon, V.; Baburin, I. A.; Bönisch, N.; Raschke, S.; Evans, J. D.; Kaskel, S. *Angew. Chem. Int. Ed.* **2018**, *57* (42), 13780–13783.

(76) Frost, H.; Düren, T.; Snurr, R. Q. *J. Phys. Chem. B* **2006**, *110* (19), 9565–9570.

(77) Cui, Y.; Li, B.; He, H.; Zhou, W.; Chen, B.; Qian, G. *Acc. Chem. Res.* **2016**, *49* (3), 483–493.

(78) Chen, Z.; Mian, M. R.; Lee, S.-J.; Chen, H.; Zhang, X.; Kirlikovali, K. O.; Shulda, S.; Melix, P.; Rosen, A. S.; Parilla, P. A.; Gennett, T.; Snurr, R. Q.; Islamoglu, T.; Yildirim, T.; Farha, O. K. *J. Am. Chem. Soc.* **2021**, *143* (45), 18838–18843.

(79) Vellingiri, K.; Szulejko, J. E.; Kumar, P.; Kwon, E. E.; Kim, K.-H.; Deep, A.; Boukhvalov, D. W.; Brown, R. J. C. *Sci. Rep.* **2016**, *6* (1), 27813.

(80) Bobbitt, N. S.; Mendonca, M. L.; Howarth, A. J.; Islamoglu, T.; Hupp, J. T.;

Farha, O. K.; Snurr, R. Q. *Chem. Soc. Rev.* **2017**, *46* (11), 3357–3385.

(81) Britt, D.; Furukawa, H.; Wang, B.; Glover, T. G.; Yaghi, O. M. *Proc. Natl. Acad. Sci.* **2009**, *106* (49), 20637–20640.

(82) Cui, W.; Hu, T.; Bu, X. *Adv. Mater.* **2020**, *32* (3), 1806445.

(83) Peng, J.; Wang, H.; Olson, D. H.; Li, Z.; Li, J. *Chem. Commun.* **2017**, *53* (67), 9332–9335..

(84) Fakhraei Ghazvini, M.; Vahedi, M.; Najafi Nobar, S.; Sabouri, F. *J. Environ. Chem. Eng.* **2021**, *9* (1), 104790.

(85) Han, X.; Godfrey, H. G. W.; Briggs, L.; Davies, A. J.; Cheng, Y.; Daemen, L. L.; Sheveleva, A. M.; Tuna, F.; McInnes, E. J. L.; Sun, J.; Drathen, C.; George, M. W.; Ramirez-Cuesta, A. J.; Thomas, K. M.; Yang, S.; Schröder, M. *Nat. Mater.* **2018**, *17* (8), 691–696.

(86) Clemente-León, M.; Coronado, E.; Martí-Gastaldo, C.; Romero, F. M. *Chem. Soc. Rev.* **2011**, *40* (2), 473.

(87) Ferrando-Soria, J.; Serra-Crespo, P.; de Lange, M.; Gascon, J.; Kapteijn, F.; Julve, M.; Cano, J.; Lloret, F.; Pasán, J.; Ruiz-Pérez, C.; Journaux, Y.; Pardo, E. *J. Am. Chem. Soc.* **2012**, *134* (37), 15301–15304.

(88) Abhervé, A.; Grancha, T.; Ferrando-Soria, J.; Clemente-León, M.; Coronado, E.; Waerenborgh, J. C.; Lloret, F.; Pardo, E. *Chem. Commun.* **2016**, *52* (46), 7360–7363.

(89) Zhang, J.-P.; Zhang, Y.-B.; Lin, J.-B.; Chen, X.-M. *Chem. Rev.* **2012**, *112* (2), 1001–1033.

(90) Faust, T. B.; D'Alessandro, D. M. *RSC Adv.* **2014**, *4* (34), 17498–17512.

(91) Maspoch, D.; Ruiz-Molina, D.; Wurst, K.; Domingo, N.; Cavallini, M.; Biscarini, F.; Tejada, J.; Rovira, C.; Veciana, J. A *Nat. Mater.* **2003**, *2* (3), 190–195.

(92) Bousseksou, A.; Molnár, G.; Salmon, L.; Nicolazzi, W. *Chem. Soc. Rev.* **2011**, *40* (6), 3313.

(93) Ohtani, R.; Hayami, S. *Chem. - A Eur. J.* **2017**, *23* (10), 2236–2248.

(94) Mon, M.; Pascual-Álvarez, A.; Grancha, T.; Cano, J.; Ferrando-Soria, J.; Lloret, F.; Gascon, J.; Pasán, J.; Armentano, D.; Pardo, E. *Chem. - A Eur. J.* **2016**, *22* (2), 539–545.

(95) Kreno, L. E.; Leong, K.; Farha, O. K.; Allendorf, M.; Van Duyne, R. P.; Hupp, J. T. *Chem. Rev.* **2012**, *112* (2), 1105–1125.

(96) Kumar, P.; Deep, A.; Kim, K.-H. *TrAC Trends Anal. Chem.* **2015**, *73*, 39–53.

(97) Kajal, N.; Singh, V.; Gupta, R.; Gautam, S. *Environ. Res.* **2022**, *204*, 112320.

(98) Allendorf, M. D.; Bauer, C. A.; Bhakta, R. K.; Houk, R. J. T. *Chem. Soc. Rev.*

2009, *38* (5), 1330.

(99) Tang, Y.-Y.; Ding, C.-X.; Ng, S.-W.; Xie, Y.-S. *RSC Adv.* **2013**, *3* (39), 18134.

(100) Liu, X.-G.; Wang, H.; Chen, B.; Zou, Y.; Gu, Z.-G.; Zhao, Z.; Shen, L. *Chem. Commun.* **2015**, *51* (9), 1677–1680.

(101) Wang, K.; Lv, X.-L.; Feng, D.; Li, J.; Chen, S.; Sun, J.; Song, L.; Xie, Y.; Li, J.-R.; Zhou, H.-C. *J. Am. Chem. Soc.* **2016**, *138* (3), 914–919.

(102) Dou, Z.; Yu, J.; Cui, Y.; Yang, Y.; Wang, Z.; Yang, D.; Qian, G. *J. Am. Chem. Soc.* **2014**, *136* (15), 5527–5530.

(103) Zhang, H.-T.; Zhang, J.-W.; Huang, G.; Du, Z.-Y.; Jiang, H.-L. *Chem. Commun.* **2014**, *50* (81), 12069–12072.

(104) Zhu, Y.-M.; Zeng, C.-H.; Chu, T.-S.; Wang, H.-M.; Yang, Y.-Y.; Tong, Y.-X.; Su, C.-Y.; Wong, W.-T. *J. Mater. Chem. A* **2013**, *1* (37), 11312.

(105) Li, Y. T *Polyhedron* **2020**, *179*, 114413.

(106) Jiang, H.-L.; Feng, D.; Wang, K.; Gu, Z.-Y.; Wei, Z.; Chen, Y.-P.; Zhou, H.-C. *J. Am. Chem. Soc.* **2013**, *135* (37), 13934–13938.

(107) Huang, Y.-B.; Liang, J.; Wang, X.-S.; Cao, R. *Chem. Soc. Rev.* **2017**, *46* (1), 126–157.

(108) Dhakshinamoorthy, A.; Li, Z.; Garcia, H. *Chem. Soc. Rev.* **2018**, *47* (22), 8134–8172.

(109) Schlichte, K.; Kratzke, T.; Kaskel, S. *Microporous Mesoporous Mater.* **2004**, *73* (1–2), 81–88.

(110) Gascon, J.; Aktay, U.; Hernandez-Alonso, M.; Vanklink, G.; Kapteijn, F. *J. Catal.* **2009**, *261* (1), 75–87.

(111) Wang, S.; McGuirk, C. M.; D'Aquino, A.; Mason, J. A.; Mirkin, C. A. *Adv. Mater.* **2018**, *30* (37), 1800202.

(112) Mon, M.; Adam, R.; Ferrando−Soria, J.; Corma, A.; Armentano, D.; Pardo, E.; Leyva−Pérez, A. *ACS Catal.* **2018**, *8* (11), 10401–10406.

(113) Majewski, M. B.; Howarth, A. J.; Li, P.; Wasielewski, M. R.; Hupp, J. T.; Farha, O. K. *CrystEngComm* **2017**, *19* (29), 4082–4091.

(114) Fang, X.; Shang, Q.; Wang, Y.; Jiao, L.; Yao, T.; Li, Y.; Zhang, Q.; Luo, Y.; Jiang, H.-L. S *Adv. Mater.* **2018**, *30* (7), 1705112.

(115) Huxley, M. T.; Burgun, A.; Ghodrati, H.; Coghlan, C. J.; Lemieux, A.; Champness, N. R.; Huang, D. M.; Doonan, C. J.; Sumby, C. J. *J. Am. Chem. Soc.* **2018**, *140* (20), 6416–6425.

(116) Horcajada, P.; Gref, R.; Baati, T.; Allan, P. K.; Maurin, G.; Couvreur, P.; Férey, G.; Morris, R. E.; Serre, C. *Chem. Rev.* **2012**, *112* (2), 1232–1268.

(117) Miller, S. R.; Heurtaux, D.; Baati, T.; Horcajada, P.; Grenèche, J.-M.; Serre,

C. *Chem. Commun.* **2010**, *46* (25), 4526.

(118) Rieter, W. J.; Taylor, K. M. L.; An, H.; Lin, W.; Lin, W. *J. Am. Chem. Soc.* **2006**, *128* (28), 9024–9025.

(119) Taylor, K. M. L.; Rieter, W. J.; Lin, W. *J. Am. Chem. Soc.* **2008**, *130* (44), 14358–14359.

(120) Rojas, S.; Horcajada, P. *Chem. Rev.* **2020**, *120* (16), 8378–8415.

(121) Alvaro, M.; Carbonell, E.; Ferrer, B.; Llabrés i Xamena, F. X.; Garcia, H. *Chem. - A Eur. J.* **2007**, *13* (18), 5106–5112.

(122) Grancha, T.; Mon, M.; Ferrando-Soria, J.; Armentano, D.; Pardo, E. *Cryst. Growth Des.* **2016**, *16* (9), 5571–5578.

(123) Mon, M.; Bruno, R.; Elliani, R.; Tagarelli, A.; Qu, X.; Chen, S.; Ferrando-Soria, J.; Armentano, D.; Pardo, E. *Inorg. Chem.* **2018**, *57* (21), 13895–13900.

(124) Ruiz, R.; Faus, J.; Lloret, F.; Julve, M.; Journaux, Y. *Coord. Chem. Rev.* **1999**, *193–195*, 1069–1117.

(125) Pardo, E.; Ruiz-García, R.; Cano, J.; Ottenwaelder, X.; Lescouëzec, R.; Journaux, Y.; Lloret, F.; Julve, M. *Dalt. Trans.* **2008**, No. 21, 2780.

(126) Dul, M.-C.; Pardo, E.; Lescouëzec, R.; Journaux, Y.; Ferrando-Soria, J.; Ruiz-García, R.; Cano, J.; Julve, M.; Lloret, F.; Cangussu, D.; Pereira, C. L. M.; Stumpf, H. O.; Pasán, J.; Ruiz-Pérez, C. *Coord. Chem. Rev.* **2010**, *254* (19–20), 2281–2296.

(127) Grancha, T.; Ferrando-Soria, J.; Cano, J.; Amorós, P.; Seoane, B.; Gascon, J.; Bazaga-García, M.; Losilla, E. R.; Cabeza, A.; Armentano, D.; Pardo, E. *Chem. Mater.* **2016**, *28* (13), 4608–4615.

(128) Mon, M.; Qu, X.; Ferrando-Soria, J.; Pellicer-Carreño, I.; Sepúlveda-Escribano, A.; Ramos-Fernandez, E. V.; Jansen, J. C.; Armentano, D.; Pardo, E. *J. Mater. Chem. A* **2017**, *5* (38), 20120–20125.

(129) Grancha, T.; Mon, M.; Ferrando-Soria, J.; Gascon, J.; Seoane, B.; Ramos-Fernandez, E. V.; Armentano, D.; Pardo, E. *J. Mater. Chem. A* **2017**, *5* (22), 11032–11039.

(130) Mon, M.; Bruno, R.; Tiburcio, E.; Grau-Atienza, A.; Sepúlveda-Escribano, A.; Ramos-Fernandez, E. V.; Fuoco, A.; Esposito, E.; Monteleone, M.; Jansen, J. C.; Cano, J.; Ferrando-Soria, J.; Armentano, D.; Pardo, E. *Chem. Mater.* **2019**, *31* (15), 5856–5866.

(131) Mon, M.; Lloret, F.; Ferrando-Soria, J.; Martí-Gastaldo, C.; Armentano, D.; Pardo, E. *Angew. Chem. Int. Ed.* **2016**, *55* (37), 11167–11172.

(132) Mon, M.; Ferrando-Soria, J.; Grancha, T.; Fortea-Pérez, F. R.; Gascon, J.;

Leyva-Pérez, A.; Armentano, D.; Pardo, E. *J. Am. Chem. Soc.* **2016**, *138* (25), 7864–7867.

(133) Mon, M.; Bruno, R.; Tiburcio, E.; Casteran, P.-E.; Ferrando-Soria, J.; Armentano, D.; Pardo, E. *Chem. - A Eur. J.* **2018**, *24* (67), 17712–17718.

(134) Mon, M.; Bruno, R.; Ferrando-Soria, J.; Bartella, L.; Di Donna, L.; Talia, M.; Lappano, R.; Maggiolini, M.; Armentano, D.; Pardo, E. *Mater. Horizons* **2018**, *5* (4), 683–690.

(135) Tiburcio, E.; Greco, R.; Mon, M.; Ballesteros-Soberanas, J.; Ferrando-Soria, J.; López-Haro, M.; Hernández-Garrido, J. C.; Oliver-Meseguer, J.; Marini, C.; Boronat, M.; Armentano, D.; Leyva-Pérez, A.; Pardo, E. *J. Am. Chem. Soc.* **2021**, *143* (6), 2581–2592.

(136) Mon, M.; Rivero-Crespo, M. A.; Ferrando-Soria, J.; Vidal-Moya, A.; Boronat, M.; Leyva-Pérez, A.; Corma, A.; Hernández-Garrido, J. C.; López-Haro, M.; Calvino, J. J.; Ragazzon, G.; Credi, A.; Armentano, D.; Pardo, E. *Angew. Chem. Int. Ed.* **2018**, *57* (21), 6186–6191.

(137) Negro, C.; Bilanin, C.; Qu, X.; Oliver-Meseguer, J.; Ferrando-Soria, J.; Leyva-Pérez, A.; Armentano, D.; Pardo, E. *Chem. Commun.* **2022**, *58* (37), 5578–5581.

(138) Mon, M.; Bruno, R.; Tiburcio, E.; Viciano-Chumillas, M.; Kalinke, L. H. G.; Ferrando-Soria, J.; Armentano, D.; Pardo, E. *J. Am. Chem. Soc.* **2019**, *141* (34), 13601–13609.

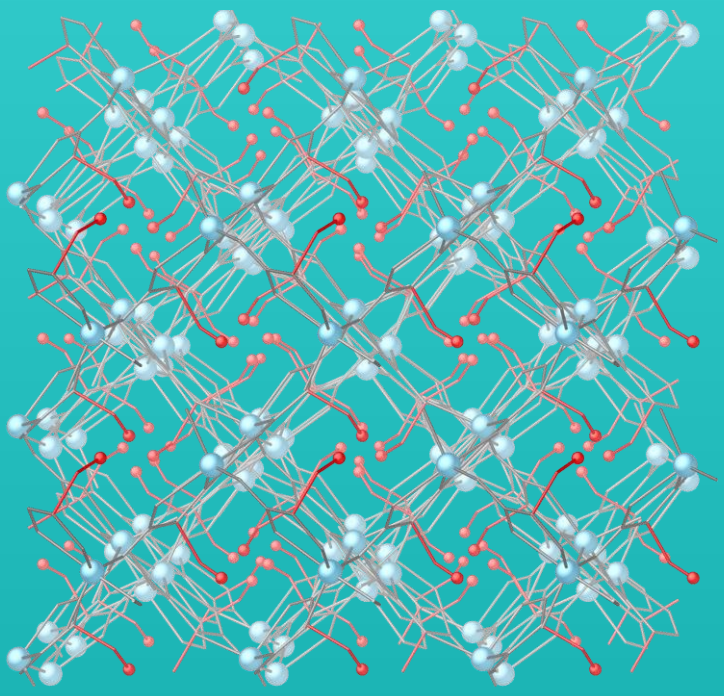

CHAPTER 2

Photodegradation of Brilliant Green Dye by a Zinc bioMOF

2.1. Introduction

One of the main challenges that modern society faces is related, undoubtedly, to the contamination of aquatic environments, which is mainly caused by human/industrial activities (Figure 2.1).[1,2] Among the wide diversity of inorganic/organic chemical pollutants, organic dyes –wastes generated in cosmetic, textile, tannery or food industries, among others– constitute one of the major contaminants of industrial wastewater.[3]

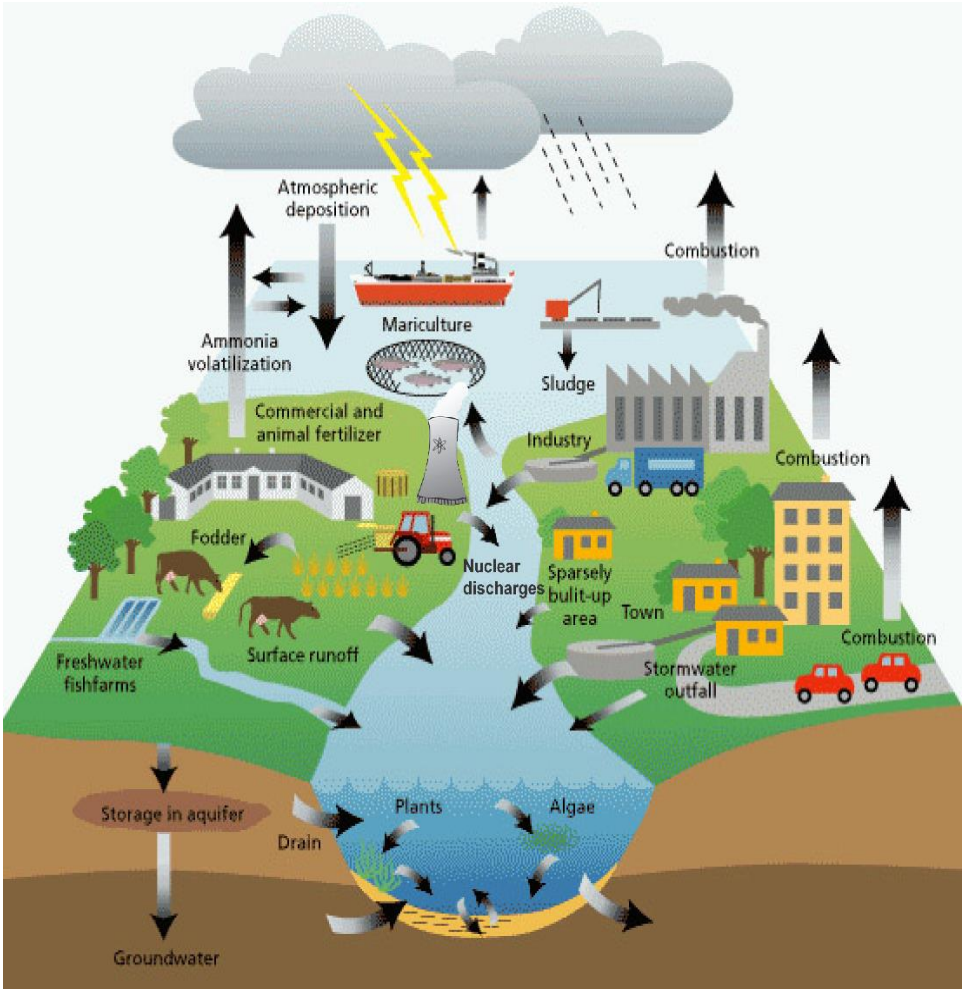

Figure 2.1. Sources of groundwater contamination in the hydrologic cycle. Reproduced from ref. 8.

Proposed solutions for the removal of such organic contaminants include precipitation, coagulation/flocculation, membrane technology or biological processes (Figure 2.2).[4] However, probably the two most promising technologies for this purpose are based on the straightforward capture of the organic dyes by a porous material or their *in-situ* photocatalytic degradation.[5,6] In particular, Metal-organic frameworks (MOFs) are porous crystalline materials that have already been shown efficient in the last two approaches.[7–13]

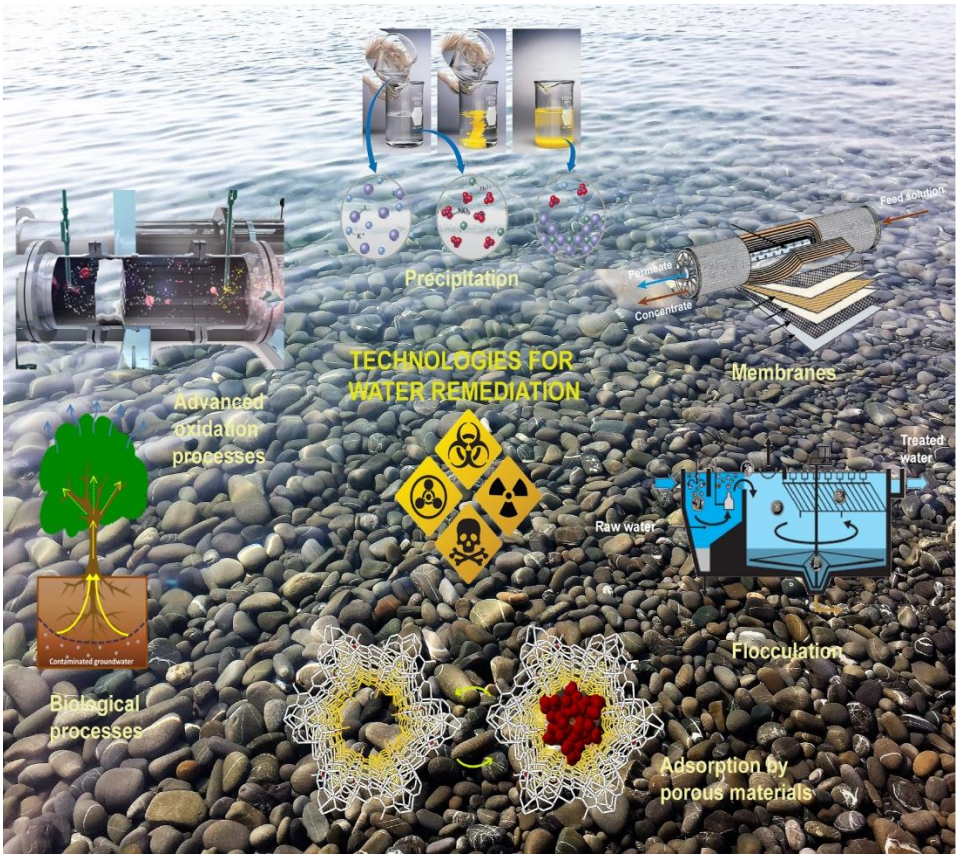

Figure 2.2. Current technologies and processes for water decontamination. Reproduced from ref. 8.

MOFs[14,15] attract broad attention from many research groups given the great variety of applications they can exhibit.[9,16–45] The reasons for such variety of applications are related to a number of unique characteristics such as

permanent porosity,[46,47] a thrilling host-guest chemistry[48–81] –which can be somehow tuned by a fine control over the size, shape and functionality of MOF channels– and the possibility to use single-crystal X-ray diffraction[82–87] (SCXRD) to visualize what is going on within their channels.[88–91]

In particular, MOFs have been recently used in water remediation with exceptional results. For example, the easy of functionalizing, pre- or post-synthetically, MOF channels has led to the preparation of specifically designed MOFs for the selective and efficient capture of both, organic and inorganic contaminants.[9,34–37,39] Moreover, certain specifically designed MOFs have already been shown effective as photocatalysts to degrade organic pollutants –*i.e.* organic dyes– into less toxic intermediates or fully degrade them into CO_2 and H_2O.[92–95] In particular, several Zn(II)-based MOFs have been recently reported, showing, by analogy to zinc oxide based photocatalysts,[9697] moderately good efficiencies as photocatalysts towards different organic dyes.[92,98]

2.2. Objectives

Considering the problematic exposed on the introduction (section 2.1.), I pretended to go one step further on the use of porous materials for the encapsulation and photodegradation of organic contaminants. For that, I planned to synthesize a biomimetic Zn-based MOF capable to efficiently degrade brilliant green (BG), a well-known organic dye. The specific objectives of the chapter are summarized as:

- Preparation of a Zn(II) MOF with the natural amino acid *S*-serine, as ligand, featuring medium-sized channels, densely decorated with *L*-serine residues. The pores should be large enough to accommodate and immobilize, at least partially and with the help of amino acid residues, BG dyes. Once the organic

dyes are inserted, total or partially, Zn(II) cations should be capable to photodegrade them.

- Considering the well-known robustness and crystallinity of oxamidato-based MOFs, we expect to be capable to use SCXRD to determine the crystal structure of the Zn(II) MOF as well as obtaining snapshots about the photocatalytic process.

- Study of the photocatalytic activity shown by this material.

2.3. Results and discussion

In this chapter, we report the preparation and total characterization of a novel eco-friendly Zn-based MOF, derived from the natural amino acid *L*-serine, with formula $\{Zn^{II}_2[(S,S)\text{-serimox}](H_2O)_2\} \cdot H_2O$ (**Zn^{II}_2-serimox**) ((*S,S*)-serimox = [bis[(*S*)-serine]oxalyl diamide] (Figures 2.3a and 2.3b). The final material is capable to photodegrade the BG dye (Figure 2.3c) in only 120 min. with an efficiency of 100%, in the absence of any other oxidant or co-catalyst. In addition, the high robustness and crystallinity of **Zn^{II}_2-serimox** also allowed to obtain its crystal structure –with the help of SCXRD– after the photocatalytic process, which shows, unambiguously, the presence, within the channels, of CO_2 molecules resulting from the photodegradation of BG dyes.

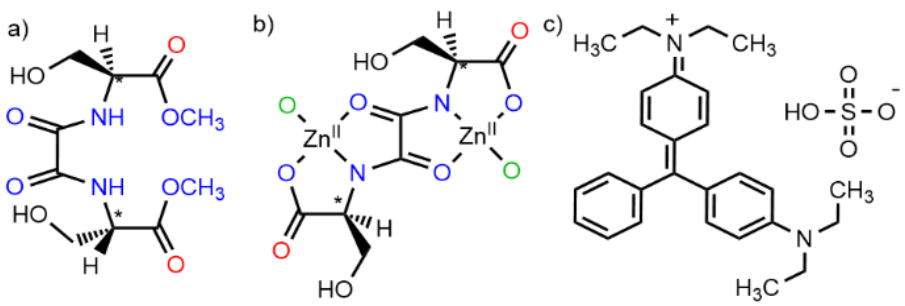

Figure 2.3. Chemical formulas of the proligand (*S,S*)-serimox (a) and the secondary building units (SBU) consisting of Zn(II) dinuclear units (b). Red oxygen atoms coordinate Zn(II) atoms from another SBU, whereas green oxygen atoms belong to neighboring SBUs. c) Chemical formula of BG dye.

2.3.1. General synthetic procedure

Compound **Zn^{II}_2-serimox** ({Zn^{II}_2[(*S,S*)-serimox](H$_2$O)$_2$} · H$_2$O) can be obtained in two ways, first one consisting on the direct precipitation in water, after mixing Zn(II) cations, and the deprotonated ligand, and the second one consisting on the previous synthesis of a Ni(II) precursor (with formula (Me$_4$N)$_2${Ni$_2$[(*S,S*)-serimox](OH)$_2$}·5H$_2$O), that experiences a methatesis in contact to Zn(II) cations, forming the same MOF **Zn^{II}_2-serimox**. The first strategy is used to obtain MOF **Zn^{II}_2-serimox** in large scale, whereas the second indirect strategy allows the formation of well-defined crystals, suitable for SCXRD.

Moreover, the crystal structure of MOF **Zn^{II}_2-serimox**, immersed for one week in an aqueous BG solution and after irradiating with a with an UV lamp in the range of λ = 250-350 nm, for 60 min, could be also obtained. In so doing, the crystal structure of a host-guest aggregate, containing CO_2 molecules within the pores could be also unveiled and the novel material {Zn^{II}_2[(*S,S*)-serimox](H$_2$O)$_2$] · CO_2 (**CO_2@Zn^{II}_2-serimox**) was chemically defined with the help of other techniques (see characterization section, 2.3.2.). All synthesis mentioned above are fully described in the experimental section (see 2.5.1.).

2.3.2. Characterization of the MOFs

2.3.2.1. Crystal structure

The crystal structure of **Zn^{II}_2-serimox** was first determined at 100 K. It crystallises in the chiral $P4_12_12$ space group of the tetragonal system and consist of a chiral 3D pillared square grid where [Zn^{II}_2(*S,S*)-serimox] moieties are located on the vertices of the edges (Figures 2.4 and 2.5). The robust uni-nodal three-connected **srs** nets are built up from *trans* oxamidato-bridged Zn(II) dimeric units,

{Zn^{II}_2[(S,S)-serimox]} (Figures 2.4 and 2.6), assembled each other through the carboxylate groups (Figures 2.4, 2.6 and 2.7).

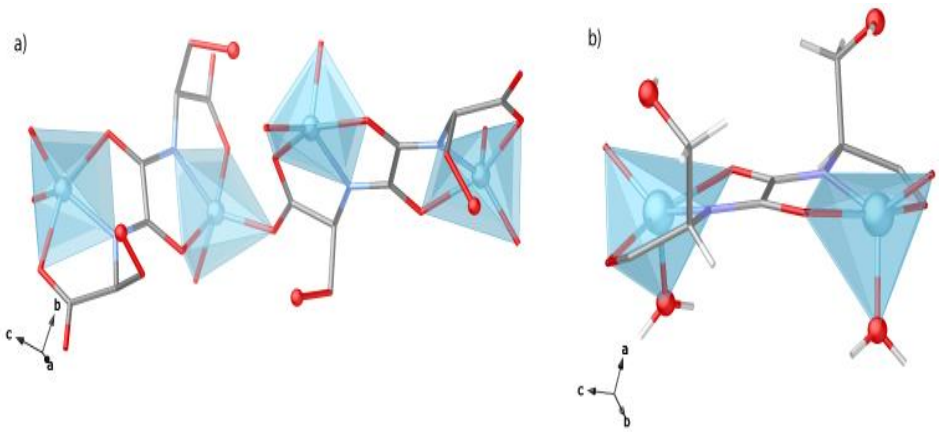

Figure 2.4. Perspective view of a fragment of **Zn^{II}_2-serimox** emphasizing the central dinuclear Zn_2 SBU unit and their connection to neighboring Zn(II) cations. Color code: Zn, O and N atoms are represented as cyan, red and deep blue spheres, respectively, whereas C atoms are depicted as grey sticks.

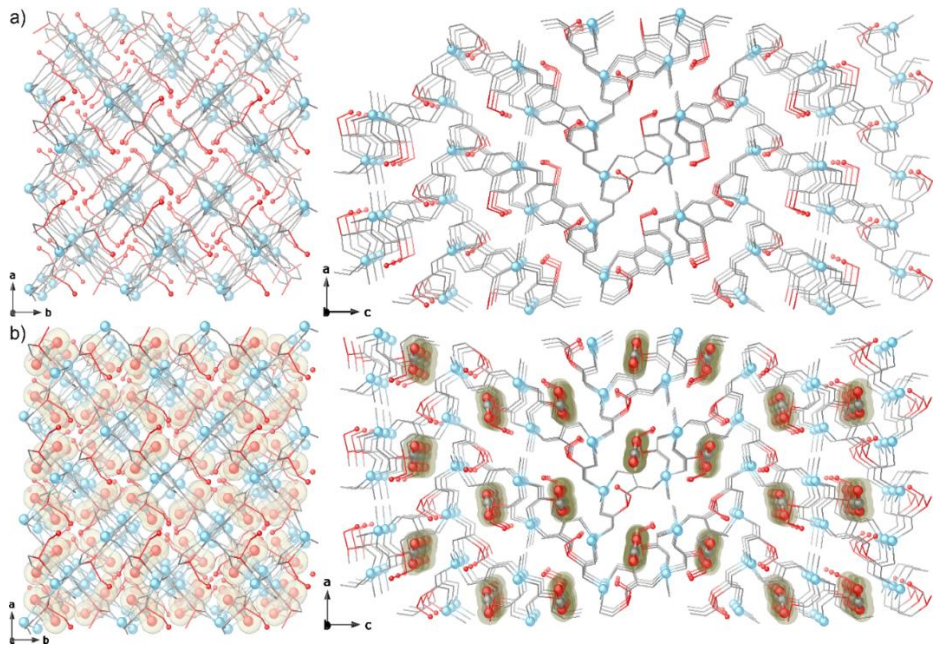

Figure 2.5. Perspective views of the porous networks of **Zn^{II}_2-serimox** (a) and **CO_2@ Zn^{II}_2-serimox** (b) along the *c* (left) and *b* (right) axes. Colour code: Zn atoms and C and O from guest CO_2 molecules are represented as cyan, grey and red spheres, whereas serimox ligands –with the exception of serine residues– are represented as grey sticks. –CH_2OH groups and N atoms are represented as cyan, red and deep blue spheres, respectively, whereas C atoms are depicted as grey sticks.

Within the {Zn^{II}_2[(S,S)-serimox]} moieties, each Zn(II) metal ion results in a highly distorted pyramidal coordination being linked by nitrogen and oxygen atoms from the serimox ligand [Zn-N 1.985(4)Å and Zn-O_{ser} ranging from 1.958(3) to 2.215(4) Å] and a terminal water molecule [Zn-O_{water} 2.011(4) Å] (Figure 2.4b). The 3D network features two types of small pore, different in size and shape, propagating along the *b* and *c* axes (Figures 2.5, 2.7 and 2.8). Hydrophilic square sized pores (Figures 2.5a left and 2.8) and a kind of hydrophilic irregular pores of medium size (virtual diameters of *ca.* 0.30 and 0.40 nm, respectively) (Figures 2.5a right and 2.7) are decorated by the primary alcohol group of serine moieties, pointing inwards of the voids, and accountable of its host-guest resulting chemistry.

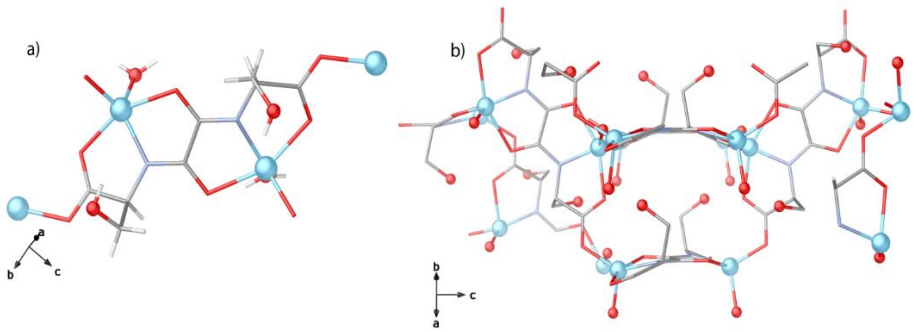

Figure 2.6. Perspective views of SBUs a) and their assembly by means the carboxylate groups b) in **Zn^{II}_2-serimox**. Colour code: Zn atoms are represented as cyan spheres, C, N, H and O atoms from serimox ligands –with the exception of OH of serine residues– are represented as grey, cyan, white and red sticks. Oxygen atoms from -OH groups are represented as red spheres.

Crystals of **Zn^{II}_2-serimox**, were left in a sealed glass tube containing aqueous solution of BG dye for one week, after irradiation in the range 250-350 nm for 60 min. were analysed by SCXRD at a temperature of 100 K and the crystal structure of **CO_2@Zn^{II}_2-serimox** was determined revealing a slightly deformation of the framework –likely correlated to CO_2 adsorption process–, but still isomorphous to **Zn^{II}_2-serimox**, crystallizing in the $P4_12_12$ space group. Adsorption of CO_2 gas –produced by the photocatalytic process at 298 K– results in linear negative expansion. Pores that run parallel to the *c*-axis contract upon CO_2

inclusion (Δa, Δb slightly < 0; Δc < 0; ΔV < 0). The largest change in dimensions is observed for *c* axis, accounting for a small decrease in the unit-cell volume ($\Delta V \approx$ 48 Å^3, Table 2.1).

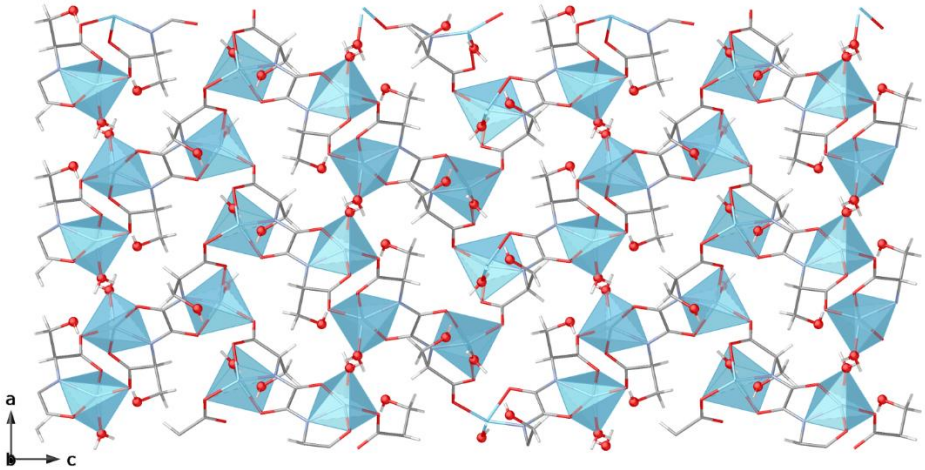

Figure 2.7. View of the network of **Zn^{II}_2-serimox** along the *b* axes. Colour code: Zn atoms are represented as cyan polyhedra, C, N, H and O atoms from serimox ligands –with the exception of OH of serine residues– are represented as grey, cyan, white and red sticks. Oxygen atoms from -OH groups are represented as red spheres.

The crystal structure of the adsorbate **CO_2@Zn^{II}_2-serimox** clearly evidences the presence of CO_2 guest molecules hosted in the hydrophilic irregular pores of **Zn^{II}_2-serimox** (Figures 2.5b and 2.9-2.11). For the CO_2 molecule, can be identified a primary adsorption site (Figure 2.12) where the plane containing the ligands are situated at only 2.83(1) Å [distance between centroid of oxamate core and C atom of CO_2 molecule] from the C atom of CO_2 molecules occupying the primary site, suggesting an interaction between the C(δ^+) atom of the CO_2 molecule and the O lone pair of the oxamate core of the ligand, as observed before.[99] The secondary adsorption sites identified, are situated at the center of the pores, where CO_2 molecules are packed with closest contacts with the framework through the H_2C- and HC- of the ligand [shortest O-C-O··· H-C- at 2.04(3) and 2.09(3) Å, for H_2C- and HC- fragments, respectively] (Figures 2.9, 2.10 and 2.12). The alcoholic fragment gives its contribution as well, being situated

very close to CO_2 molecules [O-C-O···H-O- and HO···O-C-O at 2.11(6) and 2.63(3) Å, respectively]. Despite the supposed flexibility and structural adaptability that serine residues could offer, no important differences in the alcoholic chain conformations have been observed in the **CO_2@Zn^{II}_2-serimox** adsorbate with respect to **Zn^{II}_2-serimox**, where only Zn-O_{ser} [ranging from 1.935(3) to 2.191(4) Å] distances show a slight contraction respect to **Zn^{II}_2-serimox**, while Zn-O_{water} [1.992(4) Å], and Zn-N bond lengths [1.959(4) Å] fall in the range of the expected values for Zn(II) metal ions.[100]

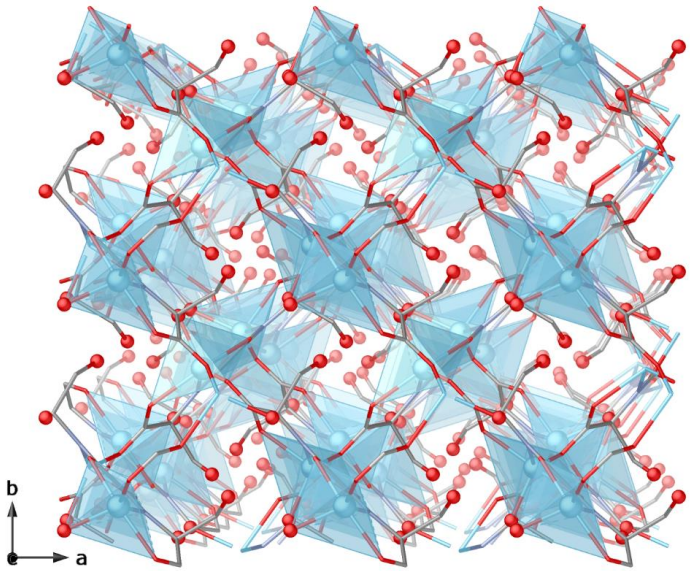

Figure 2.8. Perspective view of the network of **Zn^{II}_2-serimox** along the *c* axes. Color code: Zn atoms are represented as cyan polyhedra, C, N, H and O atoms from serimox ligands – with the exception of OH of serine residues– are represented as grey, cyan, white and red sticks. Oxygen atoms from -OH groups are represented as red spheres.

It is worth to underline the unusual penta-coordination of Zn(II) ions observed in **Zn^{II}_2-serimox** and **CO_2@Zn^{II}_2-serimox**, reminiscent (in geometry) of that observed for the catalytic metal ions of the di-zinc aminopeptidase from Aeromonas proteolytica (AAP).[101] Surveys of the Cambridge Structural Database (CSD) show zinc ion coordination number frequencies of *ca*. 60% and 25% for 4 and 6 coordination numbers, respectively. Interestingly, the zinc ion coordination

prevalence in protein sites depends on whether the zinc plays a structural or a catalytic role. In structural zinc sites, the occurrence rate for 4, 5, and 6 coordination numbers is 80%, 6%, and 12%, respectively; whereas in catalytic zinc sites, the occurrence rate for 4, 5, and 6 coordination is 47%, 45%, and 6%, respectively.[102] Thus, five coordinate, or geometrically strained zinc sites, may represent sites equipped for catalysis; whereas, four coordinate ideal tetrahedral zinc sites, may represent stable sites affiliated for structural support.

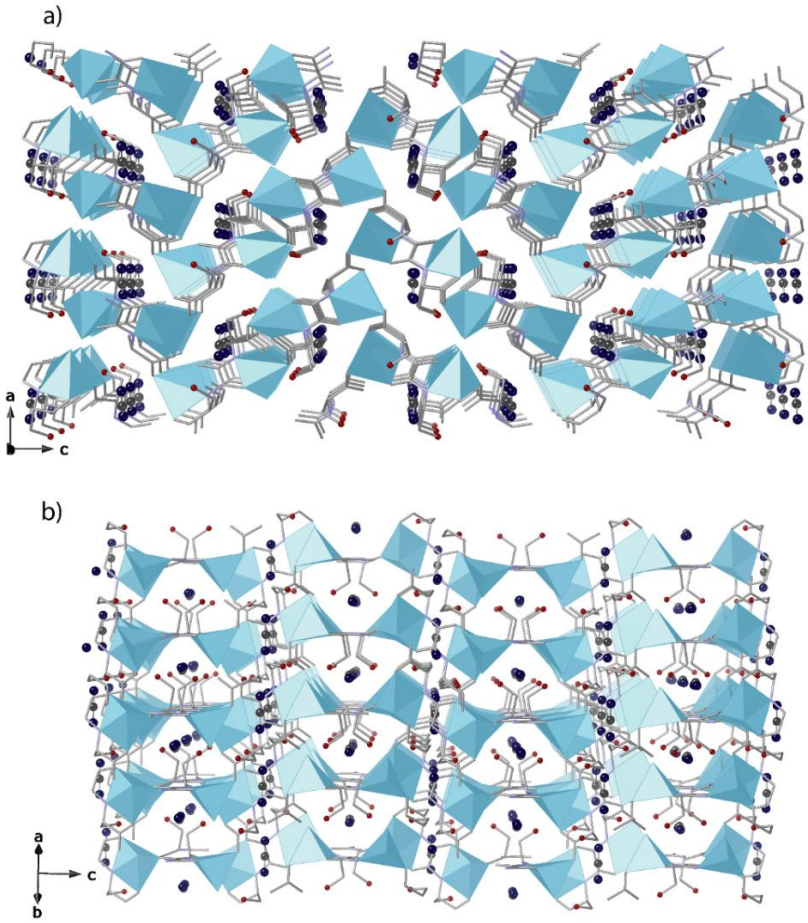

Figure 2.9. Perspective views of the network of **CO_2@Zn^{II}_2-serimox** along the *b* and [1 1 0] directions (a and b, respectively) unveiling CO_2 molecules retained within voids. Color code: Zn atoms are represented as cyan polyhedra, C, N, and O atoms from serimox ligands –with the exception of OH of serine residues– are represented as grey sticks. Oxygen atoms from -OH groups are represented as red spheres whereas oxygen atoms from guest molecules are represented as deep blue spheres. Hydrogen atoms have been omitted for the sake of clarity.

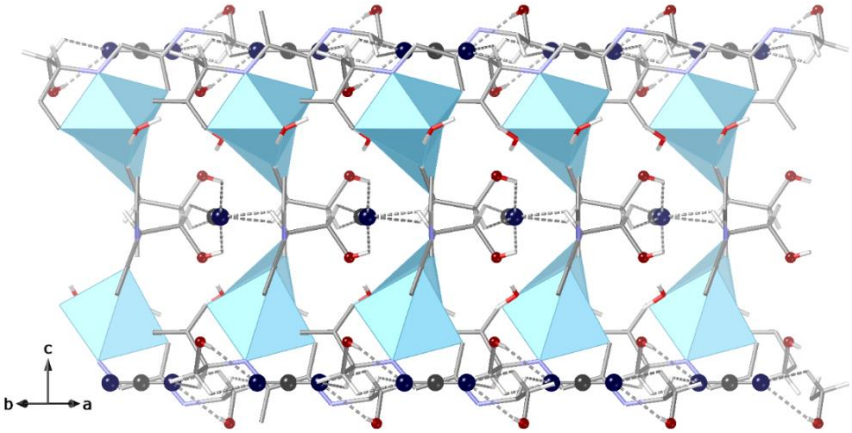

Figure 2.10. Details of host-guest interactions in **CO_2@Zn^{II}_2-serimox** along the *c* [1 1 0] direction. Zn atoms are represented as cyan polyhedra, C, N, and O atoms from serimox ligands –with the exception of OH of serine residues– are represented as grey sticks. Oxygen atoms from -OH groups are represented as red spheres whereas oxygen atoms from guest molecules are represented as deep blue spheres.

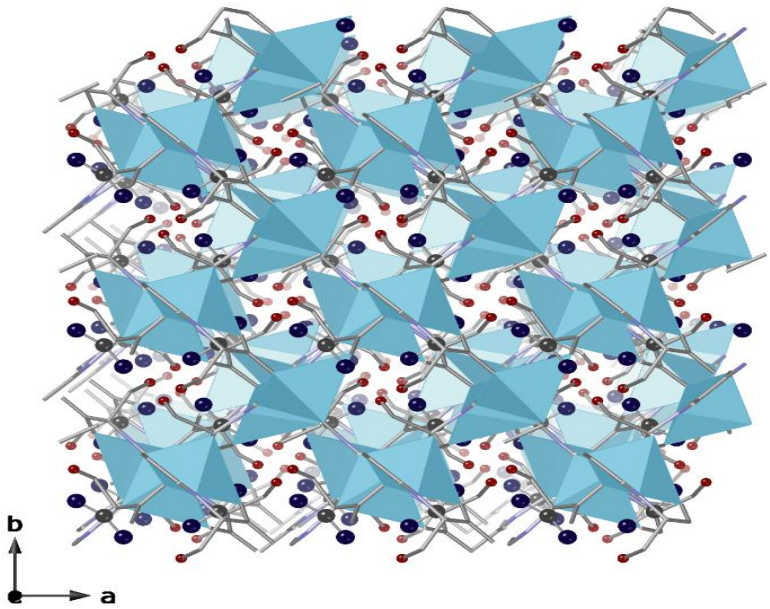

Figure 2.11. Perspective view of the network of **CO_2@Zn^{II}_2-serimox** along the *c* direction unveiling CO_2 molecules retained within voids. Color code: Zn atoms are represented as cyan polyhedra, C, N, and O atoms from serimox ligands –with the exception of OH of serine residues– are represented as grey sticks. Oxygen atoms from -OH groups are represented as red spheres whereas oxygen atoms from guest molecules are represented as deep blue spheres. Hydrogen atoms have been omitted for the sake clarity.

Table 2.1. Summary of Crystallographic Data for **Zn^{II}_2-serimox** and **CO_2@Zn^{II}_2-serimox.**

Compound	**Zn^{II}_2-serimox**	**CO_2@Zn^{II}_2-serimox**
Formula	$C_8Zn_2H_{12}N_2O_{10}$	$C_{8.5}Zn_2H_{12}N_2O_{11}$
M (g mol^{-1})	426.94	448.94
λ (Å)	0.71073	0.71073
Crystal system	Tetragonal	Tetragonal
Space group	$P4_12_12$	$P4_12_12$
a (Å)	7.6380(10)	7.5543(3)
c (Å)	24.390(4)	24.0962(12)
V (Å^3)	1422.9(4)	1375.11(12)
Z	4	4
ρ_{calc} (g cm^{-3})	1.993	2.169
μ (mm^{-1})	3.425	3.555
T (K)	100	100
θ range for data collection (°)	3.147 to 26.675	2.826 to 26.987
Completeness to θ = 25.0	100%	100%
Measured reflections	20277	4650
Unique reflections (Rint)	1507 (0.0672)	1449 (0.0301)
Observed reflections [$I > 2\sigma(I)$]	1319	1360
Goof	1.003	1.107
R^a [$I > 2\sigma(I)$] (all data)	0.0311 (0.0401)	0.0293 (0.0315)
wR^b [$I > 2\sigma(I)$] (all data)	0.0808 (0. 0.0855)	0.0845 (0.0837)
Flack parameter	0.00(1)	0.00(1)
CCDC	2062289	2062290

^{a} $R = \sum(||F_o| - |F_c||)/\sum|F_o|$. ^{b} $wR = [\sum w(|F_o| - |F_c|)^2/\sum w|F_o|^2]^{1/2}$.

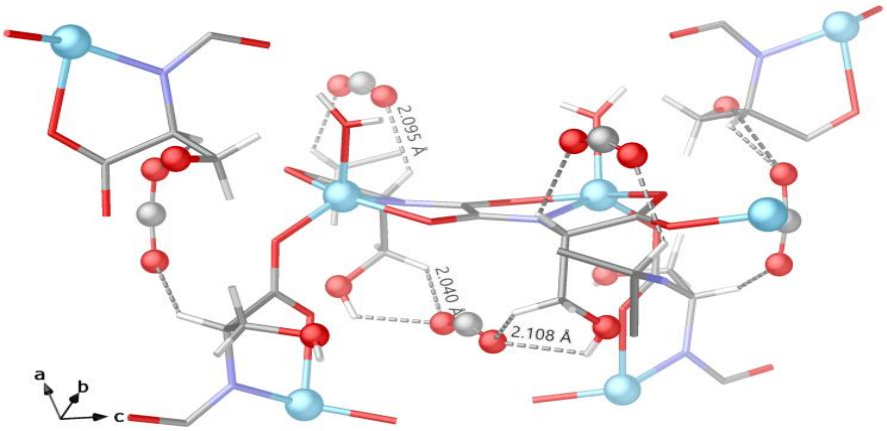

Figure 2.12. Details of **CO_2@Zn^{II}_2-serimox** crystal structure showing the adsorption sites identified for CO_2 adsorbed molecules. Color code as in Figure 2.5.

2.3.2.2. Powder X-Ray diffraction and chemical analyses

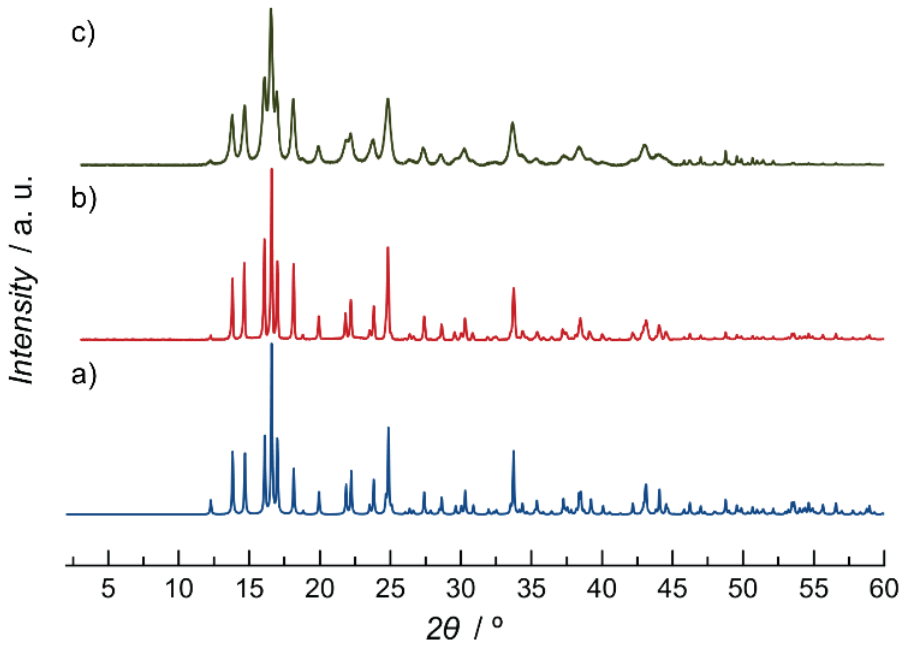

Figure 2.13. Calculated (a) and experimental (b) PXRD patterns of **Zn^{II}_2-serimox** in the 2θ range 2.0–60.0° at R.T. (c) Experimental PXRD pattern of **Zn^{II}_2-serimox** after three consecutive cycles of photocatalytic degradation of BG.

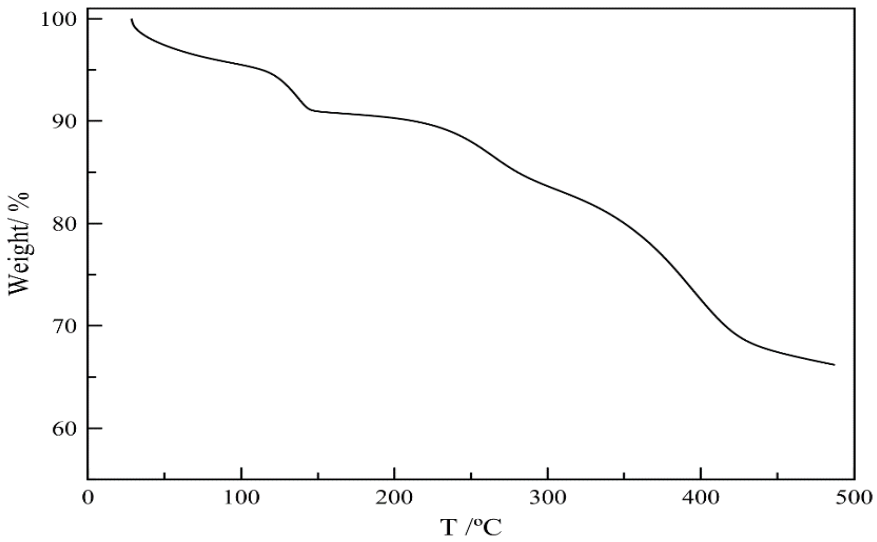

Figure 2.14. Thermo-Gravimetric Analysis (TGA) of **Zn^{II}_2-serimox** under dry N_2 atmosphere.

In addition to the structural characterization (see 1.3.2.1), the chemical identity of **Zn^{II}_2-serimox** and **CO_2@Zn^{II}_2-serimox**) was confirmed by elemental analyses (C, H, S, N), inductively coupled plasma–mass spectrometry (ICP–MS), powder X–ray diffraction (PXRD) and thermo–gravimetric (TGA) analyses. Both C, H, S, N analyses and ICP–MS measurements, together with TGA analyses, allowed to determine the chemical formulas of **Zn^{II}_2-serimox** and **CO_2@Zn^{II}_2-serimox**. Thus, the chemical formulas given in the experimental section are extracted from these analyses. The experimental powder X-ray diffraction (PXRD) pattern of a polycrystalline sample of **Zn^{II}_2-serimox** is shown in Figure 2.13. It is consistent with the theoretical one, and confirms the purity and homogeneity of the bulk sample. The solvent contents were determined by thermogravimetric analysis (TGA) under dry N_2 atmosphere (see Figure 2.14) and helped to establish the final chemical formula. Attempts to activate **Zn^{II}_2-serimox** –under different protocols– for measuring N_2 isotherms resulted unsuccessful, most likely related to its loss of structural stability when all molecule solvents were removed.

2.3.3. Photocatalytic experiments

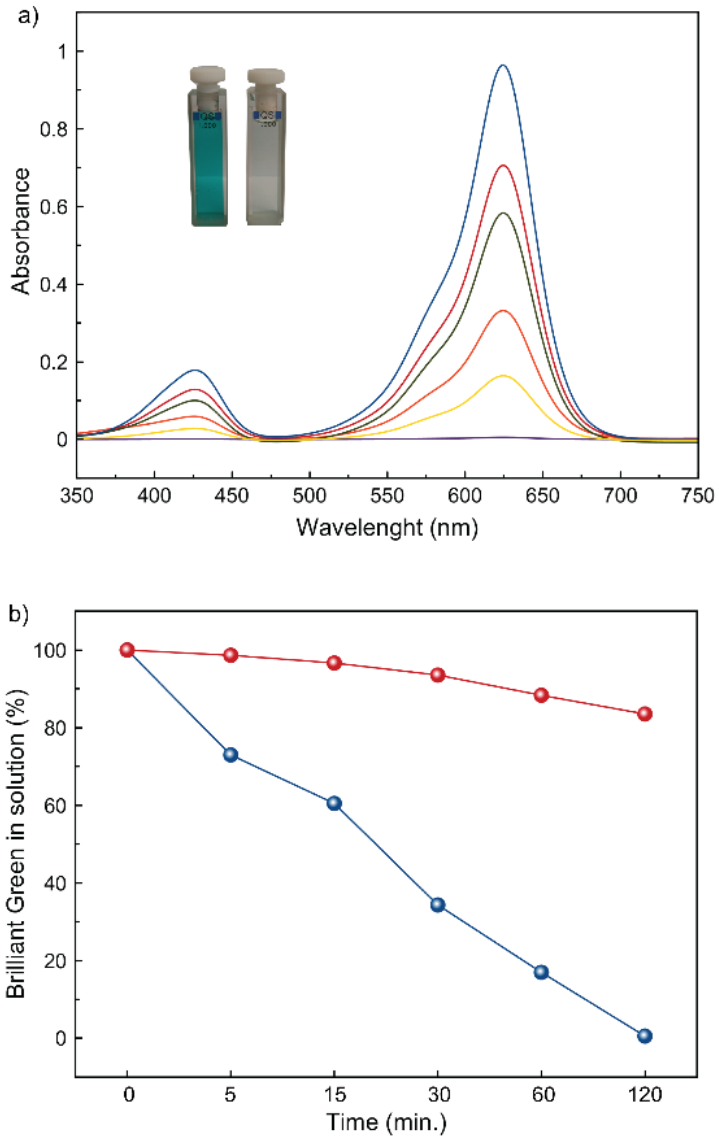

Figure 2.15. (a) Evolution with time of the UV-Vis absorption spectra of 10 ppm solutions of BG in water in the presence of 25 mg of a polycrystalline sample of **Zn^{II}_2-serimox**. Blue: *t* = 0; Red: *t* = 5 min.; Green: *t* = 15 min.; Orange = 30 min.; Yellow: *t* = 60 min.; Purple: *t* = 120 min. The inset shows the BG solutions at t = 0 min. (left) and 120 min. (right) of exposure of the BG solution with MOF **Zn^{II}_2-serimox**. (b) Kinetic profile of the degradation of BG under irradiation centered at 250 nm in the presence of MOF **Zn^{II}_2-serimox** (blue) and with no photocatalyst (red).

The photocatalytic activity of MOF **Zn^{II}_2-serimox** for the degradation of BG dye was then investigated. For this purpose, 25 mg of **Zn^{II}_2-serimox** were suspended in 50 mL of a 10 ppm aqueous solution of BG. Prior to irradiation, the mixture was kept in the dark for 30 min to verify that degradation only occurs under irradiation. After that period, the suspension started to be irradiated, under mild stirring, centered at 250 nm. At different times (5, 15, 30, 60 and 120 min), 1 mL aliquots were taken, centrifuged and diluted, and their UV–Vis absorption spectra were registered (Figure 2.15a). An identical experiment was performed, under the same conditions, in the absence of **Zn^{II}_2-serimox** (Figure 2.16). In order to have a better characterization of **Zn^{II}_2-serimox**, we have performed UV-Vis diffuse reflectance spectroscopy, which revealed a strong adsorption band below 350 nm (Figure 2.17).

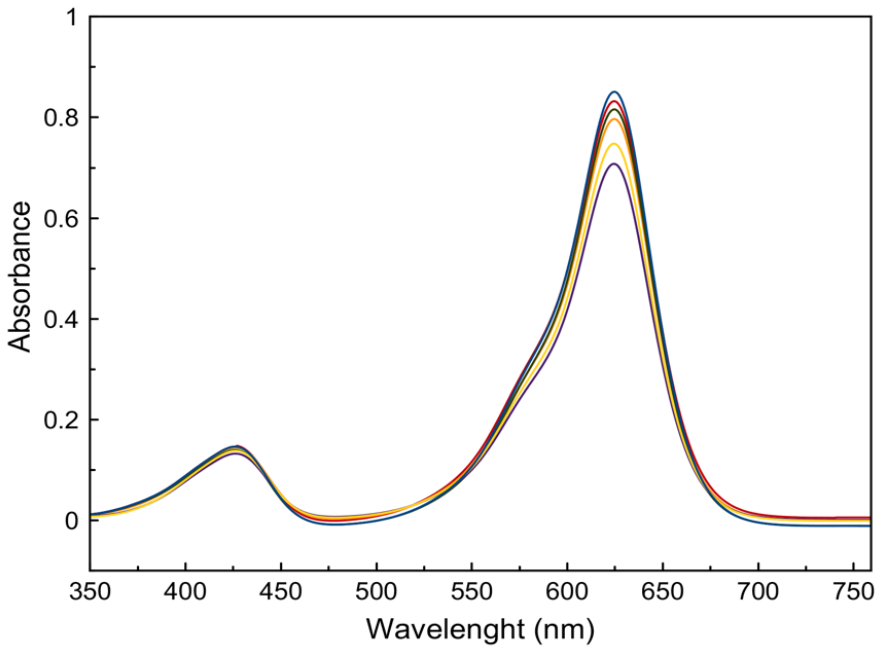

Figure 2.16. Evolution with time of the UV-Vis absorption spectra of 10 ppm solutions of BG in water under irradiation centered at 250 nm. Blue: *t* = 0; Red: *t* = 5 min.; Green: *t* = 15 min.; Orange = 30 min.; Yellow: *t* = 60 min.; Purple: *t* = 120 min.

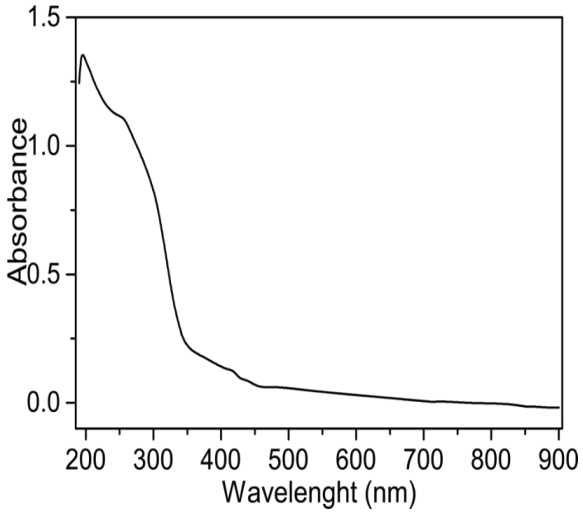

Figure 2.17. UV-Vis spectrum of a polycrystalline sample of **Zn^{II}_2-serimox**.

Figure 2.15 shows the photodegradation efficiency of **Zn^{II}_2-serimox** towards BG. Such efficiency was evaluated by measuring the decrease of the characteristic absorption bands of BG dye, which appear at 420 and 625 nm, respectively. Thus, under irradiation in the presence of **Zn^{II}_2-serimox**, it can be observed a gradual decrease of both peaks with time to vanish, completely, after only 120 min (Figure 2.15a), which indicates that the 100 % of BG dye is eliminated after that time (Figure 2.15b). In turn, the same experiment, in the absence of **Zn^{II}_2-serimox**, (Figures 2.15b and 2.16), shows a very smooth decrease of the UV–Vis absorption bands, confirming the key role of **Zn^{II}_2-serimox** as photocatalyst. Tauc plot of the Kubelka-Munk function (Figure 2.18) allowed to obtain an estimation of the optical band of **Zn^{II}_2-serimox** (3.03 eV), which evidenced the suitability of it to perform the degradation of BG. Moreover, the reuse capability of **Zn^{II}_2-serimox** was established by both UV–Vis and PXRD experiments. On the one hand, two more UV–Vis *vs*. time experiments were carried out, using **Zn^{II}_2-serimox** as a photocatalyst, with identical results (Figure 2.19), confirming that **Zn^{II}_2-serimox** can be employed in at least 3 cycles. On the other hand, PXRD patterns of **Zn^{II}_2-serimox**, after such 3 cycles are identical to

those of the as-synthesised material suggesting that no degradation occurs during the photocatalytic process (Figure 2.13c).

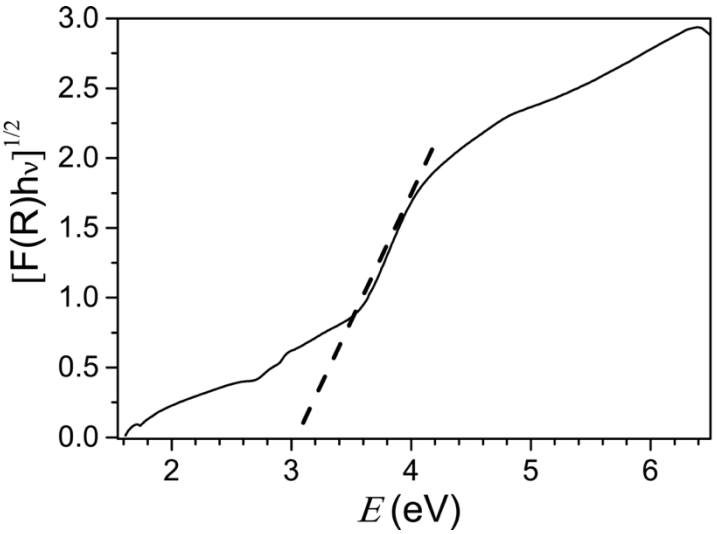

Figure 2.18. Tauc plot of the Kubelka-Munk function of **Zn^{II}_2-serimox**. The dotted line corresponds to the regression fitting of the linear part of the plot. The optical band-gap of **Zn^{II}_2-serimox** was 3.03 eV.

The full degradation of the organic dye was also supported by thermogravimetric analysis coupled with mass spectrometry (TGA-MS) on **CO_2@Zn^{II}_2-serimox** (Figure 2.20). The weight loss in TGA led to two peaks in MS spectra with the mass to charge ratio (*m*/*z*) of 18 and 44, which can be attributed to water and carbon dioxide. However, the amount of CO_2 desorbed was lower than the obtained from X-ray crystallography. Most likely, this is related to some losses of CO_2 during the handling of the measurement itself. The larger size of BG dye compared to **Zn^{II}_2-serimox** pore size precluded the adsorption of the organic dye on MOFs channels to perform the photocatalytic event. Thus, the photocatalytic activity of **Zn^{II}_2-serimox** most likely will arise from the crystal surface. With the aim to confirm that the photodegradation occurs at the surface of **Zn^{II}_2-serimox**, we have measured the evolution of the BG concentration in solution when it is put in contact with **Zn^{II}_2-serimox** during 30 min in the dark. As

it could be observed in Figure 2.21, there is no appreciable difference in the BG concentration in solution, which supported our hypothesis. A leaching test have ruled out the possibility of decomposition products of Zn-based MOF have been responsible of the photocatalytic degradation of BG. This was also supported, in an indirect manner, from the maintenance of both the activity in the recyclability studies (Figure 2.19) and the high crystallinity of PXRD diffraction patterns after the photocatalytic process (Figure 2.13c).

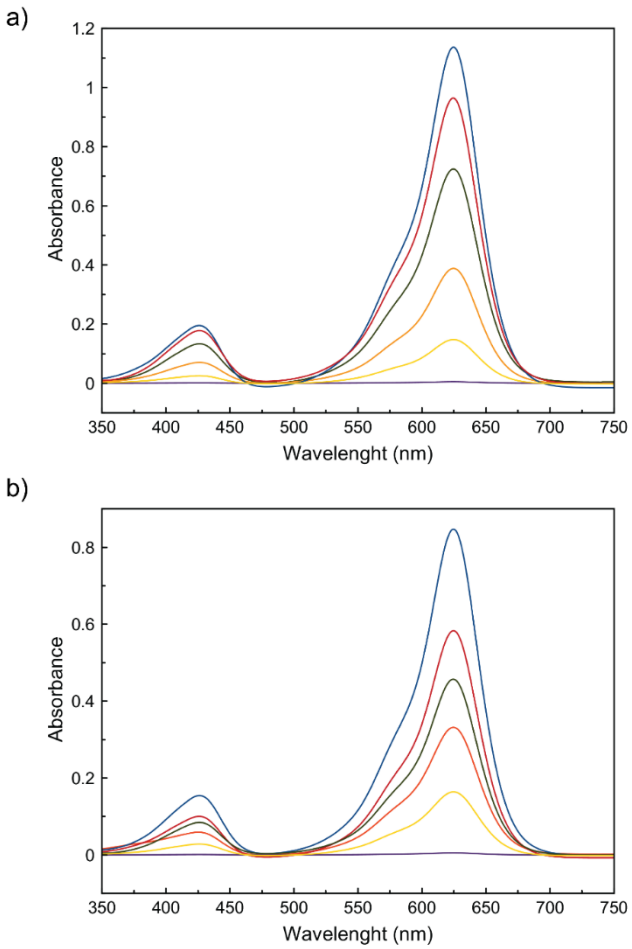

Figure 2.19. Second (a) and third (b) cycle of the evolution with time of the UV-Vis absorption spectra of 10 ppm solutions of BG in water in the presence of 25 mg of a polycrystalline sample of **Zn^{II}_2-serimox**. Blue: *t* = 0; Red: *t* = 5 min.; Green: *t* = 15 min.; Orange = 30 min.; Yellow: *t* = 60 min.; Purple: *t* = 120 min.

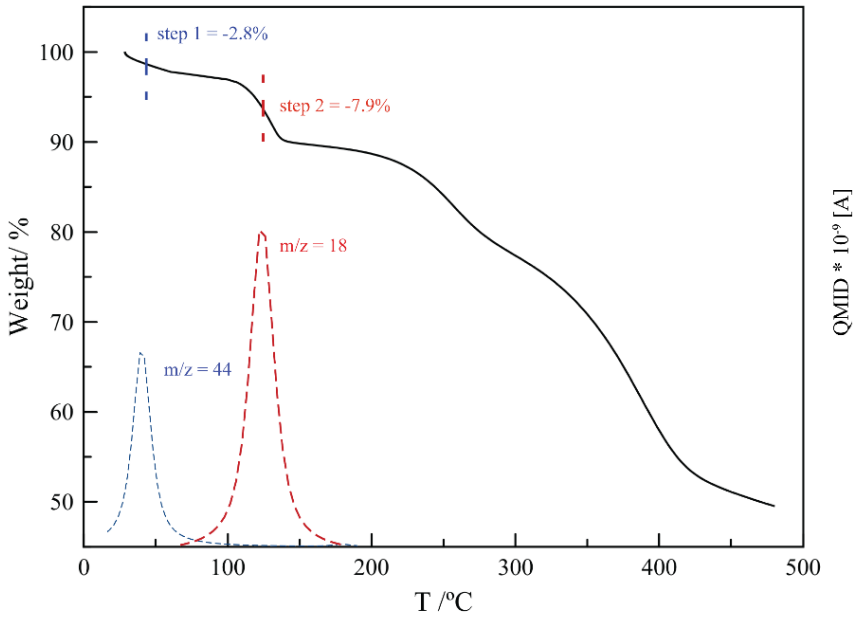

Figure 2.20. Thermo-Gravimetric coupled with Mass Spectrometry (TG-MS) of **CO@Zn$^{II}_2$-serimox**. The emission of CO_2 (*m*/*z* = 44) and water (*m*/*z* = 18) was monitored with mass spectrometry.

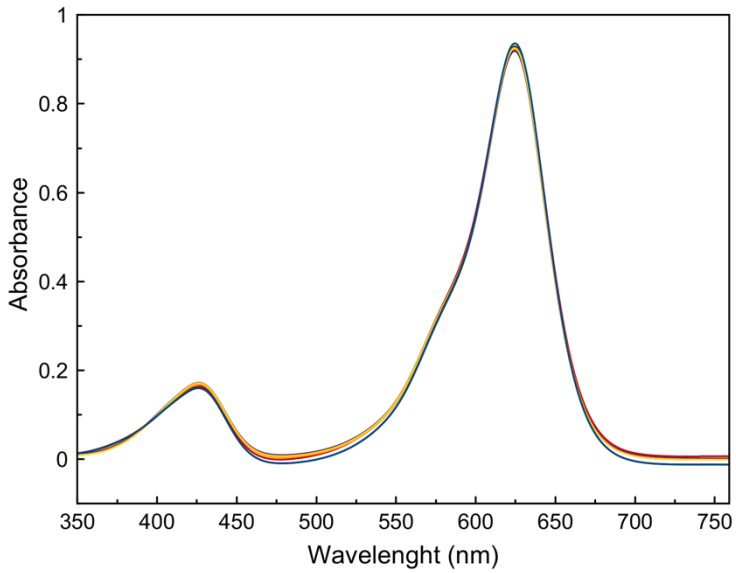

Figure 2.21. Evolution with time of the UV-Vis absorption spectra of 10 ppm solutions of BG in water in the dark. Blue: *t* = 0; Red: *t* = 5 min.; Green: *t* = 10 min.; Orange = 20 min.; Yellow: *t* = 25 min.; Purple: *t* = 30 min.

A plausible mechanism for the degradation of BG dye is shown in Figure 2.22. With the aid of UVC light **Zn^{II}_2-serimox** generates electron and hole pairs. While the electrons jump to the conducting band, the holes remain in the valence band. The holes were scavenged by water molecules leading to energetically reactive hydroxyl radicals, and the photogenerated electrons react with O_2 producing the superoxide radical anions of oxygen. From them, based on literature precedents,[103–106] the OH• is believed to be the dominant oxidizing agent for the mineralization of BG dye into CO_2 and H_2O.

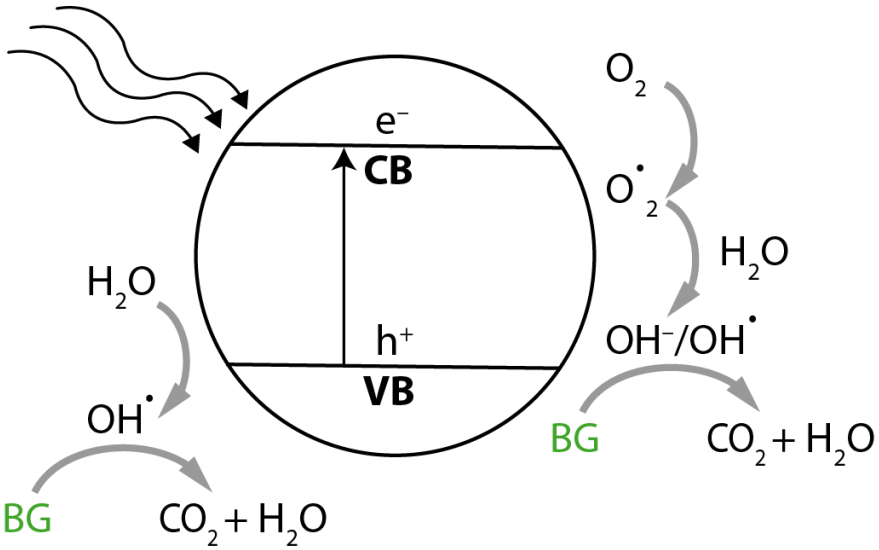

Figure 2.22. Plausible photocatalytic mechanism of BG dye degradation by **Zn^{II}_2-serimox**.

2.4. Conclusions

In summary, we have reported a novel eco-friendly Zn-based MOF with formula $\{Zn_2[(S,S)\text{-serimox}](H_2O)_2] \cdot H_2O$ (**Zn^{II}_2-serimox**) and its performance as photocatalyst of BG aqueous solutions. This MOF with a good water stability was able to efficiently photodegrade 10 ppm aqueous solutions of BG in 120 min. Indeed, UV-Vis spectroscopy measurements of irradiated solutions with and without the presence of **Zn^{II}_2-serimox**, clearly unveiled the photodegradation role of the framework. Single-crystal X-ray crystallography was applied not only to

structurally characterize the pristine structure of **Zn^{II}_2-serimox**, but, more interestingly, observe its structure after the photocatalytic process. The resolution of crystal structure of **CO_2@Zn^{II}_2-serimox** allowed to confirm the total degradation of the dye and the presence of CO_2 molecules (from degradation process) retained within the irregular hydrophilic channels of **Zn^{II}_2-serimox**. Reusability tests of **Zn^{II}_2-serimox**, with up to 3 cycles of photodegradation process, evidenced structural and performance robustness, which further confirm the viability of **Zn^{II}_2-serimox** as an efficient photocatalyst. Our current work is focused on extend this study to other Zn-based MOFs derived from natural amino acids.

2.5. Experimental section

2.5.1. Preparation of the MOFs

Preparation of $(Me_4N)_2\{Ni_2[(S,S)\text{-serimox}](OH)_2\} \cdot 5H_2O$: An aqueous solution (100 mL) of H_2Me_2-(*S*,*S*)-serimox (5.00 g, 17 mmol) was treated with a 25% methanolic solution of Me_4NOH (28 mL, 68 mmol). Then, to the resulting solution, $NiCl_2 \cdot 6H_2O$ (4.43 g, 34 mmol) in 30 mL of water was added dropwise under magnetic stirring. The green solution was filtered to remove the solid precipitate and concentrated in a rotatory evaporator to afford a green solid that was gently washed with acetone filtered off and dried under vacuum. Yield: 7.97 g, 83%. IR (KBr): ν = 3389 cm^{-1} (O−H), 3019 and 2961 cm^{-1} (C−H), 1604 cm^{-1} (C=O).

Synthesis of $\{Zn^{II}_2[(S,S)\text{-serimox}](H_2O)_2] \cdot H_2O$ (**Zn^{II}_2-serimox**): Two synthetic procedures can be followed to obtain **Zn^{II}_2-serimox**. In a direct one, an aqueous solution (30 mL) of H_2Me_2-(*S*,*S*)-serimox (3.6 g, 12 mmol) and a 25% methanolic solution of Me_4NOH (19.8 mL, 48 mmol) was added dropwise to an aqueous solution $Zn(NO_3)_2 \cdot 6H_2O$ (7.15 g, 26 mmol) in 5 mL. The solution mixture was stirred overnight and a white powder was obtained and collected by

filtration, washed with water and methanol. Yield: 4.7 g, 88%. Anal.: calcd for $C_8H_{14}N_2O_{11}Zn_2$ (444.96): C, 21.59; H, 3.17; N, 6.30%. Found: C, 21.83; H, 3.23; N, 6.42%. IR (KBr): ν = 1604 cm^{-1} (C=O).

Alternatively, it could be followed an indirect pathway. For that, $(Me_4N)_2\{Ni_2[(S,S)\text{-serimox}](OH)_2\} \cdot 5H_2O$ (1.37 g, 2.44 mmol) was dissolved in 10 mL mixture water/methanol (1:1) and then, $Zn(NO_3)_2{\cdot}6H_2O$ (1.45 g, 4.88 mmol) was added under stirring. After further stirring for 10 h, at room temperature, a white powder was obtained and collected by filtration, washed with water and methanol. Yield: 0.91 g, 83%; Anal.: calcd for $C_8H_{14}N_2O_{11}Zn_2$ (444.96): C, 21.59; H, 3.17; N, 6.30%. Found: C, 20.99; H, 3.14; N, 6.09%. IR (KBr): ν = 1604 cm^{-1} (C=O).

Suitable single crystals of **Zn^{II}_2-serimox** for X-ray structural analysis were obtained by slow diffusion, in an H-shaped tube, of H_2O/MeOH (1:1) solutions containing stoichiometric amounts of $(Me_4N)_2\{Ni_2[(S,S)\text{-serimox}](OH)_2\} \cdot 5H_2O$ (0.13 g, 0.18 mmol) in one arm and $Zn(NO_3)_2{\cdot}6H_2O$ (0.072 g, 0.36 mmol) in the other. They were isolated by filtration on paper and air-dried.

Synthesis of $\{Zn^{II}_2[(S,S)\text{-serimox}](H_2O)_2] \cdot CO_2$ (**CO_2@Zn^{II}_2-serimox**): Suitable single crystals of **CO_2@Zn^{II}_2-serimox** for X-ray structural analysis were obtained by irradiating crystals of **Zn^{II}_2-serimox** with a UV lamp in the range of λ = 250-350 nm, for 60 min and then left crystals in a sealed glass tube containing aqueous solution of BG dye for one week.

2.5.2. Physical techniques

Elemental (C, H, S, N) analyses were performed at the Microanalytical Service of the Universitat de València. FT–IR spectra were recorded on a Perkin-Elmer 882 spectrophotometer as KBr pellets. The thermogravimetric analyses were performed on crystalline samples under a dry N_2 atmosphere with a Mettler

Toledo TGA/STDA 851^{e} thermobalance operating at a heating rate of 10 °C min^{-1}. Thermogravimetric analysis coupled with mass spectrometry was performed at the Servicios Técnicos de Investigación of the Universidad de Alicante.

2.5.3. X–ray powder diffraction measurements

Polycrystalline samples of **Zn^{II}_2-serimox** –before and after photocatalytic experiments– were introduced into 0.5 mm borosilicate capillaries prior to being mounted and aligned on an Empyrean PANalytical powder diffractometer, using Cu Kα radiation (λ = 1.54056 Å). For each sample, five repeated measurements were collected at room temperature (2θ = 2–60°) and merged in a single diffractogram.

2.5.4. X–ray crystallographic data collection and structure refinement

Crystals of **Zn^{II}_2-serimox**, and **CO_2@Zn^{II}_2-serimox** (crystals of **Zn^{II}_2-serimox** left in a sealed glass tube containing aqueous solution of BG dye for one week, after irradiation in the range 250-350 nm for 60 min) were selected and mounted on a MiTeGen MicroMount in Paratone oil and very quickly placed on a liquid nitrogen stream cooled at 100 K, to avoid the possible degradation upon exposure to air. Diffraction data were collected on a Bruker-Nonius X8 APEX II CCD area detector diffractometer using graphite-monochromated Mo-K_α radiation (λ = 0.71073 Å). The data were processed through SAINT[107] reduction and SADABS[108] multi-scan absorption software. The structures were solved with the SHELXS structure solution program, using the Patterson method. The model was refined with version 2018/3 of SHELXL against F^2 on all data by full-matrix least squares.[109–111]

In the refinement of crystal structures all non–hydrogen atoms of the network were refined anisotropically. In **CO_2@Zn^{II}_2-serimox**, the C-C and C-O

bond lengths of serine moieties have been restrained. It is reasonable and related to flexibility of aminoacid chains confined within pores, which are dynamic components of the frameworks. Restrains on bond lengths and angles of CO_2 molecules, to make the refinement more efficient, have been also applied.

All the hydrogen atoms of the network were set in calculated position and refined isotropically using the riding model. Hydrogen atoms on water molecules were found form ΔF map and refined with restrains on O-H length and H-O-H angle. In crystal structure of **Zn^{II}_2-serimox**, lattice water molecules, detected by TGA analysis, were not found by density map. It is likely due to dynamic disorder, as suggested by light residual diffuse densities. CO_2 molecules reside on special positions. They exhibit large thermal disorder as expected and have been refined considering a population of 50% of the cells (0.5 as occupancy factor). Furthermore, atomic displacement parameters in carbon and oxygen atoms of CO_2 molecules expected to have essentially similar ADPs, have been restrained using EADP instruction.

A summary of the crystallographic data and structure refinement for the two compounds is given in Table S1. The comments for the alerts of level A and B (in **CO_2@Zn^{II}_2-serimox**, related to thermal and statistic disorder of CO_2 molecules) are described in the CIFs using the validation reply form (vrf). CCDC reference numbers are 2062289-2062290 for **Zn^{II}_2-serimox** and **CO_2@Zn^{II}_2-serimox**, respectively.

The final geometrical calculations and the graphical manipulations were carried out with PLATON[112,113] implemented in WinGX,[114] and CRYSTAL MAKER[115] programs, respectively.

2.5.5. Photocatalytic experiments

Photoirradiation experiments were performed inside a commercial photoreactor (LuzChem LZC-4V) with 14 UVC (with radiation centered at 250 nm) lamps. Absorption spectra were recorded on a Jasco V-670.

2.6. References

(1) US EPA. *Drinking Water Requirements for States and Public Water Systems 2018 Edition of the Drinking Water Standards and Health Advisories Tables (EPA 822-F-18-001)*; 2018.

(2) United Nations. Transforming our world: the 2030 Agenda for Sustainable Development https://sustainabledevelopment.un.org/post2015/transformingourworld .

(3) Yagub, M. T.; Sen, T. K.; Afroze, S.; Ang, H. M. *Adv. Colloid Interface Sci.* **2014**, *209*, 172–184.

(4) Ahmad, A.; Mohd-Setapar, S. H.; Chuong, C. S.; Khatoon, A.; Wani, W. A.; Kumar, R.; Rafatullah, M. *RSC Adv.* **2015**, *5* (39), 30801–30818.

(5) Yang, Z.; Wang, F.; Zhang, C.; Zeng, G.; Tan, X.; Yu, Z.; Zhong, Y.; Wang, H.; Cui, F. *RSC Adv.* **2016**, *6* (83), 79415–79436.

(6) Gupta, N. K.; Ghaffari, Y.; Kim, S.; Bae, J.; Kim, K. S.; Saifuddin, M. *Sci. Rep.* **2020**, *10* (1), 4942.

(7) Dias, E. M.; Petit, C. *J. Mater. Chem. A* **2015**, *3* (45), 22484–22506.

(8) Mon, M.; Bruno, R.; Ferrando-Soria, J.; Armentano, D.; Pardo, E. *J. Mater. Chem. A* **2018**, *6*, 4912-4947.

(9) Hashemi, B.; Zohrabi, P.; Raza, N.; Kim, K.-H. *TrAC Trends Anal. Chem.* **2017**, *97*, 65–82.

(10) Wang, Q.; Gao, Q.; Al-Enizi, A. M.; Nafady, A.; Ma, S. *Inorg. Chem. Front.* **2020**, *7* (2), 300–339.

(11) Rojas, S.; Horcajada, P. *Chem. Rev.* **2020**, *120* (16), 8378–8415.

(12) Jiang, D.; Chen, M.; Wang, H.; Zeng, G.; Huang, D.; Cheng, M.; Liu, Y.; Xue, W.; Wang, Z. *Coord. Chem. Rev.* **2019**, *380*, 471–483.

(13) Parmar, B.; Bisht, K. K.; Rajput, G.; Suresh, E. *Dalt. Trans.* **2021**, *50* (9), 3083–3108.

(14) Furukawa, H.; Cordova, K. E.; O'Keeffe, M.; Yaghi, O. M. *Science* **2013**, *341* (6149), 974.

(15) Maurin, G.; Serre, C.; Cooper, A.; Férey, G. *Chem. Soc. Rev.* **2017**, *46* (11), 3104–3107.

(16) Navarro-Sánchez, J.; Argente-García, A. I.; Moliner-Martínez, Y.; Roca-Sanjuán, D.; Antypov, D.; Campíns-Falcó, P.; Rosseinsky, M. J.; Martí-Gastaldo, C. *J. Am. Chem. Soc.* **2017**, *139* (12), 4294–4297.

(17) Darago, L. E.; Aubrey, M. L.; Yu, C. J.; Gonzalez, M. I.; Long, J. R. *J. Am. Chem. Soc.* **2015**, *137* (50), 15703–15711.

(18) Hendon, C. H.; Tiana, D.; Fontecave, M.; Sanchez, C.; D'arras, L.; Sassoye, C.; Rozes, L.; Mellot-Draznieks, C.; Walsh, A. *J. Am. Chem. Soc.* **2013**, *135* (30), 10942–10945.

(19) Narayan, T. C.; Miyakai, T.; Seki, S.; Dincă, M. *J. Am. Chem. Soc.* **2012**, *134* (31), 12932–12935.

(20) Simon-Yarza, T.; Giménez-Marqués, M.; Mrimi, R.; Mielcarek, A.; Gref, R.; Horcajada, P.; Serre, C.; Couvreur, P. *Angew. Chem. Int. Ed.* **2017**, *56* (49), 15565–15569.

(21) Hidalgo, T.; Giménez-Marqués, M.; Bellido, E.; Avila, J.; Asensio, M. C.; Salles, F.; Lozano, M. V.; Guillevic, M.; Simón-Vázquez, R.; González-Fernández, A.; et al. *Sci. Rep.* **2017**, *7*, 43099.

(22) Teplensky, M. H.; Fantham, M.; Li, P.; Wang, T. C.; Mehta, J. P.; Young, L. J.; Moghadam, P. Z.; Hupp, J. T.; Farha, O. K.; Kaminski, C. F.; et al. *J. Am. Chem. Soc.* **2017**, *139* (22), 7522–7532.

(23) Deng, K.; Hou, Z.; Li, X.; Li, C.; Zhang, Y.; Deng, X.; Cheng, Z.; Lin, J. A. *Sci. Rep.* **2015**, *5*, 7851.

(24) Zhu, X.; Gu, J.; Wang, Y.; Li, B.; Li, Y.; Zhao, W.; Shi, J. *Chem. Commun.* **2014**, *50* (63), 8779–8782.

(25) Agostoni, V.; Chalati, T.; Horcajada, P.; Willaime, H.; Anand, R.; Semiramoth, N.; Baati, T.; Hall, S.; Maurin, G.; Chacun, H.; et al. *Adv. Healthc. Mater.* **2013**, *2* (12), 1630–1637.

(26) Gao, P. F.; Zheng, L. L.; Liang, L. J.; Yang, X. X.; Li, Y. F.; Huang, C. Z. *J. Mater. Chem. B* **2013**, *1* (25), 3202.

(27) Kim, K.; Seo, J. S.; Whang, D.; Lee, H.; Jun, S. I.; Oh, J.; Jeon, Y. J. *Nature* **2000**, *404* (6781), 982–986.

(28) Sun, C.; Qin, C.; Wang, X.-L.; Yang, G.-S.; Shao, K.; Lan, Y.-Q.; Su, Z.-M.; Huang, P.; Wang, C.-G.; Wang, E.-B. *Dalt. Trans.* **2012**, *41* (23), 6906.

(29) Baati, T.; Horcajada, P.; Gref, R.; Couvreur, P.; Serre, C. *J. Pharm. Biomed.*

Anal. **2011**, *56* (4), 758–762.

(30) Miller, S. R.; Heurtaux, D.; Baati, T.; Horcajada, P.; Grenèche, J.-M.; Serre, C. *Chem. Commun.* **2010**, *46* (25), 4526.

(31) Yuan, W.; Garay, A. L.; Pichon, A.; Clowes, R.; Wood, C. D.; Cooper, A. I.; James, S. L. *CrystEngComm* **2010**, *12* (12), 4063.

(32) Rieter, W. J.; Pott, K. M.; Taylor, K. M. L.; Lin, W. *J. Am. Chem. Soc.* **2008**, *130* (35), 11584–11585.

(33) Morris, R. E.; Wheatley, P. S. *Angew. Chem. Int. Ed.* **2008**, *47* (27), 4966–4981.

(34) Wen, Y.; Zhang, P.; Sharma, V. K.; Ma, X.; Zhou, H.-C. *Cell Reports Phys. Sci.* **2021**, *2* (2), 100348.

(35) *Metal-Organic Frameworks (MOFs) for Environmental Applications*; Ghosh, S. K., Ed.; Elsevier, 2019.

(36) Gao, Q.; Xu, J.; Bu, X.-H. *Coord. Chem. Rev.* **2019**, *378*, 17–31.

(37) Liu, X.; Zhou, Y.; Zhang, J.; Tang, L.; Luo, L.; Zeng, G. *ACS Appl. Mater. Interfaces* **2017**, *9* (24), 20255–20275.

(38) Bradshaw, D.; Prior, T. J.; Cussen, E. J.; Claridge, J. B.; Rosseinsky, M. J. *J. Am. Chem. Soc.* **2004**, *126* (19), 6106–6114.

(39) Khan, N. A.; Hasan, Z.; Jhung, S. H. *J. Hazard. Mater.* **2013**, *244–245*, 444–456.

(40) Li, B.; Wen, H.-M.; Zhou, W.; Xu, J. Q.; Chen, B.. *Chem.* **2016**, *1* (4), 557–580.

(41) Campbell, M. G.; Liu, S. F.; Swager, T. M.; Dincă, M. *J. Am. Chem. Soc.* **2015**, *137* (43), 13780–13783.

(42) Campbell, M. G.; Sheberla, D.; Liu, S. F.; Swager, T. M.; Dincă, M. *Angew. Chem. Int. Ed.* **2015**, *54* (14), 4349–4352.

(43) Sun, L.; Hendon, C. H.; Minier, M. A.; Walsh, A.; Dincă, M. *J. Am. Chem. Soc.* **2015**, *137* (19), 6164–6167.

(44) Park, S. S.; Hontz, E. R.; Sun, L.; Hendon, C. H.; Walsh, A.; Van Voorhis, T.; Dinca, M. *J. Am. Chem. Soc.* **2015**, *137* (5), 1774–1777.

(45) Han, S.; Warren, S. C.; Yoon, S. M.; Malliakas, C. D.; Hou, X.; Wei, Y.; Kanatzidis, M. G.; Grzybowski, B. A. *J. Am. Chem. Soc.* **2015**, *137* (25),

8169–8175.

(46) Chen, Z.; Li, P.; Anderson, R.; Wang, X.; Zhang, X.; Robison, L.; Redfern, L. R.; Moribe, S.; Islamoglu, T.; Gómez-Gualdrón, D. A.; et al. *Science* **2020**, *368* (6488), 297–303.

(47) Wu, H.; Zhou, W.; Yildirim, T. *J. Am. Chem. Soc.* **2009**, *131* (13), 4995–5000.

(48) Kondo, M.; Yoshitomi, T.; Matsuzaka, H.; Kitagawa, S.; Seki, K. *Angew. Chem. Int. Ed.* **1997**, *36* (16), 1725–1727.

(49) Yaghi, O. M.; Li, G.; Li, H. *Nature* **1995**, *378* (6558), 703–706.

(50) Pei, X.; Bürgi, H.-B.; Kapustin, E. A.; Liu, Y.; Yaghi, O. M. *J. Am. Chem. Soc.* **2019**, *141* (47), 18862–18869.

(51) Chae, H. K.; Siberio-Pérez, D. Y.; Kim, J.; Go, Y.; Eddaoudi, M.; Matzger, A. J.; O'Keeffe, M.; Yaghi, O. M. *Nature* **2004**, *427* (6974), 523–527.

(52) Inokuma, Y.; Arai, T.; Fujita, M. *Nat. Chem.* **2010**, *2* (9), 780–783.

(53) Inokuma, Y.; Kawano, M.; Fujita, M. *Nat. Chem.* **2011**, *3* (5), 349–358.

(54) Inokuma, Y.; Yoshioka, S.; Ariyoshi, J.; Arai, T.; Hitora, Y.; Takada, K.; Matsunaga, S.; Rissanen, K.; Fujita, M. *Nature* **2013**, *495* (7442), 461–466.

(55) Ning, G.-H.; Inokuma, Y.; Fujita, M. *Chem. Asian J.* **2014**, *9* (2), 466–468.

(56) Inokuma, Y.; Yoshioka, S.; Ariyoshi, J.; Arai, T.; Fujita, M. *Nat. Protoc.* **2014**, *9* (2), 246–252.

(57) Matsuzaki, S.; Arai, T.; Ikemoto, K.; Inokuma, Y.; Fujita, M. *J. Am. Chem. Soc.* **2014**, *136* (52), 17899–17901.

(58) Ikemoto, K.; Inokuma, Y.; Rissanen, K.; Fujita, M. *J. Am. Chem. Soc.* **2014**, *136* (19), 6892–6895.

(59) Yoshioka, S.; Inokuma, Y.; Hoshino, M.; Sato, T.; Fujita, M. *Chem. Sci.* **2015**, *6* (7), 3765–3768.

(60) Venkataraman, D.; Gardner, G. B.; Lee, S.; Moore, J. S. *J. Am. Chem. Soc.* **1995**, *117* (46), 11600–11601.

(61) Zigon, N.; Hoshino, M.; Yoshioka, S.; Inokuma, Y.; Fujita, M. *Angew. Chem. Int. Ed.* **2015**, *54* (31), 9033–9037.

(62) Duplan, V.; Hoshino, M.; Li, W.; Honda, T.; Fujita, M. *Angew. Chem. Int. Ed.* **2016**, *55* (16), 4919–4923.

(63) Hoshino, M.; Khutia, A.; Xing, H.; Inokuma, Y.; Fujita, M. *IUCrJ* **2016**, *3* (2),

139–151.

(64) Urban, S.; Brkljača, R.; Hoshino, M.; Lee, S.; Fujita, M. *Angew. Chem. Int. Ed.* **2016**, *55* (8), 2678–2682.

(65) Yoshioka, S.; Inokuma, Y.; Duplan, V.; Dubey, R.; Fujita, M. *J. Am. Chem. Soc.* **2016**, *138* (32), 10140–10142.

(66) Cuenca, A. B.; Zigon, N.; Duplan, V.; Hoshino, M.; Fujita, M.; Fernández, E. *Chem. Eur. J.* **2016**, *22* (14), 4723–4726.

(67) Inokuma, Y.; Ukegawa, T.; Hoshino, M.; Fujita, M. *Chem. Sci. J.* **2016**, *00*, 1–3.

(68) Ning, G.-H.; Matsumura, K.; Inokuma, Y.; Fujita, M. *Chem. Commun.* **2016**, *52* (43), 7013–7015.

(69) Matsuda, Y.; Mitsuhashi, T.; Lee, S.; Hoshino, M.; Mori, T.; Okada, M.; Zhang, H.; Hayashi, F.; Fujita, M.; Abe, I. *Angew. Chem. Int. Ed.* **2016**, *55* (19), 5785–5788.

(70) Kawahata, M.; Komagawa, S.; Ohara, K.; Fujita, M.; Yamaguchi, K. *Tetrahedron Lett.* **2016**, *57* (41), 4633–4636.

(71) Fujita, M.; Kwon, Y. J.; Washizu, S.; Ogura, K. *J. Am. Chem. Soc.* **1994**, *116* (3), 1151–1152.

(72) Kersten, R. D.; Lee, S.; Fujita, D.; Pluskal, T.; Kram, S.; Smith, J. E.; Iwai, T.; Noel, J. P.; Fujita, M.; Weng, J.-K. *J. Am. Chem. Soc.* **2017**, *139* (46), 16838–16844.

(73) Zigon, N.; Kikuchi, T.; Ariyoshi, J.; Inokuma, Y.; Fujita, M. *Chem. Asian J.* **2017**, *12* (10), 1057–1061.

(74) Sakurai, F.; Khutia, A.; Kikuchi, T.; Fujita, M. *Chem. Eur. J.* **2017**, *23* (60), 15035–15040.

(75) Lee, S.; Hoshino, M.; Fujita, M.; Urban, S. *Chem. Sci.* **2017**, *8* (2), 1547–1550.

(76) Yan, Y.; Carrington, E. J.; Pétuya, R.; Whitehead, G. F. S.; Verma, A.; Hylton, R. K.; Tang, C. C.; Berry, N. G.; Darling, G. R.; Dyer, M. S.; et al. *J. Am. Chem. Soc.* **2020**, *142* (35), 14903–14913.

(77) Katsoulidis, A. P.; Park, K. S.; Antypov, D.; Martí-Gastaldo, C.; Miller, G. J.; Warren, J. E.; Robertson, C. M.; Blanc, F.; Darling, G. R.; Berry, N. G.; et al. *Angew. Chem. Int. Ed.* **2014**, *53* (1), 193–198.

(78) Matsuda, R. *Nature* **2014**, *509* (7501), 434–435.

(79) Warren, J. E.; Perkins, C. G.; Jelfs, K. E.; Boldrin, P.; Chater, P. A.; Miller, G. J.; Manning, T. D.; Briggs, M. E.; Stylianou, K. C.; Claridge, J. B.; et al. *Angew. Chem. Int. Ed.* **2014**, *53* (18), 4592–4596.

(80) Rabone, J.; Yue, Y.-F.; Chong, S. Y.; Stylianou, K. C.; Bacsa, J.; Bradshaw, D.; Darling, G. R.; Berry, N. G.; Khimyak, Y. Z.; Ganin, A. Y.; et al. *Science* **2010**, *329* (5995), 1053–1057.

(81) Bradshaw, D.; Claridge, J. B.; Cussen, E. J.; Prior, T. J.; Rosseinsky, M. J. *Acc. Chem. Res.* **2005**, *38* (4), 273–282.

(82) Bloch, W. M.; Burgun, A.; Coghlan, C. J.; Lee, R.; Coote, M. L.; Doonan, C. J.; Sumby, C. J. *Nat. Chem.* **2014**, *6* (10), 906–912.

(83) Gándara, F.; Bennett, T. D. *IUCrJ* **2014**, *1* (6), 563–570.

(84) Bloch, W. M.; Champness, N. R.; Doonan, C. J. *Angew. Chem. Int. Ed.* **2015**, *54* (44), 12860–12867.

(85) Burgun, A.; Coghlan, C. J.; Huang, D. M.; Chen, W.; Horike, S.; Kitagawa, S.; Alvino, J. F.; Metha, G. F.; Sumby, C. J.; Doonan, C. J. *Angew. Chem. Int. Ed.* **2017**, *56* (29), 8412–8416.

(86) Huang, R.-W.; Wei, Y.-S.; Dong, X.-Y.; Wu, X.-H.; Du, C.-X.; Zang, S.-Q.; Mak, T. C. W. *Nat. Chem.* **2017**, *9* (7), 689–697.

(87) Rissanen, K. *Chem. Soc. Rev.* **2017**, *46* (9), 2638–2648.

(88) Young, R. J.; Huxley, M. T.; Pardo, E.; Champness, N. R.; Sumby, C. J.; Doonan, C. J. *Chem. Sci.* **2020**, *11* (16), 4031–4050.

(89) Escamilla, P.; Guerra, W. D.; Leyva-Pérez, A.; Armentano, D.; Ferrando-Soria, J.; Pardo, E. *Chem. Commun.* **2023**, *59* (7), 836–851.

(90) Viciano-Chumillas, M.; Mon, M.; Ferrando-Soria, J.; Corma, A.; Leyva-Pérez, A.; Armentano, D.; Pardo, E. *Acc. Chem. Res.* **2020**, *53* (2), 520–531.

(91) Mon, M.; Bruno, R.; Ferrando-Soria, J.; Bartella, L.; Di Donna, L.; Talia, M.; Lappano, R.; Maggiolini, M.; Armentano, D.; Pardo, E. *Mater. Horizons* **2018**, *5* (4), 683–690.

(92) Wang, C.-C.; Li, J.-R.; Lv, X.-L.; Zhang, Y.-Q.; Guo, G. *Energy Environ. Sci.* **2014**, *7* (9), 2831–2867.

(93) Zeng, L.; Guo, X.; He, C.; Duan, C. *ACS Catal.* **2016**, *6* (11), 7935–7947.

(94) Zhang, T.; Lin, W. *Chem. Soc. Rev.* **2014**, *43* (16), 5982–5993.

(95) Wu, Z.; Yuan, X.; Zhang, J.; Wang, H.; Jiang, L.; Zeng, G. *ChemCatChem* **2017**, *9* (1), 41–64.

(96) Tian, C.; Zhang, Q.; Wu, A.; Jiang, M.; Liang, Z.; Jiang, B.; Fu, H. *Chem. Commun.* **2012**, *48* (23), 2858.

(97) Chimupala, Y.; Phromma, C.; Yimklan, S.; Semakul, N.; Ruankham, P. *RSC Adv.* **2020**, *10* (48), 28567–28575.

(98) Wu, Z.; Yuan, X.; Zhang, J.; Wang, H.; Jiang, L.; Zeng, G. *ChemCatChem* **2017**, *9* (1), 41–64.

(99) Mon, M.; Bruno, R.; Tiburcio, E.; Grau-Atienza, A.; Sepúlveda-Escribano, A.; Ramos-Fernandez, E. V.; Fuoco, A.; Esposito, E.; Monteleone, M.; Jansen, J. C.; et al. *Chem. Mater.* **2019**, *31* (15), 5856–5866.

(100) Rufino-Felipe, E.; Caballero-Jiménez, J.; Guerrero-Ramírez, L.-G.; Flores-Álamo, M.; Muñoz-Hernández, M.-Á. *Inorg. Chem. Commun.* **2016**, *63*, 107–110.

(101) Desmarais, W. T.; Bienvenue, D. L.; Bzymek, K. P.; Holz, R. C.; Petsko, G. A.; Ringe, D. *Structure* **2002**, *10* (8), 1063–1072.

(102) Ataie, N. J.; Hoang, Q. Q.; Zahniser, M. P. D.; Tu, Y.; Milne, A.; Petsko, G. A.; Ringe, D. *Biochemistry* **2008**, *47* (29), 7673–7683.

(103) Sood, S.; Umar, A.; Kumar Mehta, S.; Sinha, A. S. K.; Kumar Kansal, S. *Ceram. Int.* **2015**, *41* (3), 3533–3540.

(104) Shanmugam, N.; Sathya, T.; Viruthagiri, G.; Kalyanasundaram, C.; Gobi, R.; Ragupathy, S. *Appl. Surf. Sci.* **2016**, *360*, 283–290.

(105) Migliorini, F. L.; Steter, J. R.; Rocha, R. S.; Lanza, M. R. V.; Baldan, M. R.; Ferreira, N. G. *Diam. Relat. Mater.* **2016**, *65*, 5–12.

(106) Kaur, S.; Sharma, S.; Umar, A.; Singh, S.; Mehta, S. K.; Kansal, S. K.. *Superlattices Microstruct.* **2017**, *103*, 365–375.

(107) SAINT, version 6.45, Bruker Analytical X-ray Systems, Madison, W. SAINT, Version 6.45, Bruker Analytical X-Ray Systems, Madison, WI. Bruker Analytical X-ray Systems: Madison, WI 2003.

(108) Sheldrick G.M. SADABS Program for Absorption Correction, version 2.10, Analytical X-ray Systems, Madison, W. SADABS Program for Absorption Correction, Version 2.10, Analytical X-Ray Systems, Madison, WI. Bruker

Analytical X-ray Systems: Madison, WI 2003.

(109) Sheldrick, G. M. *Acta Crystallogr. A.* **2008**, *64* (1), 112–122..

(110) Sheldrick, G. M. *Acta Crystallogr. Sect. C Struct. Chem.* **2015**, *71* (1), 3–8.

(111) Madison, W. S.-2013/4 B. A. X. I. SHELXTL-2013/4, Bruker Analytical X-Ray Instruments, Madison, WI. Bruker Analytical X-ray Instruments: Madison, WI 2013.

(112) Spek, A. L. *Acta Crystallogr. Sect. D Biol. Crystallogr.* **2009**, *65* (2), 148–155.

(113) Spek, A. L. *Acta Crystallogr. Sect. C Struct. Chem.* **2015**, *71* (1), 9–18.

(114) Farrugia, L. J. *J. Appl. Crystallogr.* **1999**, *32* (4), 837–838.

(115) Palmer, D. CRYSTAL MAKER, Cambridge University Technical Services, C. CRYSTAL MAKER, Cambridge University Technical Services, Cambridge. Cambridge University Technical Services: Cambridge 1996.

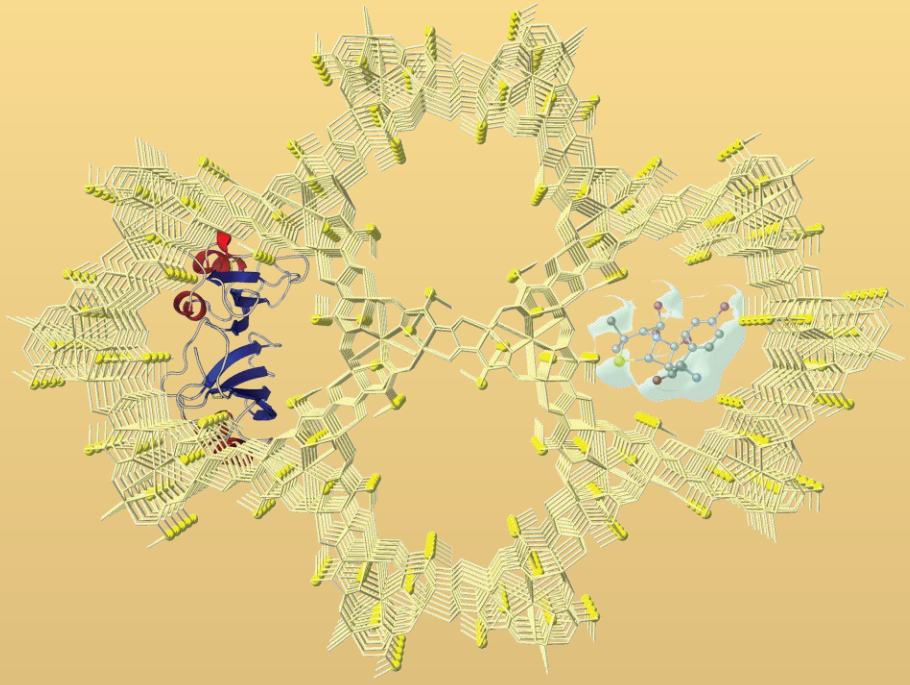

CHAPTER 3

Degradation of penicillinic antibiotics by biomimetic Zn-based metal–organic frameworks

3.1. Introduction

β-lactam antibiotics –including penicillins, cephalosporins and cephamycins, monobactams, carbapenems and carbacephems– are the most commonly used group of antibiotics against bacterial infections.[1] They all have in common the presence of a four-membered beta-lactam ring in their chemical structure, which lies at the origin of their antibacterial properties.[1] However, this feature also represents the main drawback of this family of antibiotics as certain bacteria are capable to, among other resistance mechanisms, secrete β-lactamase enzymes that are capable to inactivate most β-lactam antibiotics by degrading the mentioned four-membered ring.[2]

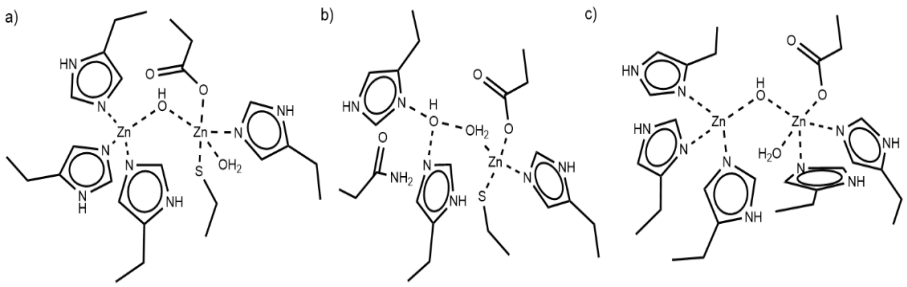

Figure 3.1. Typical Zn(II) coordination environments for B1 (a), B2 (b), and B3 (c) MBLs active sites.

There are two basic mechanisms for the opening of the β-lactam ring: (*i*) *S*erine β-lactamases (SBLs),[2] whose catalytic action occurs *via* acylation-deacylation reactions and (*ii*) Metallo-β-lactamases (MBLs),[3–11] possessing one or two metal (usually Zn(II)) cations that are capable to hydrolyze the β-lactam ring by deprotonating a coordinated water molecule (Figure 3.1), which acts as a powerful nucleophile.[12,13] Regarding MBLs, many scientists have devoted their efforts to elucidate their structures as well as catalytic mechanisms,[12,13] aiming at developing efficient inhibitors, which seems to be a titanic effort considering the wide variety of molecular and structural diversity in this family of enzymes.[14,15] In

this context, a type of hybrid porous materials, the so-called metal-organic frameworks (MOFs),[16–21] can be helpful to gain information about both structures and catalytic mechanisms of MBLs.

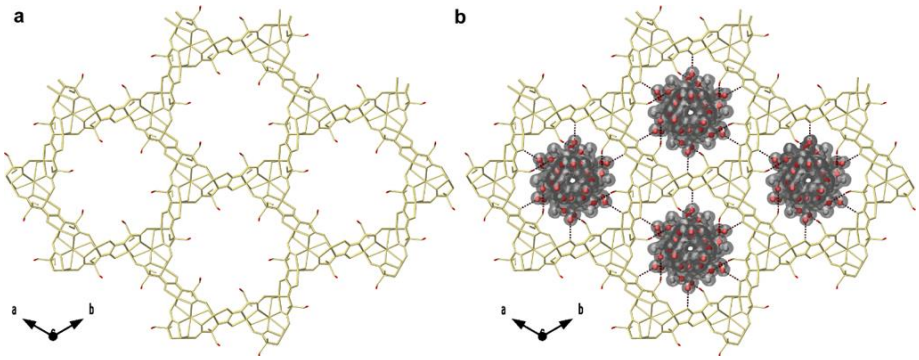

Figure 3.2. Views of the 3D open–framework of MOF $\{Ca^{II}Cu^{II}_6[(S,S)\text{–serimox}]_3(OH)_2(H_2O)\} \cdot 39H_2O$ (a) and also that of the host-guest aggregate containing 1,3,4,6–Tetra–*O*–acetylfructofuranoside within MOF channels resulting from the enzymatic catalysis (b) along the *c* axis (the crystallization water molecules are omitted for clarity). The 3D networks are depicted as gold sticks, with the only exception of serine residues oxygen atoms which are represented as red sticks. Reproduced from ref. 39.

MOFs are crystalline porous materials,[22] formed by the combination of metal atoms and organic ligands, which exhibit a seemingly endless diversity of architectures and have found application, in recent years, in many different important research fields like gas adsorption and separation,[23] transport,[24] water remediation[25] or catalysis.[26,27] More recently, MOFs have become relevant in another emergent field of research as enzymatic catalysis.[28,29] Indeed, several recent publications report MOFs that are capable to carry out, efficiently, enzymatic catalytic reactions.[30–34] The amazing host-guest chemistry[35,36] of MOFs lie at the origin of such efficiency, as MOFs offer the possibility to mimic active sites of enzymes,[30] by a proper combination of metal cations and functional groups within their channels or even encapsulating fragments of small enzymes. For example, we recently reported a metal organic framework with formula $\{Ca^{II}Cu^{II}_6[(S,S)\text{–serimox}]_3(OH)_2(H_2O)\} \cdot 39H_2O$ (Figure 3.2) (where serimox[36–38] =

bis[(*S*)–serine]oxalyl diamide), presenting hexagonal channels densely decorated with methyl alcohol "arms", which exhibited efficient hydrolase–like catalysis.[39]

3.2. Objectives

On the basis of the situation described in section 3.1, we pretend to synthesize a biomimetic Zn-based MOF capable to exhibit β-lactamase activity in order to further unveil the mechanisms governing this catalytic reaction. The specific objectives of the chapter are summarized as:

- Preparation of a $Ca^{II}Zn^{II}_6$ MOF with the natural amino acid *S*-methyl-*L*-cysteine, as ligand, featuring: (*i*) dinuclear Zn(II) entities reminiscent to those observed in MBLs and (*ii*) functional channels large enough to accommodate and immobilize penicillinic antibiotics such as amoxicillin.

- Study of the β-lactamase activity of the Zn-based MOF in order to confirm the biomimetic behavior of this material.

- Resolution of the crystal structure (by means of SCXRD) of a host-guest aggregate consisting of the MOF containing the corresponding penicillinic antibiotic. The well-known robustness and crystallinity of oxamidate MOFs permits to expect a successful result in this point.

- Last but not least, with the help of the crystal structure unveiled by SCXRD (see previous objective), we pretend to perform theoretical calculations to ascertain a plausible mechanism of β-lactamases.

3.3. Results and discussion

In this chapter, we report the preparation of a new highly robust and crystalline Zn_6Ca MOF (Figure 3.3) –derived from the amino acid *S*-methyl-*L*-

cysteine and whose micro-channels are thus decorated with thioether groups– with formula $\{Ca^{II}Zn^{II}_6[(S,S)\text{-Mecysmox}]_3(OH)_2(H_2O)\} \cdot 12H_2O$ (**$Ca^{II}Zn^{II}_6$-Mecysmox**) [Mecysmox = bis[*S*-methyl-*L*-cysteine]oxalyl diamide], which is capable to accommodate and degrade, very efficiently, amoxicillin and ceftriaxone antibiotics by following two different mechanisms (see catalysis, section 3.3.4). For amoxicillin, MOF **$Ca^{II}Zn^{II}_6$-Mecysmox** acts as a β-lactamase mimic and expands the very limited number of MOFs capable to mimic catalytic enzymatic processes.[40–42] Remarkably, given the high crystallinity of the Zn_6Ca MOF, single-crystal X-ray diffraction (SCXRD) studies (Table 3.1) allowed to gain insightful views about the chemical environment of Zn(II) cations, aiming at further unveiling the mechanisms governing the catalytic action of MBLs. In turn, MOF **$Ca^{II}Zn^{II}_6$-Mecysmox** is also capable to degrade ceftriaxone, but following a different mechanism. Indeed, **$Ca^{II}Zn^{II}_6$-Mecysmox** is capable to efficiently hydrolyze ceftriaxone into thiotriazinone and 3-desacetyl cefotaxime, a reaction that without catalyst only occurs after 12 h. at pH = 5,[43] while leaving unchanged its four-membered β-lactam ring.

Moreover, we have been capable to isolate and characterize, by single-crystal X-ray diffraction (SCXRD), a host guest aggregate containing MOF **$Ca^{II}Zn^{II}_6$-Mecysmox** and amoxicillin (see 3.3.2.1), aiming at achieving unique snapshots of the host-guest interactions, ultimately responsible for the β-lactamase activity. The crystal structure of this aggregate allowed us to carry out density functional calculations, which somehow confirm that the hydrolysis of the amoxicillin proceeds through the activation of a water molecule, promoted by Zn-bridging

hydroxyl group, concertedly to the nucleophilic attack to the carbonyl moiety and the cleaving of C-N bond of the lactam ring.

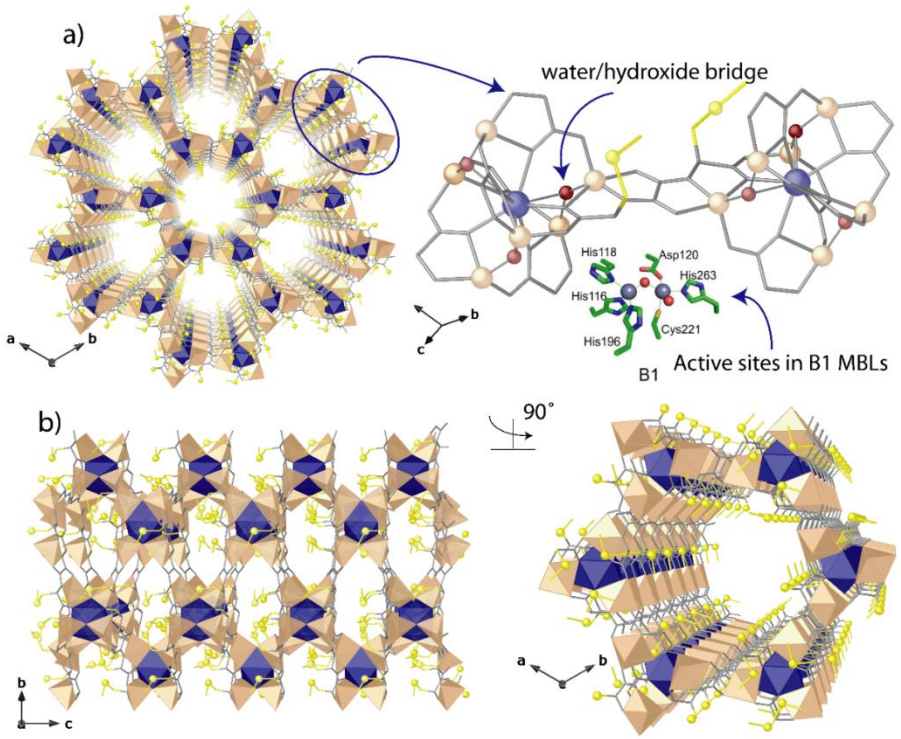

Figure 3.3. Crystal structure of **$Ca^{II}Zn^{II}_6$-Mecysmox**. a) Perspective views of 3D porous network of **$Ca^{II}Zn^{II}_6$-Mecysmox** along *c* crystallographic axis and a fragment (SBU) of **$Ca^{II}Zn^{II}_6$-Mecysmox** showing the dianionic bis(hydroxo)dizinc(II) building blocks. The inset shows a representative active-site Zn(II) coordination geometry for B1 enzymes from Metallo-β-lactamases (MBLs), where Zn(II) ions and water molecules/hydroxide ions are displayed as gray and red spheres, respectively. (b) Views of a fragment of **$Ca^{II}Zn^{II}_6$-Mecysmox** in the *bc* and *ab* planes. Zn, Ca and S atoms are represented by pale orange polyhedra, blue polyhedra, and yellow spheres, respectively, whereas the ligands (except sulfur) are depicted as gray sticks.

Table 3.1. Summary of Crystallographic Data for **$Ca^{II}Zn^{II}_6$-Mecysmox** and **amoxicillin@$Ca^{II}Zn^{II}_6$-Mecysmox.**

Compound	**$Ca^{II}Zn^{II}_6$-Mecysmox**	**amoxicillin@$Ca^{II}Zn^{II}_6$-Mecysmox**
Formula	$C_{30}Zn_6CaH_{64}S_6N_6O_{33}$	$C_{47}Zn_6CaH_{40}S_7N_9O_{30}$
M (g mol^{-1})	1585.31	1771.60
λ (Å)	0.71073	0.71073
Crystal system	Hexagonal	Hexagonal
Space group	$P6_3$	$P6_3$
a (Å)	18.662(5)	18.675(2)
c (Å)	11.724(5)	11.6907(17)
V (Å^3)	3536(2)	3530.8(10)
Z	2	2
ρ_{calc} (g cm^{-3})	1.560	1.666
μ (mm^{-1})	2.331	2.362
T (K)	100	296
θ range for data collection (°)	2.146 to 26.486	1.32 to 26.38
Completeness to θ = 25.0	100%	100%
Measured reflections	51351	53994
Unique reflections (Rint)	4833(0.1361)	4837 (0.1748)
Observed reflections [$I > 2\sigma(I)$]	3012	2871
Goof	1.069	1.036
R^a [$I > 2\sigma(I)$] (all data)	0.0595 (0.12)	0.0776 (0.1460)
wR^b [$I > 2\sigma(I)$] (all data)	0.1581 (0.1873)	0.2092 (0.2493)
Flack parameter	0.074(2)	0.08(2)
CCDC	2258088	2258089

^{a} $R = \sum(||F_o| - |F_c||)/\sum|F_o|$. ^{b} $wR = [\sum w(|F_o| - |F_c|)^2/\sum w|F_o|^2]^{1/2}$.

3.3.1. General synthetic procedure

Compound **$Ca^{II}Zn^{II}_6$-Mecysmox** ($\{Ca^{II}Zn^{II}_6[(S,S)\text{-Mecysmox}]_3(OH)_2(H_2O)\} \cdot 12H_2O$) was first synthesized, in a multigram scale, by direct precipitation in water (see experimental section (section 3.5) for further details). The resulting polycrystalline powdered sample of **$Ca^{II}Zn^{II}_6$-Mecysmox** was used to carry out analytical/catalytic experiments. Alternatively, compound **$Ca^{II}Zn^{II}_6$-Mecysmox** could be also obtained as colorless hexagonal prisms, using a slow diffusion technique (see experimental section (section 3.5)). Then, single crystals of **$Ca^{II}Zn^{II}_6$-Mecysmox** were used to determine the crystal structures of the pristine MOF **$Ca^{II}Zn^{II}_6$-Mecysmox** and also a hybrid host-guest aggregate, so-called **amoxicillin@$Ca^{II}Zn^{II}_6$-Mecysmox** ($C_{16}H_{19}N_3O_5S$)@$\{Zn^{II}Cu^{II}_6[(S,S)\text{-Mecysmox}]_3(OH)_2(H_2O)\} \cdot 9H_2O$, that was obtained after immersing crystals of **$Ca^{II}Zn^{II}_6$-Mecysmox** in saturated DMF solutions of amoxicillin for 72 h.

3.3.2. Characterization of the MOFs

3.3.2.1. Crystal structure

The crystal structure of **$Ca^{II}Zn^{II}_6$-Mecysmox** could be determined by SCXRD (see Experimental section (section 3.5) for structural details). **$Ca^{II}Zn^{II}_6$-Mecysmox** crystallizes in the chiral $P6_3$ space group and consists of chiral honeycomb-like three-dimensional (3D) calcium(II)-zinc(II) networks (Figure 3.3) featuring hexagonal channels, of approximately 0.7 nm, where the methylenethiomethyl chains of the amino acid are located (Figures 3.3b and 3.4). The 3D porous structure of **$Ca^{II}Zn^{II}_6$-Mecysmox** offers a functional space capable to accommodate/stabilize substrates, in a similar manner to that observed in the active sites in B1 enzymes. The network is constructed from trans-oxamidato-bridged dizinc(II) units, $\{Zn^{II}_2[(S,S)\text{-Mecysmox}]\}$ (Figure 3.3a), which act as linkers between the Ca(II) cations through the carboxylate groups (Figure 3.3) and are

further interconnected, with neighboring dizinc(II) moieties, by water/hydroxide groups (Figure 3.3a). This situation is reminiscent to that observed in certain MBLs like *S. maltophilia* and *B. fragilis enzimes* (Figure 3.1),[44] where hydroxide ions bridge zinc(II) cations. This feature is closely related to metallo-β-lactamases activity, as it is postulated that the catalytic mechanism involves an attack of the metal-bound hydroxide on the carbonyl group of the β-lactam ring, which must be accompanied by the collapse of the four-membered ring.[45]

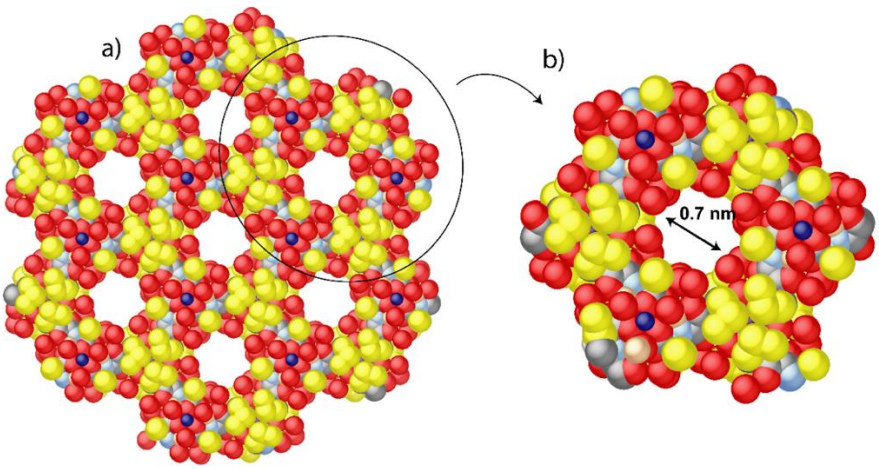

Figure 3.4. a) View of 3D network of **$Ca^{II}Zn^{II}_6$-Mecysmox** and b) details of one single pore along *c* crystallographic axis showing the porous structure in space filling model (van deer Waals radii). Zn(II) and Ca(II) metal ions are represented by pale orange and blue spheres, respectively, whereas the oxygen, carbon, nitrogen and sulfur atoms from the ligands are depicted as red, grey, blue and yellow spheres.

Indeed, it is well established[44] that Zn(II) coordination environment is crucial for substrate binding and catalysis in MBLs. Figures 3.3a and 3.5 show a detail of the two crystallographically distinct Zn(II) metal ions in **$Ca^{II}Zn^{II}_6$-Mecysmox**, in similarity with B1 MBLs active sites. B1 enzymes are Zn(II)-dependent metalloproteins and belong to the Ambler class B enzymes (or metallo-β-lactamases), being one of the three subclasses: B1, B2 and B3.[46] They possess two, Zn1 and Zn2, binding sites containing both a bridging hydroxide and three amino acid residues, but only Zn2 ion is bound to a water molecule (see

inset of Figure 3.3). As a result, the Zn1 site adopts a tetrahedral coordination geometry (Figure 3.5), while the Zn2 is trigonal bipyramidal, as both Zn(II) sites present in MOF **$Ca^{II}Zn^{II}_6$-Mecysmox**. Indeed, in crystal structure of **$Ca^{II}Zn^{II}_6$-Mecysmox**, Zn(II) environment is described by a trigonal bipyramidal geometry being coordinated by a nitrogen and three oxygen atoms belonging to the Mecysmox ligand, and a water/hydroxide bridging group (in a 1:2 statistic distribution) as found in B1 enzymes. In the literature there is a general agreement supporting that the active and relevant species of the B1 (and B3) enzymes is the binuclear form.[47] The canonical binuclear site of B1 MBLs exhibit Zn–Zn and Zn-OH distances ranging from 3.5 to 3.9 and 1.9 to 2.2 Å, respectively in the inactive state. In **$Ca^{II}Zn^{II}_6$-Mecysmox**, the Zn-OH bond length is of 1.97(1) Å, with a Zn–Zn distance across the hydroxide bridge of 3.70 Å.

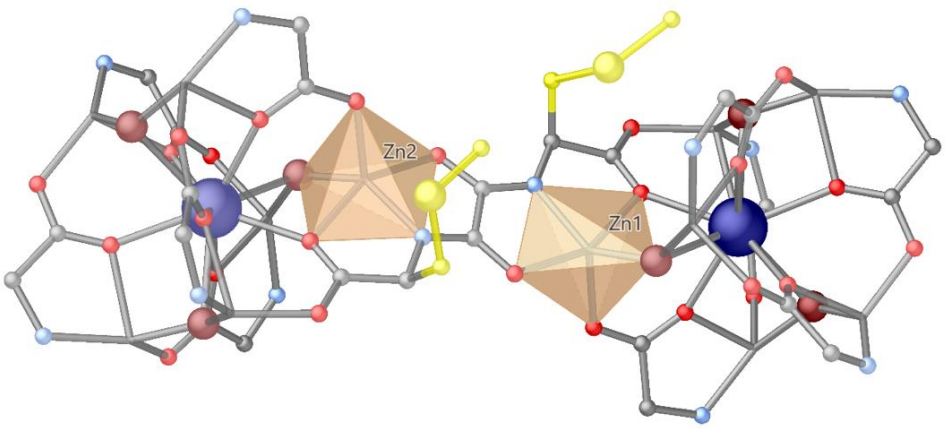

Figure 3.5. View of the dianionic bis(hydroxo)dizinc(II) building blocks in **$Ca^{II}Zn^{II}_6$-Mecysmox**, highlighting with polyhedra the pentacoordinated Zn(II) ions. Zn(II), Ca(II) ions and water molecules/hydroxide ions are displayed as pale pink polyhedral, blue and big red spheres, respectively. The carbon, oxygen, nitrogen and sulfur from the ligand are depicted as gray, red, sky-blue and yellow small spheres.

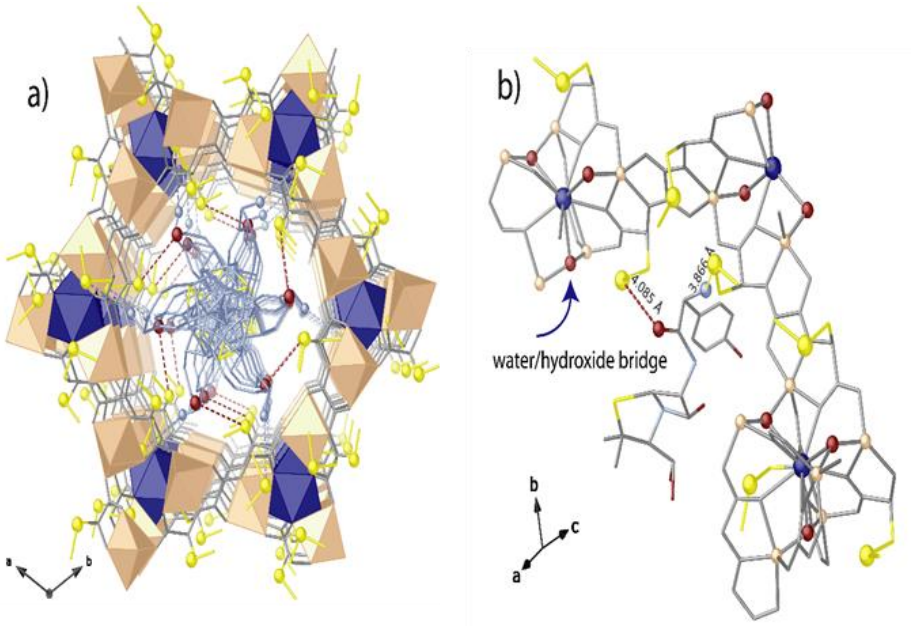

Figure 3.6. Crystal structure of **amoxicillin@Ca^{II}Zn$^{II}_6$-Mecysmox**. a) Perspective view of a single channel along *c* crystallographic axis. b) Details of host-guest interactions. Zn, Ca and S atoms are represented by pale orange polyhedral (a) or spheres (b), blue polyhedra (a) or spheres (b), and yellow spheres, respectively, whereas the ligands and amoxicillin guest molecules (except nitrogen and oxygen atoms from amoxicillin involved in interactions, sky blue and red spheres, respectively) are depicted as gray, yellow, red and sky-blue sticks for carbon, sulfur, nitrogen and oxygen, respectively.

The crystal structure of the host-guest aggregate **amoxicillin@Ca^{II}Zn$^{II}_6$-Mecysmox** could be also determined by SCXRD (see Experimental section (section 3.5) for structural details). It helps to gain further information about the nature of the host-guest interaction as well as the concomitant β-lactamase activity. Aiming at acquiring structural insights, we soaked crystals of **Ca^{II}Zn$^{II}_6$-Mecysmox** within water, methanol and dimethylformamide saturated solutions containing amoxicillin (details in Experimental Section (section 3.5)). Only DMF solution allowed to observe a single-crystal-to-single-crystal process of amoxicillin insertion, further supporting the proposed catalytic reaction mechanism. Indeed, in water and methanol, after 24h the HPLC-ESI(+)-Orbitrap MS analysis detected the formation of amoxicillin penicilloic acid and its methyl

ester, respectively, with the consequent loss of crystallinity of **$Ca^{II}Zn^{II}_6$-Mecysmox**, likely related to the required rearrangement of Zn(II) metal nodes during the catalytic reaction. After the encapsulation in DMF, we have obtained amoxicillin@{$Ca^{II}Zn^{II}_6$[(*S*,*S*)-Mecysmox]$_3$(OH)$_2$(H_2O)} · 9H_2O (**amoxicillin@$Ca^{II}Zn^{II}_6$-Mecysmox**) adsorbate. The retained crystallinity of the **amoxicillin@$Ca^{II}Zn^{II}_6$-Mecysmox** adsorbate allowed the use of SCXRD to determine its crystal structure. This allows visualizing the robustness of **$Ca^{II}Zn^{II}_6$-Mecysmox**, the accomplished molecules captured and the structural stability of the final adsorbate. Although the guest molecules were highly disordered in the pores (section 3.5 for refinement details), we succeeded in obtaining their most probable locations and even their interaction sites with MOF **$Ca^{II}Zn^{II}_6$-Mecysmox** hosting matrix (Figures 3.6-3.8).

Amoxicillin@$Ca^{II}Zn^{II}_6$-Mecysmox is isomorphic to **$Ca^{II}Zn^{II}_6$-Mecysmox**, crystallizing in the *P*6$_3$ chiral space group of the hexagonal system. This structural feature confirms the robustness of the 3D network of **$Ca^{II}Zn^{II}_6$-Mecysmox**, even after antibiotic encapsulation. In the crystal structure, amoxicillin guest molecules are confined in the hexagonal pores of **$Ca^{II}Zn^{II}_6$-Mecysmox**, being recognized by the sulfur atoms of the methylcysteine residues (Figure 3.6). They are stabilized by σ-hole interactions[48] involving nitrogen and oxygen atoms of the target molecules with the amino acid moieties. As expected, after process of encapsulation in MOFs, amoxicillin molecules show statistical and thermal disorder. In fact, it was not possible to found from ΔF maps the terminal methyl and carboxylic fragments of the guest molecules (Figure 3.8), because an overlapping with equivalent detected carbon and nitrogen atoms occurs (see Crystallographic section for details (section 3.5)). The evidence of σ-hole interactions is given by -CH_2SCH_3 methylcysteine arms pointing toward the -NH_2 group [S···N distance of 3.87(1) Å] and the internal carbonyl groups atoms [S···O distance of 4.09(1) Å] of the amoxicillin (Figure 3.6b). These interactions

represent an intrinsic feature of this sulfur containing MOFs, for which non-covalent contacts can be ensured via the low-lying σ* orbitals of the C– S bond (σ-hole), available for interaction with electron donors.[48]

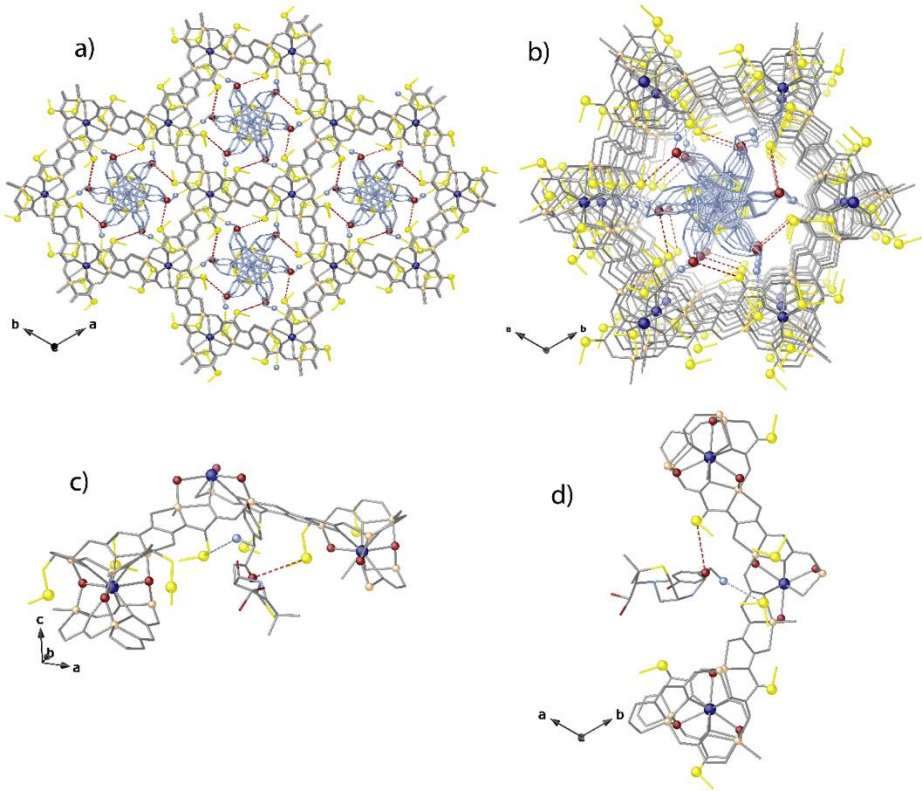

Figure 3.7. Crystal structure of **amoxicillin@Ca^{II}Zn$^{II}_6$-Mecysmox** adsorbate. a) View of the 3D network along the *c* axis. b) Perspective view of a single channel for the porous structure with amoxicillin guest adsorbed along the *c* axis. c-d) Details of host-guest interactions along *b* and *c* crystallographic axis. Ligands from the network are depicted as gray sticks with the exception of *L*-methylcysteine (–CH_2SCH_3) residues, which are represented as yellow sticks (carbon) and spheres (Sulfur). Zinc(II) and calcium(II) ions from the network are represented as pale pink and blue spheres, respectively.

As previously anticipated, the active site of MBLs resides sandwiched between two β-sheets that represent the borders of the two halves of the protein (Figure 3.3a, inset). The general shared mechanism of the active site proposes one or two zinc ions, responsible for substrate binding and catalysis, located in these particular positions by ligands' coordination. In similarity with this picture,

in pores of **$Ca^{II}Zn^{II}_6$-Mecysmox**, substrate molecules, thanks to the clutching action of sulfur atoms from the methylcysteine moieties, and water-mediated host-guest hydrogen bonds ensured by lattice waters in confined space and nucleophilic hydroxide/water bridge, easily approach one of the two Zn trigonal bipyramidal positions in each Zn–$(OH)_2(H_2O)$–Zn dimeric entity. In so doing, one of the two activated Zn sites acts in substrate binding by coordinating one of the carboxylates present in the non-β-lactam ring of the antibiotic and likely stabilizing an anionic intermediate. In this scenario, the nucleophilic hydroxide/water remains coordinated only to the second activated Zn site. This second step is not observed in DMF, where water-mediated non-covalent interactions are not provided, as shown in **amoxicillin@$Ca^{II}Zn^{II}_6$-Mecysmox** crystal structure and explains the loss of crystallinity of **$Ca^{II}Zn^{II}_6$-Mecysmox** in H_2O and MeOH, related to the required metal nodes environment rearrangement.

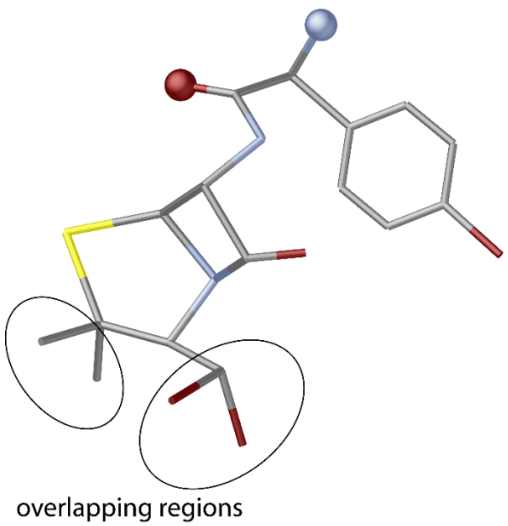

Figure 3.8. Amoxicillin conformation detected in **amoxicillin@$Ca^{II}Zn^{II}_6$-Mecysmox** crystal structure underlining overlapping regions as a consequence of statistic and thermal disorder.

Overall, crystal structure of **amoxicillin@$Ca^{II}Zn^{II}_6$-Mecysmox** permits to unveil certain aspects of the mechanism governing the β-lactamase activity of

MOF **$Ca^{II}Zn^{II}_6$-Mecysmox**. It relies on a proper immobilization of the guest molecule, by the properly designed thioether groups within MOF channels, and the concomitant hydrolysis by the water positioned by one of the two metal binding sites water/hydroxo bridged, which show an essential and functional role.

3.3.2.2. Chemical analyses

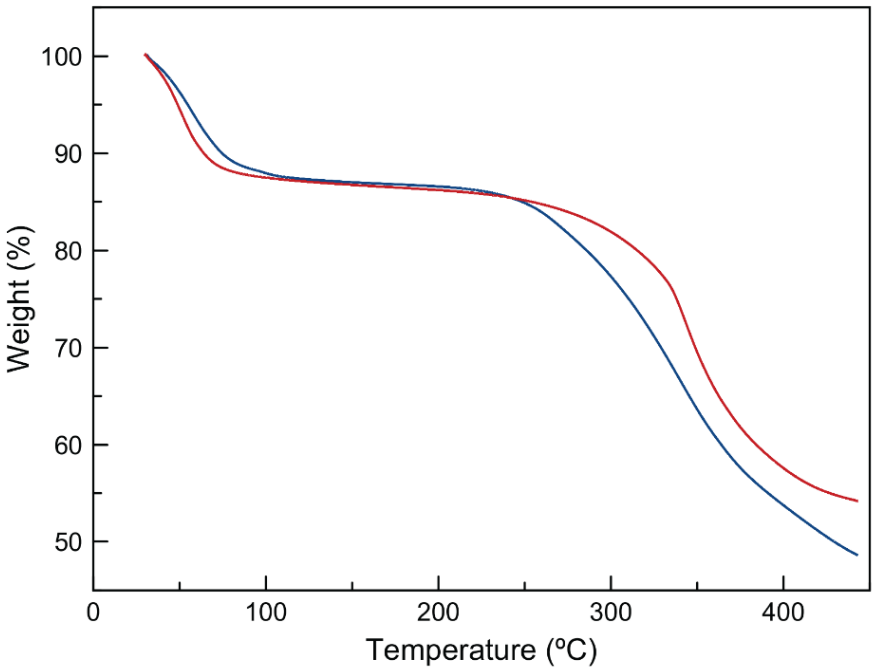

Figure 3.9. Thermo-Gravimetric Analyses (TGA) of single crystals (blue) and a polycrystalline sample of **$Ca^{II}Zn^{II}_6$-Mecysmox** (red) under dry N_2 atmosphere.

In addition to the structural characterization (see 3.3.2.1), the chemical identity of **$Ca^{II}Zn^{II}_6$-Mecysmox** (and also that of **amoxicillin@$Ca^{II}Zn^{II}_6$-Mecysmox**) was further established by elemental analyses (C, H, S, N), inductively coupled plasm–mass spectrometry (ICP–MS), powder X–ray diffraction (PXRD) and thermo–gravimetric (TGA) analyses. Both C, H, S, N analyses and ICP–MS measurements, together with TGA analyses, allowed to determine the chemical

formulas of **$Ca^{II}Zn^{II}_6$-Mecysmox** and **amoxicillin@$Ca^{II}Zn^{II}_6$-Mecysmox** (see experimental section). Figures 3.9 and 3.10 show the TGA analyses for **$Ca^{II}Zn^{II}_6$-Mecysmox** and **amoxicillin@$Ca^{II}Zn^{II}_6$-Mecysmox**, respectively, which establish the water contents established in the chemical formulas (see experimental section (3.5.1)).

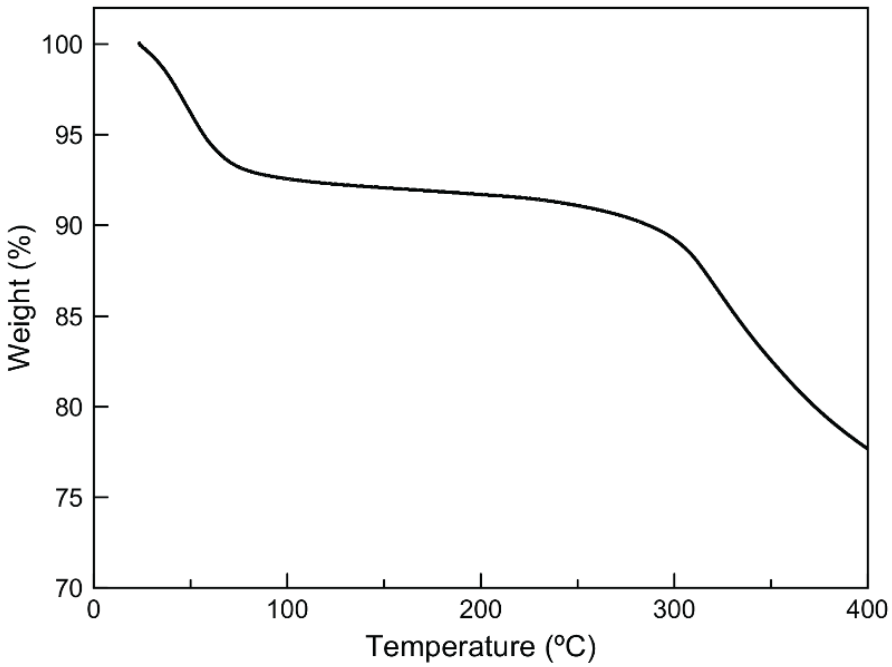

Figure 3.10. Thermo-Gravimetric Analyses (TGA) of **amoxicillin@$Ca^{II}Zn^{II}_6$-Mecysmox** under dry N_2 atmosphere.

Figures 3.11 and 3.12 show the experimental powder X-ray diffraction (PXRD) patterns of **$Ca^{II}Zn^{II}_6$-Mecysmox** and **amoxicillin@$Ca^{II}Zn^{II}_6$-Mecysmox**, which are identical to the theoretical ones (blue lines in Figures 3.11-3.12), confirming the purity and homogeneity of the bulk samples of **$Ca^{II}Zn^{II}_6$-Mecysmox** and **amoxicillin@$Ca^{II}Zn^{II}_6$-Mecysmox**.

3.3.2.3. Powder X-ray diffraction

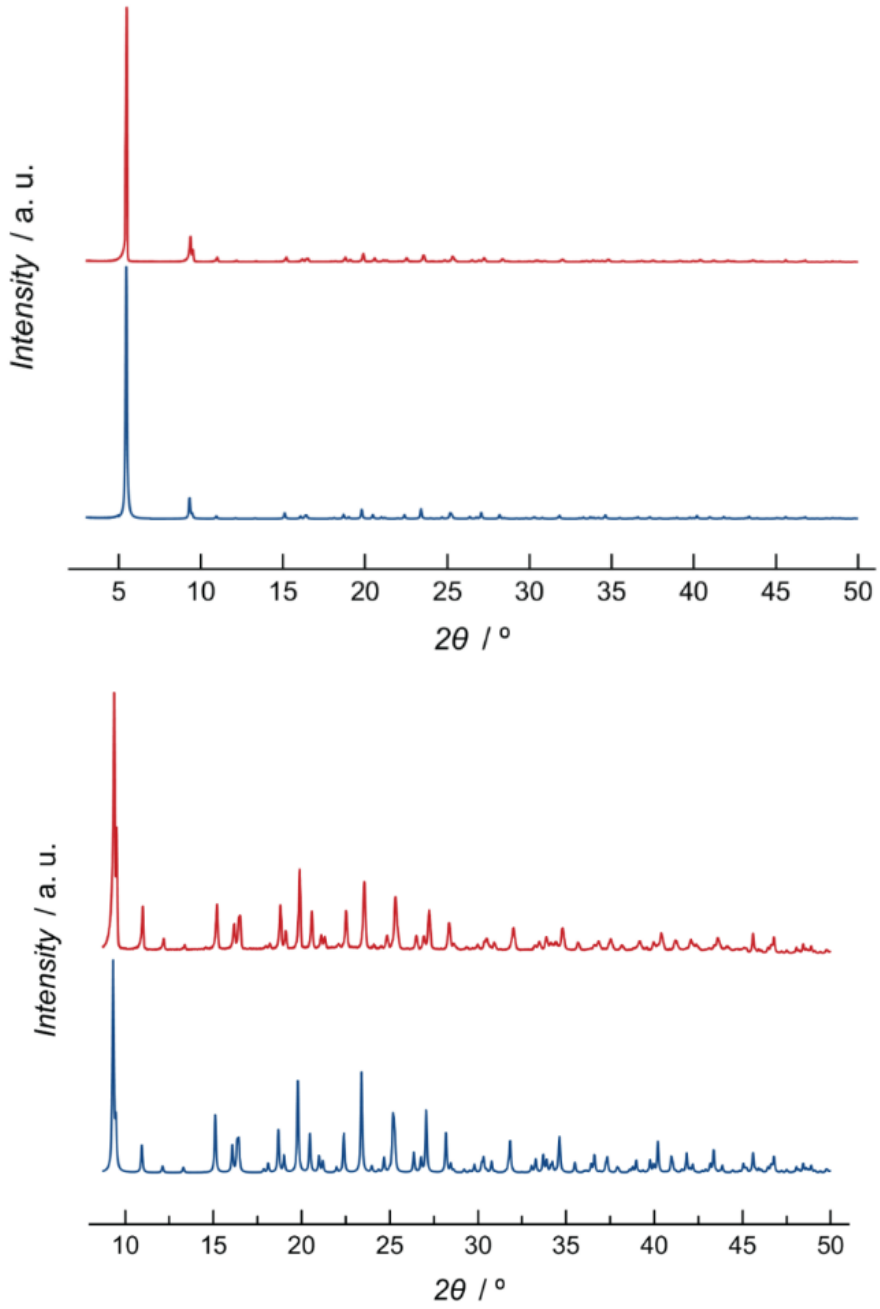

Figure 3.11. Calculated (blue) and experimental (red) PXRD pattern profiles of **$Ca^{II}Zn^{II}_6$-Mecysmox** in the 2ϑ ranges 3.0–50.0° (top) and 8.5–50.0° (bottom).

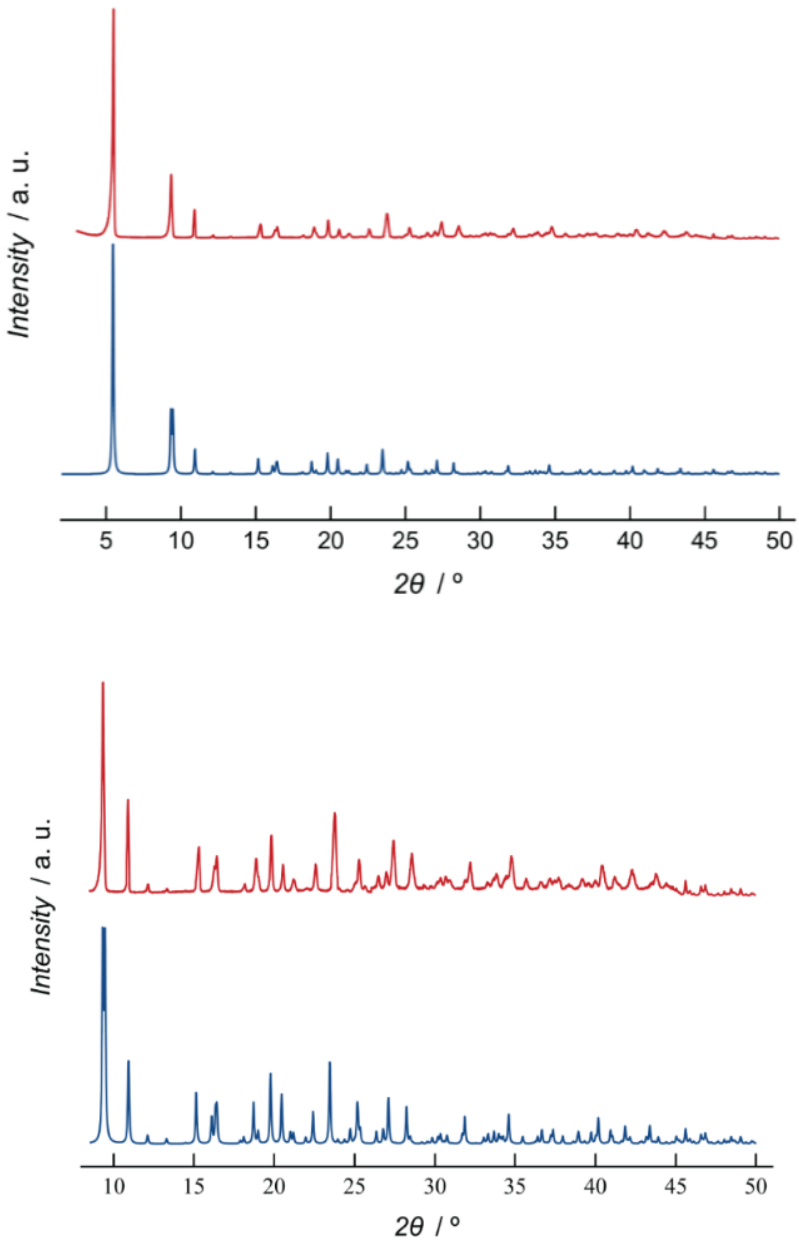

Figure 3.12. Calculated (blue) and experimental (red) PXRD pattern profiles of **amoxicillin@$Ca^{II}Zn^{II}_6$-Mecysmox** in the 2ϑ ranges 3.0–50.0° (top) and 10.0–50.0° (bottom).

3.3.2.4. Gas adsorption measurements

Aiming at confirming that **$Ca^{II}Zn^{II}_6$-Mecysmox** is capable to host antibiotic molecules, its permanent porosity was also evaluated by measuring its N_2 adsorption isotherm (Figure 3.13). Indeed, the isotherm for **$Ca^{II}Zn^{II}_6$-Mecysmox** shows a type I behavior with large uptake at low pressures. The Brunauer-Emmett-Teller (BET) surface area calculated was 571 m^2/g.[49]

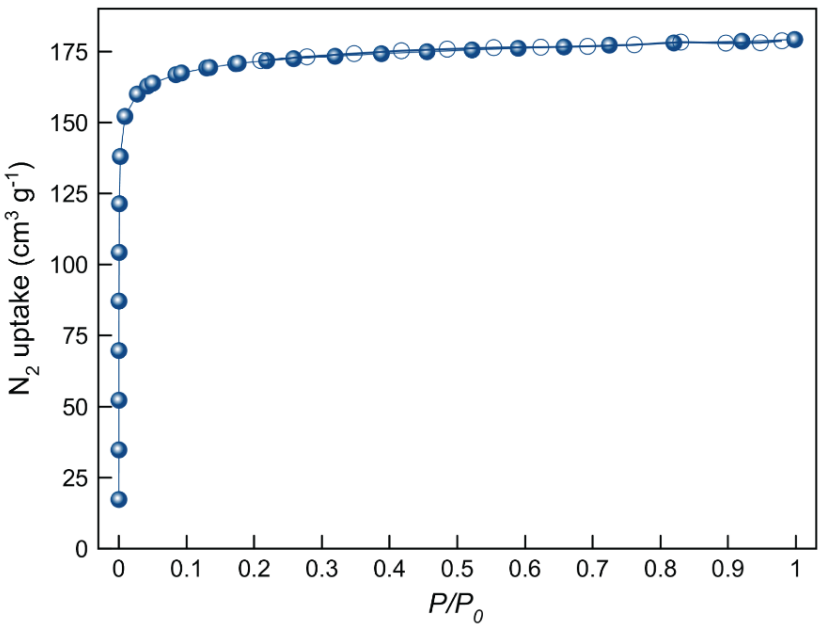

Figure 3.13. N_2 sorption (filled circles) and desorption (empty circles) isotherms for the activated compound **$Ca^{II}Zn^{II}_6$-Mecysmox** at 77 K.

3.3.3. Analytical experiments

On the basis of the structural characteristic observed for the Zn(II) active sites of the MOF **$Ca^{II}Zn^{II}_6$-Mecysmox**, we carried out analytical experiments to observe if, as we expected, **$Ca^{II}Zn^{II}_6$-Mecysmox** was capable to degrade, selectively, the four-membered rings of amoxicillin and ceftriaxone antibiotics,

together with non-penicillinic antibiotics like clindamycin and cholesterol absorption inhibitor ezetimibe, for the sake of comparison (Figure 3.14). Notice that ezetimibe also contains a β-lactam ring but not the fused thiazolidine ring. The uptake efficiency of MOF **$Ca^{II}Zn^{II}_6$-Mecysmox** for amoxicillin, ceftriaxone and clindamycin was first evaluated by HPLC-UV analyses in water (see Experimental section for further details).

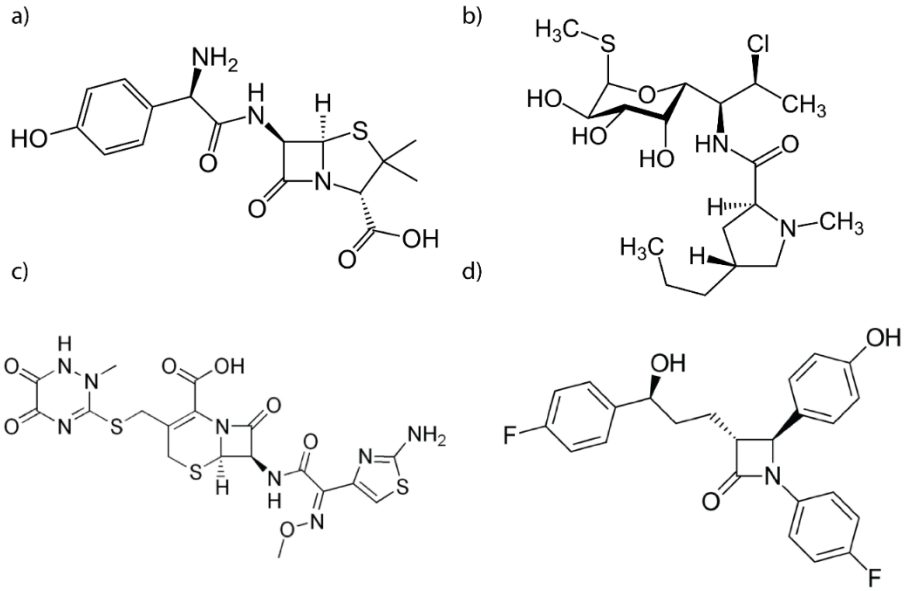

Figure 3.14. Chemical structures of amoxicillin (a) clindamycin (b), ceftriaxone (c) and ezetimibe (d) used for the adsorption and degradation studies.

Regarding amoxicillin degradation, after just 30 min of soaking, the HPLC chromatogram shows the appearance of two UV peaks at r.t. 6.28 (**f1**) and 7.12 min (**f2**), in addition to the amoxicillin peak (r.t. 9.57 min). The area of the first peak (r.t. 6.28 min) increases as the area relative to amoxicillin peak (9.57 min) decreases, reaching a maximum after 4 hours and remaining constant (after 24h, Figure 3.15). This evidence suggests the formation of probable degradation products of amoxicillin**.** The fractions **f1** and **f2** collected from HPLC separation were, hence, analyzed by mass spectrometry in order to retrieve structural information. The HPLC-MS determination was performed at high resolution using

an Orbitrap Exploris 120 equipped with an ESI source. The full MS spectra of both fractions carried out in positive mode showed similar protonated molecular ions at m/z 384.1224, which matches with the formula $C_{16}H_{22}N_3O_6S$. The elemental composition corresponds to the amoxicillin penicilloic acid compound (Figure 3.16). The presence of the same m/z signal at different retention times may be rationalized by the formation in solution of two epimers, as already reported in the literature.[50] Furthermore, the HR-MS analysis showed the presence of the two epimers of amoxicillin penicilloic acid compounds (m/z 340.1311), derived from a consecutive decarboxylation of amoxicillin penicilloic acid (m/z 384.1224). This decarboxylation probably occurs in solution and it is not affected by MOF. The presence of stereoisomers was confirmed by MS/MS experiments, which disclose the same fragmentation pattern (Figure 3.17).

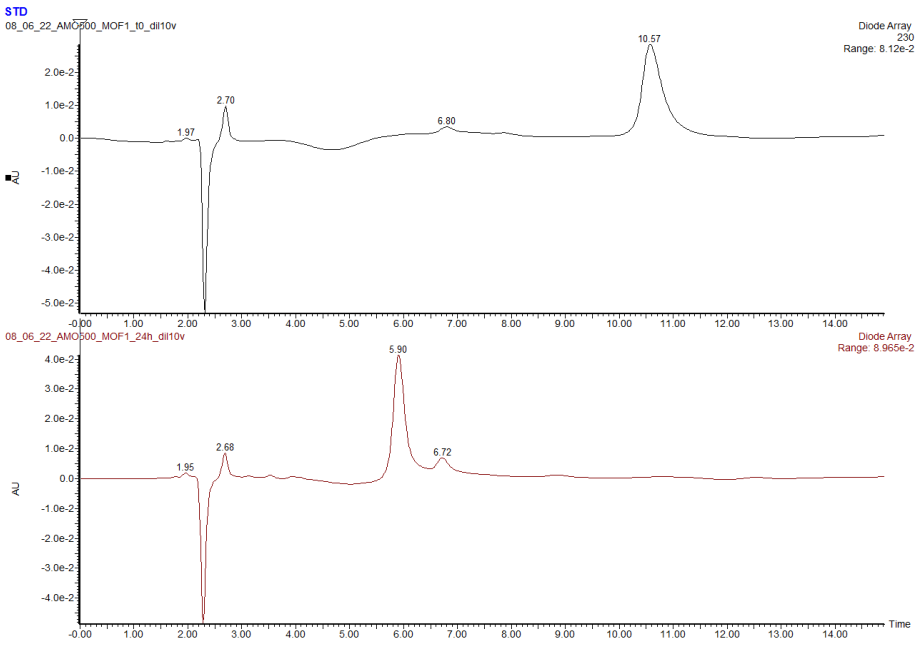

Figure 3.15. HPLC-UV chromatogram of the soaked solution of Amoxicillin with MOF in water at t = 0 (top) and t = 24 h (bottom). Amoxicillin @ r.t. = 10.57 min; Amoxicillin penicilloic acid epimers @ r.t. = 5.90 min and 6.72 min.

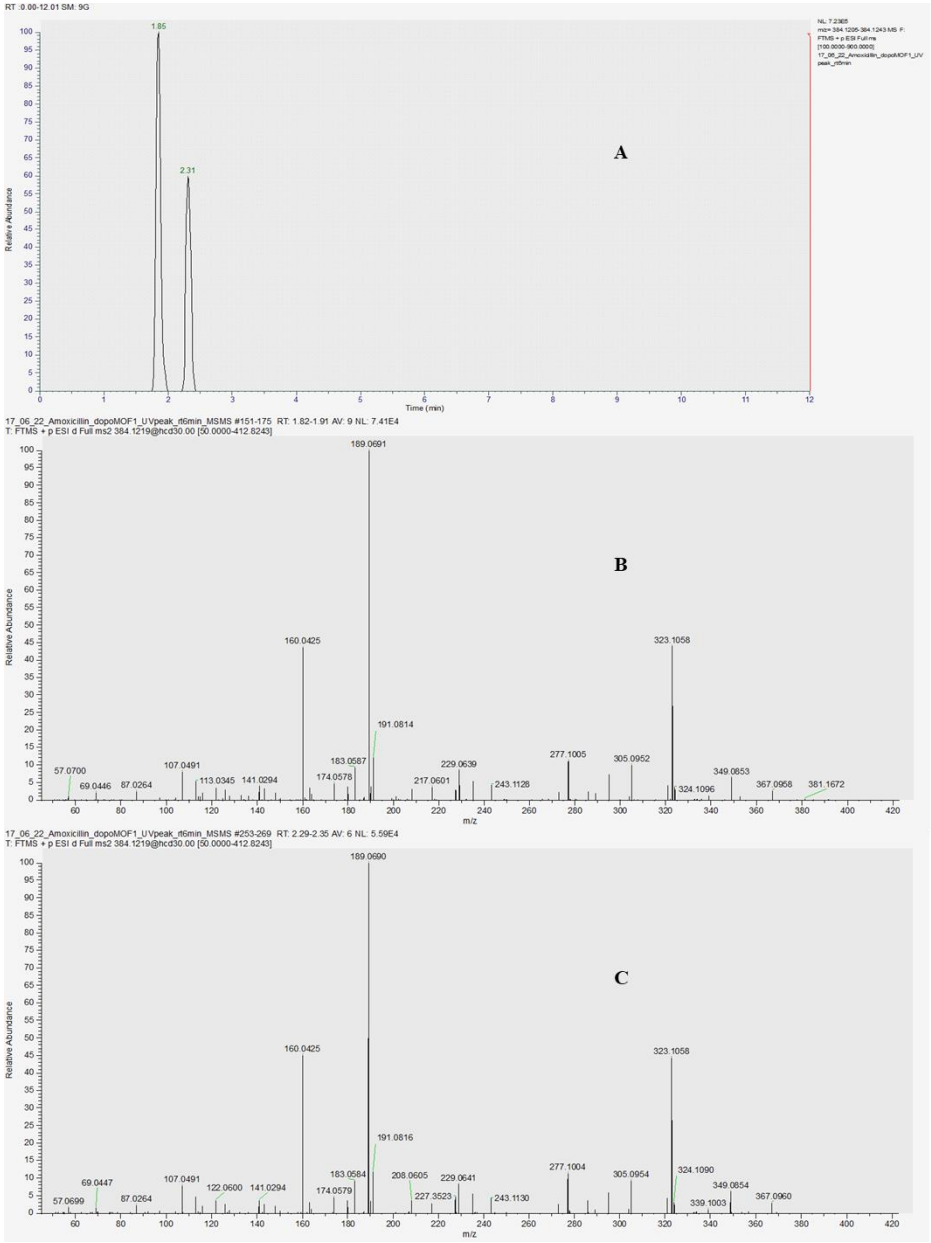

Figure 3.16. HPLC-ESI(+)-MS/MS spectra of the fraction **f1** collected by HPLC-UV experiments. (A) Extracted ion chromatograms (XIC) of m/z 384.1224 corresponding to the elemental composition $C_{16}H_{22}N_3O_6S^+$; (B) MS/MS spectrum of amoxicillin penicilloic acid epimer 1 @ r.t. 1.85 min; (C) MS/MS spectrum of amoxicillin penicilloic acid epimer 2 @ r.t. 2.31 min.

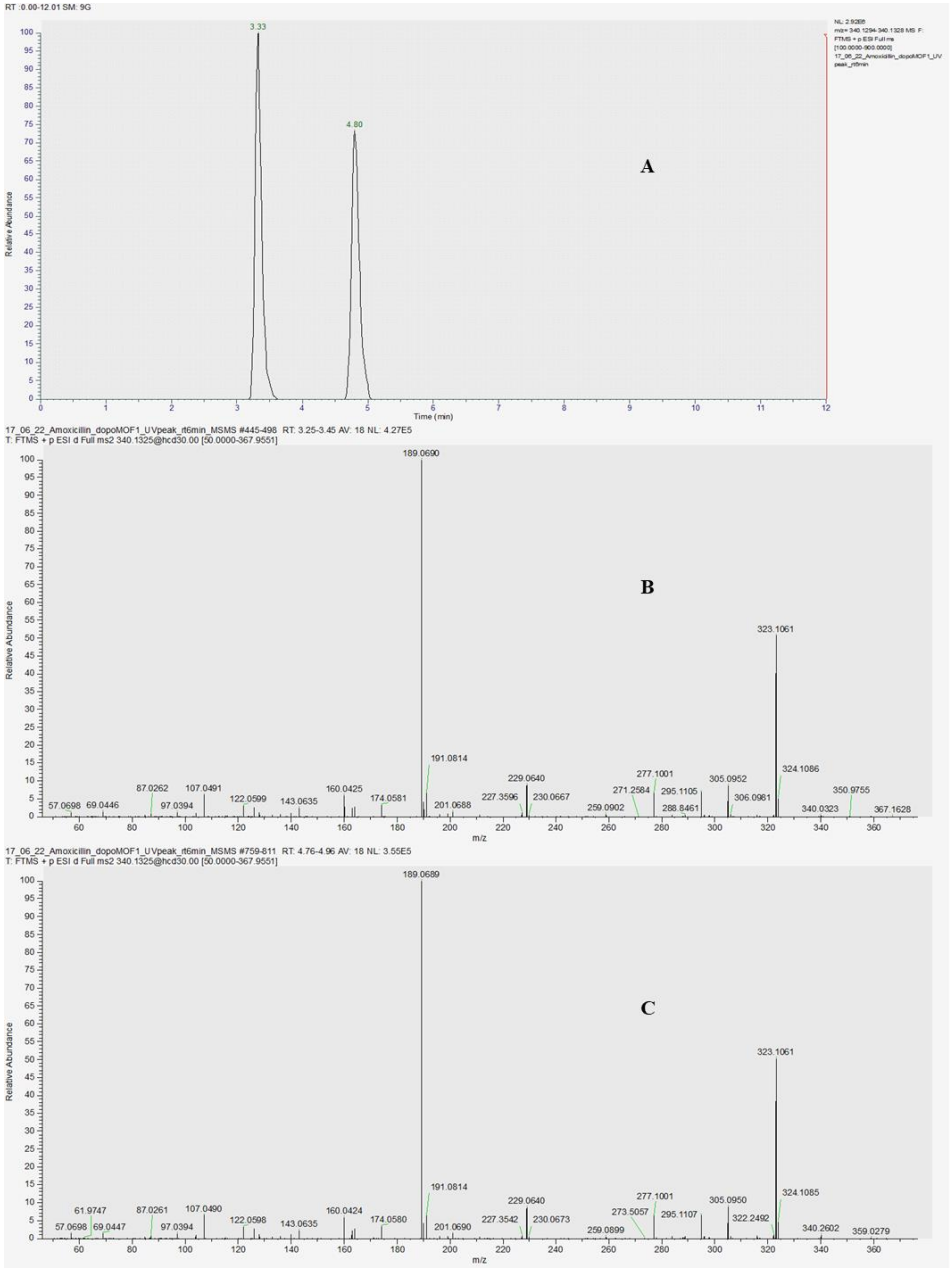

Figure 3.17. HPLC-ESI(+)-MS/MS spectra of the fraction **f2** collected by HPLC-UV experiments. (A) XIC of m/z 340.1311 corresponding to the elemental composition $C_{15}H_{22}N_3O_4S^+$; (B) MS/MS spectrum of decarboxylated amoxicillin penicilloic acid epimer 1 @ r.t. 3.33 min; (C) MS/MS spectrum of decarboxylated amoxicillin penicilloic acid epimer 2 @ r.t. 4.80 min.

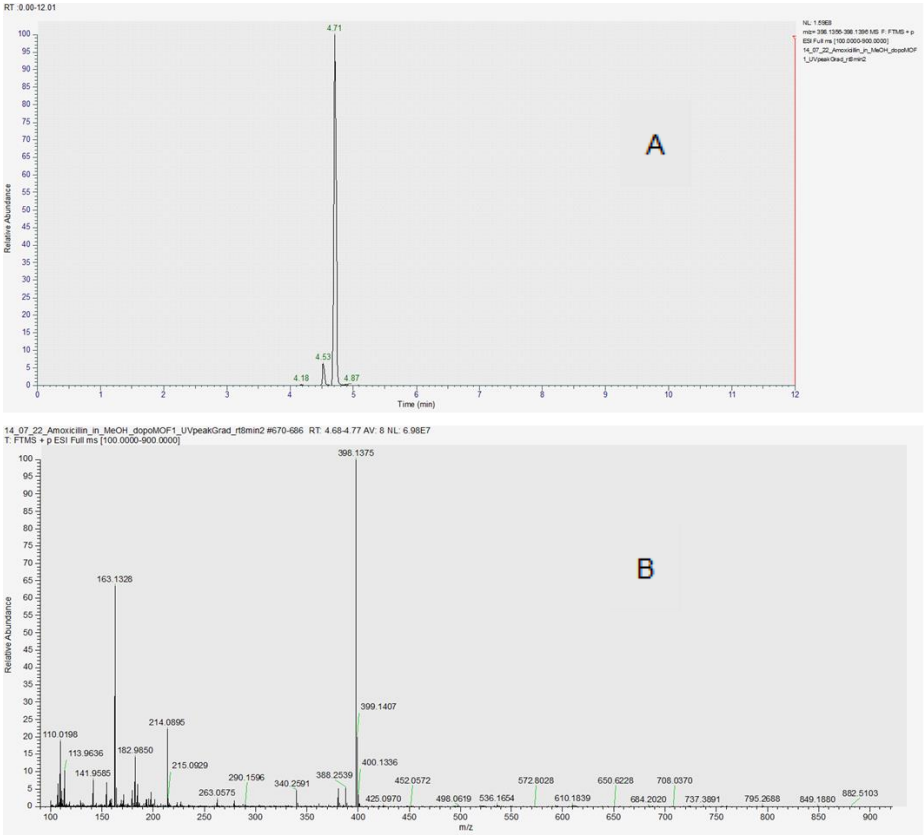

Figure 3.18. HPLC-ESI(+)-MS/MS spectra of the methyl ester of penicilloic acid obtained by the soaking of amoxicillin with MOF **$Ca^{II}Zn^{II}_6$-Mecysmox** in methanol. (A) XIC of the reaction product at m/z 398.1376 corresponding to the elemental composition $C_{17}H_{24}N_3O_6S^+$; (B) MS spectrum of m/z 398.1376 at r.t. 4.71 min.

In order to support the ring opening reaction mechanism, the soaking was performed also in MeOH. After 24h the HPLC-ESI MS analysis showed the presence of just one peak relative to the formation of the methyl ester of the amoxicillin penicilloic acid (Figure 3.18). In this case, as expected, no decarboxylation product was detected, and no epimerization occurred.[51]

The situation is drastically different for the cephalosporin β-lactam antibiotic ceftriaxone. Indeed, a different hydrolysis reaction mechanism is observed when ceftriaxone is soaked with MOF **$Ca^{II}Zn^{II}_6$-Mecysmox**. The HPLC-UV analysis shows, as a matter of fact, the formation of only one degradation

product (Figure 3.19), which has been identified by HPLC-ESI-HRMS as the ion at m/z 414.0535 (Figure 3.20). This compound is produced by the hydrolysis of ceftriaxone at the sulfur atom of the carbamimidothioate group, previously characterized after hydrolysis at pH = 5 after 12 days.[43]

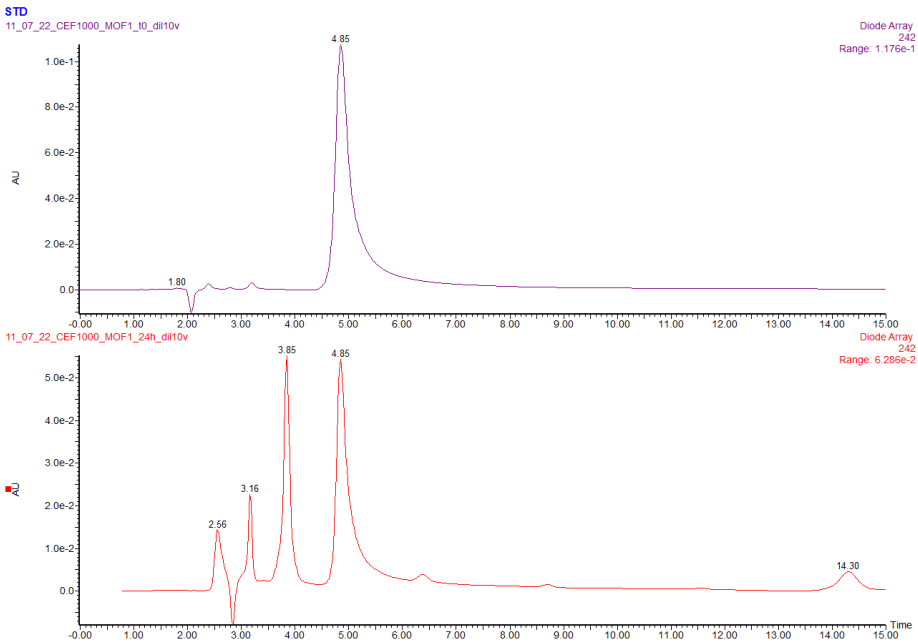

Figure 3.19. HPLC-UV chromatogram of the soaked solution of Ceftriaxone with MOF in water at (top) t = 0 min and (bottom) t = 24 min. Ceftriaxone @ r.t. = 4.85 min; degradation product @ r.t. = 3.85 min.

Finally, clindamycin, which belongs to the class of lincosamide antibiotics, does not show any hydrolytic behavior when soaked with MOF **$Ca^{II}Zn^{II}_6$-Mecysmox**. Furthermore, the uptake of the molecule reaches a maximum at 5h, and then decreases at the initial level, showing a behavior governed almost completely by physisorption mechanisms.

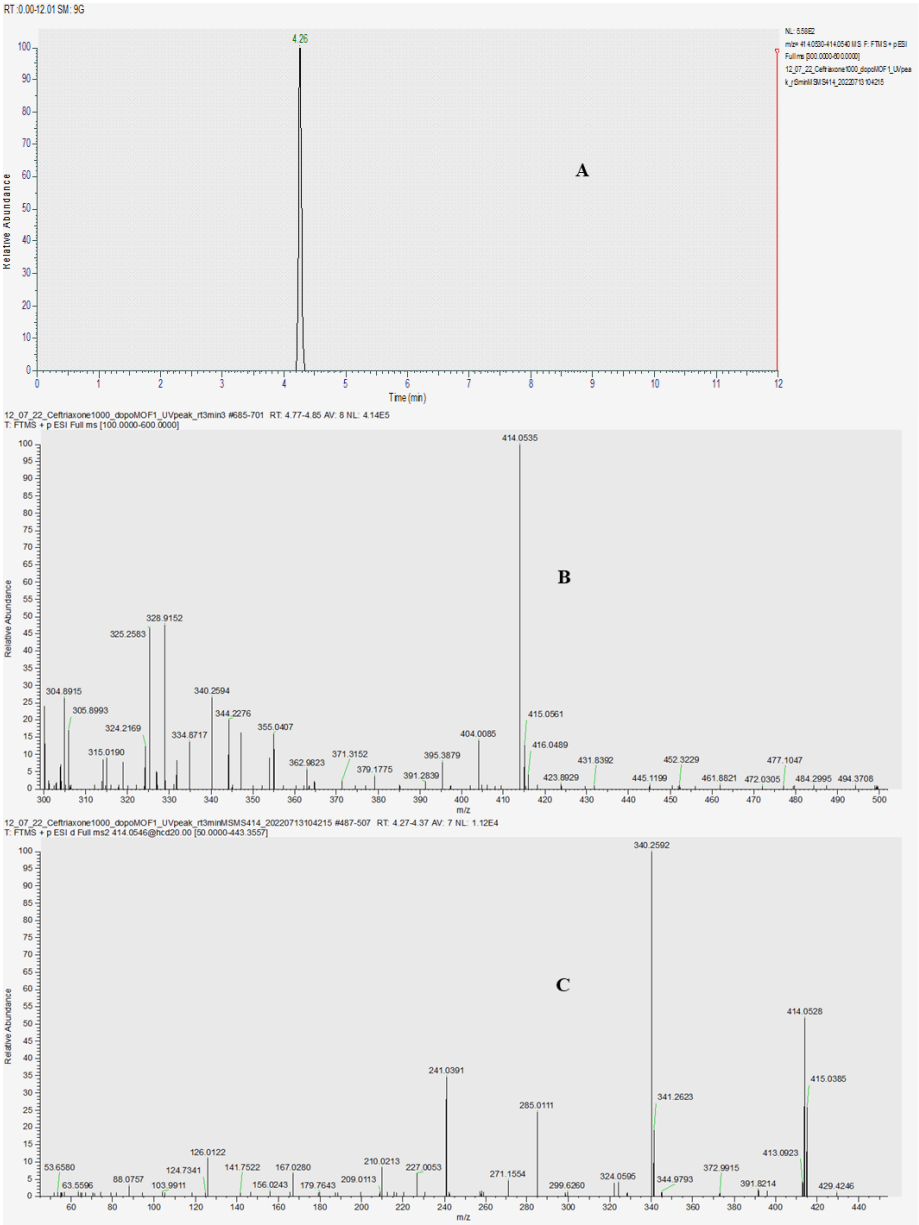

Figure 3.20. HPLC-ESI(+)-MS/MS spectra of the hydrolysis product obtained by the soaking of ceftriaxone with MOF **$Ca^{II}Zn^{II}_6$-Mecysmox** in water. (A) XIC of the reaction product at m/z 414.0535 corresponding to the elemental composition $C_{14}H_{16}N_5O_6S_2^+$; (B) MS spectrum at r.t. 4.71 min of m/z 414.0535. (C) MS/MS spectrum of m/z 414.0535.

3.3.4. Catalytic experiments

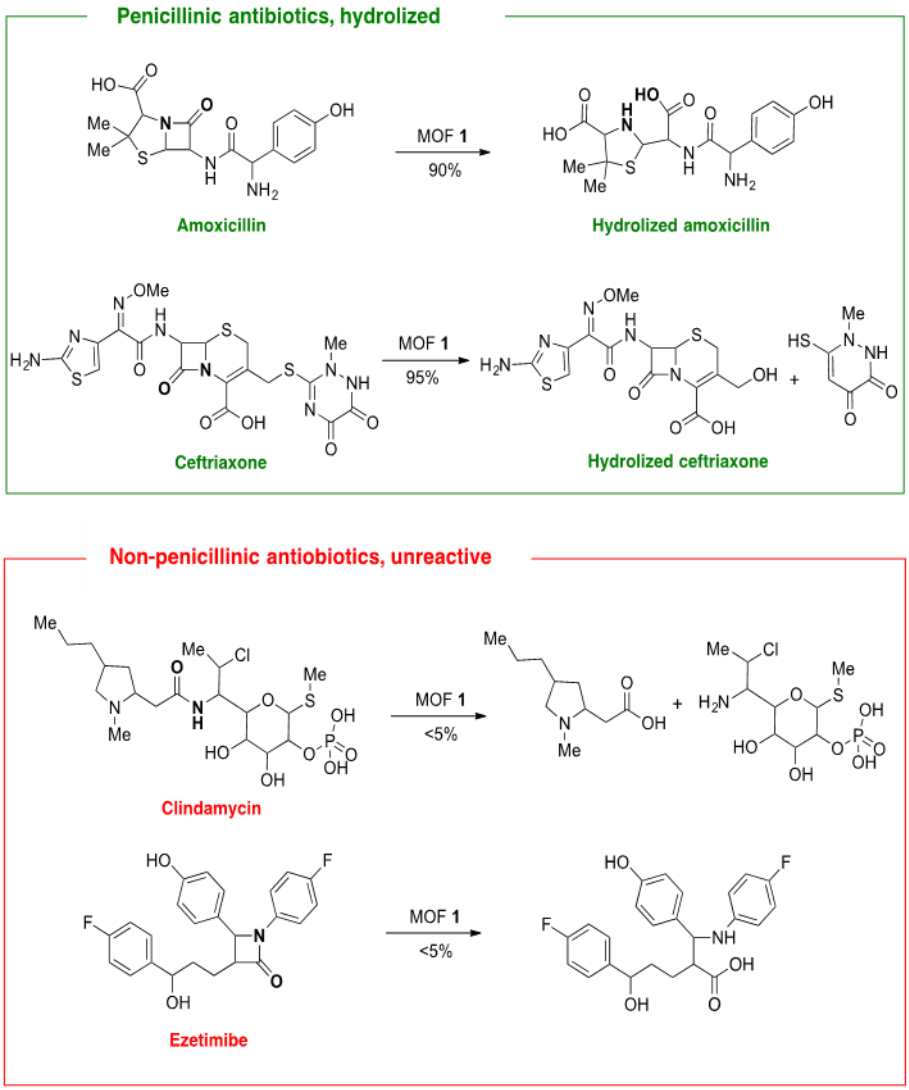

Figure 3.21. Hydrolysis products of the different penicillinic (top) and non-penicillinic antibiotics (bottom) catalyzed by MOF **$Ca^{II}Zn^{II}_6$-Mecysmox**.

Aiming at further confirming the degrading activity of MOF **$Ca^{II}Zn^{II}_6$-Mecysmox** towards amoxicillin and ceftriaxone, we also carried out catalytic experiments. Reactions were followed by *in-situ* proton nuclear magnetic resonance (^{1}H NMR), diffuse reflectance ultraviolet-visible spectrophotometry

(DR-UV-vis) and Fourier transformed infrared spectroscopy (FT-IR). A parent MOF, non-containing Zn but Cu, with formula ({$Ca^{II}Cu^{II}_6$[(*S,S*)-Mecysmox]$_3$$(OH)_2(H_2O)$}·$16H_2O$ (MOF **$Ca^{II}Cu^{II}_6$-Mecysmox**))[52,53] and also ZnO were evaluated as catalysts for the same reaction. The results are shown in Table 3.2 and Figure 3.21.

Table 3.2. Catalytic results for the hydrolysis reaction of different penicillinic and non-penicillinic antibiotics in the presence of different solids. 20 mol % Zn. [a]Conversions measured by ^{1}H NMR.

Entry	Substrate	Catalyst	Conversion (%)[a]
1	Amoxicillin	**$Ca^{II}Zn^{II}_6$-Mecysmox**	90
2		**$Ca^{II}Cu^{II}_6$-Mecysmox**	<5
3		ZnO	60
4	Ceftriaxone	**$Ca^{II}Zn^{II}_6$-Mecysmox**	95
5		**$Ca^{II}Cu^{II}_6$-Mecysmox**	<5
6		ZnO	50
7	Clindamycin and ezetimibe	**$Ca^{II}Zn^{II}_6$-Mecysmox**	<5
8		**$Ca^{II}Cu^{II}_6$-Mecysmox**	<5
9		ZnO	<5

^{1}H NMR results (Figure 3.22) show that MOF **$Ca^{II}Zn^{II}_6$-Mecysmox**, containing Zn(II) sites, catalyzes very efficiently and selectively (90 % yield) the hydrolysis of the β-lactam ring in amoxicillin, keeping untouched the rest of bonds in the molecules, which include, among others, linear amide, oxime, thioamines and diazine bonds. The same efficiency (> 90 % yield) is observed for the degradation of ceftriaxone to give into thiotriazinone and 3-desacetyl

cefotaxime (Figure 3.23). DR-UV-vis (Figure 3.24) and FT-IR (Figure 3.25) measurements confirm the presence of the hydrolyzed products inside the framework of MOF **$Ca^{II}Zn^{II}_6$-Mecysmox** after reaction. In accordance, the linear amide bond of the non-penicillinic antibiotic clindamycin does not react under identical reaction conditions (Figure 3.26), and even the β-lactam ring of the cholesterol absorption inhibitor ezetimibe is completely unreactive (Figure 3.27), which supports the high selectivity of MOF **$Ca^{II}Zn^{II}_6$-Mecysmox** towards the fused β-lactam-thiazolidine ring core and discards an enhanced amide hydrolysis reaction by pure confinement effects.[54]

MOF **$Ca^{II}Cu^{II}_6$-Mecysmox** containing Cu(II) in its framework instead of Zn(II) is completely inactive towards the hydrolysis reaction, and ZnO shows some catalytic activity, but much lower than MOF **$Ca^{II}Zn^{II}_6$-Mecysmox**. These results, together, support the uniqueness of the Zn(II) sites in MOF **$Ca^{II}Zn^{II}_6$-Mecysmox** to catalyze the hydrolysis of the β-lactam ring in penicillinic antibiotics, such as β-lactamases do, and the potential role of simple MOFs as biocatalysts.[55]

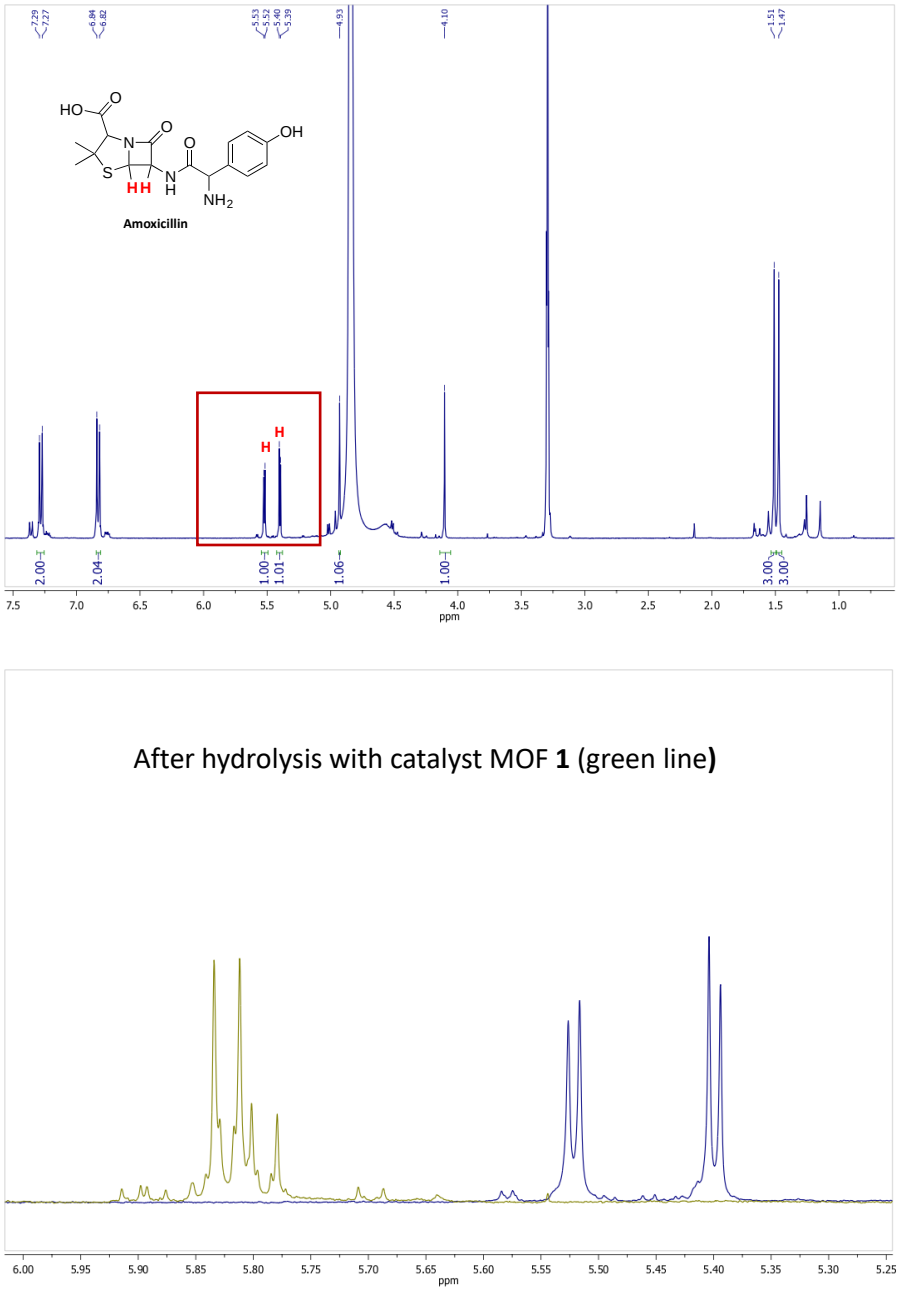

Figure 3.22. Full ^{1}H NMR spectrum for amoxicillin (top) and selected region (5.25-6 ppm) of the ^{1}H NMR spectrum (highlighted in red) after the hydrolysis reaction with MOF **$Ca^{II}Zn^{II}_{6}$-Mecysmox** catalyst (green line, bottom).

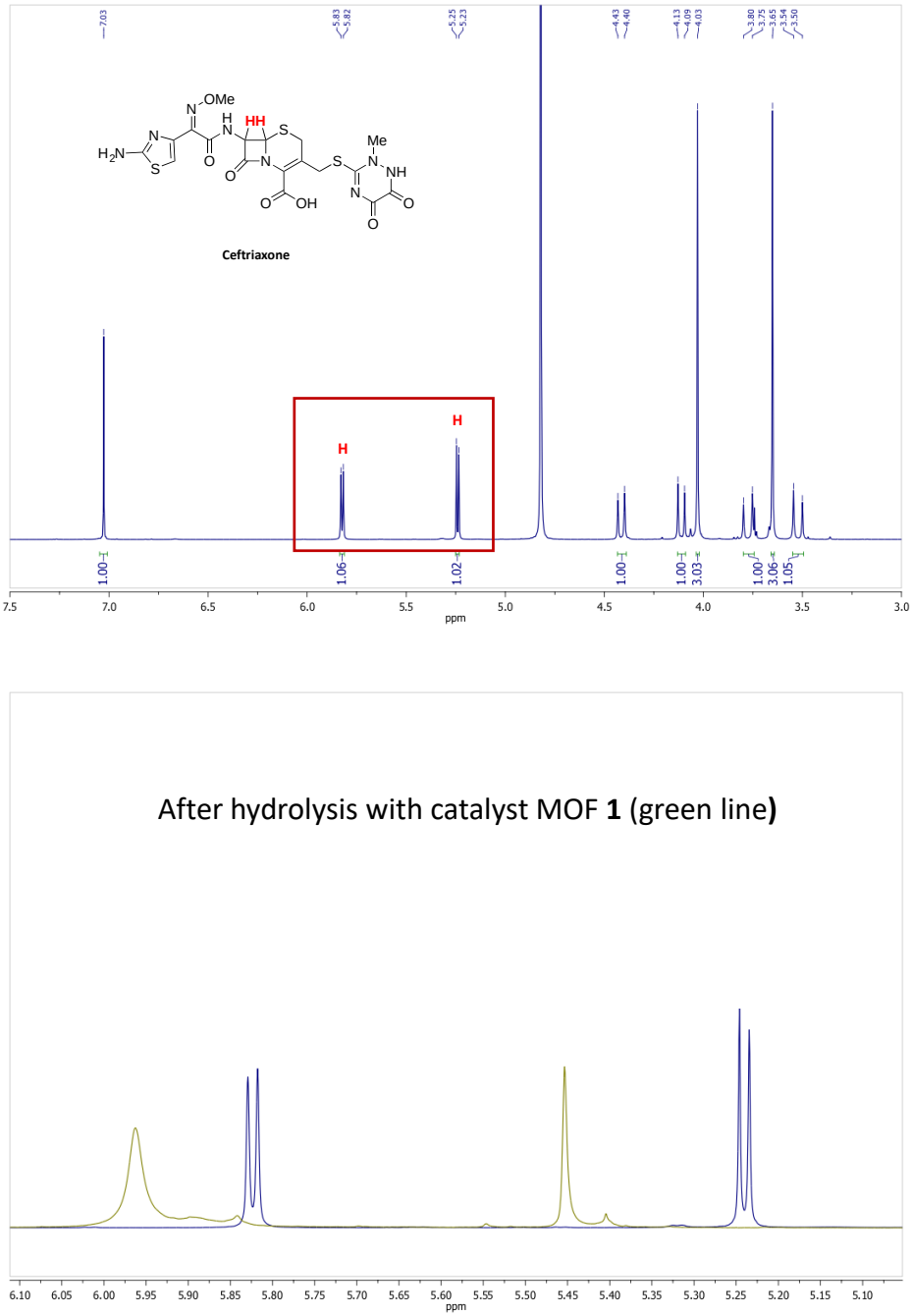

Figure 3.23. Full ^{1}H NMR spectrum for ceftriaxone (top) and selected region (5.05-6.10 ppm) of the ^{1}H NMR spectrum (highlighted in red) after the hydrolysis reaction with MOF **$Ca^{II}Zn^{II}_{6}$-Mecysmox** catalyst (green line, bottom).

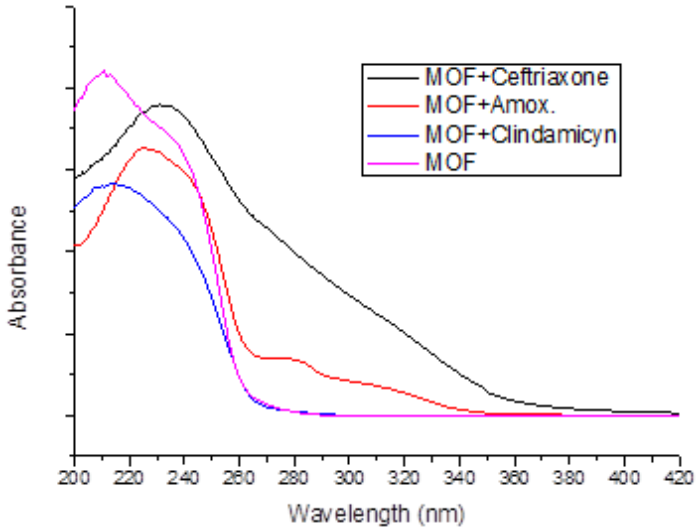

Figure 3.24. DR-UV-vis spectra of MOF **$Ca^{II}Zn^{II}_6$-Mecysmox** after catalyzing the hydrolysis of the different antibiotics. Only those hydrolyzed (the penicillin amoxicillin and ceftriaxone compounds) remain inside the MOF structure after reaction.

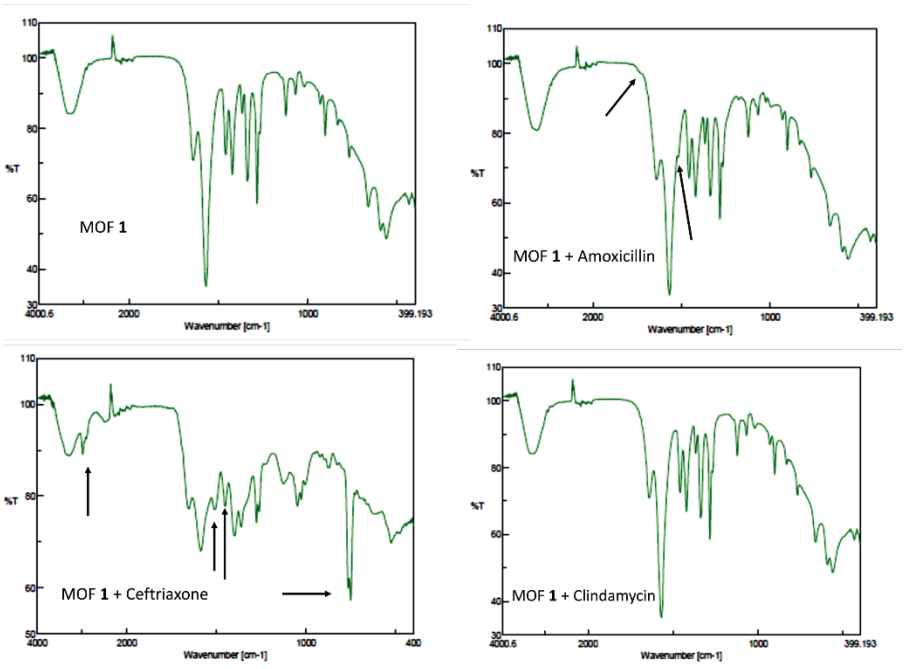

Figure 3.25. FT-IR spectra of MOF **$Ca^{II}Zn^{II}_6$-Mecysmox** after catalyzing the hydrolysis of the different antibiotics. Only those hydrolyzed (the penicillin amoxicillin and ceftriaxone compounds) remain inside the MOF structure after reaction. Arrows show the diagnostic signals of the presence of the product.

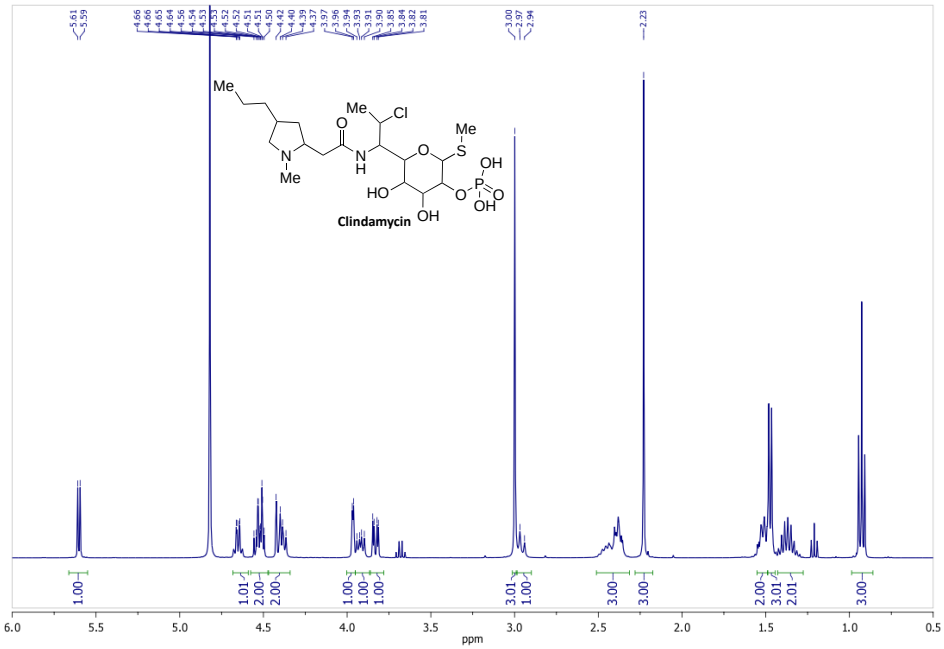

Figure 3.26. Full ^{1}H NMR spectrum for clindamycin, which does not vary after the hydrolysis reaction with MOF **$Ca^{II}Zn^{II}_{6}$-Mecysmox** catalyst.

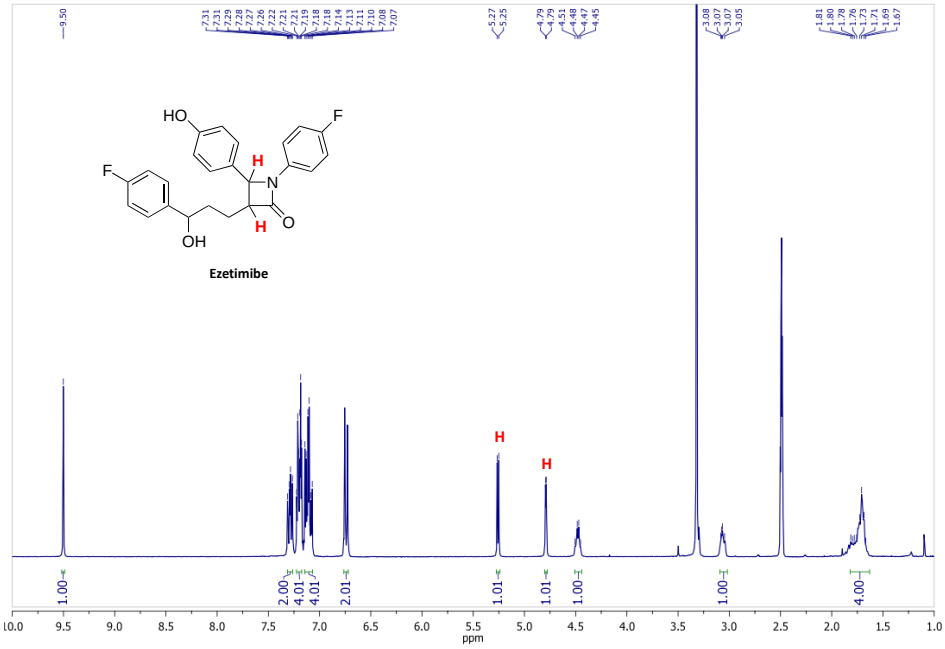

Figure 3.27. Full ^{1}H NMR spectrum for ezetimibe, which does not vary after the hydrolysis reaction with MOF **$Ca^{II}Zn^{II}_{6}$-Mecysmox** catalyst.

3.3.5. Theoretical calculations

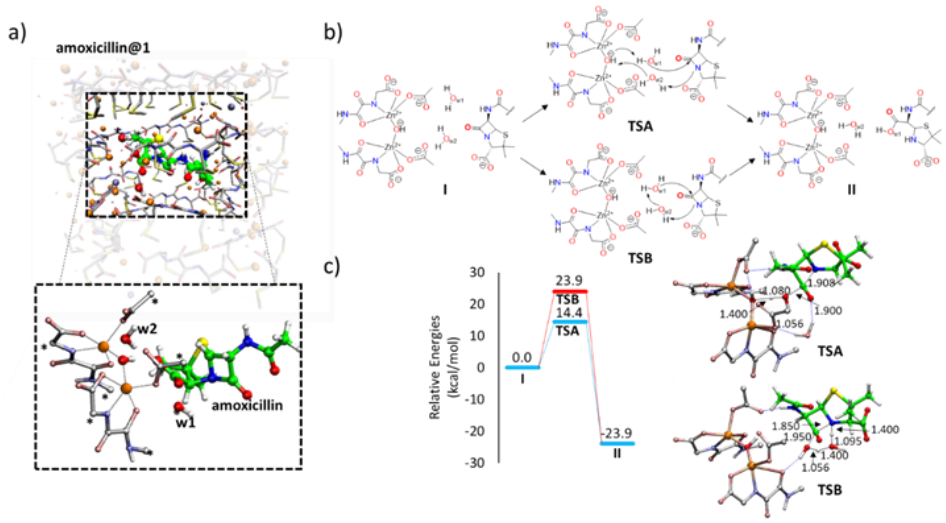

Figure 3.28. DFT study of amoxicillin hydrolysis by MOF **$Ca^{II}Zn^{II}_6$-Mecysmox**. a) The adopted model where the atoms labelled with "*" were kept fixed in their crystal coordinates. b) The investigated water-mediated mechanisms, c) the related calculated energy profiles and the optimized geometries of transition states (distances in Å). In a) and c) Zn, O, S, N and H were represented by orange, red, yellow, blue and white spheres, respectively, while C atoms of amoxicillin were represented as green spheres (in silver the others). For clarity, most of the non-polar hydrogens were omitted in the representation.

Table 3.3. Binding affinity obtained for the calculated docked poses of amoxicillin in MOF **$Ca^{II}Zn^{II}_6$-Mecysmox**.

Docked pose	Binding affinity (kcal/mol)
1	-6.1
2	-6.0
3	-5.9
4	-5.9
5	-5.9
6	-5.8
7	-5.8
8	-5.8
9	-5.8

To further confirm the β-lactamase activity of MOF **$Ca^{II}Zn^{II}_6$-Mecysmox**, Density Functional Theory (DFT) calculations were carried out on a model (Table 3.3) of **amoxicillin@$Ca^{II}Zn^{II}_6$-Mecysmox** system as depicted in Figures 3.28-3.30. The model was built up following the quantum-chemical cluster approach scheme, which was successfully applied on a number of similar chemical systems[56,57] (see experimental section). The technical details are fully described in the experimental section. Two water mediated reaction mechanisms were investigated for the hydrolysis of the amoxicillin (see Figure 3.28b). In mechanism **A**, the Zn-bridging hydroxyl group activates the water molecule, by accepting one proton, and the formed nucleophilic species ($O_{w1}H^-$) is able to attack the β-lactam carbonyl group of the substrate, causing the opening of the four-membered ring. In the alternative **B** mechanism, the nucleophilic attack to the carbonyl group takes place directly by the O_{w1} with the consequent cleavage of C-N bond. The final product, for both considered mechanisms, is characterized by the formed carboxylic and NH- groups originating from the opening of the ring (Figure 3.28b). The analysis of the energy barriers reveals a more energetic feasibility of the mechanism **A**, since **TSB** lies at 9.5 kcal/mol higher than the **TSA** (23.9 kcal/mol vs 14.4 kcal/mol, see Figure 3.28b). Despite both calculated barriers are not prohibitive for the catalysis, in mechanism **A** is evident the role played by the Zn(II) centers, which boost the reaction promoting the formation of a good nucleophile. The driving force of the reaction is the concerted formation of C-C and breaking of C-N bonds, further confirmed by the imaginary frequency of 376.1*i* cm^{-1}, and the formation of NH group, which occurs spontaneously due to the hydrogen-bond network involving the w1, w2 and the scaffold of the MOF **$Ca^{II}Zn^{II}_6$-Mecysmox** (see Figure 3.28c). The ordered composition of MOF **$Ca^{II}Zn^{II}_6$-Mecysmox** is therefore the origin of the catalytic action, leading to the occurrence of the reaction with reasonable kinetic, in addition to the favorable thermodynamics (-23.9 kcal/mol). The proposed mechanism, and the here-described role of the Zn(II) ions, invokes the working mechanism proposed for β-

lactamases.[7,8,12] Furthermore, the calculated energy barrier for **TSA** (14.4 kcal/mol) is in good agreement with the available kinetic data, concerning the action of the enzyme from different microorganisms on amoxicillin, as evidenced by turnover numbers from 2 s^{-1} to 910 s^{-1}.[58,59] These values converted in activation energies correspond to barriers in the range of 13 to 17 kcal/mol, which and are close to the calculated one.

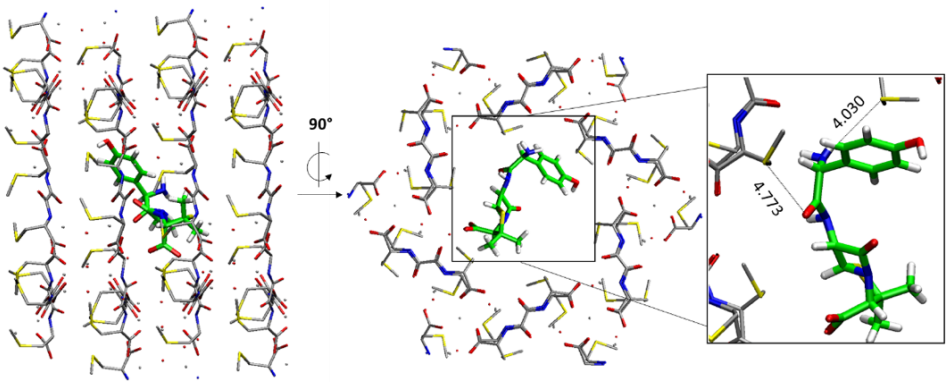

Figure 3.29. Lowest binding modes of amoxicillin (green carbons) in MOF **$Ca^{II}Zn^{II}_6$-Mecysmox**.

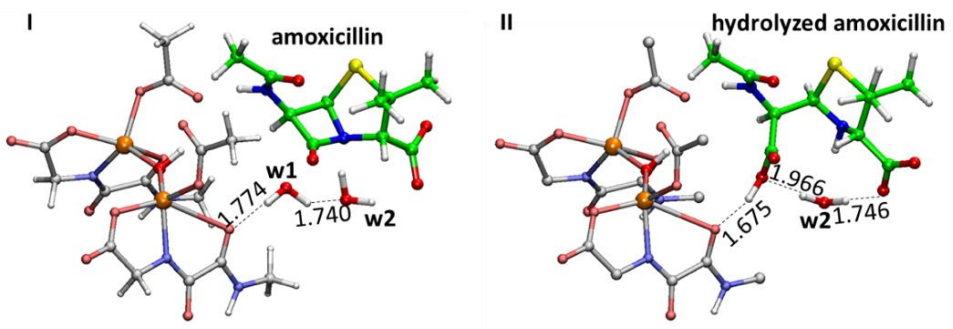

Figure 3.30. Lowest binding modes of amoxicillin (green carbons) in MOF **$Ca^{II}Zn^{II}_6$-Mecysmox**.

3.4. Conclusions

In summary, we report a novel 3D Zn-based MOF (**$Ca^{II}Zn^{II}_6$-Mecysmox**), derived from amino acid *S*-methyl-*L*-cysteine, possessing functional channels, densely decorated with thioether functional groups, which are capable to immobilize, amoxicillin and ceftriaxone antibiotics by means of efficient host-guest interactions. Then, in a second step, **$Ca^{II}Zn^{II}_6$-Mecysmox** catalyzes the selective hydrolysis of these penicillinic antibiotics. For ceftriaxone, **$Ca^{II}Zn^{II}_6$-Mecysmox** induces its hydrolysis into thiotriazinone and 3-desacetyl cefotaxime, a reaction that usually only occurs without the catalyst at pH = 5. On the other hand, **$Ca^{II}Zn^{II}_6$-Mecysmox** degrades, very efficiently, the four-membered β-lactam ring of amoxicillin, acting as a β-lactamase mimic and expands the very limited number of MOFs capable to mimic catalytic enzymatic processes. Single crystal X-ray diffraction studies allowed to resolve the crystal structure of the host-guest aggregate **amoxicillin@$Ca^{II}Zn^{II}_6$-Mecysmox**, which permits to gain unique snapshots on the host guest-interactions between the functional channels of the MOF and amoxicillin, responsible for the guest encapsulation/retention, as well as on the Zn(II) coordination environment responsible for the enzymatic catalysis. On the basis of this crystallographic data, a plausible mechanism for this β-lactamase activity has been proposed by means of DFT calculations, which is a clear step forward on the understanding of β-lactamase enzymes.

3.5. Experimental section

3.5.1. Preparation of the MOFs

Preparation of $\{Zn_6Ca[(S,S)\text{-Mecysmox}]_3(OH)_2(H_2O)\} \cdot 12H_2O$ (**$Ca^{II}Zn^{II}_6$-Mecysmox**): An aqueous solution (35 mL) of H_2Me_2-(*S,S*)-Mecysmox (2.1 g, 6 mmol) and a 25% methanolic solution of Me_4NOH (7.25 mL, 18 mmol) were

added dropwise to another aqueous solution of $Zn(NO_3)_2 \cdot 6H_2O$ (3.55 g, 12 mmol) and $CaCl_2$ (0.22 g, 2 mmol) in 20 mL. The solution mixture was stirred overnight and a white powder was obtained and collected by filtration, washed with water and methanol. Yield: 1.87 g, 56%. Anal.: calcd. for $C_{30}H_{64}N_6O_{33}S_6Zn_6Ca$ (1661.7): C, 21.68; H, 3.88; N, 5.06; S, 11.58%. Found: C, 21.67; H, 3.72; N, 5.06; S, 11.47%. IR (KBr): ν = 1603 cm^{-1} (C=O).

Suitable single crystals of **$Ca^{II}Zn^{II}_6$-Mecysmox** for X-ray structural analysis were obtained by slow diffusion, in an H-shaped tube, of H_2O/DMF (1:1) solutions containing stoichiometric amounts of H_2Me_2-(*S,S*)-Mecysmox (0.064 g, 0.18 mmol) and a 25% aqueous solution of Me_4NOH (0.22 mL, 0.54 mmol) in one arm and $Zn(NO_3)_2 \cdot 6H_2O$ (0.11 g, 0.36 mmol) and $CaCl_2$ (0.007 g, 0.06 mmol) in the other. They were isolated by filtration on paper and air-dried. Anal.: calcd. for $C_{30}H_{64}N_6O_{33}S_6Zn_6Ca$ (1661.7): C, 21.68; H, 3.88; N, 5.06; S, 11.58%. Found: C, 21.71; H, 3.93; N, 4.99; S, 11.67%. IR (KBr): ν = 1601 cm^{-1} (C=O).

Synthesis of $(C_{16}H_{19}N_3O_5S)@\{Zn^{II}Cu^{II}_6[(S,S)\text{-Mecysmox}]_3(OH)_2(H_2O)\} \cdot 9H_2O$ (**amoxicillin@$Ca^{II}Zn^{II}_6$-Mecysmox**): Well-formed hexagonal white prisms of **amoxicillin@$Ca^{II}Zn^{II}_6$-Mecysmox**, which were suitable for X-ray diffraction, were obtained by soaking crystals of **$Ca^{II}Zn^{II}_6$-Mecysmox** (5.0 mg) in a saturated dimethylformamide solution of amoxicillin for 72 hours. The crystals were washed with water, isolated by filtration on paper and air-dried. Anal.: calcd for $C_{46}Zn_6CaH_{77}S_7N_9O_{35}$ (1973.0): C, 28.00; H, 3.93; S, 11.38; N, 6.39%. Found: C, 28.07; H, 3.81; S, 11.29; N, 6.41%. IR (KBr): *ν* = 1603 cm^{-1} (C=O).

3.5.2. Analytical experiments

The uptake measurements for amoxicillin and ceftriaxone were performed by using a HPLC-UV instrument (Water FractionLynx System). The chromatographic separations were carried out employing a reverse-phase Luna

C_{18} (2) column (250 × 4.6 mm; Phenomenex, Torrance, CA). An isocratic elution with 0.1% formic acid and methanol (96:4 v/v) was used for the amoxicillin determination, while an isocratic elution with 0.1% formic acid in water and acetonitrile (85:15 v/v) was used for the determination of ceftriaxone. The run time was 15 min, whereas the flow rate and the UV wavelength were set to 1.5 and 230 nm for amoxicillin and 1.0 mL/min and 242nm for ceftriaxone. The injection volume was 20 µl. The calibration curve was obtained by injecting the standard solutions in the range of concentration from 25 to 400 mg/L. The chromatograms have been collected after 30 min, 4 hours and 24 hours of soaking.

3.5.3. High resolution mass spectrometry experiments

The high resolution ESI-MS and MS/MS experiments were performed using an Exploris 120 high-resolution mass spectrometer (Thermo Fisher Scientific, San José, CA, USA) furnished by a heated electrospray (H-ESI II) ionization probe and an Orbitrap analyzer; the hyphenated HPLC was a Vanquish system composed by an HPLC pump and an autosampler (Thermo Fisher Scientific, San José, CA, USA). Fractions coming from the HPLC-UV analysis were injected into the HPLC-HRESI-MS system using the following conditions: spray voltage: 3500 V; aux gas, sheath gas and sweep gas at 10, 50, 1 a.u., respectively; vaporizer temperature 280 °C; ion transfer tube temperature: 300 °C; the range of the scan was 100–900 m/z, and the RF lens was set to 70 % of the maximum value while the orbitrap resolution was set to 60,000. MS2 experiments were carried out in data-dependent mode on the exact masses of protonated $[M + H]^+$ amoxicillin penicilloic acid, decarboxylated amoxicillin penicilloic acid, penicilloic acid methyl ester and hydrolyzed ceftriaxone. The system was externally calibrated to a maximum error of 2 ppm. The scan range of the MS/MS analysis was automatically obtained, while the collision energy was set to 30 % of the maximum value. The molecular formulae were assessed by Excalibur software

(Thermo Fisher Scientific, San José, CA, USA). The 16 min HPLC run was performed using 0.1 % formic acid in water(A) as weak solvent and Acetonitrile (B) as strong solvent at a flow rate of 0.300 mL/min and a C_{18} column from Thermo-Fisher Scientific, San José, CA, USA. For amoxicillin derivatives the run time was 16 min, and the gradient was the following: 0-10 min from 0 (B) to 70 % (B); 10-11 min isocratic at 70 % (B); 11-12.5 min from 70 (B) to 96 % (B); 12.5-14 min from 96 (B) to 4 % (B); 14-16 min isocratic at 4 % (B). For ceftriaxone derivative the run time was 16 min, and the gradient was the following: 0-1 min isocratic at 5 % (B); 1-2.5 min from 5 (B) to 15 % (B); 2.5-10 min isocratic at 15 % (B); 10-11.5 min from 15 (B) to 95 % (B); 11.5-12.5 min isocratic at 95 % (B); 12-14 min from 95 (B) to 5 % (B); 14-16 min isocratic at 5 % (B).

3.5.4. Catalysis details

All reactions were performed under aerobic solvent-free conditions. The corresponding amount of MOF **$Ca^{II}Zn^{II}_6$-Mecysmox** (typically 18 mg, 20 mol % Zn) and DMSO-d^6 (typically 0.8 mL) were placed in a 2 ml vial equipped with a magnetic stir bar. Then, the corresponding compound (for example, 20 mg, 0.05 mmol of amoxicillin) was added at room temperature. The mixture was sealed and magnetically stirred in a pre–heated steel block at 50 ^oC for 24 h. After that time, the reaction mixture was passed through a 25 μm filter syringe and submitted to NMR analysis.

3.5.5. Physical techniques

Elemental (C, H, S, N) and ICP-MS analyses were performed at the Microanalytical Service of the Universitat de València. FT–IR spectra were recorded on a Perkin-Elmer 882 spectrophotometer as KBr pellets. The thermogravimetric analysis was performed on crystalline samples under a dry N_2 atmosphere with a Mettler Toledo TGA/STDA 851^e thermobalance operating at a

heating rate of 10 °C min^{-1}. ^1H NMR spectra were recorded at room temperature on a Bruker 300 or 400 MHz spectrometer using deuterated DMSO as a solvent, containing TMS as an internal standard. DR-UV-vis spectra were recorded in the 190-1100 nm region at room temperature, using a spectrophotometer equipped with an integer sphere and a quartz cell of 1 mm pass length.

3.5.6. Gas adsorption

The N_2 adsorption-desorption isotherms at 77 K, were carried out on polycrystalline samples of **$Ca^{II}Zn^{II}_6$-Mecysmox** and **amoxicillin@$Ca^{II}Zn^{II}_6$-Mecysmox** with a BELSORP-mini-X instrument. Samples were first activated with methanol and then evacuated at 348 K during 19 hours under 10^{-6} Torr prior to their analysis.

3.5.7. X–ray powder diffraction measurements

Polycrystalline samples of **$Ca^{II}Zn^{II}_6$-Mecysmox** and **amoxicillin@$Ca^{II}Zn^{II}_6$-Mecysmox** were introduced into 0.5 mm borosilicate capillaries prior to being mounted and aligned on an Empyrean PANalytical powder diffractometer, using Cu Kα radiation (λ = 1.54056 Å). For each sample, five repeated measurements were collected at room temperature (2θ = 2–60°) and merged in a single diffractogram.

3.5.8. X-ray crystallographic data collection and structure refinement

Crystals of **$Ca^{II}Zn^{II}_6$-Mecysmox** and **amoxicillin@$Ca^{II}Zn^{II}_6$-Mecysmox** were selected and mounted on a MITIGEN holder in paratone oil. Diffraction data were collected on a Bruker-Nonius X8 APEX II CCD area detector diffractometer, at 100 K (**$Ca^{II}Zn^{II}_6$-Mecysmox**) and room temperature (**amoxicillin@$Ca^{II}Zn^{II}_6$-Mecysmox**), using graphite-monochromated Mo-Kα radiation (λ = 0.71073 Å). Crystals of both **$Ca^{II}Zn^{II}_6$-Mecysmox** and **amoxicillin@$Ca^{II}Zn^{II}_6$-Mecysmox**

samples displayed an outstanding stability at air and room temperature for at least eight weeks, as demonstrating by their diffraction patterns measured at 293-296 K as well, without displaying any relevant crystal decay. Bearing in mind that crystal structure of adsorbate **amoxicillin@Ca^{II}Zn$^{II}_6$-Mecysmox** has been obtained measuring on crystals which suffered a single-crystal to single-crystal (SC to SC) process, it is reasonable to expect some imperfection and high R_{int}(0.17). The data were processed through SAINT[60] reduction and SADABS[61] multi-scan absorption software. The structures were solved with the SHELXS structure solution program, using the Patterson method. The model was refined with version 2018/3 of SHELXL against F^2 on all data by full-matrix least squares.[62–64]

In **Ca^{II}Zn$^{II}_6$-Mecysmox**, all non-hydrogen atoms of the networks were refined anisotropically, except some highly dynamically disordered atoms belonging to the lattice water molecules confined in pores. A similar refinement has been performed for **amoxicillin@Ca^{II}Zn$^{II}_6$-Mecysmox** crystal structure refinement, where all non-hydrogen atoms of the networks were refined anisotropically, except some highly dynamically disordered atoms belonging to the aminoacidic residues confined in pores (dynamical fragments of the structure) and guest amoxicillin molecules. For such kind of single crystals, the lower data quality for adsorbates, embedding highly disordered guest molecules, makes the use of constraints and especially restraints essential. The use of some bond lengths restraints, applied on atoms belonging to highly dynamic moieties, is reasonably imposed and related to the expected high thermal motion, likely depending on the large pore's size of the frameworks (FLAT, DFIX, DANG,). In particular, amino acid chains in both samples have been refined with restrains on C-C and C-S bond lengths. In the refinement of **amoxicillin@Ca^{II}Zn$^{II}_6$-Mecysmox** crystal structure, some further restrains, to make the refinement more efficient, have been applied. For instance, ADP components have been restrained to be

similar to other related atoms, using EADP for group of atoms of the guest molecules expected to have essentially similar ADPs. In **$Ca^{II}Zn^{II}_6$-Mecysmox**, all the hydrogen atoms of the networks were set in calculated position and refined isotropically using the riding model. As far as for **amoxicillin@$Ca^{II}Zn^{II}_6$-Mecysmox** crystal structure's refinement is concerned, hydrogen atoms on the guest molecules were neither found nor calculated. In fact, it is often expected that guest molecules are severely disordered, as a direct consequence of their high thermal motion and exhibited statistic disorder.

In **amoxicillin@$Ca^{II}Zn^{II}_6$-Mecysmox** the occupancies of the guests in the pores, have been defined by CHSN analyses and, in the crystal structure, fixed at 0.333. We strongly believe that it is the more reliable way to accurately define loading instead of taking into account merely thermal factors, which can be affected by a lot of issues above all severe disorder.

As expected, in **amoxicillin@$Ca^{II}Zn^{II}_6$-Mecysmox** guest molecules are severely thermally and statistically disordered, it is likely related to the different degrees of freedom and diverse allowed conformations. The partial overlap between different orientations at atom sites makes them disordered. In detail, COOH missing (linked to C9H) is overlapped with equivalent of C5H, C7H and N1H (Figure 3.8).

Finally, the estimated empty volumes for **$Ca^{II}Zn^{II}_6$-Mecysmox**, without the crystallization water molecules, and **amoxicillin@$Ca^{II}Zn^{II}_6$-Mecysmox** are 1159.5 (1) and 120.0 (3) $Å^3$, values which represent *ca*. 32.8, and 3.6 %, respectively, of potential void per unit cell volume [V = 3536.0 (2) and 3530.8 (3) $Å^3$].

A summary of the crystallographic data and structure refinement for the two compounds is given in Table 3.1. The comments for the alerts A and B are

reported in the CIFs using the validation response form (vrf). CCDC deposition numbers are 2258088-2258089 for **$Ca^{II}Zn^{II}_6$-Mecysmox** and **amoxicillin@$Ca^{II}Zn^{II}_6$-Mecysmox**, respectively.

The final geometrical calculations on free voids and the graphical manipulations were carried out with PLATON[65,66] implemented in WinGX,[67] and CRYSTAL MAKER[68] programs, respectively.

3.5.9. Computational details

The amoxicillin substrate has been docked in a section of the MOF **$Ca^{II}Zn^{II}_6$-Mecysmox**, representing the minimal unit of the crystal (23.74 x 27.45 x 19.50 $Å^3$). For the molecular recognition, AutoDock Vina software[69] has been adopted and nine output structures of amoxicillin binding **$Ca^{II}Zn^{II}_6$-Mecysmox** have been generated. To investigate complete pore's conformational space, the box centroid has been set by geometric centre of the model (coodinates x,y,z = -0.346, 0.068, 0.809), selecting 40 for X,Y and 60 for Z as parameters for the grid point generation. The obtained docked conformations of amoxicillin have been analysed and the best one (lowest binding affinity, see Table 3.3) has been selected for later quantum chemical investigation. In the lowest binding mode, the substrate engages σ-hole interactions with the -SCH_3 groups of MOF scaffold, similarly to the observations arising from the crystal structure analysis (see Figure 3.29). The carbonyl of the amide bond indeed lies at 4.77 Å from one of thio-methyl moiety while the amino group is at 4.03 Å from another one (4.09 Å and 3.87 Å in the crystal structure, respectively).

The reaction mechanisms have been investigated selecting a model from the reactive portion of the **amoxicillin@$Ca^{II}Zn^{II}_6$-Mecysmox** aggregate. In detail, two Zn(II), including their complete first coordination sphere, and the β-lactam moiety of amoxicillin have been retained as depicted in Figure 3.28. In accordance

to the cluster approach scheme, a number of C atoms are kept fixed in the initial coordinates, in order to avoid artificial movement during the geometry optimizations (see atoms labelled with "*" in Figure 3.28). Two additional water molecules (**w1** and **w2**) have been explicitly included. The final model has a charge of -4 and consists of 88 atoms.

Calculations were carried out using Gaussian 16 package (version C.01),[70] selecting the B3LYP-D3[71–73] functional coupled to the 6-31G(d,p) basis set for the electronic treatment of H, C, N, O and S atoms, while LANL2DZ pseudopotential was employed for the Zn.[74] At the same level of theory, the effect of MOF surrounding was simulated *via* the implicit solvation model SMD (ε = 78.6)[75] and the frequency calculations was performed, in order to obtain the zero-point energy corrections. Finally, more accurate electronic energies were calculated choosing the LANL2DZ pseudopotential for the Zn atoms and the larger 6-311+G(2d,2p) basis set for the remaining atoms. The located transition states were accurately checked to be linked to the corresponding minima by means of intrinsic reaction coordinate (IRC) analysis.[76] The energy of obtained minima were later chosen as starting and final points (I and II see Figure 3.30, respectively) of the potential energy surface.

3.6. References

(1) Testero, S. A.; Llarrull, L. I.; Fisher, J. F.; Mobashery, S. Medicinal Chemistry of B-Lactam Antibiotics. In *Burger's Medicinal Chemistry and Drug Discovery*; Wiley, 2021; pp 1–188.

(2) Tooke, C. L.; Hinchliffe, P.; Bragginton, E. C.; Colenso, C. K.; Hirvonen, V. H. A.; Takebayashi, Y.; Spencer, J. *J. Mol. Biol.* **2019**, *431* (18), 3472–3500.

(3) Kaminskaia, N. V.; Spingler, B.; Lippard, S. J. *J. Am. Chem. Soc.* **2000**, *122* (27), 6411–6422.

(4) Tamilselvi, A.; Nethaji, M.; Mugesh, G. A *Chem. Eur. J.* **2006**, *12* (30), 7797–7806.

(5) Tamilselvi, A.; Mugesh, G. *JBIC J. Biol. Inorg. Chem.* **2008**, *13* (7), 1039–1053.

(6) Naik, A. D.; Beck, J.; Dîrtu, M. M.; Bebrone, C.; Tinant, B.; Robeyns, K.; Marchand-Brynaert, J.; Garcia, Y. Z *Inorganica Chim. Acta* **2011**, *368* (1), 21–28.

(7) Umayal, M.; Mugesh, G. *Inorganica Chim. Acta* **2011**, *372* (1), 353–361.

(8) Tamilselvi, A.; Mugesh, G. *Inorg. Chem.* **2011**, *50* (3), 749–756.

(9) Daumann, L. J.; Gahan, L. R.; Comba, P.; Schenk, G. *Inorg. Chem.* **2012**, *51* (14), 7669–7681.

(10) Wöckel, S.; Galezowska, J.; Dechert, S.; Meyer, F. *Inorg. Chem.* **2012**, *51* (4), 2486–2493.

(11) Daumann, L. J.; Schenk, G.; Gahan, L. R. *Eur. J. Inorg. Chem.* **2014**, *2014* (18), 2869–2885.

(12) Ullah, J. H.; Walsh, T. R.; Taylor, I. A.; Emery, D. C.; Verma, C. S.; Gamblin, S. J.; Spencer, J. *J. Mol. Biol.* **1998**, *284* (1), 125–136.

(13) Garau, G.; Bebrone, C.; Anne, C.; Galleni, M.; Frère, J.-M.; Dideberg, O. *J. Mol. Biol.* **2005**, *345* (4), 785–795.

(14) Galleni, M.; Lamotte-Brasseur, J.; Rossolini, G. M.; Spencer, J.; Dideberg, O.; Frère, J.-M. *Antimicrob. Agents Chemother.* **2001**, *45* (3), 660–663.

(15) Tomatis, P. E.; Rasia, R. M.; Segovia, L.; Vila, A. J. *Proc. Natl. Acad. Sci.* **2005**, *102* (39), 13761–13766.

(16) Furukawa, H.; Cordova, K. E.; O'Keeffe, M.; Yaghi, O. M. *Science* **2013**, *341* (6149), 974.

(17) Zhou, H.-C. "Joe"; Kitagawa, S. *Chem. Soc. Rev.* **2014**, *43* (16), 5415–5418.

(18) Cui, Y.; Li, B.; He, H.; Zhou, W.; Chen, B.; Qian, G. *Acc. Chem. Res.* **2016**, *49* (3), 483–493.

(19) Maurin, G.; Serre, C.; Cooper, A.; Férey, G. *Chem. Soc. Rev.* **2017**, *46* (11), 3104–3107.

(20) He, T.; Kong, X.-J.; Li, J.-R. *Acc. Chem. Res.* **2021**, *54* (15), 3083–3094.

(21) Freund, R.; Zaremba, O.; Arnauts, G.; Ameloot, R.; Skorupskii, G.; Dincă, M.; Bavykina, A.; Gascon, J.; Ejsmont, A.; Goscianska, J.; et al. *Angew. Chem. Int. Ed.* **2021**, *60* (45), 23975–24001.

(22) Bloch, W. M.; Champness, N. R.; Doonan, C. J. *Angew. Chem. Int. Ed.* **2015**, *54* (44), 12860–12867.

(23) Lin, R.-B.; Xiang, S.; Zhou, W.; Chen, B. *Chem* **2020**, *6* (2), 337–363.

(24) Xie, L. S.; Skorupskii, G.; Dincă, M. *Chem. Rev.* **2020**, *120* (16), 8536–8580.

(25) Mon, M.; Bruno, R.; Ferrando-Soria, J.; Armentano, D.; Pardo, E. *J. Mater. Chem. A* **2018**, *6* (12), 4912–4947.

(26) Yang, D.; Gates, B. C. *ACS Catal.* **2019**, *9* (3), 1779–1798.

(27) Bavykina, A.; Kolobov, N.; Khan, I. S.; Bau, J. A.; Ramirez, A.; Gascon, J. *Chem. Rev.* **2020**, *120* (16), 8468–8535.

(28) Okamoto, Y.; Ward, T. R. Supramolecular Enzyme Mimics. In *Comprehensive Supramolecular Chemistry II*; Elsevier, 2017; pp 459–510.

(29) Liang, W.; Xu, H.; Carraro, F.; Maddigan, N. K.; Li, Q.; Bell, S. G.; Huang, D. M.; Tarzia, A.; Solomon, M. B.; Amenitsch, H.; et al. *J. Am. Chem. Soc.* **2019**, *141* (6), 2348–2355.

(30) Chen, K.; Wu, C.-D. *Coord. Chem. Rev.* **2019**, *378*, 445–465.

(31) Qin, J.-S.; Yuan, S.; Lollar, C.; Pang, J.; Alsalme, A.; Zhou, H.-C. *Chem. Commun.* **2018**, *54* (34), 4231–4249.

(32) Lian, X.; Fang, Y.; Joseph, E.; Wang, Q.; Li, J.; Banerjee, S.; Lollar, C.; Wang, X.; Zhou, H.-C. *Chem. Soc. Rev.* **2017**, *46* (11), 3386–3401.

(33) Gkaniatsou, E.; Sicard, C.; Ricoux, R.; Mahy, J.-P.; Steunou, N.; Serre, C. *Mater. Horizons* **2017**, *4* (1), 55–63.

(34) Nath, I.; Chakraborty, J.; Verpoort, F. *Chem. Soc. Rev.* **2016**, *45* (15), 4127–4170.

(35) Kondo, M.; Yoshitomi, T.; Matsuzaka, H.; Kitagawa, S.; Seki, K. *Angew. Chem. Int. Ed.* **1997**, *36* (16), 1725–1727.

(36) Mon, M.; Bruno, R.; Ferrando-Soria, J.; Bartella, L.; Di Donna, L.; Talia, M.; Lappano, R.; Maggiolini, M.; Armentano, D.; Pardo, E. *Mater. Horizons* **2018**, *5* (4), 683–690.

(37) Mon, M.; Bruno, R.; Elliani, R.; Tagarelli, A.; Qu, X.; Chen, S.; Ferrando-Soria, J.; Armentano, D.; Pardo, E. *Inorg. Chem.* **2018**, *57* (21), 13895–13900.

(38) Mon, M.; Bruno, R.; Tiburcio, E.; Casteran, P.-E.; Ferrando-Soria, J.; Armentano, D.; Pardo, E. *Chem. Eur. J.* **2018**, *24*, 17712–17718.

(39) Mon, M.; Bruno, R.; Sanz-Navarro, S.; Negro, C.; Ferrando-Soria, J.; Bartella, L.; Di Donna, L.; Prejanò, M.; Marino, T.; Leyva-Pérez, A.; et al. *Nat. Commun.* **2020**, *11* (1), 3080.

(40) Wright, A. M.; Wu, Z.; Zhang, G.; Mancuso, J. L.; Comito, R. J.; Day, R. W.; Hendon, C. H.; Miller, J. T.; Dincă, M. *Chem* **2018**, *4* (12), 2894–2901.

(41) Feng, D.; Gu, Z.-Y.; Li, J.-R.; Jiang, H.-L.; Wei, Z.; Zhou, H.-C. *Angew. Chem. Int. Ed.* **2012**, *51* (41), 10307–10310.

(42) Yuan, S.; Zou, L.; Li, H.; Chen, Y.-P.; Qin, J.; Zhang, Q.; Lu, W.; Hall, M. B.; Zhou, H.-C. *Angew. Chem. Int. Ed.* **2016**, *55* (36), 10776–10780.

(43) Klein, A. R.; Sarri, E.; Kelch, S. E.; Basinski, J. J.; Vaidya, S.; Aristilde, L. *ACS Earth Sp. Chem.* **2021**, *5* (6), 1511–1524.

(44) Bahr, G.; González, L. J.; Vila, A. J. *Chem. Rev.* **2021**, *121* (13), 7957–8094.

(45) Concha, N. O.; Rasmussen, B. A.; Bush, K.; Herzberg, O. *Structure* **1996**, *4* (7), 823–836.

(46) Naas, T.; Oueslati, S.; Bonnin, R. A.; Dabos, M. L.; Zavala, A.; Dortet, L.; Retailleau, P.; Iorga, B. I. *J. Enzyme Inhib. Med. Chem.* **2017**, *32* (1), 917–919.

(47) González, J. M.; Meini, M.-R.; Tomatis, P. E.; Martín, F. J. M.; Cricco, J. A.; Vila, A. J. *Nat. Chem. Biol.* **2012**, *8* (8), 698–700.

(48) Negro, C.; Escamilla, P.; Bruno, R.; Ferrando-Soria, J.; Armentano, D.; Pardo, E. *Chem. Eur. J.* **2022**, *28* (24), e202200034.

(49) Rouquerolt, J.; Avnir, D.; Fairbridge, C. W.; Everett, D. H.; Haynes, J. H.; Pernicone, N.; Ramsay, J. D. F.; Sing, K. S. W.; Unger, K. K. *Pure Appl. Chem.* **1994**, *66* (8), 1739–1758.

(50) Gozlan, I.; Rotstein, A.; Avisar, D. *Chemosphere* **2013**, *91* (7), 985–992.

(51) Taubinger, A. A.; Fenske, D.; Podlech, J. *Tetrahedron* **2008**, *64* (37), 8659–8667.

(52) Bruno, R.; Mon, M.; Escamilla, P.; Ferrando-Soria, J.; Esposito, E.; Fuoco, A.; Monteleone, M.; Jansen, J. C.; Elliani, R.; Tagarelli, A.; et al. *Adv. Funct. Mater.* **2021**, *31* (6), 2008499.

(53) Tiburcio, E.; Greco, R.; Mon, M.; Ballesteros-Soberanas, J.; Ferrando-Soria, J.; López-Haro, M.; Hernández-Garrido, J. C.; Oliver-Meseguer, J.; Marini, C.; Boronat, M.; et al. *J. Am. Chem. Soc.* **2021**, *143* (6), 2581–2592.

(54) Takezawa, H.; Shitozawa, K.; Fujita, M. *Nat. Chem.* **2020**, *12* (6), 574–578.

(55) Wei, T.-H.; Wu, S.-H.; Huang, Y.-D.; Lo, W.-S.; Williams, B. P.; Chen, S.-Y.; Yang, H.-C.; Hsu, Y.-S.; Lin, Z.-Y.; Chen, X.-H.; et al. *Nat. Commun.* **2019**, *10* (1), 5002.

(56) Blomberg, M. R. A.; Borowski, T.; Himo, F.; Liao, R.-Z.; Siegbahn, P. E. M. *Chem. Rev.* **2014**, *114* (7), 3601–3658.

(57) Prejanò, M.; Alberto, M. E.; Russo, N.; Toscano, M.; Marino, T. *Catalysts* **2020**, *10* (9), 1038.

(58) Bansal, A.; Kar, D.; Pandey, S. D.; Matcha, A.; Kumar, N. G.; Nathan, S.; Ghosh, A. S. *Protein J.* **2017**, *36* (3), 220–227.

(59) Brun, T.; Peduzzi, J.; Canica, M. M.; Paul, G.; Névot, P.; Barthélémy, M.; Labia, R. *FEMS Microbiol. Lett.* **1994**, *120* (1–2), 111–117.

(60) SAINT, version 6.45, Bruker Analytical X-ray Systems, Madison, W. SAINT, Version 6.45, Bruker Analytical X-Ray Systems, Madison, WI. Bruker Analytical X-ray Systems: Madison, WI 2003.

(61) Sheldrick G.M. SADABS Program for Absorption Correction, version 2.10, Analytical X-ray Systems, Madison, W. SADABS Program for Absorption Correction, Version 2.10, Analytical X-Ray Systems, Madison, WI. Bruker Analytical X-ray Systems: Madison, WI 2003.

(62) Sheldrick, G. M. *Acta Crystallogr. Sect. C Struct. Chem.* **2015**, *71* (1), 3–8.

(63) Sheldrick, G. M. *Acta Crystallogr. A.* **2008**, *64* (1), 112–122.

(64) Madison, W. S.-2013/4 B. A. X. I. SHELXTL-2013/4, Bruker Analytical X-Ray Instruments, Madison, WI. Bruker Analytical X-ray Instruments: Madison, WI 2013.

(65) Spek, A. L. *Acta Crystallogr. Sect. D Biol. Crystallogr.* **2009**, *65* (2), 148–155.

(66) Spek, A. L. *Acta Crystallogr. Sect. C Struct. Chem.* **2015**, *71* (1), 9–18.

(67) Farrugia, L. J. *J. Appl. Crystallogr.* **1999**, *32* (4), 837–838.

(68) Palmer, D. CRYSTAL MAKER, Cambridge University Technical Services, C. CRYSTAL MAKER, Cambridge University Technical Services, Cambridge. Cambridge University Technical Services: Cambridge 1996.

(69) Trott, O.; Olson, A. J. AutoDock Vina: Improving the Speed and Accuracy of Docking with a New Scoring Function, Efficient Optimization, and Multithreading. *J. Comput. Chem.* **2010**, *31*, 455–461. https://doi.org/10.1002/jcc.21334.

(70) Gaussian 16, Revision C.01, Frisch, M. J.; Trucks, G. W.; Schlegel, H. B.; Scuseria, G. E.; Robb, M. A.; Cheeseman, J. R.; Scalmani, G.; Barone, V.; Petersson, G. A.; Nakatsuji, H.; Li, X.; Caricato, M.; Marenich, A. V.; Bloino, J.; Janesko, B. G.; Gomperts, R.; Mennucci, B.; Hratchian, H. P.; Ortiz, J. V.; Izmaylov, A. F.; Sonnenberg, J. L.; Williams-Young, D.; Ding, F.; Lipparini, F.; Egidi, F.; Goings, J.; Peng, B.; Petrone, A.; Henderson, T.; Ranasinghe, D.; Zakrzewski, V. G.; Gao, J.; Rega, N.; Zheng, G.; Liang, W.; Hada, M.; Ehara, M.; Toyota, K.; Fukuda, R.; Hasegawa, J.; Ishida, M.; Nakajima, T.; Honda, Y.; Kitao, O.; Nakai, H.; Vreven, T.; Throssell, K.; Montgomery, J. A., Jr.; Peralta, J. E.; Ogliaro, F.; Bearpark, M. J.; Heyd, J. J.; Brothers, E. N.; Kudin, K. N.; Staroverov, V. N.; Keith, T. A.; Kobayashi, R.; Normand, J.; Raghavachari, K.; Rendell, A. P.; Burant, J. C.; Iyengar, S. S.; Tomasi, J.; Cossi, M.; Millam, J. M.; Klene, M.; Adamo, C.; Cammi, R.; Ochterski, J. W.; Martin, R. L.; Morokuma, K.; Farkas, O.; Foresman, J. B.; Fox, D. J. Gaussian, Inc., Wallingford CT, **2016**.

(71) Grimme, S.; Antony, J.; Ehrlich, S.; Krieg, H. *J. Chem. Phys.* **2010**, *132* (15), 154104.

(72) Becke, A. D. *J. Chem. Phys.* **1993**, *98* (7), 5648–5652.

(73) Lee, C.; Yang, W.; Parr, R. G. *Phys. Rev. B* **1988**, *37* (2), 785–789.

(74) Wadt, W. R.; Hay, P. J. *J. Chem. Phys.* **1985**, *82* (1), 284–298.

(75) Marenich, A. V.; Cramer, C. J.; Truhlar, D. G. *J. Phys. Chem. B* **2009**, *113*

(18), 6378–6396.

(76) Fukui, K. *Acc. Chem. Res.* **1981**, *14* (12), 363–368.

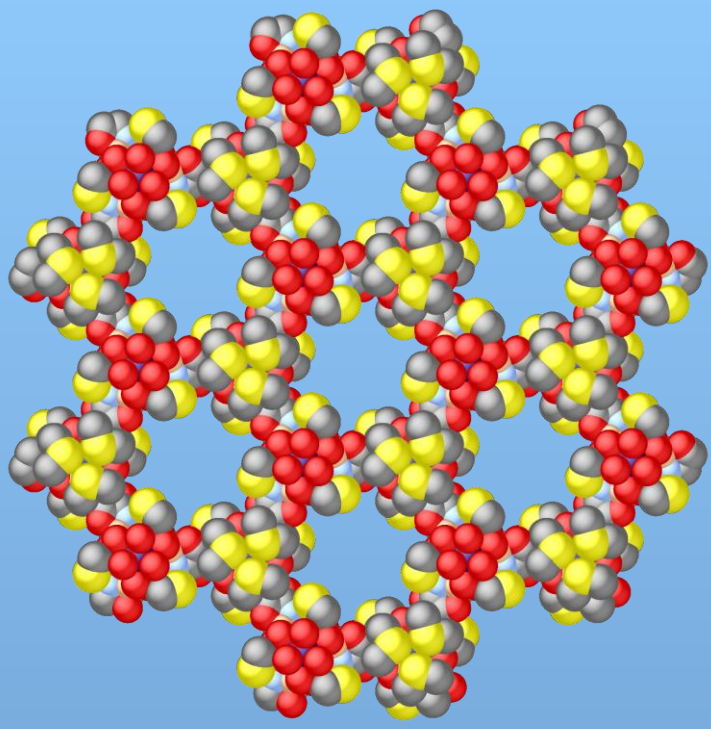

CHAPTER 4

Zinc-based metal-organic frameworks for selective cycloaddition reactions

4.1. Introduction

Metal-organic frameworks (MOFs)[1,2] have been featured among porous materials as consequence of their particular and tailorable host-guest chemistry.[3,4] This, for example, has enabled them to outperform state-of-the-art materials in different applications, such as heterogeneous catalysis, where molecular recognition interactions of guests are of paramount importance to achieve high conversion and selectivity.[5,6] This success is, in part, a direct consequence of the possibility in MOFs to precisely tune the size, shape and functionality of the MOFs pores,[7,8] which offers the opportunity to have the appropriate orientation and proximity of reactants to lead to non-default product, as well as stabilizing reaction intermediates, which otherwise could not be accessed.[9,10]

Among the wide variety of reported MOFs, Zn-based MOFs are a particularly interesting subset of MOFs because they have shown promise in water remediation,[11] biomedicine,[12,13] as batteries,[14] or in chiral drugs resolution[15] or catalysis (Figure 4.1). As many other MOFs, Zn-based MOFs possess high surface areas and can be easily tuned to have specific pore sizes and functional groups. This allows for the creation of highly selective and efficient catalysts for a wide range of chemical reactions. In addition, zinc is an abundant and inexpensive metal, which makes Zn-based MOFs very attractive for catalysis. For instance, Zn-based MOFs have been shown to be effective catalysts for a range of reactions, including oxidations[16] or cross-coupling[17] reactions. These reactions can be carried out under mild conditions and with high selectivity, making them attractive for the synthesis of complex molecules.[18]

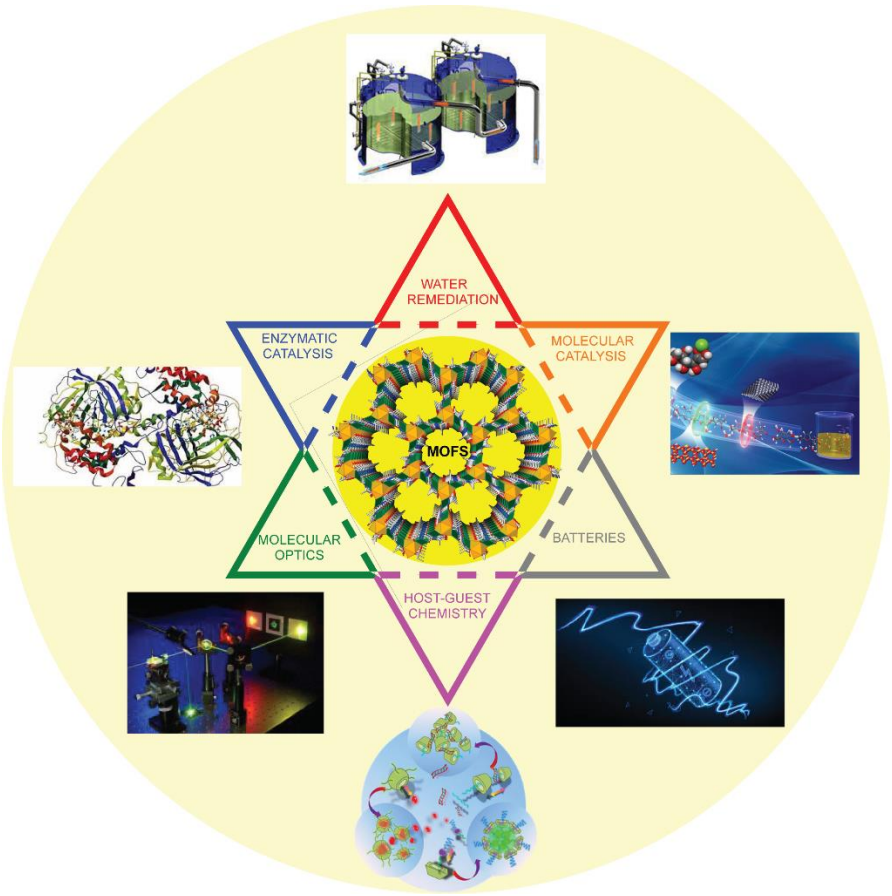

Figure 4.1. Some of the most relevant disciplines in which Zn(II)-based MOFs can situate at the cross point.

In particular, among the possible catalytic reactions that a Zn-based MOF can catalyze, the cycloaddition of ethylene oxide (EO) to CO_2 to give ethylene carbonate (EC) is a fundamental industrial reaction, since EC finds application as a general solvent in fine chemistry and electrolyte in lithium-based batteries, as well as key intermediate for the synthesis of other industrial chemicals, *i.e*. ethylene glycol (Omega Shell process).[19] The industrial synthesis employs homogeneous catalysts, despite it is recognized that solid catalysts will enable the implementation of a more practical and environmentally benign process,[20] particularly convenient when managing an extremely hazardous reactants such

as EO.[21] However, the number of studies in the open literature dealing with solid-catalyzed cycloadditions of EO to CO_2 are scarce, <30 scientific open publications according to a database searching for this specific reaction, and most of them in the last 10 years (see Figure 4.2).[22–25] This number gets more surprising when compared to the number of studies devoted to the synthesis of propylene carbonate (PC), which despite being relatively less used in industry than EC, is reported in >250 publications (one order of magnitude higher, same database searching).[26–29] Thus, more studies on the synthesis of EC with solid catalysts seem timely and necessary.

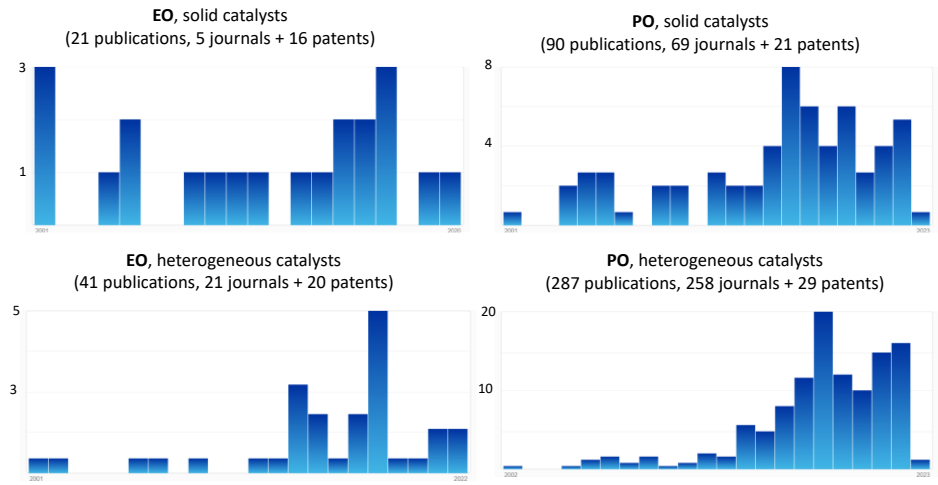

Figure 4.2. Reported studies on the cycloaddition reaction of either ethylene oxide (EO, left) or ethylene oxide (PO, right) to CO_2 to give ethylene carbonate (EC) or propylene carbonate (PO), respectively, with solid (top) or generally speaking heterogeneous catalysts (bottom). Source: Scifinder^{n,TM}, searching for the specific reaction and then truncating with the term above detailed.

4.2. Objectives

Following our previous investigations (see chapters 2 and 3), that confirmed that oxamidato-based Zn(II) MOFs are highly robust and crystalline and possess functional channels large enough to host different guest species, I was confident that these families of Zn(II) MOFs could be suitable candidates for

catalysis, also taking into account that Zn(II) cations have already shown good catalytic activity in a plethora of reactions. Thus, the main objective that I stablish for this chapter 4 is the preparation of a Zn(II)-based MOF capable to catalyze an organic reaction with potential industrial application. The specific objectives of the chapter are summarized as:

- Preparation of a $Sr^{II}Zn^{II}_6$ MOF, with ligand Mecysmox, isostructural to the $Ca^{II}Zn^{II}_6$ MOF reported in chapter 3. Preliminary experimental work has already shown that the strontium material is even more robust than the calcium analogue, which offers potential rewards in catalysis in terms of reusability. Moreover, this material will have Zn(II) cations located in the same positions as $Ca^{II}Zn^{II}_6$ MOF, which are fully accessible to reactants.

- Given the constrained space offered by the MOFs channels, and the presence of accessible Zn(II) cations, we pretend to explore its activity in the selective cycloaddition of EO to CO_2.

4.3. Results and discussion

In this chapter, we report a novel bio-friendly water-stable tridimensional (3D) MOF, derived for the amino acid *S*-methyl-*L*-cysteine, with formula $\{SrZn_6[(S,S)\text{-Mecysmox}]_3(OH)_2(H_2O)\} \cdot 9\ H_2O$ (**$Sr^{II}Zn^{II}_6$-Mecysmox**) (Mecysmox = bis[*S*-methylcysteine]oxalyl diamide), and its application as a solid catalyst for the cycloaddition reaction of EO to CO_2. The small diameter size and unique environment of the MOF pores enable the selective synthesis of EC without competitive hydrolysis[20] and polymerization,[30] even using water as a solvent. Besides, the constrained catalytic site of MOF **$Sr^{II}Zn^{II}_6$-Mecysmox** makes react propylene oxide (PO) as EO, when the former is usually ten times less reactive (see ahead for discussion).

4.3.1. General synthetic procedure

MOF **$Sr^{II}Zn^{II}_6$-Mecysmox** ($\{Sr^{II}Zn^{II}_6[(S,S)\text{-Mecysmox}]_3(OH)_2(H_2O)\} \cdot 9H_2O$) can be synthesized, in two different ways, in a similar manner to those reported for $\{Ca^{II}Zn^{II}_6[(S,S)\text{-Mecysmox}]_3(OH)_2(H_2O)\} \cdot 12H_2O$ in the previous chapter. Thus, **$Sr^{II}Zn^{II}_6$-Mecysmox** can be synthesized, in a multigram scale, by direct precipitation in water (see experimental section (section 4.5.2) for further details). The resulting polycrystalline powdered will be used to carry out catalytic experiments. On the other hand, Compound **$Sr^{II}Zn^{II}_6$-Mecysmox** was also synthesized as colorless hexagonal prisms with a slow diffusion technique (section 4.5.2). All syntheses are described in detail in the experimental section.

4.3.2. Characterization of the MOF

4.3.2.1. Crystal structure

Compound **$Sr^{II}Zn^{II}_6$-Mecysmox** was synthesized as colorless hexagonal prisms with a slow diffusion technique (see experimental section (4.5.2)). The crystal structure of **$Sr^{II}Zn^{II}_6$-Mecysmox** could be determined by single-crystal X-ray diffraction (SCXRD) (see structural section, section 4.5.3). **$Sr^{II}Zn^{II}_6$-Mecysmox** crystallizes in the chiral $P6_3$ space group (Table 4.1), presenting a honey-comb chiral 3D strontium(II)-zinc(II) network (Figure 4.3). **$Sr^{II}Zn^{II}_6$-Mecysmox** exhibits a uninodal **acs** chiral net built by strontium(II) vertexes and trans oxamidato-bridged zinc(II) units, $\{Zn^{II}_2[(S,S)\text{-Mecysmox}]\}$ (Figures 4.3d and 4.4, experimental section, section 4.5.3), which act as linkers between the Sr(II) ions through the carboxylate groups. The hexagonal channels of *ca*. 0.6 nm (Figure 4.5) are decorated with the functional flexible dimethyl thioether residues of the methylcysteine amino acid (Figure 4.3b). In the 3D porous structure of **$Sr^{II}Zn^{II}_6$-Mecysmox**, the two crystallographically independent methylcysteine chains, show a different conformation. One of them shows a distended conformation

pointing towards the center of the pores whereas the other one is pretty bent, with the terminal methyl groups pointing towards the center of the smaller interstitial voids developing along *a* axis (Figures 4.3 and Figure 4.6).

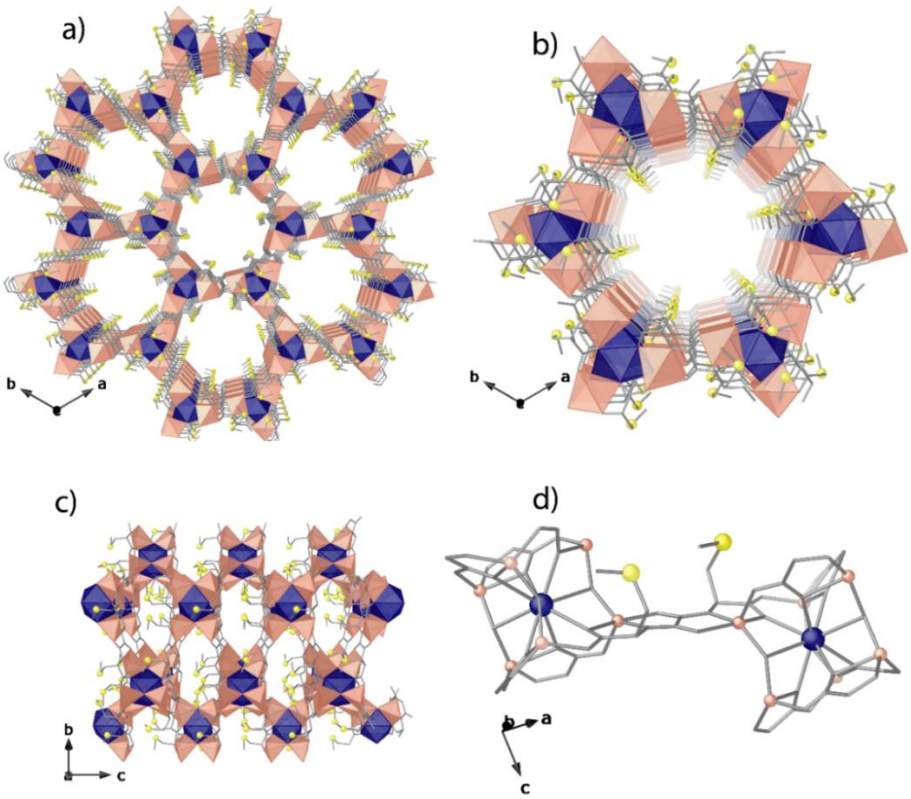

Figure 4.3. Perspective views of the porous networks of **$Sr^{II}Zn^{II}_6$-Mecysmox** (a) and a single channel along the *c* (a-b) and *a* (c) axes. Perspective view of the {Zn^{II}_2[(S,S)-Mecysmox]} dimer connecting Sr(II) cations. Colour code: Zn, Sr and S atoms are represented by salmon polyhedra, blue polyhedra, and yellow spheres, respectively, whereas the ligands (except sulfur) are depicted as gray sticks.

The confined space of the MOF allows two possible conformations for the distended dimethyl thioether residues of the methylcysteine amino acid, which show statistical disorder, and thus refined on two different positions/orientations. This is perfectly in line with the outstanding flexibility of the amino acidic moieties entirely confined in pores. The network connection involving the trans-oxamidato-bridged dizinc(II) units, {Zn^{II}_2[(S,S)-Mecysmox]}

(Figure 4.3a), and Sr(II) cations through the carboxylate groups (Figure 4.3) is further assisted by water/hydroxide groups (Figure 4.3a).

Table 4.1. Summary of crystallographic data for **$Sr^{II}Zn^{II}_6$-Mecysmox**.

Compound	**$Sr^{II}Zn^{II}_6$-Mecysmox**
Formula	$C_{30}H_{58}SrCu_6N_6O_{30}S$
M (g mol^{-1})	1655.02
λ (Å)	0.71073
Crystal system	hexagonal
Space group	$P6_3$
a (Å)	18.5594(15)
c (Å)	11.7771(13)
V (Å^3)	3513.1(7)
Z	2
ρ_{calc} (g cm^{-3})	1.565
μ (mm^{-1})	3.019
T (K)	90
θ range for data collection (°)	2.534 to 26.415
Completeness to θ = 25.0	100%
Measured reflections	50501
Unique reflections (Rint)	4811 (0.0880)
Observed reflections [$I > 2\sigma(I)$]	2941
Goof	1.096
Absolute structure parameter (Flack)	0.07(2)
R^a [$I > 2\sigma(I)$] (all data)	0.0638 (0.1244)
wR^b [$I > 2\sigma(I)$] (all data)	0.1644 (0.1951)

^{a} $R = \sum(|F_o| - |F_c|)/\sum|F_o|$. ^{b} $wR = [\sum w(|F_o| - |F_c|)^2/\sum w|F_o|^2]^{1/2}$.

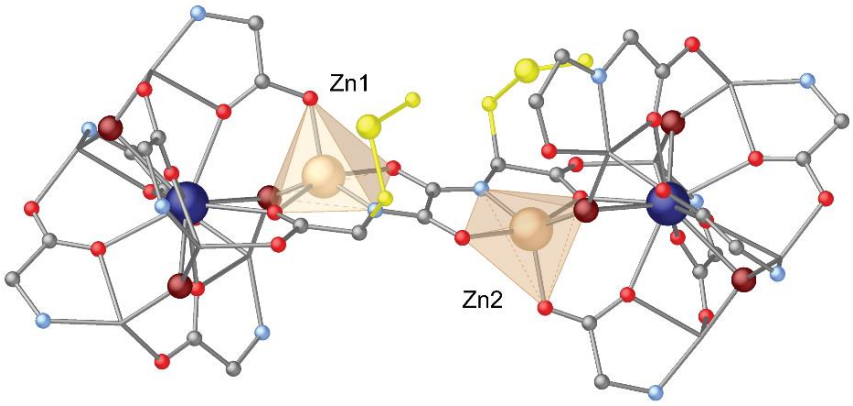

Figure 4.4. View of the dianionic bis(hydroxo)dizinc(II) building blocks in **$Sr^{II}Zn^{II}_6$-Mecysmox**, highlighting with polyhedra the pentacoordinated Zn(II) ions. Zn(II), Sr(II) ions and water molecules/hydroxide ions are displayed as salmon polyhedral, dark blue and big red spheres, respectively. The carbon, oxygen, nitrogen and sulphur from the ligand are depicted as gray, red, sky-blue and yellow small spheres.

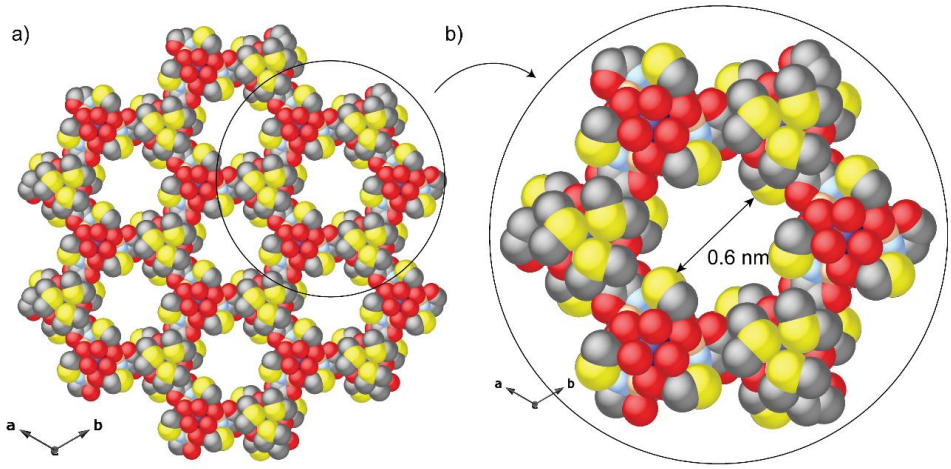

Figure 4.5. a) View of 3D network of **$Sr^{II}Zn^{II}_6$-Mecysmox** and b) details of one single pore along *c* crystallographic axis showing the porous structure in space filling model (van deer Waals radii). Zn(II) and Sr(II) metal ions are represented by salmon and blue spheres, respectively, whereas the oxygen, carbon, nitrogen and sulphur atoms from the ligands are depicted as red, grey, light blue and yellow spheres.

In **$Sr^{II}Zn^{II}_6$-Mecysmox**, the Zn(II) coordination environment is reminiscent of certain catalytic active Zn-based compounds. The two crystallographically distinct Zn(II) metal ions share a bridging water/hydroxide and reside in an

environment describing a trigonal bipyramidal geometry being coordinated by a nitrogen and three oxygen atoms belonging to the Mecysmox ligand, and a water/hydroxide bridging group (in a 1:2 statistic distribution). The Zn-OH bond length is of 1.97(2) and 1.95(2) Å for Zn1 and Zn2, respectively, and represent the shortest distance of the environment. The Zn-$N_{oxamate}$ [1.96(2) and 2.00(2) Å for Zn1 and Zn2, respectively] and the Zn-$O_{oxamate}$ bond lengths [range 1.99(2)-2-21(2) and 2.05(2)-2.25(2) Å for Zn1 and Zn2, respectively] are in agreement with those found in the literature.[31] The Zn–Zn distance across the hydroxide bridge is 3.71(1) Å.

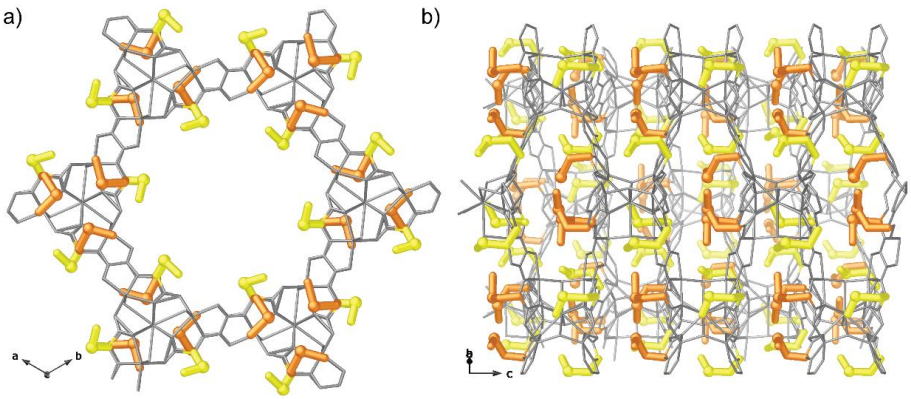

Figure 4.6. Perspective view of one single channel of **$Sr^{II}Zn^{II}_6$-Mecysmox** along the *c* (a) and *a* (b) axes. Zn, Sr and organic ligands are represented as thin grey sticks for the sake of clarity and to emphasise the amino acid residues. In turn, the more distended and more bent -CH_2SCH_3 chains (amino acid residues) are represented as thick yellow and orange sticks, respectively.

4.3.2.2. Chemical analyses

In addition, the chemical nature of **$Sr^{II}Zn^{II}_6$-Mecysmox** was also determined using different characterization techniques. At this respect, the atom composition was further established by elemental (C, H, S, N) and ICP-MS analyses (see the final chemical formulas in the experimental section, section 4.5.2).

4.3.2.3. Powder X-ray diffraction

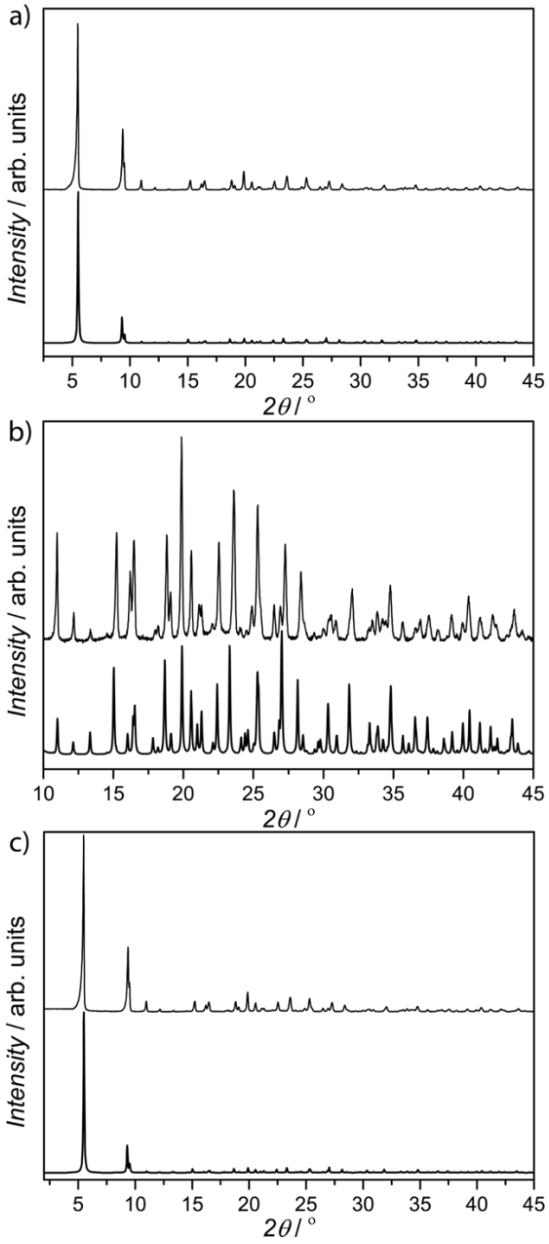

Figure 4.7. (a) Calculated (bold lines) and experimental (solid lines) PXRD pattern profiles of **$Sr^{II}Zn^{II}_6$-Mecysmox** in the 2θ range 2.0–45.0° at room temperature, and enlarged image in the range 10.0–45.0° (b). (c) Calculated (bold lines) and experimental (solid lines) PXRD pattern profile of **$Sr^{II}Zn^{II}_6$-Mecysmox** after five uses in the catalytic cycloaddition reaction of ethylene oxide (EO **1**), in the range 2.0–45.0°.

Powder X-ray diffraction (PXRD) allowed to confirm the homogeneity and purity of the bulk sample, by comparison with the theoretical pattern diffraction extracted from the solved crystal structure (Figure 4.7).

4.3.2.4. Thermogravimetric analyses

The solvent content (given in the chemical formula) was further validated by thermogravimetric analysis (TGA) (Figure 4.8), where it is observed a mass loss of *ca*. 90% that corresponds to 9 H_2O molecules.

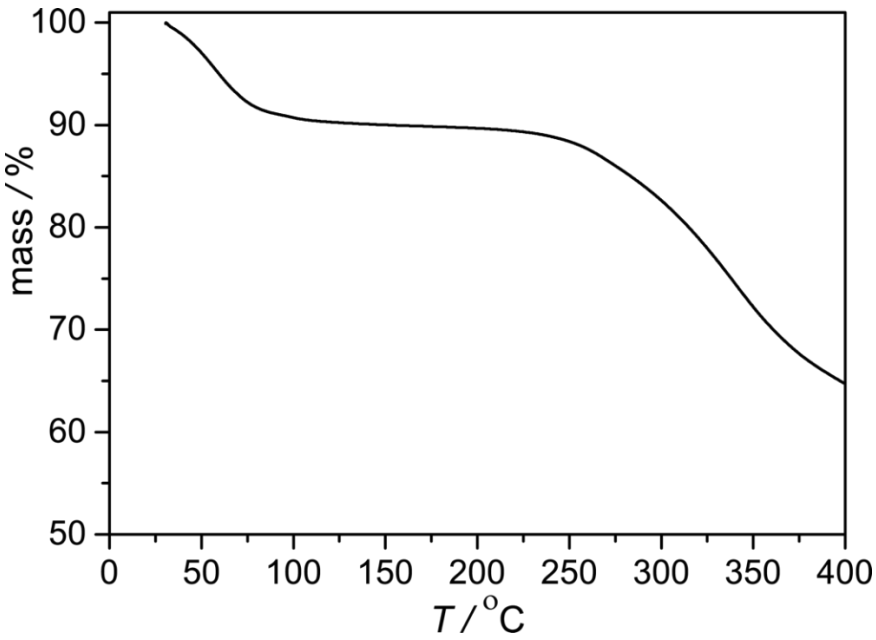

Figure 4.8. Thermo-Gravimetric Analyses (TGA) of **$Sr^{II}Zn^{II}_6$-Mecysmox** under dry N_2 atmosphere.

4.3.2.5. Gas adsorption measurements

The N_2 adsorption isotherms, at 77K, were measured for MOF 1 before and after catalysis (see section 4.3.3). They reveal a permanent microporosity for **$Sr^{II}Zn^{II}_6$-Mecysmox** in both situations (Figure 4.9). Both isotherms show a type I behavior with a moderately large uptake at low pressures. The Brunauer-

Emmett-Teller (BET)[32] surface areas calculated were 643.7 and 579.4 m^2/g,[33] before and after catalysis, respectively.

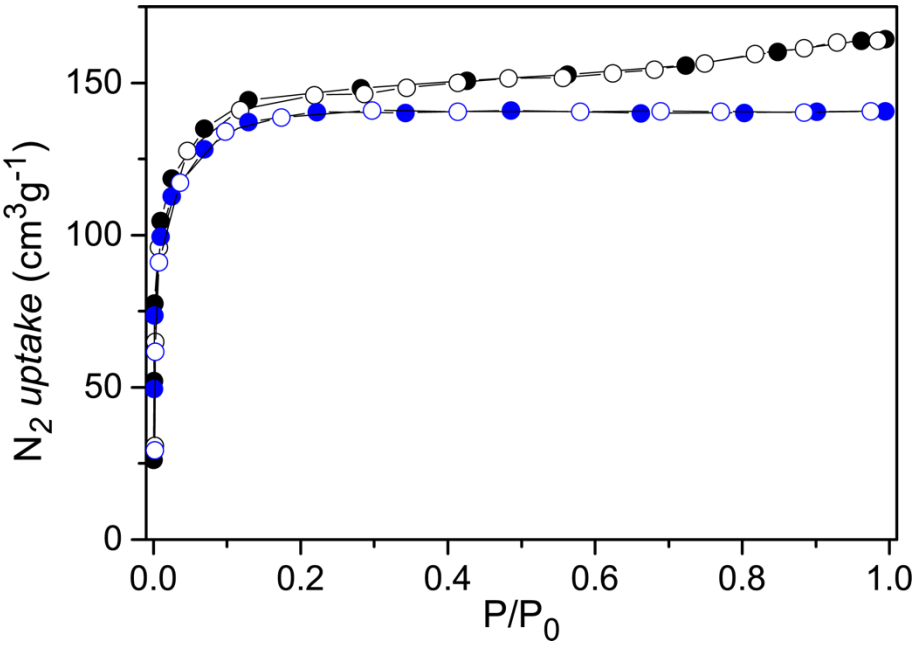

Figure 4.9. N_2 (77 K) adsorption isotherm for the activated compounds **$Sr^{II}Zn^{II}_6$-Mecysmox** before (black) and after catalysis (blue). Filled and empty symbols indicate the adsorption and desorption isotherms, respectively. The samples were activated at 348 K under reduced pressure for 19 h prior to carry out the sorption measurements.

4.3.3. Catalytic experiments

The novel solid material **$Sr^{II}Zn^{II}_6$-Mecysmox** was tested as a catalyst (6 mol %) for the cycloaddition reaction of EO (**1**) with CO_2 at 120 °C for 4 h, using tetraoctylammonium bromide (TOAB, 2 mol %) as a catalytic source of bromide anions under a CO_2 pressure of 25 bars. These reaction conditions are typical for $ZnBr_2$ and ionic liquids.[34,35] However, we introduce here the use of less expensive and more soluble TOAB. The reaction was analyzed by gas chromatography (GC) after cooling and venting out the reactor, and diluting with THF containing *n*-decane as an external standard. As it can be seen in Table 4.2, the desired product

EC (**2**) was obtained in 95% yield with complete selectivity under the indicated catalytic reaction conditions (entry 1).

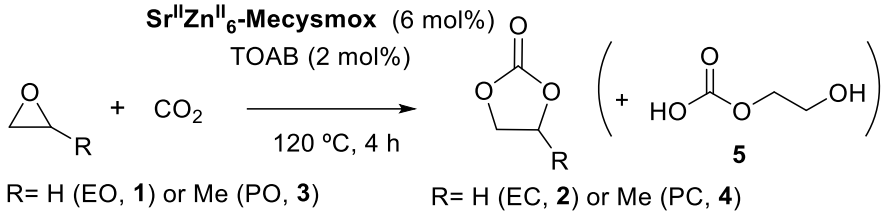

Table 4.2. Catalytic results for the cycloaddition reaction of ethylene oxide (EO **1**) with CO_2 within MOF **Sr^{II}Zn$^{II}_6$-Mecysmox**. Products are identified by GC-MS and NMR. TOAB: tetraoctylammonium bromide (the reaction does not proceed without TOAB). Selectivity is 100% to the indicated products, other by-products were not detected.[a] 3 equivalents of co-reactant to EO **1**.[b] Between brackets, the result for 1 mol % of TOAB, a similar result was obtained with *N,N´-n*-butylmethylimidazolium bromide (bmimBr).[c] 50 mol % of each reagent. [d] 25 bars of N_2. [e] Between brackets, the result with 30 equivalents of water. [f] **6** is the corresponding thioketal (see Figure 4.13). [g] 1M solution, product **5** was not detected without CO_2 pressure.

Entry	Reactant[a]	Solvent (1.6M)	CO_2 (atm)	Product (yield, %)
1	**1**	THF	25	**2** (95) [68][b]
2	**3**			**4** (94)
3	**1 + 3**			**2** (50), **4** (45)[c]
4	**1**		30	**2** (94), **5** (6)
5			5	**2** (83)[d]
6	**1** / H_2O	THF-d^4	25	**2** (66), **5** (34) **2** [56], **5** [44][e]
7	**1** / MeOH	THF		**2** (91), **5** (5)
8	**1** / NaOH			**2** (68)
9	**1** / SMe_2			**2** (42)
10	**1** / HSEt			**2** (18), **6** (46)[f]
11	**2**			**5** (20)[g]

The amount of TOAB could be reduced to the half but the yield of **2** significantly decreased (68%), and a much lower result was obtained with a typical ionic liquid as a bromide source (*i.e*. *N,N´-n*-butylmethylimidazolium bromide, bmimBr, 47% with 4 mol%), which showcases the use of TOAB as a new source of anion in this reaction.

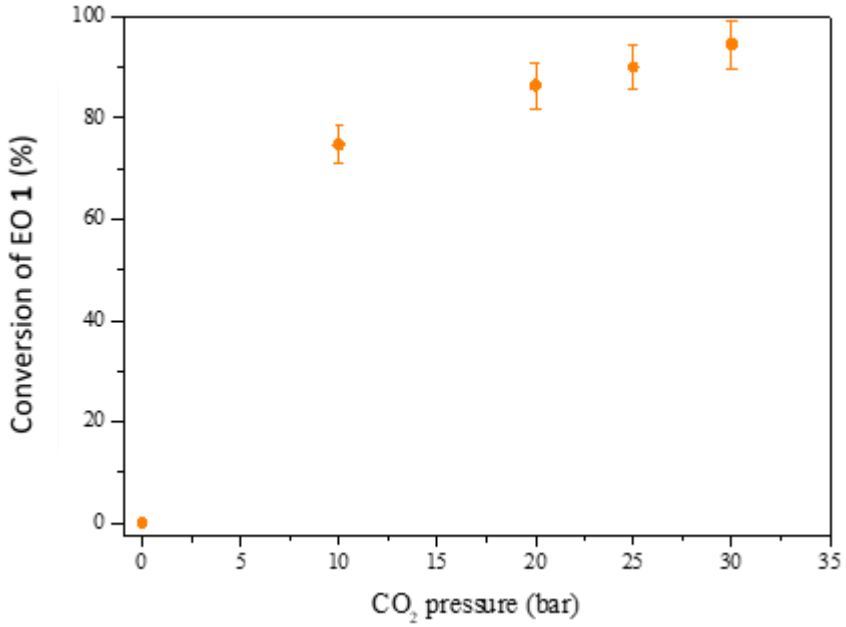

Figure 4.10. Results for the cycloaddition reaction of ethylene oxide (EO **1**) dissolved in THF (1.6M), to give ethylene carbonate (EC **2**) with catalytic amounts of MOF **$Sr^{II}Zn^{II}_6$-Mecysmox** (6 mol%) and TOAB (2 mol%) under increasing CO_2 pressures at 120 ºC reaction temperature. Selectivity is 100%. Error bars account for a 5% uncertainty.

The kinetic radii of EO **1** and EC **2** are 0.21 and 0.24 nm, respectively, calculated by molecular mechanics (MM2) after energy minimization in the vacuum, thus both molecules can diffuse across the MOF **$Sr^{II}Zn^{II}_6$-Mecysmox** pores to reach the catalytic Zn(II) sites, together with CO_2 and Br^- (this MOF family accepts anions within the pores).[36,37] Following this rationale, the kinetic radii of PO (**3**) and PC (**4**) were also calculated, to show 0.32 and 0.38 nm respectively (MM2 calculations), thus with the possibility of diffusion across the MOF´s

channels. Indeed, the reaction of **3** to **4** proceeds under the same reaction conditions with similar high yield (94%, entry 2). When both reactants **1** and **3** were co-feed in the reaction (50 mol% mixture), both products **2** and **4** were nearly quantitatively formed in equimolecular amounts (entry 3). Taken in account that PO **3** is usually less reactive than EO **1** by steric reasons,[20] the results here suggest that the constrained environment of the catalytic MOF site enables the good activation of **3** towards CO_2 cycloaddition.

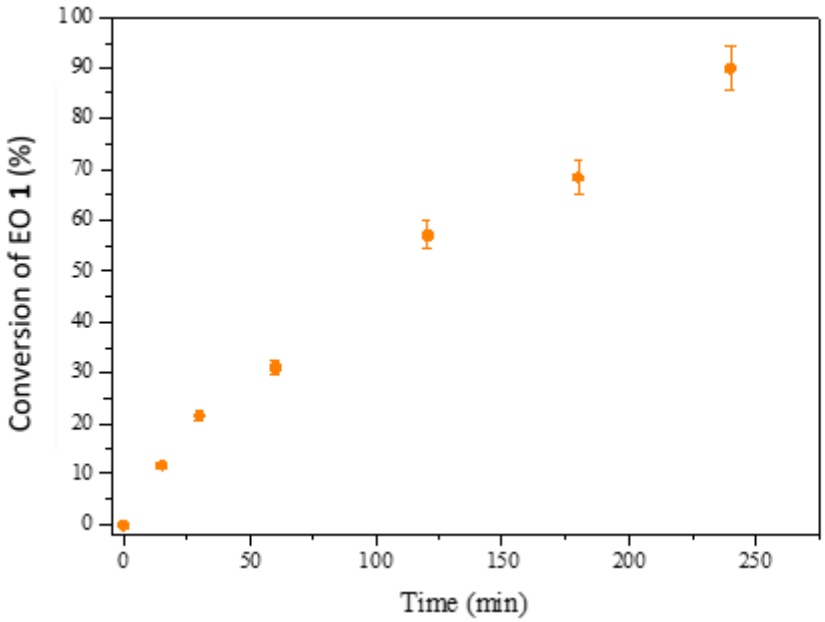

Figure 4.11. Kinetic plot for the cycloaddition reaction of ethylene oxide (EO **1**) dissolved in THF (1.6M), to give ethylene carbonate (EC **2**) with catalytic amounts of MOF **$Sr^{II}Zn^{II}_6$-Mecysmox** (6 mol%) and TOAB (2 mol%) under 25 bars of CO_2 at 120 ºC reaction temperature. Selectivity is 100%. Error bars account for a 5% uncertainty.

The CO_2 pressure finds a plateau at *ca*. 30 bars (94 %, entry 4; see also Figure 4.10). However, the use of just 5 bars of CO_2 together with 25 bars of N_2 yields a reasonable 83 % of EC **2** (entry 5). Notice here that, under this pressure, the reaction without MOF **$Sr^{II}Zn^{II}_6$-Mecysmox** proceeds in just 32 %. Kinetic studies show that high yields of EC **2** are still obtained after just 4 h reaction time

at 120 °C (Figure 4.11) and that the reaction temperature can be decreased down to 50 °C with >80 % yields of **2**, at prolonged reaction times (Figure 4.12, top). Overall, these results show that the cycloaddition reaction of EO **1** with CO_2 catalyzed by the Zn(II) MOF **$Sr^{II}Zn^{II}_6$-Mecysmox** can be performed in high yields and complete selectivity to EC **2** within a wide range of conditions, including with and without solvent, CO_2 pressures between 5-30 bars and reaction temperatures between 50-120 °C. These results should also be applicable to PO **3** and PC **4**. Remarkably, the activation energy of the MOF **$Sr^{II}Zn^{II}_6$-Mecysmox**-catalyzed reaction, calculated from the corresponding Arrhenius plot, is 8.4(7) Kcal·mol^{-1} (Figure 4.12, bottom) within the range of many homogeneous catalysts[38,39] and much lower than the best solid catalysts reported,[40] as far as we know.

The desired product EC **2** is very stable under any reaction condition employed and only partially evolves to a secondary product (entry 6), which characterization by GC coupled to mass spectrometry (GC-MS) and ^{1}H, ^{13}C and distortionless enhancement by polarization transfer (DEPT) NMR, employing THF-d^4 as the reaction solvent without isolation, suggests that could be the rarely detected compound **5**, the postulated intermediate in the hydrolysis of EC **2** to ethylene glycol. It can be seen that up to a 44 % yield of **5** can be detected when using up to 30 equivalents of H_2O respect to EO **1**, without any trace of ethylene glycol or polymerized products in the reaction medium. The amount of intermediate **5** increases with the amount of water present in the reaction, from the residual water content in the MOF (see MOF formula above and entries 3-4 in Table 4.2) to 30 equivalents (entry 6). Conversely, different competing nucleophiles such as MeOH (entry 7), NaOH (entry 8) and MeSMe (entry 9) inhibit its formation. The use of EtSH as a nucleophile lead to the formation of the corresponding thioketal **6** (entry 10), also characterized by GC-MS and NMR, which is formed though a similar reaction pathway than **5** (Figure 4.13).

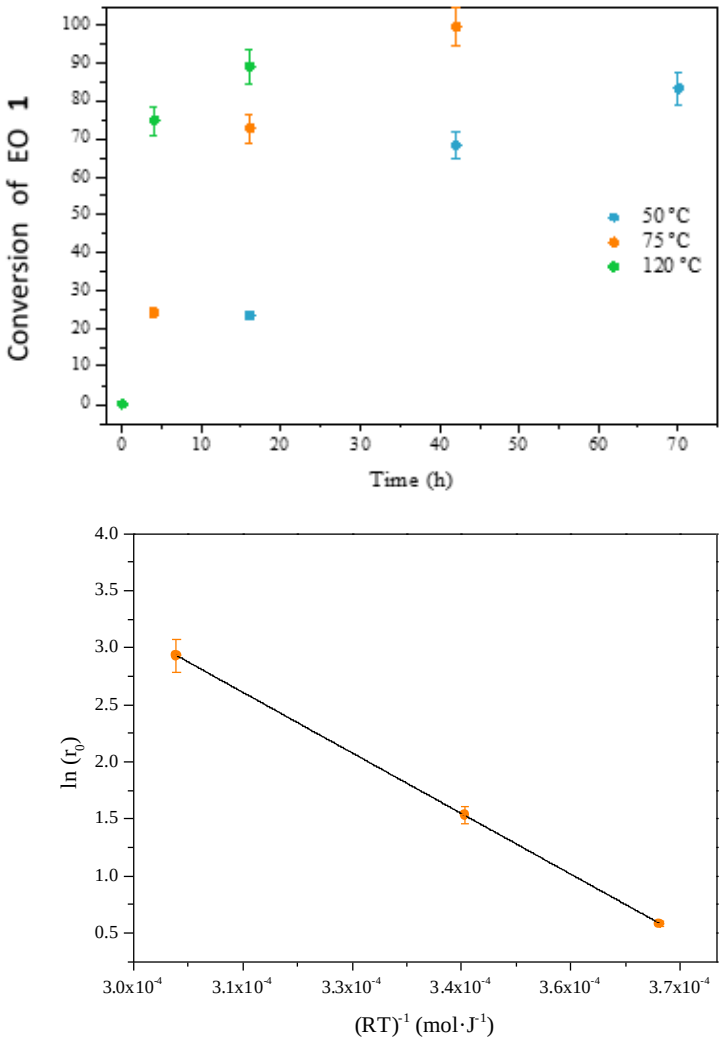

Figure 4.12. Top: Kinetic plots for the cycloaddition reaction of ethylene oxide (EO **1**) dissolved in THF (3.3M), to give ethylene carbonate (EC **2**) with catalytic amounts of MOF **$Sr^{II}Zn^{II}_6$-Mecysmox** (6 mol%) and TOAB (2 mol%) under 25 atm of CO_2 and different reaction temperatures. Selectivity is 100%. Bottom: The corresponding Arrhenius plot to calculate the activation energy of the reaction: $\ln(r_0) = 13.77 - 35434.64 \cdot \frac{1}{RT}$; E_a= 8, 47 Kcal/mol; R^2=0.99992. Error bars account for a 5% uncertainty.

EC **2** could also be used as a reactant to give a 20 % of **5**, with MOF **$Sr^{II}Zn^{II}_6$-Mecysmox** as the catalyst under 25 bars of CO_2 (entry 11), otherwise **5** is not formed. These results, together, strongly suggest that only the particular reactive

environment provided by the water-tolerant Zn(II) MOF **$Sr^{II}Zn^{II}_6$-Mecysmox**,[41] not only stabilize product EC **2** but also activate water molecules,[42,43] and under a pressurized CO_2 atmosphere, enables the formation and detection of product **5** and the complete inhibition of ethylene glycol formation.

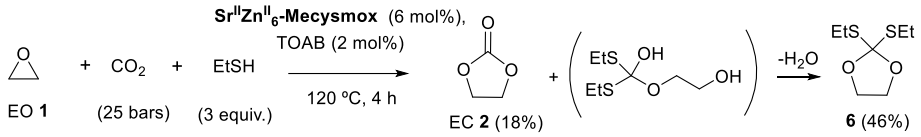

Figure 4.13. Cycloaddition reaction of ethylene oxide (EO **1**) dissolved in THF (3.3M) in the presence of EtSH (3 equivalents), to give ethylene carbonate (EC **2**) and thioketal **6**, with catalytic amounts of MOF **$Sr^{II}Zn^{II}_6$-Mecysmox** (6 mol%) and TOAB (2 mol%) under 25 atm of CO_2 at 120 ºC for 4 h.

A hot filtration test for MOF **$Sr^{II}Zn^{II}_6$-Mecysmox** shows that the catalytically active species are not leached out to the solution under the reaction conditions employed (Figure 4.14). Indeed, the solid catalyst could be reused to give a similar high yield of EC **3** (80 %, Figure 4.15), although a significant loss of efficiency was found in the third use (57 %). Nevertheless, subsequent reuses kept a stable yield of product EC **3**, *ca*. 50 %. Analysis of the reused MOF **$Sr^{II}Zn^{II}_6$-Mecysmox** by PXRD does not show any erosion of the MOF structure, thus the Zn(II) sites must still be active (Figure 4.7c). However, a N_2 adsorption isotherm of the reused solid shows a sizeable decrease in porosity, probably due to a strong adsorption of products (Figure 4.9). Fourier-transformed infrared spectroscopy (FT-IR) measurements of the used solid catalyst confirm the presence of adsorbed organic products in the MOF (Figure 4.16). These results, together, indicate that the loss of catalytic efficiency through the uses comes from a hindered diffusion though the pores in the spent catalysts, which was reasonably expected for a microporous solid with such as an ultrasmall pore.

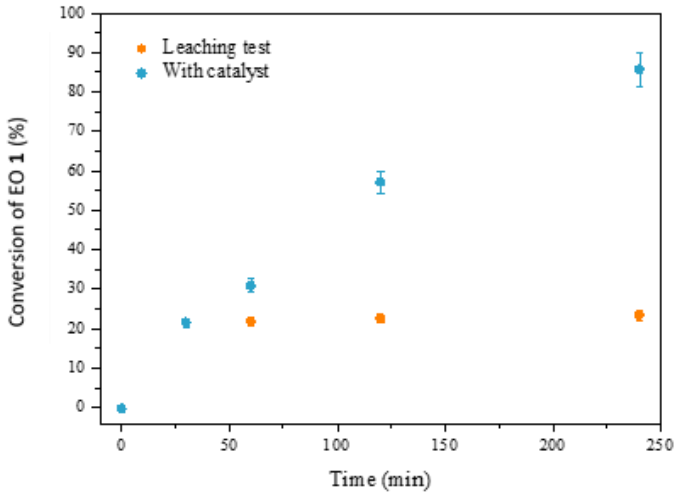

Figure 4.14. Hot filtration test for the cycloaddition reaction of ethylene oxide (EO **1**) dissolved in THF (3.3M) to give ethylene carbonate (EC **2**), with catalytic amounts of MOF **$Sr^{II}Zn^{II}_6$-Mecysmox** (6 mol%) and TOAB (2 mol%) under 25 atm of CO_2 at 120 ºC. Error bars account for a 5% uncertainty.

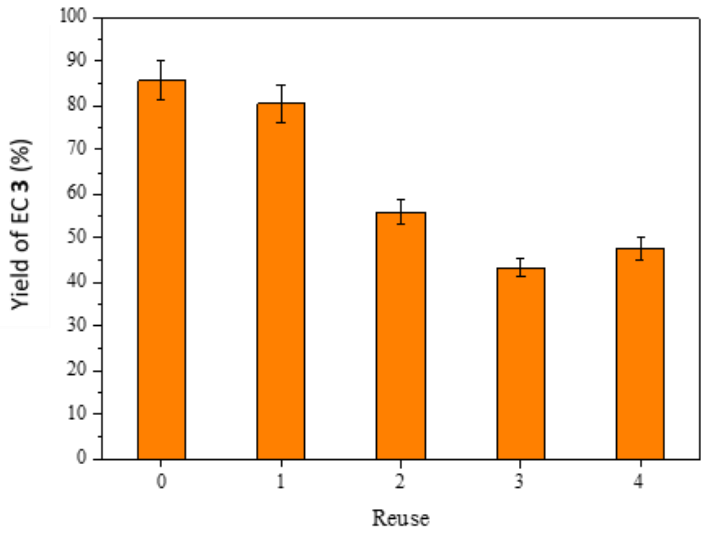

Figure 4.15. Reuses of MOF **$Sr^{II}Zn^{II}_6$-Mecysmox** (6 mol%) as a catalyst for the cycloaddition reaction of ethylene oxide (EO, **1**) dissolved in THF (1.6M) to give ethylene carbonate (EC, **2**), with TOAB (2 mol%) under 25 atm of CO_2 at 120 ºC for 4 h. Error bars account for a 5% uncertainty.

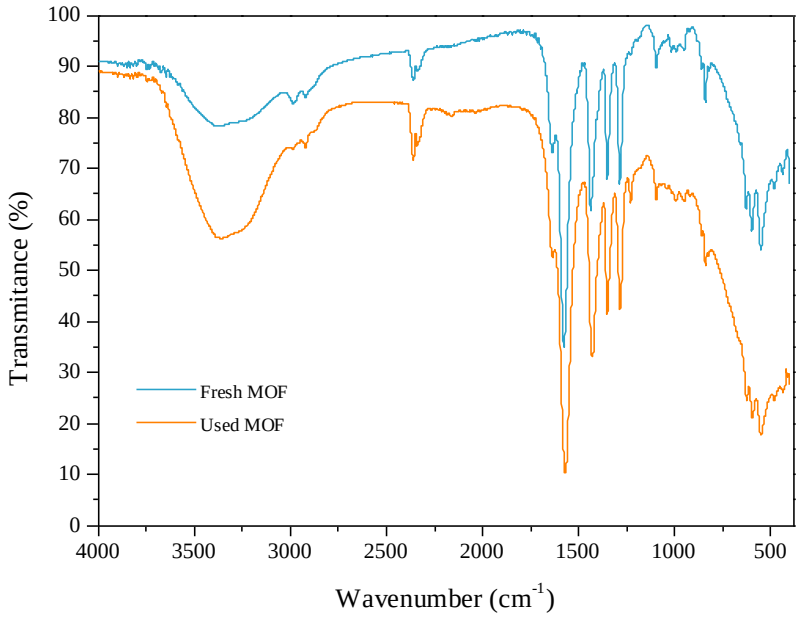

Figure 4.16. Fourier-transformed infrared (FT-IR) spectra of MOF **$Sr^{II}Zn^{II}_6$-Mecysmox** fresh (top) and after one use (bottom).

4.4. Conclusions

Overall, we have shown that the well-defined MOF **$Sr^{II}Zn^{II}_6$-Mecysmox**, characterized with atomic precision by SCXRD and possessing an ultrasmall pore size of *ca*. 0.3 nm, catalyses the cycloaddition reaction of ethylene oxide (EO **1**) or propylene oxide (PO **3**) with CO_2 to give EC **2** and PC **4**, respectively, in high yields (up to 95 %) and selectivity (up to 100 %). If water is added to the reaction, even in high excess (30 equivalents), ethylene glycol is not detected but just, tentatively, the elusive hydrolysis intermediate **5**. These results bring Zn(II)-based MOF **$Sr^{II}Zn^{II}_6$-Mecysmox** as a new solid catalyst for the selective synthesis of the industrially relevant products EC **2** and PC **4**,[44] providing an appealing alternative to the current heterogeneous catalysts based on metal-free solids[24,25,45–47] ionic liquid-microporous solid composites,[48–51] and other MOFs,[26,41,44,52–54] among other catalysts.[55,56]

4.5. Experimental section

4.5.1. General considerations

Reagents were obtained from commercial sources and used without further purification unless otherwise indicated. Anhydrous solvents were obtained from a resin-exchanger apparatus. Reactions were performed in conventional round-bottomed flasks or sealed vials equipped with a magnetic stirrer. All the products were characterized by gas chromatography-mass spectrometry (GC-MS), proton (^{1}H), carbon (^{13}C) and distortionless enhancement by polarization transfer (DEPT) nuclear magnetic resonance (NMR) spectroscopy. Gas chromatographic analyses were performed in an instrument equipped with a 25 m capillary column of 1 % phenylmethylsilicone using *n*-dodecane as an external standard. GC/MS analyses were performed on a spectrometer equipped with the same column as the GC and operated under the same conditions. ^{1}H-, ^{13}C and DEPT were recorded in a 300 MHz (or 400 MHz when available) instrument using CD_3CN as solvent unless otherwise indicated, containing TMS as internal standard. Infrared (IR) spectra of the compounds were recorded with a spectrophotometer by impregnating the windows with a dichloromethane solution of the compound and allowing to evaporate before analysis. H_2Me_2-(*S*,*S*)-Mecysmox was prepared following a reported procedure.[57]

4.5.2. Preparation of the MOF

Preparation of compound $\{Sr^{II}Zn^{II}_6[(S,S)\text{-Mecysmox}]_3(OH)_2(H_2O)\}\cdot 9H_2O$ (**$Sr^{II}Zn^{II}_6$-Mecysmox**): H_2Me_2-(*S*,*S*)-Mecysmox (4.22 g, 12.0 mmol) was suspended in 80 mL of water and treated with a 25% methanolic solution of Me_4NOH (14.5 mL, 50.0 mmol) until complete dissolution. Then, another aqueous solution (40 mL) containing $Sr(NO_3)_2$ (0.85 g, 4.0 mmol) and $Zn(NO_3)\cdot 6H_2O$ (6.98 g, 24.0 mmol) was added dropwise under stirring.

After further stirring for 10 h, at room temperature, a white polycrystalline powder was obtained and collected *via* filtration and dried with methanol. Yield: 4.83 g, 73%; Anal.: calcd for $C_{30}H_{58}N_6O_{30}S_6SrZn_6$ (1655.1): C, 21.77; H, 3.53; S, 11.62; N, 5.08%. Found: C, 21.71; H, 3.50; S, 11.65; N, 5.07%. IR (KBr): ν = 1602 cm^{-1} (C=O). Well-shaped hexagonal prisms of 1 suitable for X-ray structural analysis could be obtained by slow diffusion, in an H-shaped tube, of H_2O/DMF (1:1) solutions containing stoichiometric amounts of H_2Me_2-(*S*,*S*)-Mecysmox (0.021 g, 0.06 mmol) and Me_4NOH (0.72 mL, 2.5 mmol) in one arm and $Sr(NO_3)_2$ (0.042 g, 0.2 mmol) and $Zn(NO_3) \cdot 6H_2O$ (0.035 g, 0.12 mmol) in the other. They were isolated by filtration on paper and air-dried.

4.5.3. Single crystal X-ray diffraction studies

Crystal of **$Sr^{II}Zn^{II}_6$-Mecysmox** with 0.18 x 0.18 x 0.14 mm as dimensions was selected and mounted on a MiTeGen MicroMount in Paratone oil and very quickly placed on a liquid nitrogen stream cooled at 90 K, to avoid the possible degradation upon dehydration or exposure to air. Diffraction data were collected on a Bruker-Nonius X8APEXII CCD area detector diffractometer using graphite-monochromated Mo-K_α radiation (λ = 0.71073 Å). The data were processed through SAINT[58] reduction and SADABS[59] multi-scan absorption software. The structure was solved with the SHELXS structure solution program, using the Patterson method. The model was refined with version 2018/3 of SHELXL against F^2 on all data by full-matrix least squares.[60–62]

In the refinement, all non–hydrogen atoms of the MOF net, except the highly thermal disordered terminal methyl of the methylcysteine thioether chains from the mecysmox ligand, were refined anisotropically. The use of some C-C and C-S bond lengths restrains during the refinement, has been reasonably imposed and related to the extraordinary flexibility of methyl thioether chains from the

methionine residues, which are dynamic components of the frameworks. Disordered sites for atoms C4S and C4S' in refinement, belonging to the methylcysteine ligand, result disordered and have been refined on two different sites. All the hydrogen atoms of the net were set in calculated position and refined isotropically using the riding model.

The thermal disorder of fragments pointing towards the pores is likely related to the porosity of the network.

The solvent molecules, as normally observed for such porous crystals, were highly disordered and only a few of them were found from the ΔF map. The quite large channels featured by this series of MOFs likely account for that.

A summary of the crystallographic data and structure refinement for **$Sr^{II}Zn^{II}_6$-Mecysmox** crystal structure is given in Table 4.1.

The final geometrical calculations on free voids and the graphical manipulations were carried out with PLATON[63,64] implemented in WinGX,[65] and CRYSTAL MAKER[66] programs, respectively.

4.5.4. Gas adsorption experiments

The N_2 adsorption-desorption isotherms at 77 K were carried out on polycrystalline samples of **$Sr^{II}Zn^{II}_6$-Mecysmox**, before and after catalysis, with a BELSORP-mini-X instrument. Samples were first activated with methanol and then evacuated at 348 K during 19 hours under 10^{-6} Torr prior to the analysis.

4.5.5. X–ray powder diffraction measurements

Polycrystalline samples of **$Sr^{II}Zn^{II}_6$-Mecysmox**, before and after catalysis, were introduced into 0.5 mm borosilicate capillaries prior to being mounted and

aligned on an Empyrean PANalytical powder diffractometer, using Cu Kα radiation (λ = 1.54056 Å). For each sample, five repeated measurements were collected at room temperature (2θ = 2–45°) and merged in a single diffractogram.

4.5.6. Catalysis details

Products **2**, **4** and **5** were prepared following the same reaction scheme shown in the head of Table 4.2. Catalyst **$Sr^{II}Zn^{II}_6$-Mecysmox** (0.06 eq, 0.16 mmol), reactants **1** or **3** (1 eq, 2.72 mmol) and TOAB (0.02 eq, 0.058 mmol) in 1.7 mL of dry THF were introduced in a reactor equipped with a magnetic stirrer. Then, the reactor was closed, was purged with N_2 two times and carbon dioxide (25 bar) was introduced. The reaction was magnetically stirred in a pre-heated oil bath at 120 ºC during typically 4 h. After that time, the resulting mixture was filtered and analyzed by GC, GC-MS and NMR.

4.5.7. Physical techniques

Elemental (C, H, S, N) analysis was performed at the Microanalytical Service of the Universitat de València. FT–IR spectra were recorded on a Perkin-Elmer 882 spectrophotometer as KBr pellets. The thermogravimetric analysis was performed on crystalline samples under a dry N_2 atmosphere with a Mettler Toledo TGA/STDA 851^e thermobalance operating at a heating rate of 10 ºC min^{-1}.

4.6. References

(1) Furukawa, H.; Cordova, K. E.; O'Keeffe, M.; Yaghi, O. M. *Science* **2013**, *341* (6149), 974.

(2) Zhang, X.; Wang, B.; Alsalme, A.; Xiang, S.; Zhang, Z.; Chen, B. *Coord. Chem. Rev.* **2020**, *423*, 213507.

(3) Maurin, G.; Serre, C.; Cooper, A.; Férey, G. *Chem. Soc. Rev.* **2017**, *46* (11), 3104–3107.

(4) Mon, M.; Bruno, R.; Sanz-Navarro, S.; Negro, C.; Ferrando-Soria, J.; Bartella, L.; Di Donna, L.; Prejanò, M.; Marino, T.; Leyva-Pérez, A.; et al. *Nat. Commun.* **2020**, *11* (1), 3080.

(5) Rogge, S. M. J.; Bavykina, A.; Hajek, J.; Garcia, H.; Olivos-Suarez, A. I.; Sepúlveda-Escribano, A.; Vimont, A.; Clet, G.; Bazin, P.; Kapteijn, F.; et al. *Chem. Soc. Rev.* **2017**, *46* (11), 3134–3184.

(6) Lan, G.; Fan, Y.; Shi, W.; You, E.; Veroneau, S. S.; Lin, W. *Nat. Catal.* **2022**, *5* (11), 1006–1018.

(7) Chen, Z.; Jiang, H.; Li, M.; O'Keeffe, M.; Eddaoudi, M. *Chem. Rev.* **2020**, *120* (16), 8039–8065.

(8) Freund, R.; Canossa, S.; Cohen, S. M.; Yan, W.; Deng, H.; Guillerm, V.; Eddaoudi, M.; Madden, D. G.; Fairen-Jimenez, D.; Lyu, H.; et al. *Angew. Chem. Int. Ed.* **2021**, *60* (45), 23946–23974.

(9) Bavykina, A.; Kolobov, N.; Khan, I. S.; Bau, J. A.; Ramirez, A.; Gascon, J. *Chem. Rev.* **2020**, *120* (16), 8468–8535.

(10) Nam, D.-H.; Shekhah, O.; Lee, G.; Mallick, A.; Jiang, H.; Li, F.; Chen, B.; Wicks, J.; Eddaoudi, M.; Sargent, E. H. *J. Am. Chem. Soc.* **2020**, *142* (51), 21513–21521.

(11) Gai, S.; Zhang, J.; Fan, R.; Xing, K.; Chen, W.; Zhu, K.; Zheng, X.; Wang, P.; Fang, X.; Yang, Y. *ACS Appl. Mater. Interfaces* **2020**, *12* (7), 8650–8662.

(12) Moharramnejad, M.; Ehsani, A.; Salmani, S.; Shahi, M.; Malekshah, R. E.; Robatjazi, Z. S.; Parsimehr, H. *J. Inorg. Organomet. Polym. Mater.* **2022**, *32* (9), 3339–3354.

(13) Liu, W.; Pan, Y.; Xiao, W.; Xu, H.; Liu, D.; Ren, F.; Peng, X.; Liu, J. *Medchemcomm* **2019**, *10* (12), 2038–2051.

(14) Wei, C.; Tan, L.; Zhang, Y.; Xiong, S.; Feng, J. *ChemPhysMater* **2022**, *1* (4), 252–263.

(15) Nuzhdin, A. L.; Dybtsev, D. N.; Bryliakov, K. P.; Talsi, E. P.; Fedin, V. P. *J. Am. Chem. Soc.* **2007**, *129* (43), 12958–12959.

(16) Zhu, W.; Han, M.; Kim, D.; Zhang, Y.; Kwon, G.; You, J.; Jia, C.; Kim, J. *Environ. Res.* **2022**, *205*, 112417.

(17) Madasamy, K.; Kumaraguru, S.; Sankar, V.; Mannathan, S.; Kathiresan, M. *New J. Chem.* **2019**, *43* (9), 3793–3800.

(18) Ramish, S. M.; Ghorbani-Choghamarani, A.; Mohammadi, M. *Sci. Rep.* **2022**, *12* (1), 1479.

(19) *Zinc Catalysis*; Enthaler, S., Wu, X.-F., Eds.; Wiley-VCH Verlag GmbH & Co. KGaA: Weinheim, Germany, 2015.

(20) Oliver–Meseguer, J.; Ballesteros–Soberanas, J.; Tejeda–Serrano, M.; Martínez–Castelló, A.; Leyva–Pérez, A. *Mol. Catal.* **2021**, *515*, 111927.

(21) Hur, J.; Moon, I. *Ind. Eng. Chem. Res.* **2020**, *59* (7), 3091–3096.

(22) Tu, M.; Davis, R. J. *J. Catal.* **2001**, *199* (1), 85–91.

(23) Chang, Y.; Jiang, T.; Han, B.; Liu, Z.; Wu, W.; Gao, L.; Li, J.; Gao, H.; Zhao, G.; Huang, J. *Appl. Catal. A Gen.* **2004**, *263* (2), 179–186.

(24) Steinbauer, J.; Longwitz, L.; Frank, M.; Epping, J.; Kragl, U.; Werner, T. *Green Chem.* **2017**, *19* (18), 4435–4445.

(25) Chen, S.; Pudukudy, M.; Yue, Z.; Zhang, H.; Zhi, Y.; Ni, Y.; Shan, S.; Jia, Q. *Ind. Eng. Chem. Res.* **2019**, *58* (37), 17255–17265.

(26) Kurisingal, J. F.; Rachuri, Y.; Gu, Y.; Choe, Y.; Park, D.-W. *Chem. Eng. J.* **2020**, *386*, 121700.

(27) Wang, X.; Dong, Q.; Xu, Z.; Wu, Y.; Gao, D.; Xu, Y.; Ye, C.; Wen, Y.; Liu, A.; Long, Z.; et al. *Chem. Eng. J.* **2021**, *403*, 126460.

(28) Cavalleri, M.; Panza, N.; Biase, A.; Tseberlidis, G.; Rizzato, S.; Abbiati, G.; Caselli, A. *European J. Org. Chem.* **2021**, *2021* (19), 2764–2771.

(29) Liu, L.; Jayakumar, S.; Chen, J.; Tao, L.; Li, H.; Yang, Q.; Li, C. *ACS Appl. Mater. Interfaces* **2021**, *13* (25), 29522–29531.

(30) Upitak, K.; Thomas, C. M. *Acc. Chem. Res.* **2022**, *55* (16), 2168–2179.

(31) Escamilla, P.; Viciano-Chumillas, M.; Bruno, R.; Armentano, D.; Pardo, E.;

Ferrando-Soria, J. *Molecules* **2021**, *26* (13), 4098.

(32) Brunauer, S.; Emmett, P. H.; Teller, E. *J. Am. Chem. Soc.* **1938**, *60* (2), 309–319.

(33) Rouquerolt, J.; Avnir, D.; Fairbridge, C. W.; Everett, D. H.; Haynes, J. H.; Pernicone, N.; Ramsay, J. D. F.; Sing, K. S. W.; Unger, K. K. *Pure Appl. Chem.* **1994**, *66* (8), 1739–1758.

(34) Wang, F.; Xu, C.; Li, Z.; Xia, C.; Chen, J. *J. Mol. Catal. A Chem.* **2014**, *385*, 133–140.

(35) Cheng, W.; Fu, Z.; Wang, J.; Sun, J.; Zhang, S. *Synth. Commun.* **2012**, *42* (17), 2564–2573.

(36) Mon, M.; Ferrando-Soria, J.; Grancha, T.; Fortea-Pérez, F. R.; Gascon, J.; Leyva-Pérez, A.; Armentano, D.; Pardo, E. *J. Am. Chem. Soc.* **2016**, *138* (25), 7864–7867.

(37) Liu, W.-S.; Zhou, L.-J.; Li, G.; Yang, S.-L.; Gao, E.-Q. *ACS Sustain. Chem. Eng.* **2021**, *9* (4), 1880–1890.

(38) Zhang, Y.; Yang, G.; Xie, R.; Yang, L.; Li, B.; Wu, G. *Angew. Chem. Int. Ed.* **2020**, *59* (51), 23291–23298.

(39) Yue, Z.; Pudukudy, M.; Chen, S.; Liu, Y.; Zhao, W.; Wang, J.; Shan, S.; Jia, Q. *Appl. Catal. A Gen.* **2020**, *601*, 117646.

(40) Zhang, B.; Zhang, L.; Wu, Q.; Wang, Q.; Song, B.; Wu, W.; Lu, B.; Ren, T. *RSC Adv.* **2014**, *4* (39), 20506.

(41) Kurisingal, J. F.; Rachuri, Y.; Palakkal, A. S.; Pillai, R. S.; Gu, Y.; Choe, Y.; Park, D.-W. *ACS Appl. Mater. Interfaces* **2019**, *11* (44), 41458–41471.

(42) Rivero-Crespo, M. A.; Mon, M.; Ferrando-Soria, J.; Lopes, C. W.; Boronat, M.; Leyva-Pérez, A.; Corma, A.; Hernández-Garrido, J. C.; López-Haro, M.; Calvino, J. J.; et al. *Angew. Chem. Int. Ed.* **2018**, *57* (52), 17094–17099.

(43) Bilanin, C.; Tiburcio, E.; Ferrando-Soria, J.; Armentano, D.; Leyva-Pérez, A.; Pardo, E. *ChemCatChem* **2021**, *13* (4), 1195–1200.

(44) Wu, Y.; Song, X.; Xu, S.; Chen, Y.; Oderinde, O.; Gao, L.; Wei, R.; Xiao, G. *Dalt. Trans.* **2020**, *49* (2), 312–321.

(45) Gao, J.; Song, Q.-W.; He, L.-N.; Liu, C.; Yang, Z.-Z.; Han, X.; Li, X.-D.; Song, Q.-C. *Tetrahedron* **2012**, *68* (20), 3835–3842.

(46) Meng, X.-L.; Nie, Y.; Sun, J.; Cheng, W.-G.; Wang, J.-Q.; He, H.-Y.; Zhang, S.-

J. *Green Chem.* **2014**, *16* (5), 2771–2778.

(47) Ding, S.; Sun, L.; Ma, X.; Cheng, D.; Wu, S.; Zeng, R.; Deng, S.; Chen, C.; Zhang, N. *Catal. Letters* **2020**, *150* (10), 2970–2977.

(48) Zhang, W.; Wang, Q.; Wu, H.; Wu, P.; He, M. *Green Chem.* **2014**, *16* (11), 4767–4774.

(49) Su, Q.; Qi, Y.; Yao, X.; Cheng, W.; Dong, L.; Chen, S.; Zhang, S. *Green Chem.* **2018**, *20* (14), 3232–3241.

(50) Du, Y.-R.; Yang, X.; Wang, Y.-F.; Guan, P.-X.; Wang, R.; Xu, B.-H. *Mol. Catal.* **2022**, *520*, 112164.

(51) Li, G.; Dong, S.; Fu, P.; Yue, Q.; Zhou, Y.; Wang, J. *Green Chem.* **2022**, *24* (9), 3433–3460.

(52) Gulati, S.; Vijayan, S.; Mansi; Kumar, S.; Harikumar, B.; Trivedi, M.; Varma, R. S. *Coord. Chem. Rev.* **2023**, *474*, 214853.

(53) Wu, Q.-J.; Liang, J.; Huang, Y.-B.; Cao, R. *Acc. Chem. Res.* **2022**, *55* (20), 2978–2997.

(54) Schoedel, A.; Ji, Z.; Yaghi, O. M. *Nat. Energy* **2016**, *1* (4), 16034.

(55) Bhat, G. A.; Darensbourg, D. J. *Green Chem.* **2022**, *24* (13), 5007–5034.

(56) Yang, G.-W.; Zhang, Y.-Y.; Wu, G.-P. *Acc. Chem. Res.* **2021**, *54* (23), 4434–4448.

(57) Bruno, R.; Mon, M.; Escamilla, P.; Ferrando-Soria, J.; Esposito, E.; Fuoco, A.; Monteleone, M.; Jansen, J. C.; Elliani, R.; Tagarelli, A.; et al. *Adv. Funct. Mater.* **2021**, *31* (6), 2008499.

(58) SAINT, version 6.45, Bruker Analytical X-ray Systems, Madison, W. SAINT, Version 6.45, Bruker Analytical X-Ray Systems, Madison, WI. Bruker Analytical X-ray Systems: Madison, WI 2003.

(59) Sheldrick G.M. SADABS Program for Absorption Correction, version 2.10, Analytical X-ray Systems, Madison, W. SADABS Program for Absorption Correction, Version 2.10, Analytical X-Ray Systems, Madison, WI. Bruker Analytical X-ray Systems: Madison, WI 2003.

(60) Sheldrick, G. M. *Acta Crystallogr. Sect. C Struct. Chem.* **2015**, *71* (1), 3–8.

(61) Sheldrick, G. M. *Acta Crystallogr. A.* **2008**, *64* (1), 112–122.

(62) Madison, W. S.-2013/4 B. A. X. I. SHELXTL-2013/4, Bruker Analytical X-Ray

Instruments, Madison, WI. Bruker Analytical X-ray Instruments: Madison, WI 2013.

(63) Spek, A. L. *Acta Crystallogr. Sect. C Struct. Chem.* **2015**, *71* (1), 9–18.

(64) Spek, A. L. *Acta Crystallogr. Sect. D Biol. Crystallogr.* **2009**, *65* (2), 148–155.

(65) Farrugia, L. J. *J. Appl. Crystallogr.* **1999**, *32* (4), 837–838.

(66) Palmer, D. CRYSTAL MAKER, Cambridge University Technical Services, C. CRYSTAL MAKER, Cambridge University Technical Services, Cambridge. Cambridge University Technical Services: Cambridge 1996.

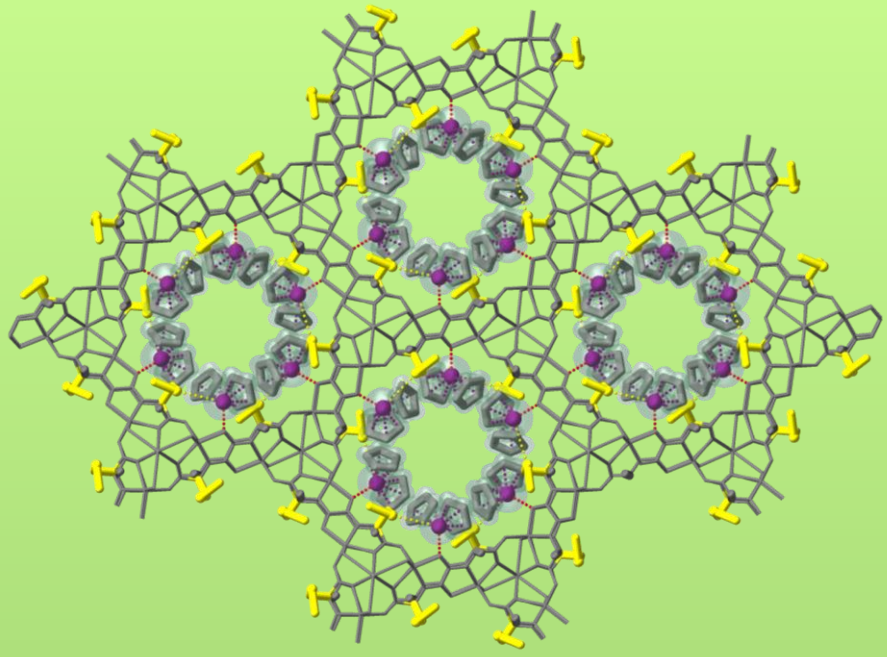

CHAPTER 5

General conclusions and perspectives

5.1. Conclusions

In the present doctoral thesis, a new family of Zn(II) oxamidato-based metal-organic frameworks (MOFs) has been successfully synthesized, fully characterized and applied in a myriad of different fields, thereby expanding the knowledge presented by my research group in the field of these porous materials. On the one hand, we have obtained a family of $Zn^{II}_6M^{II}$ (where M = Ca and Sr) oxamidato-based MOFs, which are isoreticular to a family of $Cu^{II}_6M^{II}$ MOFs, previously reported by my group. On the other hand, other families of Zn(II) oxamidato-based MOFs, exhibiting new architectures, have also been achieved. The main objective in following this strategy was to obtain MOFs with novel properties, that arise from the presence of Zn(II) cations. It is worth noting that this is the very first time that Zn(II)-based MOFs have been achieved with oxamato- or oxamidato-based ligands.

In particular, we have synthesized and fully characterized here three novel MOFs: one homometallic MOF, containing only Zn(II) cations and an oxamidato-based ligand derived from the natural amino acid *L*-serine, with formula $\{Zn^{II}_2[(S,S)\text{-serimox}](H_2O)_2\} \cdot H_2O$ and named **Zn^{II}_2-serimox**, which is used to degrade organic dyes present in wastewater (chapter 2 - MOFs for environmental decontamination), and two heterobimetallic MOFs –with formulas $\{Ca^{II}Zn^{II}_6[(S,S)\text{-Mecysmox}]_3(OH)_2(H_2O)\} \cdot 12H_2O$ (**$Ca^{II}Zn^{II}_6$-Mecysmox**) and $\{Sr^{II}Zn^{II}_6[(S,S)\text{-Mecysmox}]_3(OH)_2(H_2O)\} \cdot 9\ H_2O$ (**$Sr^{II}Zn^{II}_6$-Mecysmox**)– using, in both cases, the amino acid *S*-methyl-*L*-cysteine. I have explored the activity of **$Ca^{II}Zn^{II}_6$-Mecysmox** MOF in enzymatic catalysis. In particular, after a careful analysis of the Zn(II) coordination environment and also the functional empty space presented by this MOF, I explored the β-lactamase activity of this material, aiming at fully understanding the mechanisms governing the degradation of penicillinic antibiotics by bacteria (chapter 3 - MOFs in enzymatic catalysis). On the other side, **$Sr^{II}Zn^{II}_6$-Mecysmox** has been used, as an efficient catalyst, in the

cycloaddition reaction of ethylene oxide or propylene oxide with CO_2 for the production of ethylene and propylene carbonate (chapter 4 - MOFs as heterogeneous catalysts in industrial applications).

The synthesis of these new materials has been carried out using conventional methods of direct precipitation, which offer advantages such as ease and rapidity in synthesis, low cost, high yields, and the potential for large-scale production. The incorporation of Zn(II) cations within the frameworks cations allow the possibility to achieve new properties –not observed in the ancestor $Cu^{II}_6M^{II}$ MOFs– such as luminescence, photocatalysis or catalytic activity in certain enzymatic reactions. On the other side, the incorporation of amino acids in these ligands enables the synthesis of chiral MOFs that exhibit water stability and allow for the control of functional groups within the pore cavities, depending on the specific amino acid residue employed. This approach builds upon prior investigations conducted by my research group before the realization of this thesis.

On this basis, I expose the most relevant specific conclusions for each of the four chapters (including the introduction):

In the final section of the introduction (chapter 1), the main objective was offering a comprehensive overview of the previous results of my group, related to the preparation of Cu(II)-oxamidato based MOFs and the properties they exhibit. In so doing, we will be capable to analyze and compare advantages/disadvantages with the Zn(II)-based MOFs reported in this thesis. This comparison is not casual. It is clear that previous results of my group have somehow influenced the development and objectives of my PhD thesis.

In chapter 2, the first example of Zn(II)-based MOFs. In particular, a novel eco-friendly Zn(II) oxamidato-based MOF, derived from the amino acid *L*-serine,

named **Zn^{II}_2-serimox**, is presented. **Zn^{II}_2-serimox** structure could be solved using SCXRD, revealing a framework composed of dimeric units of Zn(II) with *trans* oxamidato-bridges, {Zn^{II}_2[(*S,S*)-serimox]}, assembled through the carboxylate groups present in the ligands. The MOF exhibits two types of pores: square-shaped pores of approximately 0.3 nm along the *b*-axis and irregular pores slightly larger, measuring 0.4 nm, along the *c*-axis, both decorated with hydrophilic groups (methyl alcohol arms) provided from the amino acid residue of the *L*-serine. This new Zn(II)-MOF acts as a photocatalyst, fully degrading the organic dye brilliant green in an aqueous solution yielding CO_2 and H_2O after only 120 minutes under UVC (250 nm) irradiation. The robustness and high crystallinity of this novel MOF also permitted to obtain the crystal structure of a host-guest aggregate containing CO_2 molecules within MOF channels after the photocatalytic process, also offering snapshots about the most plausible mechanism. The retention of CO_2 molecules within the pores is most-likely facilitated by the presence of hydroxyl arms within the cavities.

In chapter 3, another novel Zn(II) oxamidato-based MOF derived from the amino acid *S*-methyl-*L*-cysteine –with formula {$Ca^{II}Zn^{II}_6$[(*S*,*S*)-Mecysmox]$_3$(OH)$_2$(H_2O)} · 12 H_2O (**$Ca^{II}Zn^{II}_6$-Mecysmox**)– is presented. In contrast to the MOF described in chapter 2 (**Zn^{II}_2-serimox**), this new MOF –which is isostructural to a previously reported $Ca^{II}Cu^{II}_6$ MOF (**$Ca^{II}Cu^{II}_6$- Mecysmox**)– features moderately large hexagonal channels, densely decorated with thioether groups, derived from the residue of the amino acid used. These medium-sized functional channels offer the possibility to encapsulate and retain moderately large organic molecules. Moreover, as revealed by SCXRD experiments, the framework consists of dizinc(II) units, {Zn^{II}_2[(*S,S*)-Mecysmox]}, acting as linkers between the Ca(II) cations through carboxylate groups. Additionally, SCXRD showed that each Zn(II) atom is coordinated by water/hydroxide groups, allowing for enhanced interconnection with the rest of the dizinc(II) units. This zinc

coordination environment in the MOF, is reminiscent of certain enzymes from the Metallo-β-lactamase (MBLs) family. Overall, both characteristics, the functional empty space of the MOF and the coordination environment of Zn(II) cations, suggested that **$Ca^{II}Zn^{II}_6$-Mecysmox** could act as an efficient catalyst, mimicking β-lactamase enzymes, which are responsible for the degradation of penicillin antibiotics.

In this context, I tested the β-lactamase activity of **$Ca^{II}Zn^{II}_6$-Mecysmox** and I observed that it efficiently degrades the four-membered β-lactam ring present in amoxicillin antibiotic. This remarkable result, constitutes one of the very few examples of MOFs capable of mimicking catalytic enzymatic processes, which has been very limited thus far. Moreover, **$Ca^{II}Zn^{II}_6$- Mecysmox** can also hydrolyze another antibiotic such as ceftriaxone into throtriazinone and 3-desacetyl cefotaxime, a reaction that previously occurred only without a catalyst and at pH = 5. This new MOF **$Ca^{II}Zn^{II}_6$- Mecysmox**, exhibits two distinct behaviors. On one hand, the sulfur atoms present in the pore are capable of recognizing amoxicillin and ceftriaxone and immobilizing them through σ-hole interactions. On the other hand, the zinc coordination environment, reminiscent of MBLs, allows this enzymatic catalytic reaction to take place, unlike the analogous Cu(II)-MOF (**$Ca^{II}Cu^{II}_6$-Mecysmox**), which was also tested for comparison and showed conversion percentages below 5%. This demonstrates that although both MOFs are isoreticular, their properties can be significantly different due to the different nature of metal cations present in the framework. It is worth noting the robustness and crystallinity of this new MOF, which allowed for the characterization of the structure with amoxicillin hosted in its cavities. By using the crystallographic data, a plausible mechanism could be proposed through DFT calculations, representing a step forward in the understanding of β-lactamase enzymes.

In chapter 4, another previously unreported MOF, with formula $\{Sr^{II}Zn^{II}_6[(S,S)\text{-Mecysmox}]_3(OH)_2(H_2O)\} \cdot 9H_2O$ (**$Sr^{II}Zn^{II}_6$-Mecysmox**), is prepared and characterized. **$Sr^{II}Zn^{II}_6$-Mecysmox** is isostructural to the one described in chapter 3 ($\{Ca^{II}Zn^{II}_6[(S,S)\text{-Mecysmox}]_3(OH)_2(H_2O)\} \cdot 12H_2O$ (**$Ca^{II}Zn^{II}_6$- Mecysmox**)), but with slightly enhanced robustness, which seemed an important point aiming at exploring its catalytic properties. In this context, taking also into account previous results (chapter 3) regarding the ability of this family of MOFs to encapsulate a plethora of guest molecules within their functional channels and the existence of accessible Zn(II) cations within the framework, **$Sr^{II}Zn^{II}_6$-Mecysmox** has been evaluated as a heterogeneous catalyst for the cycloaddition reaction of ethylene oxide and propylene oxide with CO_2 to yield ethylene and propylene carbonates. The main objective was to offer an appealing alternative to current metal-free heterogeneous catalysts, for the production of these industrially important ethylene and propylene carbonates. Indeed, both solvents are widely used in fine chemistry, serve as electrolytes in lithium batteries, and acts as intermediates in other industrially relevant syntheses. **$Sr^{II}Zn^{II}_6$-Mecysmox** exhibited remarkable catalysis with high yields, exceeding 90%. Moreover, the ultra-small pore size and unique pore environment of the MOF enables 100% selectivity in ethylene carbonate synthesis, without competitive hydrolysis or polymerization reactions. Additionally, these two factors also explained that propylene oxide reacted similarly to ethylene oxide, despite the former being ten times less reactive.

5.2. Perspectives

Chapters 2-4, show a series of illustrative and successful examples of the strategy proposed in the initial objectives. Indeed, three novel Zn(II)-based MOFs have been obtained, fully characterised, and shown application in three important fields like photocatalysis, enzymatic catalysis and organic synthesis. However, these results, although the most complete, are not the only ones

obtained in this thesis. Thus, other very interesting Zn(II)-based MOFs have been obtained as well, and even, certain preliminary measurements have been carried out in order to assess their potential in a myriad of applications. In particular, the following isoreticular MOFs have been prepared: $\{Ca^{II}Zn^{II}_6[(S,S)\text{-alamox}]_3(OH)_2(H_2O)\} \cdot 10H_2O$ (**$Ca^{II}Zn^{II}_6$-alamox**) [where alamox = bis[*L*-alanine]oxalyl diamide], $\{Ca^{II}Zn^{II}_6[(S,S)\text{-methox}]_3(OH)_2(H_2O)\} \cdot 8H_2O$ (**$Ca^{II}Zn^{II}_6$-methox**) [where methox = bis[*L*-methionine]oxalyl diamide] and even three multivariate MOFs (MTV-MOF) with the following formulas $\{Ca^{II}Zn^{II}_6[(S,S)\text{-Mecysmox}]_{1.5}[(S,S)\text{-methox}]_{1.5}(OH)_2(H_2O)\} \cdot 9H_2O$ (**$Ca^{II}Zn^{II}_6$- Mecysmox/methox**), $\{Ca^{II}Zn^{II}_6[(S,S)\text{-Mecysmox}]_{1.5}[(S,S)\text{-alamox}]_{1.5}(OH)_2(H_2O)\} \cdot 11H_2O$ (**$Ca^{II}Zn^{II}_6$-Mecysmox/alamox**) and $\{Ca^{II}Zn^{II}_6[(S,S)\text{-methox}]_{1.5}[(S,S)\text{-alamox}]_{1.5}(OH)_2(H_2O)\} \cdot 8H_2O$ (**$Ca^{II}Zn^{II}_6$- methox/alamox**), which contain, within their isoreticular structures, 50% of two different amino acids. The most relevant prospectives for all these MOFs are gathered below.

5.2.1. Luminescent sensors

It is well-known that zinc(II) cations can exhibit luminescence under certain conditions. In particular, luminescence properties of zinc(II) coordination compounds have been broadly studied due to the fact that the ligands can affect the electronic properties of the zinc(II) cations, which can influence their luminescence behavior. This fact opens also the window for the development of luminescent sensors, considering that subtle changes in the coordination environment of Zn(II) cations fine-tune its emission properties. Zn(II)-based MOFs are the most suitable candidates to behave as a sensor. Indeed, the porous nature of these materials allows to host guest molecules within their channels, which ultimately can induce changes in the coordination environment of Zn(II) cations, fine-tuning their luminescence depending on the nature of the guest.

For example, the emission spectra of **$Ca^{II}Zn^{II}_6$-alamox** (Figure 5.1a) is shown in Figure 5.1b. It can be observed a clear emission band at *ca.* 480 nm, which must be attributed, unambiguously, to Zn(II) cations. Moreover, taking into account the previously reported ability of this family of MOFs to host guest molecules, it is quite obvious to predict that certain changes in the coordination environment of Zn(II) cations should occur depending on the nature of the guest, which ultimately leads to a sensor behavior. **$Ca^{II}Zn^{II}_6$- Mecysmox** and **$Ca^{II}Zn^{II}_6$-methox** MOFs are the most promising candidates, considering that their channels are densely decorated with thioether groups, capable to retain and encapsulate guest molecules.

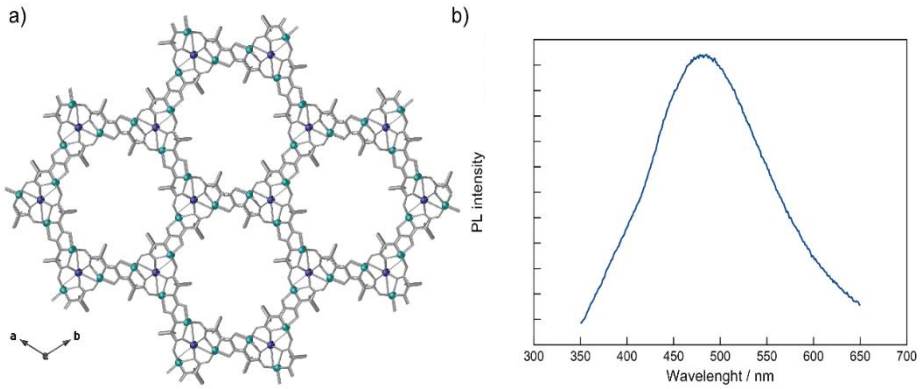

Figure 5.1. (a) Perspective view, along the crystallographic *c* axis of the porous structure of **$Ca^{II}Zn^{II}_6$-alamox**. Zinc and calcium atoms are represented by cyan and blue spheres, respectively, whereas organic ligands are depicted as gray sticks. The methyl groups (-CH_3) from the amino acid (*L*-alanine) residues are represented as thick gray sticks. (b) Emission spectra of **$Ca^{II}Zn^{II}_6$-alamox** (λ_{exc} = 300 nm).

5.2.2. Photocatalysis

One advantage of using Zn(II) as a photocatalyst is that this metal is a relatively inexpensive and abundant element, which could make its application more cost-effective and scalable. Additionally, Zn(II) has good photocatalytic properties, such as strong light absorption and efficient electron transfer. A good number of Zn(II) coordination complexes (and also coordination polymers or

MOFs) have been studied as photocatalysts, that is, they can absorb light and use that energy to drive chemical reactions. For example, there is a good number of Zn(II) compounds that have been used for the photocatalytic reduction of carbon dioxide (CO_2), which is a well-known greenhouse gas that contributes to climate change. In this reaction, when exposed to light, Zn(II) photocatalysts can reduce CO_2 to produce valuable chemicals such as CH_4 or CH_3OH. This reaction is particularly suitable aiming at industrial application of these materials.

We have proven that some Zn(II)-based MOFs, reported in this thesis, are able to act as photocatalysts to degrade organic molecules such as organic dyes (see chapter 2) giving CO_2 and H_2O. It is planned that these novel families of MOFs are explored to complete the cycle by further reducing formed CO_2.

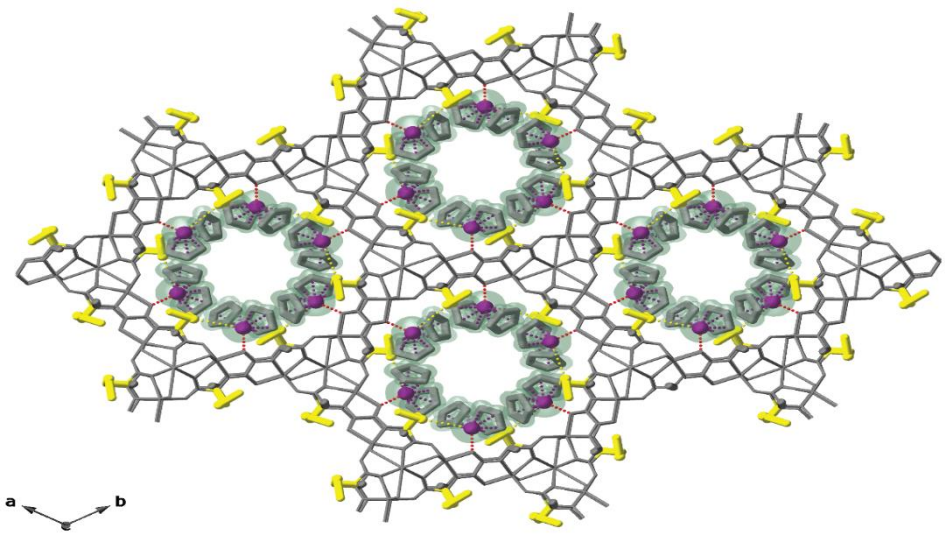

Figure 5.2. Perspective view, along the crystallographic *c* axis of the porous structure of **Ti(Cp)$_2$@Ca^{II}Zn$^{II}_6$-mecysmox/alamox**. Zinc and calcium atoms and organic ligands from the network are depicted as gray sticks for clarity. The *L*-alanine and *L*-methionine residues (-CH_3 and –$CH_2CH_2SCH_3$) are represented as thick gray and orange sticks, respectively. Titanium atoms are represented as purple spheres and the cyclopentadienyl carbon atoms are depicted as thick gray sticks. The whole **Ti(Cp)$_2$** moieties are also represented as a green surface for the sake of clarity.

Moreover, I plan to go one step further by encapsulation within the channels of the MOF, taking advantage of the already described thrilling host-guest chemistry of this family of MOFs, other photocatalytic species. For example, as a preliminary but highly promising result we have been capable to encapsulate bis(cyclopentadienyl)titanium dichloride within the MTV-MOF **$Ca^{II}Zn^{II}_6$-mecysmox/alamox**. Remarkably, we have been capable to obtain the crystal structure of this host-guest aggregate (Figure 5.2), named **$Ti(Cp)_2$@$Ca^{II}Zn^{II}_6$-mecysmox/alamox**, which was undoubtedly a challenge and helped to gain structural information about this Ti(IV) species. The photocatalytic properties of this material will be explored in a near future but I am optimistic about its performance.

5.2.3. Drug delivery

MOFs have also attracted a lot of attention for their potential applications in drug delivery due to their high surface area and tunable pore size, which can allow for the encapsulation and controlled release of drugs. One advantage of using MOFs for drug delivery is their high loading capacity, which can enable the delivery of a large amount of drug molecules. Additionally, the porous nature of MOFs can protect the drugs from degradation and improve their stability. However, one requirement that these porous material should present to be suitable candidates for drug delivery is a total biocompatibility.

In this context, the family of MOFs reported in this thesis fulfil all these requirements. First, a thrilling host-guest chemistry that ensures a proper immobilization/loading of the guest molecules. On this basis, I believe that **$Ca^{II}Zn^{II}_6$-Mecysmox** and **$Ca^{II}Zn^{II}_6$-methox** (Figure 5.3) are particularly suitable given their proven host-guest properties. Second, the use of bioligands derived from amino acids and biocompatible metals as Zn and Ca suggested us that these MOFs should be compatible. This point has already been proven with the

biocompatible tests shown in Figure 5.3b. Future works will be devoted to explore loading and release of important drugs (including *in-vitro* and *in-vivo* experiments). In fact, preliminary measurements of encapsulation and delivery of losartan (a drug that is mainly used to treat high blood pressure) are highly promising.

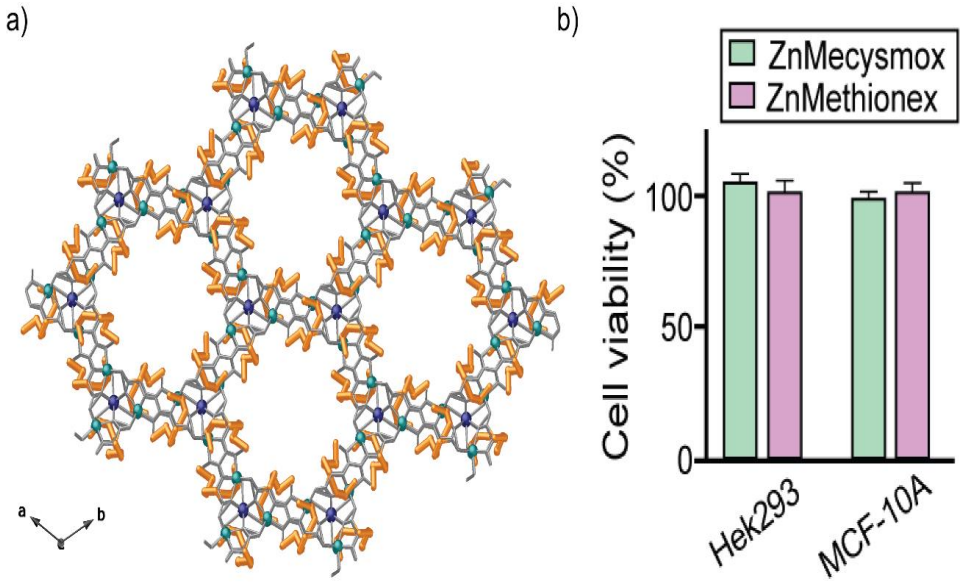

Figure 5.3. (a) Perspective view, along the crystallographic *c* axis of the porous structure of **$Ca^{II}Zn^{II}_6$-methox**. Zinc and calcium atoms are represented by cyan and blue spheres, respectively, whereas organic ligands are depicted as gray sticks. The $–CH_2$ CH_2SCH_3 chains from the amino acid (*L*-methionine) residues are represented as thick orange sticks. (b) Biocompatibility tests: cell viability of HeK293 and MCF-10A cells after exposure to **$Ca^{II}Zn^{II}_6$-Mecysmox** (green bars) and **$Ca^{II}Zn^{II}_6$-methox** (pink bars).

5.2.4. Water remediation and gas/molecules separation

MOFs have already shown application in water remediation and, of course, the separation of molecules from both aqueous or gaseous phases. In both applications, the already described thrilling host-guest chemistry of MOFs are responsible for such efficiency as they can selectively capture and remove pollutants from water or separate molecules. Thus, MOFs can be used in water

remediation for the removal of heavy metals such as lead, cadmium, and mercury or a wide variety of organic molecules (such as dyes, pharmaceuticals, and pesticides). In this sense, MOFs can be designed to have specific functional groups that can selectively bind to these metals or organic molecules, allowing them to be removed from water or selectively capture one of the components of a mixture.

In particular, isoreticular oxamidato-based **$Ca^{II}Cu^{II}_6$** MOFs from my group, have already shown excellent performances in both fields. I have described in detail these results in the last subsection of the introduction. This great efficiency can be reproduced with the **$Ca^{II}Zn^{II}_6$** MOFs presented in this thesis, which, on the other hand, present clear advantage as they are more ecofriendly and can be prepared in large-scale easier. In this respect, MTV-MOFs are particularly appealing as they offer the possibility to introduce "*a la carte*" more than one functional group, thus increasing the affinity for the molecules intended to separate/capture.

The three MTV-MOFs that I have prepared (**$Ca^{II}Zn^{II}_6$- Mecysmox/methox**, **$Ca^{II}Zn^{II}_6$-Mecysmox/alamox** and **$Ca^{II}Zn^{II}_6$- methox/alamox**) will be tested in both applications. Their crystal structures are shown in Figure 5.4.

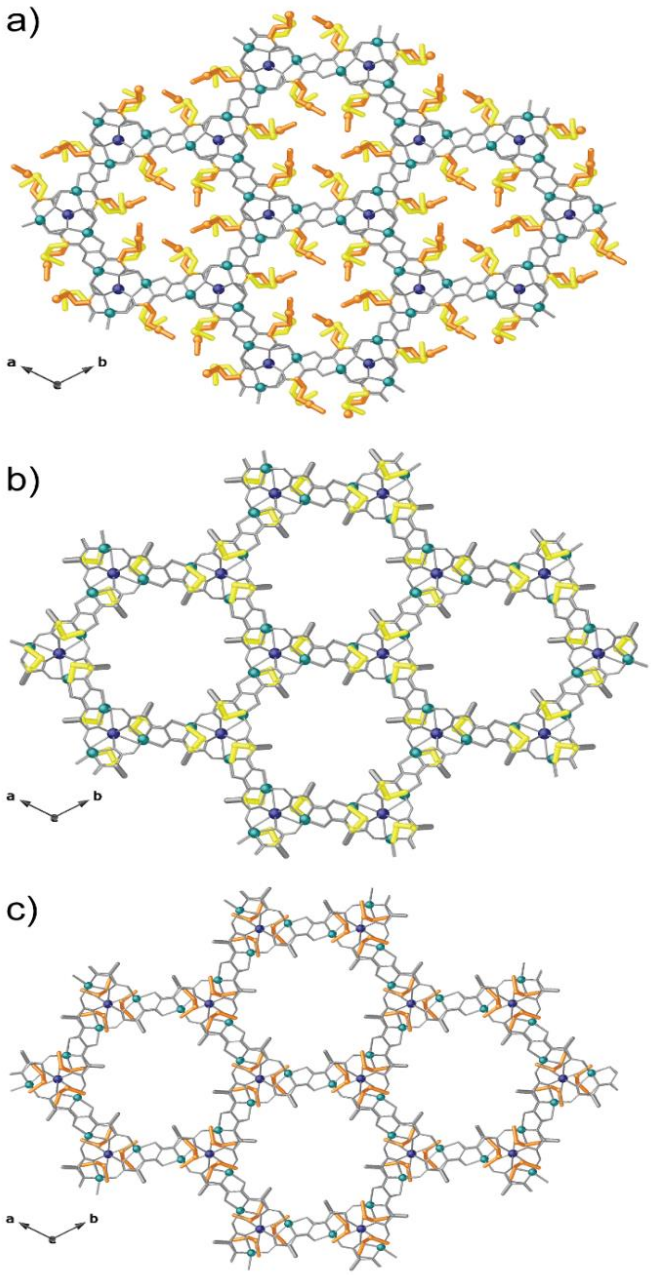

Figure 5.4. Perspective view, along the crystallographic *c* axis of the porous structures of **$Ca^{II}Zn^{II}_6$-Mecysmox/methox** (a), **$Ca^{II}Zn^{II}_6$-Mecysmox/alamox** (b) and **$Ca^{II}Zn^{II}_6$-methox/alamox** (c). Zinc and calcium atoms are represented by cyan and blue spheres, respectively, whereas organic ligands are depicted as gray sticks. The -CH_3, -CH_2SCH_3 and –$CH_2CH_2SCH_3$ chains from the amino acids *L*-alanine, *S*-methyl-*L*-cysteine and *L*-methione, respectively, are represented as thick gray, yellow and orange, respectively, sticks.

5.2.5. Metal catalysis

Technological advances are intimately ligated to the use and development of metal forms. In particular, the preparation of structurally and electronically well-defined sub-nanometer metal clusters (SNMCs) and also single atom catalysts (SACs) is extremely challenging but offer great potential rewards given their outstanding chemical properties. These sub-nanometric structures, with all atoms outer exposed and interacting between them, possess unique properties, relevant to many technological areas of interest in modern societies, from Industry to Medicine, their synthesis even at the milligram scale is far from being a reality.

Metal-organic frameworks have become relevant, in recent years, in this field. Indeed, MOFs can be used as chemical nanoreactors, taking advantage of the limited space within their functional pores, to grow these small metal species *in-situ*. In particular, the isoreticular $M^{II}Cu^{II}_6$ MOFs synthesized by my group have been shown as excellent vessels to prepare SNMCs and SACs with outstanding catalytic properties.

Following this approach, it is envisaged to use the novel family of $M^{II}Zn^{II}_6$ MOFs for the preparation of novel SNMCs and SACs in catalysis but also for the preparation of optical devices. Indeed, this is a great advantage of $M^{II}Zn^{II}_6$ versus $M^{II}Cu^{II}_6$ as a consequence of the well-known quenching effects that copper(II) cations usually exhibit. In particular **$Ca^{II}Zn^{II}_6$-Mecysmox, $Ca^{II}Zn^{II}_6$-methox** and also the MTV MOFs **$Ca^{II}Zn^{II}_6$-Mecysmox/methox**, **$Ca^{II}Zn^{II}_6$-Mecysmox/alamox** and **$Ca^{II}Zn^{II}_6$-methox/alamox**, are the most suitable candidates, as the thioether arms decorating their pores possess great affinity for noble metal atoms, and the resulting SNMCs and SACs show particularly superb catalytic properties. In this sense, I have already obtained preliminary but promising results by encapsulating noble metal cations like Ag(I) or Pd(II) within **$Ca^{II}Zn^{II}_6$-Mecysmox** and the crystal

structure of the resulting host-guest aggregates could be solved (Figure 5.5). This last point is particularly remarkable as it shows that this family of MOFs are capable to resist postsynthetic processes in the formation process maintaining also their crystallinity.

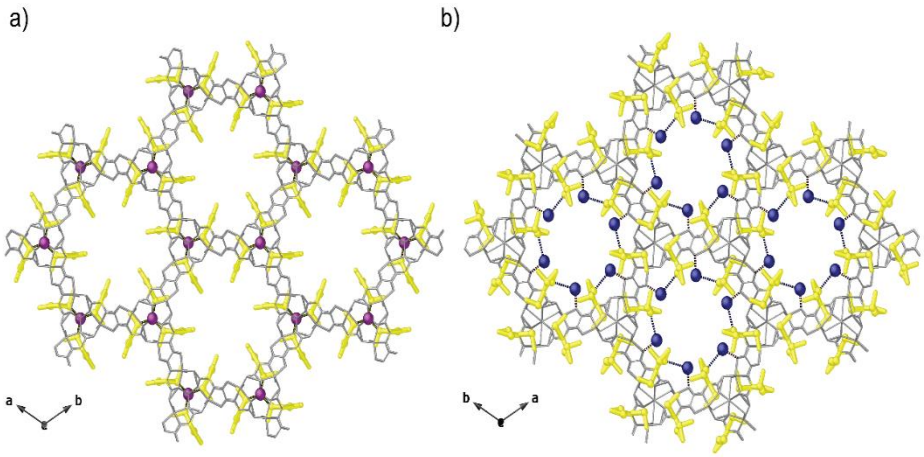

Figure 5.5. Perspective view, along the crystallographic *c* axis of the porous structures of **Ag(I)@Ca^{II}Zn$^{II}_6$-Mecysmox** (a) and **Pd(II)@Ca^{II}Zn$^{II}_6$-Mecysmox** (b). Zinc and calcium atoms from the network and organic ligands are depicted as gray sticks for the sake of clarity. The -CH_2SCH_3 chains from the amino acid S-methyl-L-cysteine are represented as thick yellow sticks. Guest silver and palladium atoms are depicted as purple and blue spheres.

Publications

Publications related to this thesis:

- Escamilla, P.; Viciano-Chumillas, M.; Bruno, R.; Armentano, D.; Pardo, E.; Ferrando-Soria, J. Photodegradation of Brilliant Green Dye by a Zinc BioMOF and Crystallographic Visualization of Resulting CO_2. *Molecules* **2021**, *26* (13), 4098.
- Escamilla, P.; Bartella, L.; Sanz-Navarro, S.; Percoco, R. M.; Di Donna, L.; Prejanò, M.; Marino, T.; Ferrando-Soria, J.; Armentano, D.; Pardo, E. Degradation of penicillinic antibiotics and β-lactamase enzymatic catalysis in a biomimetic Zn-based metal–organic framework. *Chem.- A Eur. J.* (In press)
- Escamilla, P.; Bilanin, C.; Ferrando-Soria, J.; Leyva-Pérez, J.; Armentano, D.; Pardo, E. Selective cycloaddition of ethylene oxide to CO_2 within the confined space of an amino acid-based metal-organic framework. (Submitted)

Other publications:

- Escamilla, P.; Guerra, W.D.; Leyva-Pérez, A.; Armenanto, D.; Ferrando-Soria, J.; Pardo, E. Metal-Organic Frameworks as Chemical Nanoreactos for the Preparation of Catalytically Active Metal Compounds. *Chem. Commun.* **2023**, *59* (7), 836-851.
- Negro, C.; Escamilla, P.; Bruno, R.; Ferrando-Soria, J.; Armentano, D.; Pardo, E. Metal-Organic Frameworks as Unique Platforms to Gain Insight of σ-Hole Interacttions for the Removal of Organic Dyes from Aquatic Ecosystems. *Chem.- A Eur. J.* **2022**, *28* (24), e202200034.
- Bruno, R.; Mon, M.; Escamilla, P.; Ferrando-Soria, J.; Esposito, E.; Fuoco, A.; Monteleone, M.; Jansen, J.; Elliano, R.; Tagarelli, A.; Armentano, D.; Pardo, E. Bioinspired Metal-Organic Frameworks in Mixed Matrix Memabranes for Efficient Static/Dynamic Removal of Mercury from Water. *Adv. Funct. Mater.* **2021**, *31*, e2009499.